Comparison on the digital gene expression data analyzing methods

Chia-Ching Chang, Ai-Ling Hour

Fu Jen Catholic University, Taiwan, ROC

Abstract

Modern molecular biology techniques present major challenges for the statistical methods that are used for digital gene expression (DGE) data in which the abundance is observed as a count. Therefore, the methods which are successful for microarray data are not directly applicable to DGE data. In this study, two sets of DGE data were applied to compare the manipulation of edgeR algorithm with two other methods, Z-test and weighted deviation (Wd).

Key words: Digital Gene Expression (DGE),
Serial Analysis of GeneExpression (SAGE),
Massively Parallel Signature Sequencing (MPSS), edgeR

expression profiling in all organisms. Brief Funct Genomic Proteomic 1(1): 95-104.
25. Robinson, M. D., D. J. McCarthy and G. K. Smyth (2010). edgeR: a Bioconductor package for differential expression analysis of digital gene expression data. Bioinformatics 26(1): 139-140.
26. Sasaki, T., J. Song, Y. Koga-Ban, E. Matsui, F. Fang, H. Higo, H. Nagasaki, M. Hori, M. Miya, E. Murayama-Kayano and et al. (1994). Toward cataloguing all rice genes: large-scale sequencing of randomly chosen rice cDNAs from a callus cDNA library. Plant J 6(4): 615-624.
27. Schena, M., D. Shalon, R. W. Davis and P. O. Brown (1995). Quantitative monitoring of gene expression patterns with a complementary DNA microarray. Science 270(5235): 467-470.
28. Stein, L. (2001). Genome annotation: from sequence to biology. Nat Rev Genet 2(7): 493-503.
29. Su, C. L., C. I. Chung, Y. C. Lin, P. C. Lu, F. J. Wei, Y. I. Hsing and A. L. Hour (2005). Statistical analysis of rice SAGE data. Genet Mol Biol 16(4): 248-260.
30. Torres, T. T., M. Metta, B. Ottenwalder and C. Schlotterer (2008). Gene expression profiling by massively parallel sequencing. Genome Res 18(1): 172-177.
31. Truckenmiller, M. E., M. P. Vawter, C. Cheadle, M. Coggiano, D. M. Donovan, W. J. Freed and K. G. Becker (2001). Gene expression profile in early stage of retinoic acid-induced differentiation of human SH-SY5Y neuroblastoma cells. Restor Neurol Neurosci 18(2-3): 67-80.
32. van Kampen, A. H., B. D. van Schaik, E. Pauws, E. M. Michiels, J. M. Ruijter, H. N. Caron, R. Versteeg, S. H. Heisterkamp, J. A. Leunissen, F. Baas and M. van der Mee (2000). USAGE: a web-based approach towards the analysis of SAGE data. Serial Analysis of Gene Expression. Bioinformatics 16(10): 899-905.
33. Velculescu, V. E., L. Zhang, B. Vogelstein and K. W. Kinzler (1995). Serial analysis of gene expression. Science 270(5235): 484-487.
34. Velculescu, V. E., L. Zhang, W. Zhou, J. Vogelstein, M. A. Basrai, D. E. Bassett, Jr., P. Hieter, B. Vogelstein and K. W. Kinzler (1997). Characterization of the yeast transcriptome. Cell 88(2): 243-251.
35. Wahl, M. B., U. Heinzmann and K. Imai (2005). LongSAGE analysis significantly improves genome annotation: identifications of novel genes and alternative transcripts in the mouse. Bioinformatics 21(8): 1393-1400.
36. Weber, A. P., K. L. Weber, K. Carr, C. Wilkerson and J. B. Ohlrogge (2007). Sampling the Arabidopsis transcriptome with massively parallel pyrosequencing. Plant Physiol 144(1): 32-42.

Recevied Oct 30, 2013
Revised Feb 22, 2014
Accepted Feb 22, 2014

and A. H. Meijer (2009). Deep sequencing of the zebrafish transcriptome response to mycobacterium infection. Mol Immunol 46(15): 2918-2930.

12. Huang, M. D., F. J. Wei, C. C. Wu, Y. I. Hsing and A. H. Huang (2009). Analyses of advanced rice anther transcriptomes reveal global tapetum secretory functions and potential proteins for lipid exine formation. Plant Physiol 149(2): 694-707.
13. Kal, A. J., A. J. van Zonneveld, V. Benes, M. van den Berg, M. G. Koerkamp, K. Albermann, N. Strack, J. M. Ruijter, A. Richter, B. Dujon, W. Ansorge and H. F. Tabak (1999). Dynamics of gene expression revealed by comparison of serial analysis of gene expression transcript profiles from yeast grown on two different carbon sources. Mol Biol Cell 10(6): 1859-1872.
14. Kanehisa, M. and P. Bork (2003). Bioinformatics in the post-sequence era. Nat Genet 33 Suppl: 305-310.
15. Lash, A. E., C. M. Tolstoshev, L. Wagner, G. D. Schuler, R. L. Strausberg, G. J. Riggins and S. F. Altschul (2000). SAGEmap: a public gene expression resource. Genome Res 10(7): 1051-1060.
16. Liang, P. and A. B. Pardee (1992). Differential display of eukaryotic messenger RNA by means of the polymerase chain reaction. Science 257(5072): 967-971.
17. Lisitsyn, N. and M. Wigler (1993). Cloning the differences between two complex genomes. Science 259(5097): 946-951.
18. Mardis, E. R. (2008). Next-generation DNA sequencing methods. Annu Rev Genomics Hum Genet 9: 387-402.
19. Margulies, E. H. and J. W. Innis (2000). eSAGE: managing and analysing data generated with serial analysis of gene expression (SAGE). Bioinformatics 16(7): 650-651.
20. Matsumura, H., D. H. Kruger, G. Kahl and R. Terauchi (2008). SuperSAGE: a modern platform for genome-wide quantitative transcript profiling. Curr Pharm Biotechnol 9(5): 368-374.
21. Matsumura, H., S. Reich, A. Ito, H. Saitoh, S. Kamoun, P. Winter, G. Kahl, M. Reuter, D. H. Kruger and R. Terauchi (2003). Gene expression analysis of plant host-pathogen interactions by SuperSAGE. Proc Natl Acad Sci USA 100(26): 15718-15723.
22. Nadon, R. and J. Shoemaker (2002). Statistical issues with microarrays: processing and analysis. Trends Genet 18(5): 265-271.
23. Nobuta, K., R. C. Venu, C. Lu, A. Belo, K. Vemaraju, K. Kulkarni, W. Wang, M. Pillay, P. J. Green, G. L. Wang and B. C. Meyers (2007). An expression atlas of rice mRNAs and small RNAs. Nat Biotechnol 25(4): 473-477.
24. Reinartz, J., E. Bruyns, J. Z. Lin, T. Burcham, S. Brenner, B. Bowen, M. Kramer and R. Woychik (2002). Massively parallel signature sequencing (MPSS) as a tool for in-depth quantitative gene

參考文獻

1. Adams, M. D. (1996). Serial analysis of gene expression: ESTs get smaller. Bioessays 18(4): 261-262.
2. Adams, M. D., J. M. Kelley, J. D. Gocayne, M. Dubnick, M. H. Polymeropoulos, H. Xiao, C. R. Merril, A. Wu, B. Olde, R. F. Moreno and et al. (1991). Complementary DNA sequencing: expressed sequence tags and human genome project. Science 252(5013): 1651-1656.
3. Anisimov, S. V. (2008). Serial Analysis of Gene Expression (SAGE): 13 years of application in research. Curr Pharm Biotechnol 9(5): 338-350.
4. Bainbridge, M. N., R. L. Warren, M. Hirst, T. Romanuik, T. Zeng, A. Go, A. Delaney, M. Griffith, M. Hickenbotham, V. Magrini, E. R. Mardis, M. D. Sadar, A. S. Siddiqui, M. A. Marra and S. J. Jones (2006). Analysis of the prostate cancer cell line LNCaP transcriptome using a sequencing-by-synthesis approach. BMC Genomics 7: 246.
5. Bureau, J. F., S. Chirinian, S. Ozden, C. Aubert and M. Brahic (1990). Isolation of a specific cellular mRNA by subtractive hybridization in Theiler's virus persistent infection. Microb Pathog 8(5): 335-341.
6. Chen, H., M. Centola, S. F. Altschul and H. Metzger (1998). Characterization of gene expression in resting and activated mast cells. J Exp Med 188(9): 1657-1668.
7. Cheung, F., B. J. Haas, S. M. D. Goldberg, G. D. May, Y. L. Xiao and C. D. Town (2006). Sequencing Medicago truncatula expressed sequenced tags using 454 Life Sciences technology. BMC Genomics 7: 272.
8. Datson, N. A., J. van der Perk-de Jong, M. P. van den Berg, E. R. de Kloet and E. Vreugdenhil (1999). MicroSAGE: a modified procedure for serial analysis of gene expression in limited amounts of tissue. Nucleic Acids Res 27(5): 1300-1307.
9. Diatchenko, L., Y. F. Lau, A. P. Campbell, A. Chenchik, F. Moqadam, B. Huang, S. Lukyanov, K. Lukyanov, N. Gurskaya, E. D. Sverdlov and P. D. Siebert (1996). Suppression subtractive hybridization: a method for generating differentially regulated or tissue-specific cDNA probes and libraries. Proc Natl Acad Sci USA 93(12): 6025-6030.
10. Hashimoto, S., W. Qu, B. Ahsan, K. Ogoshi, A. Sasaki, Y. Nakatani, Y. Lee, M. Ogawa, A. Ametani, Y. Suzuki, S. Sugano, C. C. Lee, R. C. Nutter, S. Morishita and K. Matsushima (2009). High-resolution analysis of the 5 '-end transcriptome using a next generation DNA sequencer. PLoS One 4(1): e4108.
11. Hegedus, Z., A. Zakrzewska, V. C. Agoston, A. Ordas, P. Racz, M. Mink, H. P. Spaink

這些資料中必定有部分包含著誤差，但也有部分包含著未知而尚待發掘的序列。

本文使用的三個顯著性測驗方法，edgeR、Z-test、Wd，應用在互相比較的兩組資料時，若兩組資料差異大，則三個方法所篩選出的資料較相似，也因為三個方法所篩選出的資料相似程度較高，取交集後，互相比較的兩組差異大的資料會篩選出較多筆有顯著差異的資料；若兩組資料差異小時，則三個方法所篩選出的資料差異較大，也因為三個方法所篩選出的資料差異較大，取交集後，互相比較的兩組差異小資料會篩選出較少筆有顯著差異的資料；如此情況與預期結果相符合，差異大的兩筆資料，能篩選出較多筆顯著差異資料；差異小的兩筆資料，篩選出較少筆顯著差異資料。而三個顯著性測驗方法依顯著值在 SAGE 的資料時挑出前 200 筆資料，在 MPSS 的資料時挑出前 5,000 筆資料互相比較，如此篩選資料筆數的設定原因在於若是設定固定 p-value 來篩選資料，則三個方法所挑選出的資料做比較時，筆數相差太大，所以必須將 p-value 做為參考來制訂一個三個方法都篩選出相同的資料筆數才方便做比較，然而以 p-value 做為參考還需要權衡基因庫與基因庫之間的差異，若相比較的基因庫之間差異較大時，則取相同資料筆數時 p-value 較小，若相比較的基因庫之間差異較小時，則取相同資料筆數時 p-value 較大，所以需要權衡基因庫與基因庫之間的差異，設定出較合適的依顯著值挑出的資料筆數。

edgeR 與 Z-test 二方法經過校正，所以當基因庫的資料筆數差異大時，容易受到影響而偏向其中一組，但 Wd 法較不易受影響；Wd 法的缺點則是，對於表現量較小的資料篩選時較為寬鬆，對於表現量較大的資料篩選時較嚴苛，edgeR 及 Z-test 正好相反，對於表現量較小的資料篩選時較為嚴苛，對於表現量較大的資料篩選時較寬鬆，可互相補充不足。類似的 MPSS 資料以 transcripts per million (TPM) 的方法篩選出的顯著基因結果 (Huang et al., 2009)，此篇文獻公開 7 個基因庫前 50 筆共 350 筆顯著的基因資料中，與本篇論文所篩選出的顯著性基因互相比較，相同的有 292 筆基因，相似程度大於 83.4%；各個資料篩選方法，都有其優缺點，互相截長補短，不同方法可以互補之間不足的部分，且綜合數個方法所篩選出的資料，較不易受不同篩選方法偏好所影響。

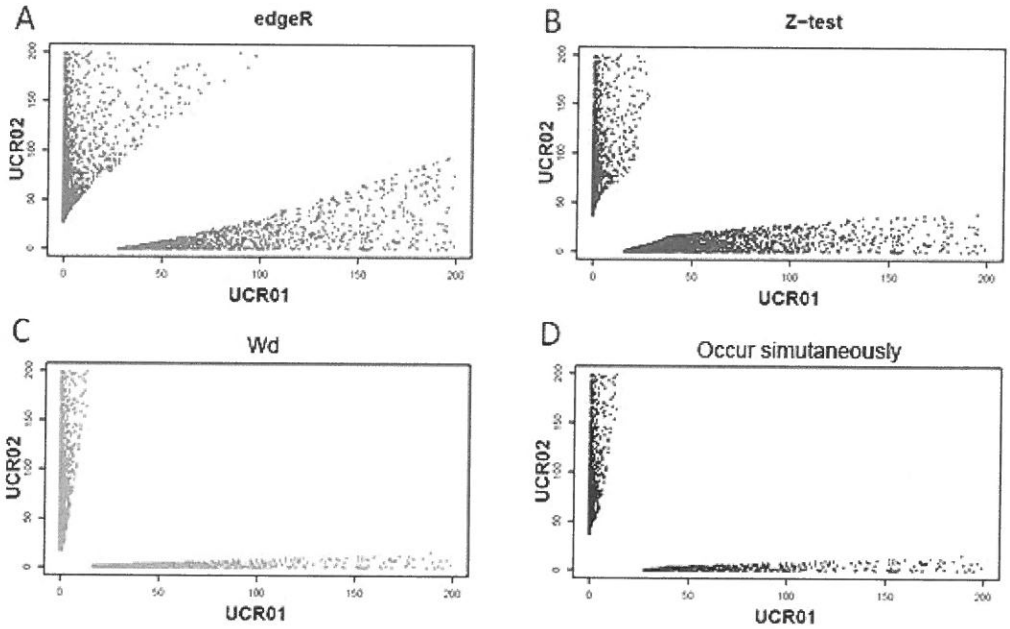

圖四、MPSS 序列標籤在花藥四分體 (UCR01) 與花藥空泡早期 (UCR02) 互相比較後的顯著性測驗分析散布圖。 A. edgeR, B. Z-test, C. Weighted deviation, D. 交集。

討　論

以 DNA 定序為基礎所產生的序列資料，分析時會特別依賴基因註解資料庫，理想的狀況是一個序列標籤對應一個基因，但實際上卻可能會有一對多、多對一或比對不到的情況，亦即同一個序列標籤對應到多個基因，或多個序列標籤對應到同一個基因，甚至是沒有對應到任何基因。一個序列標籤對應一個基因與多個序列標籤對應同一個基因，一對一的情況就以此序列標籤的出現次數來代表此基因的表現程度；而多個序列標籤對應同一個基因，把對應同一個基因的多個序列標籤的表現量加總，來代表此基因的表現程度；但同一個序列標籤對應多個基因，這樣的情況並不明確，且難以分辨該序列標籤應該歸屬於哪個被比對到的基因，無法解決的情況下只能將此部分資料排除；然而，並不是所有的序列都可以對應的到基因，通常序列資料量越大，則會有越多筆的序列比對不到任何已知序列，而這部分的資料就成為了分析上的困擾，

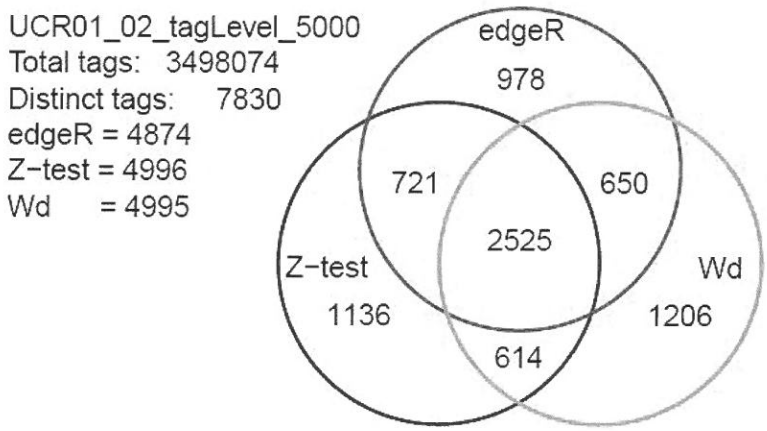

圖三、MPSS 序列標籤以 edgeR、Z-test、Wd 三個方法篩選花藥，四分體 (UCR01) 及花藥， 空泡早期 (UCR02) 兩基因庫間顯著差異的序列標籤數。

將三個方法所篩選出的序列標籤資料，以散布圖方式呈現 (圖四)，X 軸是 UCR01 (花藥 , 四分體) 的序列標籤出現次數，Y 軸是 UCR02 (花藥 , 空泡早期) 的序列標籤出現次數，圖 A、B、C、D 分別是 edgeR、Z-test、Wd、交集；由此結果觀察各個篩選方法各自的偏好，並且依保守原則取交集 (圖 D) 所篩選出的資料，較不易受方法不同所影響，在生物意義方面則是更加嚴謹的篩選出有顯著差異的序列標籤。

將三個方法所篩選出的序列標籤資料，以散布圖方式呈現 (圖二)，X 軸是幼苗的根 (Rt) 的序列標籤出現次數，Y 軸是健康的葉 (Hl) 的序列標籤出現次數，圖 A、B、C、D 分別表示 edgeR、Z-test、Wd 及交集；由此結果觀察各個篩選方法各自的偏好，並且依保守原則取交集 (圖 D) 所篩選出的資料，較不易受方法不同所影響，在生物意義方面則是更加嚴謹的篩選出有顯著差異的序列標籤。

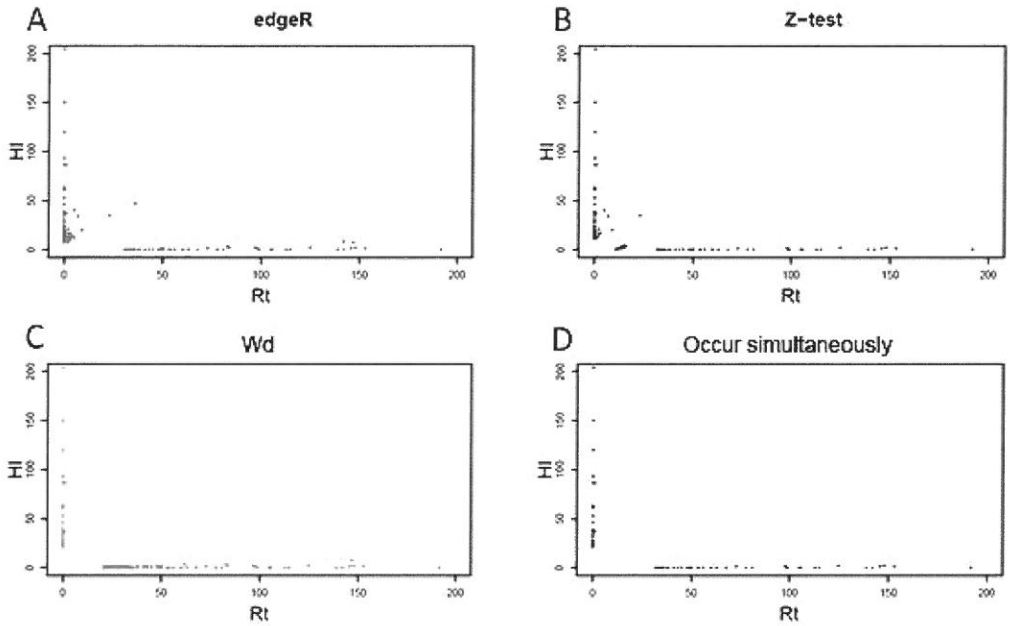

圖二、SAGE 序列標籤，幼苗的根 (Rt) 與健康的葉 (Hl) 互相比較後的顯著性測驗分析散布圖。A. edgeR, B. Z-test, C. Wd, D. 交集。

二、MPSS 資料

MPSS 技術所產生的 8 個基因庫序列標籤資料利用三個顯著性測驗方法 (edgeR、Z-test、Wd) 依顯著值三個方法各挑出前 5,000 筆資料互相比較，圖三是 UCR01 花藥，四分體及 UCR02 花藥，空泡早期的結果，三個顯著性測驗方法交集出 2,525 筆序列資料。

$(\frac{10-1}{10+1}=0.8182\,;\ \frac{1000-1}{1000+1}=0.9980)$ 來區別差異的大小。

結　果

一、SAGE 資料

以 SAGE 技術所產生的 5 個基因庫序列標籤資料利用三個顯著性測驗方法 (edgeR、Z-test、Wd) 依顯著值，於三個方法各挑出前 200 筆資料互相比較，取前 200 筆資料乃是因為若設定固定 p-value 來篩選資料，則三個方法所挑選出的資料做比較時，筆數相差太大，所以必須將 p-value 做為參考來制訂一個三個方法都篩選出相同的資料筆數才方便做比較，然而將 p-value 做為參考還需要權衡基因庫與基因庫之間的差異，若相比較的基因庫之間差異較大時，則取相同資料筆數時 p-value 較小；若相比較的基因庫之間差異較小時，則取相同資料筆數時 p-value 較大，所以需要權衡基因庫與基因庫之間的差異，設定出依顯著值挑出較合適的資料筆數；圖一是幼苗的根 (Rt) 及健康的葉 (Hl) 的交集結果，三個顯著性測驗方法交集出 80 筆序列資料；三個方法交集以藉此挑選出較為嚴謹，較不受不同分析方法所影響的顯著資料。

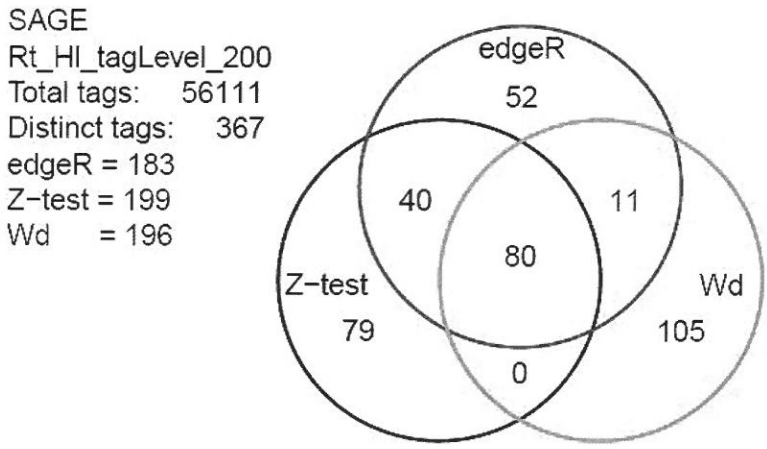

圖一、SAGE 序列以 edgeR、Z-test 及 Wd 三個方法篩選幼苗的根 (Rt) 及健康的葉 (Hl) 間有顯著差異的序列標籤數目。

三、統計方法

DGE 資料不使用常態分布的 t 檢定與變異數分析之原因在於，雖然資料屬於大樣本，但其分布明顯不符合鐘型左右對稱的常態分布，因此採用下列三種顯著性測驗方法。

1、edgeR

edgeR (empirical analysis of digital gene expression data in R)(Robinson et al., 2010) 由 Robinson 與 Smyth 所發展出，以負二項分布為模型，利用條件加權概似估計法 (conditional weighted likelihood method)，估計兩個基因庫之間，序列標籤出現次數的過度離散程度 (overdispersion)，進而挑選出具有顯著差異的序列標籤或基因。

2、Z-test

檢測基因庫 i, j 之間，序列標籤出現次數在比例上的差異。

$$Z = \frac{(P_i - P_j)}{\sqrt{\frac{\bar{P} \times \bar{Q}}{n_i} + \frac{\bar{P} \times \bar{Q}}{n_j}}}$$

$$\bar{P} = \frac{X_i + X_j}{n_i + n_j}$$

$$\bar{Q} = 1 - \bar{P}$$

P (累計機率)，X (累計頻度)，n (資料筆數)，為減少低表現度干擾，分析前過濾掉相差小於 5 的資料，前人研究中也有去除掉 TPM (transcripts per million) 小於 5 的類似方法 (Huang et al., 2009)。

3、Weighted deviation (Wd)

$$\mathrm{Wd} = \frac{X_j - X_i}{X_j + X_i}$$

結合相減和相除的特性，使所有的檢測值落在 ±1 之間，方便做比較，檢測值若為正，表示表現量上升，若檢測值為負，表示表現量下降，越接近 +1 或 -1 表示表現量差異越大；為減少低表現度干擾，分析前過濾掉相差小於 5 的資料，並將出現次數為 0 次的資料取代為 1 次，如此計算出的檢定值才不會直接等於 ±1 而無法分辨出表現量 0 與 10 ($\frac{10-0}{10+0}=1$) 和 0 與 1,000 ($\frac{1000-0}{1000+0}=1$) 的差異，而會出現接近 ±1 的小數點資料

1. UCR01：花藥 , 四分體 (anther, tetrad stage)
2. UCR02：花藥 , 空泡早期 (anther, early vacuolated stage)
3. UCR03：花藥 , 空泡晚期 (anther, late vacuolated stage)
4. UCR04：花藥 , 有絲分裂期 (anther, mitosis stage)
5. UCR05：花藥 , 花粉成熟期 (anther, mature pollen stage)
6. UCR06：花粉 (pollen)
7. UCR07：成熟的胚 (mature embryo)
8. UCR08：未成熟的穀粒 (immature grain)

在 MPSS 資料之中 (表二)，各組都定序出超過 100,000 個不同的序列標籤，8 個基因庫總和超過 800,000 個不同的序列標籤，總共定序的鹼基數目超過 300,000,000 個。

表二、MPSS 資料簡介

基因庫	序列標籤總數 [a]	序列標籤種類 [b]	序列標籤表現範圍 [c]
UCR01	1,774,208	182,491	1-88,239
UCR02	1,723,866	194,009	1-87,870
UCR03	1,598,479	145,672	1-56,458
UCR04	1,150,116	125,415	1-38,094
UCR05	1,128,456	117,430	1-51,468
UCR06	3,802,071	156,637	1-84,190
UCR07	3,340,211	194,904	1-107,510
UCR08	1,196,602	145,471	1-71,998
Total	15,714,009	841,355	1-107,510

[a] 總共定序出序列標籤的個數。

[b] 總共定序出序列標籤的種類數。

[c] 序列標籤出現次數最小與最大的範圍。

in R)(Robinson et al., 2010) 與另外兩種直覺分析法 Z-test 與 Wd 法在實際操作上之異同。

一、水稻 SAGE 資料

依 Velculescu et al., 1995 的方法進行 SAGE 分析，使用的 anchoring enzyme 為 NlaIII，切點位置是 CATG，tagging enzyme 為 BsmFI，序列標籤長度為 14 個鹼基，5 個 SAGE 基因庫分別是：

1. 授粉後五天的種子 (Seeds of 5 days after pollination, Sd5),
2. 授粉後十天的種子 (Seeds of 10 DAP, Sd10),
3. 幼苗的根 (Roots of seedling, Rt),
4. 健康的葉 (Healthy leave, Hl),
5. 白葉枯病菌感染的葉 (bacterial blight-infected leaves, Il)。

在 SAGE 資料之中 (表一)，各組都定序出超過 5,000 種不同的序列標籤，5 個基因庫總和超過 25,000 種不同的序列標籤，總共定序的鹼基數目超過 1,500,000 個。

表一、SAGE 資料簡介

基因庫	Sd5	Sd10	Rt	Hl	Il	Total
序列標籤總數 [a]	18,186	13,034	45,050	11,061	21,047	108,378
序列標籤種類 [b]	8,508	4,787	16,266	5,588	8,722	29,897
序列標籤表現次數範圍(次)[c]	1-508	1-852	1-339	1-234	1-362	1-852

[a] 總共定序出序列標籤的個數。

[b] 總共定序出序列標籤的種類個數。

[c] 序列標籤出現次數最小與最大的範圍。

二、MPSS 資料

MPSS 使用的 anchoring enzyme 為 Sau3AI 切點位置是 GATC (Reinartz et al., 2002)，tagging enzyme 為 MmeI，序列標籤長度為 20 個鹼基，8 個 MPSS 基因庫分別是：

sequencing, ligation-based sequencing)，提供了產生序列標籤，一個定序更快速且較低成本的方法 (Mardis, 2008)，目前已經有數個研究合併使用 SAGE、MPSS 及 NGS 技術 (Bainbridge et al., 2006; Cheung et al., 2006; Nobuta et al., 2007; Weber et al., 2007; Torres et al., 2008; Hashimoto et al., 2009)；其中 Hashimoto 所發表的研究，結合了 NGS 以及 SAGE 對結腸癌細胞株 (HT-29) 做全基因體表現的分析，傳統的 SAGE 大約產生了 70,000 個 tags，而結合了 NGS 的技術則定序出 20,000,000 (20 million) 個序列標籤來代表 14,000 個在單一細胞中所表現的基因，這樣的資料相較於傳統的 SAGE，敏感度提高約有 1,000 倍 (Hashimoto et al., 2009)。

SAGE 雖是高通量的技術，但仍然有其缺點，SAGE 不適合應用在微量樣品待測物，這樣的問題可以利用 MicroSAGE (Datson et al., 1999) 來解決這樣的缺點，相較於原來 SAGE 的方法，所需要的樣品量減少 500-5,000 倍；另外，14-base 的序列標籤對於鑑定基因來說似乎不夠長 (Matsumura et al., 2008)，針對這樣的問題，也有 21 bases (Long SAGE) 及 26 bases (Super SAGE) 的方法可以使用 (Wahl et al., 2005; Matsumura et al., 2008)，增加了序列標籤長度，可以提高基因比對的專一性。

如此大量的資料要進行分析，就必須借重於生物資訊與生物統計學領域的專長來執行，因此有許多的分析處理軟體可以使用 (Velculescu et al., 1997; Lash et al., 2000; Margulies and Innis, 2000; van Kampen et al., 2000)；而用來比較基因庫之間的差異，所使用的統計分析軟體，大致上有幾個不同的理論依據，包含 Monte Carlo simulation (Velculescu et al., 1997)、Bayesian statistical analysis (Chen et al., 1998; Lash et al., 2000)、Z-test statistics (Kal et al., 1999)；在比較了不同的基因庫之後，可能會發現數百到數千個有差異表現的基因，為了找出有興趣的部分，接下來會藉由搜尋基因註解及基因資料庫，進一步為基因功能分群，找出有興趣且有差異表現的相關基因。

材料及方法

SAGE 及 MPSS 的資料都是來自於定序後，計算不同序列標籤出現次數的離散計數資料，序列標籤的種類不同，可以代表不同的基因，而序列標籤出現不同次數的原因，是因為基因表現量不同。

本研究利用水稻 SAGE(Su et al., 2005) 及 MPSS(Huang et al., 2009) 之實際資料，比較目前常用於 DGE 資料分析之 edgeR (Empirical analysis of digital gene expression data

時，有一定的難度 (Nadon and Shoemaker, 2002)；其敏感度在轉錄本 (transcripts) 表現量小於 50 個重複時難以偵測；同一個基因家族的轉錄本之間可能發生非專一性的雜交 (cross-hybridization)；這些問題對於 SAGE 及衍生的相關技術，幾乎可以完全規避這些缺點 (Matsumura et al., 2008)。

表現序列標記 (expressed sequence tags, ESTs)(Adams et al., 1991) 也是以雜合反應為基礎，其大概流程為：從有興趣的細胞或組織分離出 mRNA，再反轉錄成 cDNA，將這些 cDNA 轉至載體 (vector)，建構 cDNA 基因庫 (library)，再從基因庫中隨機挑選出個別的序列，定序約 300-500 bp 的 cDNA，用這樣的序列標籤來代表特定的轉錄本；在水稻中，大規模的 cDNA 分析 (EST analysis) 所產生的水稻 EST 資料庫則是在 1994 年所發表 (Sasaki et al., 1994)；大規模的 EST 定序，使得基因表現分析變得方便、發現許多新的基因、定出基因圖譜、確認編碼區 (coding regions) 的位置。儘管 EST 技術既簡單又有效，但其所需的定序相關費用，很有可能造成此技術無法被廣泛應用的原因 (Anisimov, 2008)。

1995 年 Velculescu 等人所發展出的 serial analysis of gene expression (SAGE) ，在大規模基因表現上特別受到關注 (Velculescu et al., 1995)，基本上 SAGE 技術可以說是從 EST 所發展出，差異在於定序序列標籤的長度變短，一次 SAGE 所可以鑑定分析的轉錄本數量，大約是 EST 的 40 倍 (Adams, 1996)；隨著技術不斷的改良與進步，在 2003 年 Invitrogen 所開發出的實驗套裝組件 I-SAGETM，已經有能力產生具有 100,000 個序列標籤以上的基因庫。而在 2000 年 Brenner 等人所發展出的 massively parallel signature sequencing (MPSS)，原理大致上與 SAGE 類似，因磁珠與定序技術的進步，使得 MPSS 得以在同一時間產出大量序列標籤，研究者就能更加節省時間與成本，得到更大規模的小片段序列標籤資料 (Reinartz et al., 2002)。SAGE 與 MPSS 技術的特點：(一) 假設核酸的種類是屬於隨機分布時，理論上 14-bp 長度的序列標籤，可以定義出 4^{14} (268,435,456) 個特定基因 (一般細胞的基因約 30,000-40,000 個、人類的基因約 70,000-140,000 個)，小片段 DNA 序列標籤，已經擁有足夠的頻度來代表樣本所表現的基因。(二) 小片段的序列標籤可以互相連接起來，一起被定序及計算 mRNA 的表現量，形成這樣的 tags 並不需要事先知道待測物的組成以及表現程度的高低，可檢測未知轉錄樣本 (Hegedus et al., 2009)。以定序數量作為基因表現量的測度，具有在序列標籤上的數位化 (digital) 特性，使得不同基因庫之間可以直接做比較 (Velculescu et al., 2000)，以 SAGE 及 MPSS 技術所產生的基因表現量資料即數位化基因表現資料 (DGE data)。

配合次世代定序技術 (next generation sequencing, NGS)，利用不同於傳統的序列倍增 (Emulsion PCR, Bridge amplification) 以及定序策略 (pyrosequencing, polymerase-based

前 言

長久以來，基因表現的差異一直是研究者相當有興趣的議題，大量的序列及基因註解資料，使得生物學領域得以針對全基因組為目標，達成各項基因表現研究與分析，這樣的成就，大部分該歸功於實驗技術的不斷進步，傳統上檢測 messenger RNA (mRNA) 來分析基因表現的技術有：北方轉漬法 (northern blots)、mRNA 點轉漬法 (mRNA dot blots)、及逆轉錄聚合鏈鎖反應 (reverse transcriptase-polymerase chain reaction, RT-PCR)，前兩項技術受限於探針 (probes) 的種類個數，一次實驗僅能分析少量的基因；RT-PCR 則由於仰賴序列樣品倍增，誤差也會放大、再現性不佳且受不同樣本及不同引子對 (primer pairs) 的影響 (Adams, 1996)，在比較兩個樣本之間的基因表現量差異，也可以使用差異顯示技術 (differential display)(Liang and Pardee, 1992)，但當檢測數量變多，規模變大時，這幾個方法會變得較不準確。

後基因體時代所面臨的挑戰，將會是在大量的序列資料之中，找出有用的生物之資訊 (Wahl et al., 2005)，包含基因的註解 (Stein, 2001) 以及大規模的基因表現分析 (Kanehisa and Bork, 2003)，針對大量的基因分析研究將會越來越常見，因此許多技術，逐漸被發展與應用，例如：相減雜交法 (subtractive hybridization)、差異篩選法、競爭型逆轉錄聚合鏈鎖反應 (competitive RT-PCR) 和微陣列 (microarray) 技術以及大規模表現序列標記 (expressed sequence tags, ESTs) 定序與分析。

在高通量的基因表現相關分析技術之中，相減雜交法及差異顯示技術是以聚合鏈鎖反應為基礎，此二技術都有敏感度不足及過高的偽陽率 (false positive rate) 等缺點 (Bureau et al., 1990; Liang and Pardee, 1992)；經後續的改良發展後，分別是抑制扣除雜交法 (suppressive subtraction hybridization, SSH)(Diatchenko et al., 1996) 及表現差異分析法 (representational difference analysis, RDA)(Lisitsyn and Wigler, 1993)，在定量的可靠性及通量上獲得改善，但此二技術與競爭型逆轉錄聚合鏈鎖反應，均以聚合鏈鎖反應為基礎，所有以聚合鏈鎖反應為基礎的共同缺點是，必須利用對序列的預備知識設計出合適的引子，否則將會無法合成出產物。

微陣列技術乃以雜合反應為基礎，技術開發後數年，於 2001 年後已經可以接近整個基因組的規模 (Truckenmiller et al., 2001)，許多相關的文獻都把 SAGE 和微陣列技術拿來做比較，甚至相當巧合的，cDNA microarray 與 SAGE 的技術恰巧發表在同一期的 Science 中 (Schena et al., 1995; Velculescu et al., 1995)；相較之下，微陣列晶片的建立，需要對於材料的序列了解清楚，並不適合用以鑑定新的基因之目標；且不同的研究材料、不同的研究平台或不同實驗室的資料，因為隨機系統性的誤差導致互相比較

數位化基因表現資料分析方法之比較

張嘉慶　侯藹玲
天主教輔仁大學 生命科學系

摘　要

分子生物學技術快速進展，使得定序成本下降、效率急速增加，以定序為基礎的數位化基因表現 (DGE) 資料量快速累積，分析此類資料的統計方法不同於微陣列的分析方法。本文利用水稻 SAGE 及 MPSS 之實際資料，比較目前常用於 DGE 資料分析之 edgeR 演算法與另外兩種直覺分析法 Z-test 與 Wd 法實際操作之異同。

關鍵詞：數位化基因表現、基因表現系列分析、大規模平行信號測序、edgeR。

圖的 Mycielskian 的等距路徑數

潘俊杰

輔仁大學 數學系

摘　要

在這篇文章中，我們得到完全圖、完全 r 部圖、路徑及圈的 Mycielskian 的等距路徑數。

關鍵字：完全圖、完全 r 部圖、路徑、圈、Mycielskian、等距路徑數。

References

1. M. Aigner, M. Fromme, A game of cops and robbers, Discrete Math. 8 (1984) 1–12.
2. D. C. Fisher, S. L. Fitzpatrick, The isometric number of a graph, J. Combin. Math. Combin. Comput. 38 (2001) 97–110.
3. D. C. Fisher, P. A. Mckenna, E. D. Boyer, Hamiltonicity, diameter, domination, packing, and biclique partitions of Mycielski' s graphs, Discrete Appl. Math. 84 (1998) 93–105.
4. S. L. Fitzpatrick, Aspects of Domination and Dynamic Domination, Ph.D. Thesis, Dalhousie University, Nova Scotia, Canada, 1997.
5. S. L. Fitzpatrick, The isometric path number of the Cartesian product of paths, Congr. Numer. 137 (1999) 109–119.
6. S. L. Fitzpatrick, R. J. Nowakowski, D. Holton, I. Caines, Covering hypercubes by isometric paths, Discrete Math. 240 (2001) 253-260.
7. R. Nowakowski, P. Winkler, Vertex-to-vertex pursuit in a graph, Discrete Math. 43 (1983) 235–239.
8. A. Quilliot, Thèse de 3^{e} cycle, Université de Paris VI, 1978.
9. J.-J. Pan, G. J. Chang, Isometric path numbers of block graphs, Inform. Process. Lett. 93 (2005) 99–102.
10. J.-J. Pan, G. J. Chang, Isometric path numbers of graphs, Discrete Math. 306 (2006) 2091–2096.
11. M. Valencia-Pabona, J.-C. Verab, On the diameter of Kneser graphs, Discrete Math. 305 (2005) 383–385.

Recevied Oct 30, 2013
Revised Mar 19, 2014
Accepted Mar 19, 2014

Theorem 4.5 *For a cycle* C_n,

$$\mathrm{ip}(\mu(C_n)) = \begin{cases} 3 & if \quad n = 3, \\ \lceil (2n+1)/(\lfloor n/2 \rfloor + 1) \rceil & if \quad 4 \leq n \leq 7, \\ \lceil n/2 \rceil & if \quad n \geq 8. \end{cases}$$

The theorems in this paper show that the lower bound in Lemma 1.1 is tight. We therefore propose the following conjecture.

Conjecture 4.6 *Suppose that* G *is a connected graph and let* $c(A) = \max\{|V(P) \cap A| : P$ *is a maximal isometric path of the graph* $\mu(G) = (V(\mu(G)), E(\mu(G))\}$ *for a subset* A *of* $V(\mu(G))$. *Then*

$$\mathrm{ip}(\mu(G)) = \max_{A \subseteq V(\mu(G))} \lceil |A|/c(A) \rceil.$$

Acknowledgement The author thanks to an anonymous referee for his/her suggestions which contributed to improve the presentation of this paper.

On the other hand, we construct the following isometric path covers for $\mu(P_n)$ with $3 \le n \le 4$ and $\mu(C_n)$ with $4 \le n \le 7$, respectively.

$\mathcal{C}(\mu(P_3)) = \{v_1v'_2v_3, v'_1v_2v'_3, u\}$;
$\mathcal{C}(\mu(P_4)) = \{v_1v'_2v_3, v_2v'_3v_4, v'_1uv'_4\} = \mathcal{C}(\mu(C_4))$;
$\mathcal{C}(\mu(C_5)) = \{v_1v'_2v_3, v_2v'_3v_4, v'_4v_5, v'_1uv'_5\}$;
$\mathcal{C}(\mu(C_6)) = \{v_1v'_2v_3v'_4, v_2v'_3v_4v'_5, v_5v'_6, uv'_1v_6\}$;
$\mathcal{C}(\mu(C_7)) = \{v_1v'_2v_3v'_4, v_2v'_3v_4v'_5, v'_1uv'_6v_5, v'_7v_6v_7\}$;

Therefore, $\mathrm{ip}(\mu(P_n)) \le 3$ for $3 \le n \le 4$,and $\mathrm{ip}(\mu(C_n)) \le \lceil (2n+1)/(\lfloor n/2 \rfloor + 1) \rceil$ for $4 \le n \le 7$.

Lemma 4.3 $\mathrm{ip}(\mu(P_n)) = \lceil n/2 \rceil$ *for* $n \ge 5$ *and* $\mathrm{ip}(\mu(C_n)) = \lceil n/2 \rceil$ *for* $n \ge 8$.

Proof. Since u is adjacent to every $x' \in V'(P_n)$ (respectively, $V'(C_n)$), every maximal isometric path has at most two vertices in $V'(P_n)$ (respectively, $V'(C_n)$). Together with $|V'(P_n)| = n = |V'(C_n)|$ and by Lemma 1.1, $\mathrm{ip}(\mu(P_n)) \ge \lceil n/2 \rceil$ and $\mathrm{ip}(\mu(C_n)) \ge \lceil n/2 \rceil$.

On the other hand, we use induction on n to prove that $\mathrm{ip}(\mu(P_n)) \le \lceil n/2 \rceil$ for $n \ge 5$ and $\mathrm{ip}(\mu(C_n)) \le \lceil n/2 \rceil$ for $n \ge 8$. Let $\mathcal{C}_1 = \{v_1v'_2v_3v'_4v_5, v_2v'_3v_4v'_5v_6\}$. When $5 \le n \le 10$ for $\mu(P_n)$ and $8 \le n \le 10$ for $\mu(C_n)$, the following isometric path covers prove the assertion:

$\mathcal{C}(\mu(P_5)) = \{v_1v'_2v_3v'_4v_5, v_2v'_3v_4, v'_1uv'_5\}$;
$\mathcal{C}(\mu(P_6)) = \mathcal{C}_1 \cup \{v'_1uv'_6\}$; $\mathcal{C}(\mu(P_7)) = \mathcal{C}_1 \cup \{v'_1uv'_7, v'_6v_7\}$;
$\mathcal{C}(\mu(P_8)) = \mathcal{C}_1 \cup \{v'_1uv'_7v_8, v'_6v_7v'_8\}$;
$\mathcal{C}(\mu(C_8)) = \{v_1v'_2uv'_6v_5, v_2v'_3v_4v'_5v_6, v_3v'_4uv'_8v_7, v'_1v_8v'_7\}$.
$\mathcal{C}(\mu(P_9)) = \mathcal{C}(\mu(P_6)) \cup \{v_7v'_8v_9, v'_7v_8v'_9\} = \mathcal{C}(\mu(C_9))$;
$\mathcal{C}(\mu(P_{10})) = \mathcal{C}(\mu(P_6)) \cup \{v_7v'_8v_9v'_{10}, v'_7v_8v'_9v_{10}\} = \mathcal{C}(\mu(C_{10}))$;

Suppose that $n \ge 11$ and the assertion holds for $n' < n$. Let $n' = n - 6$. Then by the induction hypothesis, $\mathrm{ip}(\mu(P_{n-6})) \le \lceil (n-6)/2 \rceil$. Since we can cover the vertex set of $\mu(P_n)$ (respectively, $\mu(C_n)$) with the vertex sets of two distance invariant induced subgraphs $\mu(P_{n-6})$ and $\mu(P_6)$, $\mathrm{ip}(\mu(P_n)) \le \lceil (n-6)/2 \rceil + \lceil 6/2 \rceil = \lceil n/2 \rceil$ and $\mathrm{ip}(\mu(C_n)) \le \lceil (n-6)/2 \rceil + \lceil 6/2 \rceil = \lceil n/2 \rceil$. Hence this theorem holds. ■

According to Lemmas 4.2–4.3, we have the following theorems.

Theorem 4.4 *For a path* P_n,

$$\mathrm{ip}(\mu(P_n)) = \begin{cases} 2 & \text{if } n = 1,2 \\ 3 & \text{if } 3 \le n \le 4, \\ \lceil n/2 \rceil & \text{if } n \ge 5. \end{cases}$$

Lemma 3.7 *Suppose that* $1 \le n_1 \le n_2 \le \cdots \le n_r$. *If* $3n_r > 2n$, *then* $\mathrm{ip}(\mu(G)) = n_r$.

Proof. By Lemma 3.2, $\mathrm{ip}(\mu(G)) \ge n_r$. On the other hand, we use induction on $n - n_r$ to prove that $\mathrm{ip}(\mu(G)) \le n_r$. When $n - n_r = 1$, we have $r = 2$ and $\mu(G) = \mu(K_{1,n_2})$. Since $n_1 = 1$ and $3n_2 > 2n$, $n_2 > 2n_1 = 2$. Thus, by Lemma 3.4, $\mathrm{ip}(\mu(K_{1,n_2})) \le n_2$.

Suppose that $n - n_r \ge 2$ and the claim holds for $n' - n'_r < n - n_r$. As $n - n_r \ge 2$, $n_1 \ge 2$ for $r = 2$. Since $n - n_r \ge 2$ and $3n_r > 2n$, we have $n_r - 2 > n - n_r + n - n_r - 2 \ge n - n_r \ge n_{r-1} > 0$. Thus, by Lemma 3.5, $\mathrm{ip}(\mu(G)) \le \mathrm{ip}(\mu(K_{n_1,\ldots,n_{r-1}-1,n_r-2})) + 2$. Let $G' = K_{n_1,\ldots,n_{r-1}-1,n_r-2}$. Then $n'_r = n_r - 2 \ge n_i$ for all $1 \le i \le r-1$ and $n' = n - 3$. Thus $n' - n'_r = n - n_r - 1 < n - n_r$. Since $3n_r > 2n$, $3n'_r = 3(n_r - 2) > 2n - 6 = 2n'$. Hence, by the induction hypothesis, $\mathrm{ip}(\mu(G)) \le \mathrm{ip}(\mu(G')) + 2 \le n_r - 2 + 2 = n_r$.

According to Lemmas 3.6–3.7, we have the following theorem.

Theorem 3.8 *For a complete* r*-partite graph* $K_{n_1,n_2,\ldots,n_r}$ *with* $r \ge 2$, $1 \le n_1 \le n_2 \le \cdots \le n_r$, *and* $n = n_1 + n_2 + \cdots + n_r$,

$$\mathrm{ip}(\mu(K_{n_1,n_2,\ldots,n_r})) = \begin{cases} \lceil (2n+1)/3 \rceil & \text{if } 3n_r \le 2n, \\ n_r & \text{if } 3n_r > 2n. \end{cases}$$

4. Paths and cycles

This section establishes the isometric path numbers of $\mu(P_n)$ and $\mu(C_n)$. Recall that a path P_n is the graph with vertex set $\{v_i : 1 \le i \le n\}$ and edge set $\{v_i v_{i+1} : 1 \le i \le n-1\}$. A cycle C_n is the graph with vertex set $\{v_i : 1 \le i \le n\}$ and edge set $\{v_i v_{i+1} : 1 \le i \le n-1\} \cup \{v_n v_1\}$.

Lemma 4.1 *If a graph* G *is a path* P_n *or a cycle* C_n, *then*

$$\mathrm{diam}(\mu(G)) = \begin{cases} 2 & \text{if } G = P_2, P_3, C_3, C_4 \text{ or } C_5, \\ 3 & \text{if } G = P_4, C_6 \text{ or } C_7, \\ 4 & \text{otherwise}. \end{cases}$$

Proof. Since $\mathrm{diam}(P_n) = n - 1$ and $\mathrm{diam}(C_n) = \lfloor n/2 \rfloor$, by Theorem 1.3 this lemma holds. ∎

Lemma 4.2 $\mathrm{ip}(\mu(P_1)) = 2$, $\mathrm{ip}(\mu(P_2)) = 2$, $\mathrm{ip}(\mu(C_3)) = 3$, $\mathrm{ip}(\mu(P_n)) = 3$ *for* $3 \le n \le 4$, *and* $\mathrm{ip}(\mu(C_n)) = \lceil (2n+1)/(\lfloor n/2 \rfloor + 1) \rceil$ *for* $4 \le n \le 7$.

Proof. By Theorem 2.3, $\mathrm{ip}(\mu(P_1)) = 2$, $\mathrm{ip}(\mu(P_2)) = 2$ and $\mathrm{ip}(\mu(C_3)) = 3$. By Corollary 1.2 and Lemma 4.1, we have $\mathrm{ip}(\mu(P_n)) \ge \lceil (2n+1)/(n-1+1) \rceil = 2 + \lceil 1/n \rceil$ implies that $\mathrm{ip}(\mu(P_n)) \ge 3$ for every $3 \le n \le 4$ and $\mathrm{ip}(\mu(C_n)) \ge \lceil (2n+1)/(\lfloor n/2 \rfloor + 1) \rceil$ for $4 \le n \le 7$.

Proof. Let $V(G)$ be the disjoint union of $V(K_{n_1,\dots,n_{r-1}-1,n_r-2})$ and $\{a_{r-1,n_{r-1}}, a_{r,n_r-1}, a_{r,n_r}\}$ for $a_{r-1,n_{r-1}} \in A_{r-1}$, and $a_{r,n_r-1}, a_{r,n_r} \in A_r$.
If $\mathcal{C}$ is an isometric path cover of $\mu(K_{n_1,\dots,n_{r-1}-1,n_r-2})$ with $|\mathcal{C}| = \mathrm{ip}(\mu(K_{n_1,\dots,n_{r-1}-1,n_r-2}))$, then $\mathcal{C} \cup \{a'_{r,n_r-1}a_{r-1,n_{r-1}}a'_{r,n_r}, a_{r,n_r-1}a'_{r-1,n_{r-1}}a_{r,n_r}\}$ is an isometric path cover of $\mu(G)$. Hence, $\mathrm{ip}(\mu(G)) \le \mathrm{ip}(\mu(K_{n_1,\dots,n_{r-1}-1,n_r-2})) + 2$. ■

Lemma 3.6 *Suppose that* $1 \le n_1 \le n_2 \le \cdots \le n_r$. *If* $3n_r \le 2n$, *then* $\mathrm{ip}(\mu(G)) = \lceil (2n+1)/3 \rceil$.

Proof. By Lemma 3.2, $\mathrm{ip}(\mu(G)) \ge \lceil (2n+1)/3 \rceil$. On the other hand, we use induction on n to prove that $\mathrm{ip}(\mu(G)) \le \lceil (2n+1)/3 \rceil$. When $n \le 4$, by the assumption $3n_r \le 2n$, Lemma 3.4, $\mu(K_{1,1,1}) = \mu(K_3)$, $\mu(K_{1,1,1,1}) = \mu(K_4)$, isometric path covers $\mathcal{C}\left(\mu(K_{2,2})\right) = \{a'_{1,1}ua'_{1,2}, a'_{2,1}a_{1,1}a'_{2,2}, a_{2,1}a_{1,2}a_{2,2}\}$, and $\mathcal{C}\left(\mu(K_{1,1,2})\right) = \{a'_{1,1}ua'_{2,1}, a'_{3,2}a_{1,1}a_{3,2}, a'_{3,1}a_{2,1}a_{3,1}\}$, the claim holds for $G \in \{\mu(K_{1,1}), \mu(K_{1,2}), \mu(K_{1,1,1}), \mu(K_{2,2}), \mu(K_{1,1,2}), \mu(K_{1,1,1,1})\}$.

Suppose that $n \ge 5$ and the claim holds for $n' < n$. Note that if $r = 2$, then $n_1 \ge 2$ and $n_2 \ge 3$ because $n \ge 5$ and $3n_r \le 2n$. For $r \ge 3$, if $n_r = 1$, then $\mu(G) = \mu(K_n)$ and by Theorem 2.3, the claim holds. Thus, we only consider $n_r \ge 2$ for $r \ge 3$. By Lemma 3.5, $\mathrm{ip}(\mu(G)) \le \mathrm{ip}(\mu(K_{n_1,\dots,n_{r-1}-1,n_r-2})) + 2$. Let $G' = K_{n_1,\dots,n_{r-1}-1,n_r-2}$. Then $n' = n-3$ implies that $n' < n$. In order to show that the graph G' satisfies the induction hypothesis, we shall prove that $3n'_r \le 2n'$ according to the following cases.

Case 1: $n_r \ge n_{r-1} + 2$.

In this case, $n_r - 2 \ge n_{r-1} \ge n_i$ for all $i \ge 2$ and so $n'_r = n_r - 2$. Therefore, $3n'_r = 3(n_r - 2) \le 2(n-3) = 2n'$.

Case 2: $n_r \le n_{r-1} + 1$, $n_{r-1} \ge 4$, and $r = 2$.

In this case, $n'_2 \le n_1 - 1$ and $n' = n - 3 = n_1 + n_2 - 3 \ge 2n_2 - 3$. Then $3n'_2 \le 3n_1 - 3 \le 4n_1 - 7 < 4n_1 - 6 \le 2n'$.

Case 3: $n_r \le n_{r-1} + 1$, $n_{r-1} \ge 4$, and $r \ge 3$.

In this case, $n'_r \le n_{r-1}$ and $n' = n - 3 \ge n_r + n_{r-1} + 1 - 3 \ge 2n_{r-1} - 2$. Then $3n'_r \le 3n_{r-1} \le 4n_{r-1} - 4 \le 2n'$.

Case 4: $n_r \le n_{r-1} + 1$, and $n_{r-1} \le 3$. There are three subcases.

Subcase 4.1. $n \ge 8$.

In this subcase, $n'_r \le n_{r-1} \le 3$ and $n' = n - 3 \ge 8 - 3 = 5$. Then $3n'_r \le 9 < 10 \le 2n'$.

Subcase 4.2. $6 \le n \le 7$.

In this subcase, $3n_r \le 2n \le 14$ implies that $n_r \le 4$. As $n \le 7$, $n_{r-1} \le 3$ and $n_{r-2} \le 2$. Thus, $n'_r \le 2$ and $n' = n - 3 \ge 6 - 3 = 3$. Then $3n'_r \le 6 \le 2n'$.

Subcase 4.3. $n = 5$.

In this subcase, $3n_r \le 2n = 10$ implies that $n_r \le 3$. As $n = 5$, $n_{r-1} \le 2$ and $n_{r-2} \le 1$. Thus, $n'_r = 1$ and $n' = 5 - 3 = 2$. Then $3n'_r = 3 < 4 = 2n'$.

Hence, by the induction hypothesis, we have

$\mathrm{ip}(\mu(G)) \le \mathrm{ip}(\mu(G')) + 2 \le \lceil (2n'+1)/3 \rceil + 2 = \lceil (2n+1)/3 \rceil$. ■

3. Complete γ -partite graphs

The purpose of this section is to determine exact values of the isometric path numbers of Mycielskians of all complete r-partite graphs. Suppose that G is the complete r-partite graph $K_{n_1,n_2,\ldots,n_r}$ of n vertices with $r \geq 2$, $n_i \geq 1$, $n = n_1 + n_2 + \cdots + n_r$, and partite sets $A_i = \{a_{i,1}, a_{i,2}, \ldots, a_{i,n_i}\}$ for all $1 \leq i \leq r$.

Lemma 3.1 $\mathrm{diam}(\mu(G)) = 2$.

Proof. By Theorem 1.3 and $\mathrm{diam}(G) \leq 2$, this lemma holds. ■

Lemma 3.2 $\mathrm{ip}(\mu(G)) \geq \max_{1\leq i\leq r}\{\lceil(2n+1)/3\rceil, n_i\}$.

Proof. By Lemma 3.1, every maximal isometric path has at most two vertices in $A'_i \cup A_i$ for all $1 \leq i \leq r$. And $|A'_i \cup A_i| = 2n_i$, so by Lemma 1.1, $\mathrm{ip}(\mu(G)) \geq \lceil 2n_i/2 = n_i \rceil$ for all $1 \leq i \leq r$. By Lemma 3.1 and Corollary 1.2, $\mathrm{ip}(\mu(G)) \geq \lceil(2n+1)/3\rceil$. Hence, this lemma holds. ■

Lemma 3.3 $\mathrm{ip}(\mu(K_{1,n_2})) \leq \mathrm{ip}(\mu(K_{1,n_2-2})) + 2$ *for* $n_2 \geq 3$.

Proof. Let $V(K_{1,n_2})$ be the disjoint union of $V(K_{1,n_2-2})$ and $\{a_{2,n_2-1}, a_{2,n_2}\}$. If $\mathcal{C}$ is an isometric path cover of $\mu(K_{1,n_2-2})$ with $|\mathcal{C}| = \mathrm{ip}\,(\mu(K_{1,n_2-2}))$, then $\mathcal{C} \cup \{a'_{2,n_2-1}a_{1,1}a'_{2,n_2}, a_{2,n_2-1}a'_{1,1}a_{2,n_2}\}$ is an isometric path cover of $\mu(K_{1,n_2})$. Hence, $\mathrm{ip}(\mu(K_{1,n_2})) \leq \mathrm{ip}(\mu(K_{1,n_2-2})) + 2$. ■

Lemma 3.4 *For a complete bipartite graph* K_{1,n_2},

$$\mathrm{ip}(\mu(K_{1,n_2})) \leq \begin{cases} n_2 + 1 & \text{if } n_2 = 1,2, \\ n_2 & \text{if } n_2 \geq 3. \end{cases}$$

Proof. Since $\mu(K_{1,1}) = \mu(K_2)$, by Theorem 2.3, $\mathrm{ip}(\mu(K_{1,1})) = 2$. For $n_2 = 2$, we have the isometric path cover $\mathcal{C}\left(\mu\left(K_{1,2}\right)\right) = \{a_{2,1}a'_{1,1}a_{2,2}, a'_{2,1}a_{1,1}a'_{2,2}, u\}$. Therefore, $\mathrm{ip}(\mu(K_{1,2})) \leq 3$.

For $n_2 \geq 3$, we use induction on n_2 to prove that $\mathrm{ip}(\mu(K_{1,n_2})) \leq n_2$. When $n = 3,4$, let isometric path covers $\mathcal{C}(\mu(K_{1,3})) = \{a'_{2,1}a_{1,1}a_{2,1}, a_{2,2}a'_{1,1}a_{2,3}, a'_{2,2}ua'_{2,3}\}$ and $\mathcal{C}\left(\mu\left(K_{1,4}\right)\right) = \{a'_{2,1}a_{1,1}a'_{2,2}, a_{2,1}a'_{1,1}a_{2,2}, a_{2,3}a_{1,1}a_{2,4}, a'_{2,3}ua'_{2,4}\}$. Thus, $\mathrm{ip}(\mu(K_{1,n_2})) \leq n_2$ for $n_2 = 3,4$.

Suppose $n_2 \geq 5$ and the claim holds for $n'_2 < n_2$. Let $n'_2 = n_2 - 2$. Then by Lemma 3.3 and the induction hypothesis, we have $\mathrm{ip}(\mu(K_{1,n_2})) \leq \mathrm{ip}(\mu(K_{1,n_2-2})) + 2 \leq n_2 - 2 + 2 = n_2$. Hence, this lemma holds. ■

Lemma 3.5 *Suppose that* $r \geq 3$ *with* $n_r \geq 2$ *or* $r = 2$ *with* $2 \leq n_1 \leq n_2$. *Then* $\mathrm{ip}(\mu(G)) \leq \mathrm{ip}(\mu(K_{n_1,\ldots,n_{r-1}-1,n_r-2})) + 2$.

2. Complete graphs

Recall that a complete graph K_n is the graph with vertex set $\{v_i: 1 \le i \le v_n\}$ and edge set $\{v_i v_j: 1 \le i < j \le n\}$. In order to determine exact values of isometric path numbers of Mycielskians of complete graphs $\mu(K_n)$, we remove an isometric path of 3 vertices from $\mu(K_n)$. So we shall give exact values of isometric path number for the remaining graph. Therefore, we define a graph $\mu_1(K_n) = \mu(K_{n+1})\backslash\{v_{n+1}\}$ with vertex set $V(\mu(K_n)) \cup \{v'_{n+1}\}$ and edge set is $E(\mu(K_n)) \cup \{v'_{n+1}u\} \cup \{v_i v'_{n+1}: 1 \le i \le n\}$, and shall give exact values of isometric path numbers of $\mu_1(K_n)$.

Lemma 2.1 $\mathrm{diam}(\mu(K_n)) = 2$ *and* $\mathrm{diam}(\mu_1(K_n)) = 2$ *for* $n \ge 2$.

Proof. By Theorem 1.3, $\mathrm{diam}(K_n) = 1$, and the definition of $\mu_1(K_n)$, this lemma holds.■

Theorem 2.2 $\mathrm{ip}(\mu_1(K_1)) = 1$ *and* $\mathrm{ip}(\mu_1(K_n)) = \lceil (2n+2)/3 \rceil$ *for* $n \ge 2$.

Proof. Since $\mu_1(K_1)$ is a path P_4, $\mathrm{ip}(\mu_1(K_1)) = 1$. By Corollary 1.2 and Lemma 2.1, we have $\mathrm{ip}(\mu_1(K_n)) \ge \lceil (2n+2)/3 \rceil$ for $n \ge 2$.

On the other hand, we shall construct isometric path covers $\mathcal{C}(\mu_1(K_n))$ for $n \ge 2$ inductively as follows. When $n = 2,3$, let $\mathcal{C}(\mu_1(K_2)) = \{v'_1 u v'_3, v'_2 v_1 v_2\}$ and $\mathcal{C}(\mu_1(K_3)) = \{v'_1 u v'_2, v_1 v'_4, v'_3 v_2 v_3\}$.

Suppose that $n \ge 4$ and we have constructed the isometric path cover $\mathcal{C}(\mu_1(K_{n-2}))$. Then we construct the isometric path cover $\mathcal{C}(\mu_1(K_n))$ as follows.

$\mathcal{C}(\mu_1(K_n)) = \mathcal{C}(\mu_1(K_{n-2})) \cup \{v'_n v_{n-1} v'_{n+1}, v_n\}$ for $n = 3k+1$ with $k \ge 1$;

$\mathcal{C}(\mu_1(K_n)) = \mathcal{C}(\mu_1(K_{n-2}))\backslash\{v_{n-4} v'_{n-1}\} \cup \{v'_n v_{n-1} v_n, v'_{n+1} v_{n-4} v'_{n-1}\}$ for $n = 3k+2$ with $k \ge 1$;

$\mathcal{C}(\mu_1(K_n)) = \mathcal{C}(\mu_1(K_{n-2}))\backslash\{v_{n-2}\} \cup \{v'_n v_{n-1} v_n, v_{n-2} v'_{n+1}\}$ for $n = 3k+3$ with $k \ge 1$.

Thus, we have $\mathrm{ip}(\mu_1(K_n)) \le |\mathcal{C}(\mu_1(K_n))| = \lceil (2(n-2)+2)/3 \rceil + 2 = \lceil (2n+4)/3 \rceil = \lceil (2n+2)/3 \rceil$ for $n = 3k+1$ with $k \ge 1$, and $\mathrm{ip}(\mu_1(K_n)) \le |\mathcal{C}(\mu_1(K_n))| = \lceil (2(n-2)+2)/3 \rceil - 1 + 2 = \lceil (2n+1)/3 \rceil = \lceil (2n+2)/3 \rceil$ for $n = 3k+2$ and $n = 3k+3$ with $k \ge 1$. ■

Theorem 2.3 $\mathrm{ip}(\mu(K_1)) = 2$ *and* $\mathrm{ip}(\mu(K_n)) = \lceil (2n+1)/3 \rceil$ *for* $n \ge 2$.

Proof. Since $\mu(K_1)$ is the disjoint union of K_2 and K_1, $\mathrm{ip}(\mu(K_1)) = 2$. By Corollary 1.2 and Lemma 2.1, we have $\mathrm{ip}(\mu(K_n)) \ge \lceil (2n+1)/3 \rceil$ for $n \ge 2$. On the other hand, when $n = 2,3$, let $\mathcal{C}(\mu(K_2)) = \{v'_1 u, v'_2 v_1 v_2\}$ and $\mathcal{C}(\mu(K_3)) = \{v'_1 u v'_2, v_1, v'_3 v_2 v_3\}$. Then the assertion hold for $n = 2,3$. For $n \ge 4$, as we can partition the vertex set of $\mu(K_n)$ into the vertex sets of two distance invariant induced subgraphs $\mu_1(K_{n-2})$ and $v'_n v_{n-1} v_n$. Therefore, $\mathrm{ip}(\mu(K_n)) \le \mathrm{ip}(\mu_1(K_{n-2})) + 1 = \lceil (2(n-2)+2)/3 \rceil + 1 = \lceil (2n+1)/3 \rceil$ for $n \ge 4$. ■

As not all graphs are cop-win graphs, Aigner and Fromme [1] introduced the concept of *cop number* of a general graph G, denoted by $c(G)$, which is the minimum number of cops needed to put into the graph in order to catch the robber. They showed that a single cop moving on an isometric path P guarantees that after a finite number of moves the robber will be immediately caught if he moves onto P. Observing this fact, Fitzpatrick [4] then introduced the concept of isometric path number and pointed out that $c(G) \leq \mathrm{ip}(G)$.

The isometric path number of the Cartesian product $P_{n_1} \square P_{n_2} \square \cdots \square P_{n_r}$ has been studied in the literature. Fitzpatrick [5] gave bounds for the case when $n_1 = n_2 = \cdots = n_r$. Fisher and Fitzpatrick [2] gave exact values for the case $r = 2$. Fitzpatrick et al. [6] gave a lower bound, which is in fact the exact value if $r + 1$ is a power of 2, for the case when $n_1 = n_2 = \cdots = n_r = 2$. There are other results on some graphs. Fisher and Fitzpatrick [2] gave exact values of isometric path numbers of trees. Pan and Chang [9] gave a linear-time algorithm to solve the isometric path problem on block graphs. Pan and Chang [10] gave exact values of isometric path numbers of complete r-partite graphs and Cartesian products of 2 or 3 complete graphs.

In this paper, we determine exact values of isometric path numbers of Mycielskians of complete graphs, complete bipartite graphs, paths and cycles, respectively.

The *diameter* of a graph G, denoted by $\mathrm{diam}(G)$, is defined as the maximum distance between any pair of vertices in G. An *isometric path cover* for a graph G is a set consisting of the isometric paths of G which contains all vertices of G. Throughout this paper, $\mathcal{C}(G)$ denotes an isometric path cover of a graph G.

Lemma 1.1 *Let* $c(A) = \max\{|V(P) \cap A| : P$ *is a maximal isometric path of* $G = (V(G), E(G))\}$ *for a subset* A *of* $V(G)$. *Then* $\mathrm{ip}(G) \geq \max_{A \subseteq V(G)} \lceil |A|/c(A) \rceil$.

Proof. Suppose that A is a subset of $V(G)$, $\mathcal{C}$ is an isometric path cover of G with $|\mathcal{C}| = \mathrm{ip}(G)$, and let $\mathcal{C}_i$ be the subset of $\mathcal{C}$ consisting of maximal isometric paths having exactly i vertices in A for all $1 \leq i \leq c(A)$. Then $c(A)\mathrm{ip}(G) = c(A)|\mathcal{C}| = c(A)\sum_{i=1}^{c(A)} |\mathcal{C}_i| \geq \sum_{i=1}^{c(A)} i|\mathcal{C}_i| \geq |A|$ implies that $\mathrm{ip}(G) \geq \lceil |A|/c(A) \rceil$. Hence, this lemma holds. ∎

Corollary 1.2 [2] $\mathrm{ip}(G) \geq \lceil |V(G)|/(\mathrm{diam}(G) + 1) \rceil$ *for a connected graph* G.

Proof. Let a set $A = V(G)$. Since $c(A) \leq \mathrm{diam}(G) + 1$ for a connected graph G, by Lemma 1.1, this corollary holds. ∎

The *Mycielskian* of a graph $G = (V(G), E(G))$ is the graph $\mu(G)$ with vertex set $V(G) \cup V'(G) \cup \{u\}$, where $V'(G) = \{x' : x \in V(G)\}$ and edge set $E(G) \cup \{xy' : xy \in E(G)\} \cup \{y'u : y' \in V'(G)\}$.

Theorem 1.3 [3] *For a graph* G *without isolated vertices,*

$$\mathrm{diam}(\mu(G)) = \min\{\max\{2, \mathrm{diam}(G)\}, 4\}.$$

Isometric path number of the Mycielskian of a graph[1]

Jun-Jie Pan [2,3]

Department of Mathematics
Fu-Jen Catholic University, Taiwan, R.O.C.

Abstract

In this paper, we determine exact values of isometric path numbers of Mycielskians of complete graphs, complete r-partite graphs, paths and cycles, respectively.

Key words: Isometric path, Mycielskian of a graph

1. Introduction

An *isometric path* between two vertices in a graph G is a shortest path joining them. The *isometric path number* of G, denoted by $\mathrm{ip}(G)$, is defined to be the minimum number of isometric paths required to cover all the vertices of G. This concept has a close relationship with the game of cops and robbers described as follows.

The game is played by two players, the *cop* and the *robber*, on a graph. The two players move alternatively, starting with the cop. Each player's first move consists of choosing a vertex at which to start. At each subsequent move, a player may choose either to stay at the same vertex or to move to an adjacent vertex. The object for the cop is to catch the robber, and for the robber is to prevent this from happening. Nowakowski and Winkler [7], and Quilliot [8] independently proved that the cop wins if and only if the graph can be reduced to a single vertex by successively removing pitfalls, where a *pitfall* is a vertex whose closed neighborhood is a subset of the closed neighborhood of another vertex.

[1] Supported in part by the National Science Council under grant NSC98-2628-M-030-001
[2] Department of Mathematics, Fu Jen Catholic University, New Taipei City 24205, Taiwan.
[3] E-mail: jackpan@math.fju.edu.tw.

嚴密證明：特定毛細重力波所涉問題之數個微分運算子與不定積分的可交換性

葉乃實

輔仁大學 數學系

摘　要

本論文的目的，在於證明特定的微分運算子及積分運算的交換性。此種交換性，是造就柱狀造波器外、無窮深受激毛細重力波在哈京氏邊界條件下，問題可解性的基礎認知。

關鍵字：毛細重力波，柱狀造波器，哈京氏邊界條件。

A radiation condition is prescribed as follows:

$$\Phi \to C_0 e^{k_0 z} H_m^{(1)}(k_0 r) e^{\mathrm{i}(\omega t \pm m\theta)} \text{ as } r \to \infty,$$

where $\alpha = k_0$ is the unique positive root of equation

$$\Delta(\alpha) = \alpha(\mathrm{T}\alpha^2 + 1) - \omega^2 = 0,$$

$H_m^{(1)}(\cdot)$ is the Hankel's function of the first kind with order m, and C_0 is an unknown constant.

The edge condition prescribed for the problem here is **Hocking's edge condition,** and is given by

$$Z_t = \lambda Z_r, \quad \left(\lambda \equiv \frac{1}{\delta}\right) \qquad \text{at} \qquad r = a, \ z = 0,$$

where λ is a constant determined by experiment. Since the above equations are all linear, we may time–reduce and $\theta-$reduce the problem and assume

$$\begin{aligned} \Phi(r, \theta, z, t) &= \varphi_\infty(r, z) e^{\mathrm{i}(\omega t \pm m\theta)}, \\ Z(r, \theta, t) &= \overset{\wedge}{\zeta}(r) e^{\mathrm{i}(\omega t \pm m\theta)}. \end{aligned}$$

Now we measure r, z, Z and $\overset{\wedge}{\zeta}$ in units of 1, t in units of $\mathrm{g}^{-\frac{1}{2}}$; Φ, φ, T and λ in units of g; ω and f in units of $\mathrm{g}^{\frac{1}{2}}$. Then writing down the equations for the linearized and time-and-θ- reduced problem, we obtain the governing equations from (2.1) to (2.6).

Appendix A. Formulations

We shall consider capillary–gravity waves generated by a cylindrical wave-maker in an incompressible, inviscid fluid, and assume that the fluid motion is irrotational. Let us use a cylindrical coordinate system in which the z-axis is pointing vertically upwards, so that $z = 0$, $r > a$ is the undisturbed state of the fluid. The fluid region is exterior ($r > a$) to the wave maker. At equilibrium it is of uniform depth h. We may describe the fluid motion by a velocity potential $\Phi(r, \theta, z, t)$. The linearized equations governing the fluid motion are the following:

$$\nabla_3^2 \Phi = 0 \qquad \text{in the fluid region} \qquad V;$$

$$\left.\begin{aligned} \Phi_z &= Z_t, \\ \Phi_t + \mathrm{g} Z &= \mathrm{T} \nabla_2^2 Z \end{aligned}\right\} \quad \text{on} \quad z = 0,\ r > a;$$

where

$$V = \{ (r, z) |\ r > a > 0, \text{ and } z \in (-\infty, 0) \};$$

∇_3^2 and ∇_2^2 denote three–dimensional and two–dimensional cylindrical Laplacians respectively, g is the gravitational constant, ρT is the surface tension constant, ρ is the fluid density, $\theta \in [0, 2\pi]$, and Z represents free surface of the fluid.

$$\Phi_r = f(z) e^{\mathrm{i}(\omega t \pm m\theta)} \qquad \text{on} \qquad r = a,$$

where ω is the angular frequency, m is the azimuthal number (i.e. the waves are generated asymmetrically,) and f is an arbitrary smooth function. The bottom condition is given by

$$\Phi_z \to 0 \qquad \text{on} \qquad z \to -\infty.$$

References

1. D. V. Evans, "The influence of surface tension on the re.ection of water waves by a plane vertical barrier" , *Proc. Cambridge Philos. Soc*,. **64**, 795 (1968).
2. D. V. Evans, "The effect of surface tension on the waves produced by a heaving circular cylinder" , *Proc. Cambridge Philos. Soc*., **64**, 833 (1968).
3. L.M. Hocking, "The damping of capillary-gravity waves at a rigid boundary" , *J. Fluid Mech*., **179**, 253 (1987).
4. J. W. Miles, "Capillary-viscous forcing of surface waves" , *J. Fluid Mech*., **219**, 635 (1990).
5. J. W. Miles, "On forced capillary-gravity waves in a circular cylinder" , *Wave Motion,* **23**, 387 (1996).
6. C.-L. Ting and M. Perlin, "Boundary conditions in the vicinity of the contact line at a vertically oscillating upright plate: an experimental investigation" , *J. Fluid Mech*., **295**, 263 (1995).
7. P. F. Rhodes-Robinson, "On the forced surface waves due to a vertical wave-maker in the presence of surface tension" , *Proc. Cambridge Philos. Soc*., **70**, 323 (1971).
8. M. C. Shen, S. M. Sun and D. Y. Hsieh, "Forced capillary-gravity waves in a circular basin" , *Wave Motion*, **18**, 401 (1993).
9. M.-C. Shen and N.-S. Yeh, "Exact solution for forced capillary-gravity waves in a circular basin under Hocking' s edge condition" , *Wave Motion*, **26**, 117 (1997).
10. M.-C. Shen and N.-S. Yeh, "On a special case of forced capillary-gravity waves in a circular basin under Hocking' s edge condition" , *Wave Motion*, **30**, 91 (1999).
11. N.-S. Yeh, "Rigorous proofs of the expansion theorems for the problems of forced capillary-gravity waves" , *Fu-Jen Studies*, **35**, 1 (2001).

Recevied Oct 30, 2013
Revised Mar 22, 2014
Accepted Mar 22, 2014

So the improper integral in (2.18) converges. Thus we have proved the Theorem completely.

3. Conclusion

By using expansion theorem and a special assumption, we find that in order to construct the solution, the interchangeability of some differential operators and an improper integral should be verified first. Therefore the plausibility of proposing the theorem is asserted. We do not get into detail of solution finding because it involves other technical details and has no relevance to our proof. Construction of solution as well as possible application of the model shall be discussed in another paper.

4. Acknowledgement

The author wishes to express his gratitude to the National Science Council of Taiwan, R. O. C. for its support of this research.

where $l \cdot a >> m$. Note that when α is small,

$$Q_{1z}(\alpha, z) = \alpha^2 \cdot \frac{\alpha(\mathrm{T}\alpha^2 - 1)\sin\alpha z + \omega^2 \cos\alpha z}{\alpha^2(1 - \mathrm{T}\alpha^2)^2 + \omega^4} = O\left(\alpha^2\right),$$

$$\begin{aligned}\left|\int_0^l Q_{1z}(\alpha, z)R_1(\alpha, r)\mathrm{d}\alpha\right| &\leq \int_0^l |Q_{1z}(\alpha, z)R_1(\alpha, r)|\,\mathrm{d}\alpha \\ &= \int_0^l O\left(\alpha^4\right)\mathrm{d}\alpha < \infty.\end{aligned}$$

Also for $\alpha > l$,

$$Q_{1z}(\alpha, z) = \alpha^2 \cdot \frac{\alpha(\mathrm{T}\alpha^2 - 1)\sin\alpha z + \omega^2 \cos\alpha z}{\alpha^2(1 - \mathrm{T}\alpha^2)^2 + \omega^4} = O\left(\alpha\right),$$

$$\begin{aligned}\left|\int_l^\infty Q_{1z}(\alpha, z)R_1(\alpha, r)\mathrm{d}\alpha\right| &\leq \int_l^\infty |Q_{1z}(\alpha, z)R_1(\alpha, r)|\,\mathrm{d}\alpha \\ &= \int_l^\infty O\left(\frac{\alpha}{e^{\alpha(r-a)}}\right)\mathrm{d}\alpha < \infty.\end{aligned}$$

So we have (2.17) being convergent. Next, let's consider the improper integral in (2.18):

$$2\mathrm{T}\mu\int_0^\infty Q_{1z}(\alpha, z)R_{1r}(\alpha, r)\mathrm{d}\alpha = 2\mathrm{T}\mu\left[\int_0^l Q_{1z}(\alpha, z)R_{1r}(\alpha, r)\mathrm{d}\alpha + \int_l^\infty Q_{1z}(\alpha, z)R_{1r}(\alpha, r)\mathrm{d}\alpha\right]$$

where $l \cdot a >> m$. When α is small,

$$\begin{aligned}\left|\int_0^l Q_{1z}(\alpha, z)R_{1r}(\alpha, r)\mathrm{d}\alpha\right| &\leq \int_0^l |Q_{1z}(\alpha, z)R_{1r}(\alpha, r)|\,\mathrm{d}\alpha \\ &= \int_0^l O\left(\alpha\right)\mathrm{d}\alpha < \infty.\end{aligned}$$

When $\alpha > l$,

$$\begin{aligned}\left|\int_l^\infty Q_{1z}(\alpha, z)R_{1r}(\alpha, r)\mathrm{d}\alpha\right| &\leq \int_l^\infty |Q_{1z}(\alpha, z)R_{1r}(\alpha, r)|\,\mathrm{d}\alpha \\ &= \int_l^\infty O\left(\frac{\alpha}{e^{\alpha(r-a)}}\right)\mathrm{d}\alpha < \infty, \quad r > a.\end{aligned}$$

where $l \cdot a >> m$. Note that when α is small,

$$Q_1(\alpha, z) = \alpha \cdot \frac{\alpha(1 - \mathrm{T}\alpha^2)\cos\alpha z + \omega^2 \sin\alpha z}{\alpha^2(1 - \mathrm{T}\alpha^2)^2 + \omega^4} = O\left(\alpha^2\right),$$

and

$$R_{1r}(\alpha, r) = \frac{\alpha K_m'(\alpha r)}{\alpha K_m'(\alpha a)} = \frac{\frac{m}{\alpha r}K_m(\alpha r) - K_{m+1}(\alpha r)}{\frac{m}{\alpha a}K_m(\alpha a) - K_{m+1}(\alpha a)} = O(1).$$

So

$$\begin{aligned}\left|\int_0^l Q_1(\alpha, z)R_{1r}(\alpha, r)\mathrm{d}\alpha\right| &\leq \int_0^l |Q_1(\alpha, z)R_{1r}(\alpha, r)|\,\mathrm{d}\alpha \\ &= \int_0^l O\left(\alpha^2\right)\mathrm{d}\alpha < \infty.\end{aligned}$$

Also when $\alpha > l$,

$$Q_1(\alpha, z) = \alpha \cdot \frac{\alpha(1 - \mathrm{T}\alpha^2)\cos\alpha z + \omega^2 \sin\alpha z}{\alpha^2(1 - \mathrm{T}\alpha^2)^2 + \omega^4} = O\left(\alpha^2\right),$$

$$\begin{aligned}R_{1r}(\alpha, r) &= \frac{\alpha K_m'(\alpha r)}{\alpha K_m'(\alpha a)} = \frac{\frac{m}{\alpha r}K_m(\alpha r) - K_{m+1}(\alpha r)}{\frac{m}{\alpha a}K_m(\alpha a) - K_{m+1}(\alpha a)} \sim \frac{\left(\frac{m}{\alpha r} - 1\right)\frac{e^{-\alpha r}}{\sqrt{\frac{2}{\pi}\alpha r}}}{\left(\frac{m}{\alpha a} - 1\right)\frac{e^{-\alpha a}}{\sqrt{\frac{2}{\pi}\alpha a}}} \\ &= O\left(\frac{1}{e^{\alpha(r-a)}}\right), \quad r > a.\end{aligned}$$

i. e.

$$\begin{aligned}\left|\int_l^\infty Q_1(\alpha, z)R_{1r}(\alpha, r)\mathrm{d}\alpha\right| &\leq \int_l^\infty |Q_1(\alpha, z)R_{1r}(\alpha, r)|\,\mathrm{d}\alpha \\ &= \int_l^\infty O\left(\frac{\alpha^2}{e^{\alpha(r-a)}}\right)\mathrm{d}\alpha < \infty.\end{aligned}$$

Therefore the integral converges. Look at the improper integral in (2.17):

$$2\mathrm{T}\mu\int_0^\infty Q_{1z}(\alpha, z)R_1(\alpha, r)\mathrm{d}\alpha = 2\mathrm{T}\mu\left[\int_0^l Q_{1z}(\alpha, z)R_1(\alpha, r)\mathrm{d}\alpha + \int_l^\infty Q_{1z}(\alpha, z)R_1(\alpha, r)\mathrm{d}\alpha\right],$$

And for $\alpha > l$,

$$\left|\int_l^\infty \alpha^2 R_1(\alpha,r)P_{1z}(\alpha,z)\mathrm{d}\alpha\right| \leq \int_l^\infty \left|\alpha^2 R_1(\alpha,r)P_{1z}(\alpha,z)\right|\mathrm{d}\alpha = \int_l^\infty O\left(\frac{\alpha^3}{e^{\alpha(r-a)}}\right)\mathrm{d}\alpha < \infty,$$

hence $\int_0^\infty \alpha^2 R_1(\alpha,r)P_{1z}(\alpha,z)\mathrm{d}\alpha$ converges. Because all of the integrals involving first parts of (2.10) to (2.14) converge, we may interchange the differentiation and integration for the first parts.

Next, let us examine second part of the integrals in (2.10) to (2.14). With similar structure to that of first part, we find that the improper integrals to be checked are:

$$2\mathrm{T}\mu\int_0^\infty \alpha^2\cdot\frac{\alpha(1-\mathrm{T}\alpha^2)\cos\alpha z+\omega^2\sin\alpha z}{\alpha^2(1-\mathrm{T}\alpha^2)^2+\omega^4} \times\frac{K_m'(\alpha r)}{\alpha K_m'(\alpha a)}\mathrm{d}\alpha, \tag{2.16}$$

$$2\mathrm{T}\mu\int_0^\infty \alpha^2\cdot\frac{\alpha(\mathrm{T}\alpha^2-1)\sin\alpha z+\omega^2\cos\alpha z}{\alpha^2(1-\mathrm{T}\alpha^2)^2+\omega^4} \times\frac{K_m(\alpha r)}{\alpha K_m'(\alpha a)}\mathrm{d}\alpha, \tag{2.17}$$

and

$$2\mathrm{T}\mu\int_0^\infty \alpha^3\cdot\frac{\alpha(\mathrm{T}\alpha^2-1)\sin\alpha z+\omega^2\cos\alpha z}{\alpha^2(1-\mathrm{T}\alpha^2)^2+\omega^4} \times\frac{K_m'(\alpha r)}{\alpha K_m'(\alpha a)}\mathrm{d}\alpha, \tag{2.18}$$

respectively. The improper integral in (2.16) is

$$2\mathrm{T}\mu\int_0^\infty Q_1(\alpha,z)R_{1r}(\alpha,r)\mathrm{d}\alpha = 2\mathrm{T}\mu\left[\int_0^l Q_1(\alpha,z)R_{1r}(\alpha,r)\mathrm{d}\alpha+\int_l^\infty Q_1(\alpha,z)R_{1r}(\alpha,r)\mathrm{d}\alpha\right],$$

And the second part of the integral can be estimated as follows:

$$\begin{aligned} |P_{1z}(\alpha,z)| &= \alpha\omega^2 \left| \frac{\alpha(\mathrm{T}\alpha^2-1)\sin\alpha z+\omega^2\cos\alpha z}{\alpha^2(1-\mathrm{T}\alpha^2)^2+\omega^4} \right| \\ &\quad \times \left| \int_{-\infty}^{0} f(\zeta)\left[\alpha(1-\mathrm{T}\alpha^2)\cos\alpha\zeta+\omega^2\sin\alpha\zeta\right]\mathrm{d}\zeta \right| \\ &= O(\alpha) \quad \text{for} \quad \alpha > l, \end{aligned}$$

and then

$$\begin{aligned} \left| \int_l^{\infty} R_1(\alpha,r)P_{1z}(\alpha,z)\mathrm{d}\alpha \right| &\leq \int_l^{\infty} |R_1(\alpha,r)P_{1z}(\alpha,z)|\,\mathrm{d}\alpha \\ &= \int_l^{\infty} O\left(\frac{\alpha}{e^{\alpha(r-a)}}\right)\mathrm{d}\alpha < \infty, \quad r > a. \end{aligned}$$

So $\int_0^{\infty} R_1(\alpha,r)P_{1z}(\alpha,z)\mathrm{d}\alpha$ converges. Again, look at the following improper integral

$$\begin{aligned} &\int_0^{\infty} \alpha^2 R_1(\alpha,r)P_{1z}(\alpha,z)\mathrm{d}\alpha \\ = &-\frac{2\mathrm{T}}{\pi}\int_0^{\infty} \frac{K_m(\alpha r)}{\alpha K_m'(\alpha a)} \\ &\times\alpha^3\omega^2\left[\alpha(\mathrm{T}\alpha^2-1)\sin\alpha z+\omega^2\cos\alpha z\right] \\ &\times\left\{\int_{-\infty}^{0} f(\zeta)\frac{\alpha(1-\mathrm{T}\alpha^2)\cos\alpha\zeta+\omega^2\sin\alpha\zeta}{\alpha^2(1-\mathrm{T}\alpha^2)^2+\omega^4}\mathrm{d}\zeta\right\}\mathrm{d}\alpha, \end{aligned}$$

also

$$\int_0^{\infty} \alpha^2 R_1(\alpha,r)P_{1z}(\alpha,z)\mathrm{d}\alpha = \int_0^{l} \alpha^2 R_1(\alpha,r)P_{1z}(\alpha,z)\mathrm{d}\alpha + \int_l^{\infty} \alpha^2 R_1(\alpha,r)P_{1z}(\alpha,z)\mathrm{d}\alpha,$$

where $l \cdot a >> m$. Then for α being small,

$$\begin{aligned} \left| \int_0^{l} \alpha^2 R_1(\alpha,r)P_{1z}(\alpha,z)\mathrm{d}\alpha \right| &\leq \int_0^{l} \left|\alpha^2 R_1(\alpha,r)P_{1z}(\alpha,z)\right|\mathrm{d}\alpha \\ &= \int_0^{l} O\left(\alpha^6\right)\mathrm{d}\alpha < \infty. \end{aligned}$$

and that

$$\left|\int_l^\infty R_1(\alpha,r)P_1(\alpha,z)\mathrm{d}\alpha\right| \leq \int_l^\infty |R_1(\alpha,r)P_1(\alpha,z)|\,\mathrm{d}\alpha$$
$$= \int_l^\infty O\left(\frac{\alpha^3}{e^{\alpha(r-a)}}\right)\mathrm{d}\alpha < \infty.$$

Hence (2.15) converges. Similarly, the improper integral $\int_0^\infty R_1(\alpha,r)P_{1z}(\alpha,z)\mathrm{d}\alpha$ can be expressed as

$$\int_0^\infty R_1(\alpha,r)P_{1z}(\alpha,z)\mathrm{d}\alpha$$
$$= -\frac{2}{\pi}\int_0^\infty \frac{K_m(\alpha r)}{\alpha K_m'(\alpha a)}$$
$$\times\alpha\omega^2\left[\alpha(\mathrm{T}\alpha^2-1)\sin\alpha z+\omega^2\cos\alpha z\right]$$
$$\times\left\{\int_{-\infty}^0 f(\zeta)\frac{\alpha(1-\mathrm{T}\alpha^2)\cos\alpha\zeta+\omega^2\sin\alpha\zeta}{\alpha^2(1-\mathrm{T}\alpha^2)^2+\omega^4}\mathrm{d}\zeta\right\}\mathrm{d}\alpha$$

and

$$\int_0^\infty R_1(\alpha,r)P_{1z}(\alpha,z)\mathrm{d}\alpha = \int_0^l R_1(\alpha,r)P_{1z}(\alpha,z)\mathrm{d}\alpha + \int_l^\infty R_1(\alpha,r)P_{1z}(\alpha,z)\mathrm{d}\alpha,$$

where $l\cdot a >> m$. To estimate the first part of the integral, we see that when α is small,

$$|P_{1z}(\alpha,z)| = \alpha\omega^2\left|\frac{\alpha(\mathrm{T}\alpha^2-1)\sin\alpha z+\omega^2\cos\alpha z}{\alpha^2(1-\mathrm{T}\alpha^2)^2+\omega^4}\right|$$
$$\times\left|\int_{-\infty}^0 f(\zeta)\left[\alpha(1-\mathrm{T}\alpha^2)\cos\alpha\zeta+\omega^2\sin\alpha\zeta\right]\mathrm{d}\zeta\right|$$
$$= O\left(\alpha^2\right);$$

$$\left|\int_0^l R_1(\alpha,r)P_{1z}(\alpha,z)\mathrm{d}\alpha\right| \leq \int_0^l |R_1(\alpha,r)P_{1z}(\alpha,z)|\,\mathrm{d}\alpha$$
$$= \int_0^l O\left(\alpha^4\right)\mathrm{d}\alpha < \infty.$$

$$|P_1(\alpha,z)| = \alpha(1-\mathrm{T}\alpha^2)\left|\frac{\alpha(1-\mathrm{T}\alpha^2)\cos\alpha z+\omega^2\sin\alpha z}{\alpha^2(1-\mathrm{T}\alpha^2)^2+\omega^4}\right| \times\left|\int_{-\infty}^{0} f(\zeta)\left[\alpha(1-\mathrm{T}\alpha^2)\cos\alpha\zeta+\omega^2\sin\alpha\zeta\right]\mathrm{d}\zeta\right| = O\left(\alpha^2\right).$$

Hence when α is small,

$$|R_1(\alpha,r)P_1(\alpha,z)| = O\left(\alpha^4\right),$$

and the first improper integral of (2.15) shows that

$$\left|\int_0^l R_1(\alpha,r)P_1(\alpha,z)\mathrm{d}\alpha\right| \le \int_0^l |R_1(\alpha,r)P_1(\alpha,z)|\,\mathrm{d}\alpha < \infty.$$

The second part of equation (2.15) holds for $\alpha > l$, and

$$|R_1(\alpha,r)| \sim \left|\frac{\frac{e^{-\alpha r}}{\sqrt{\frac{2}{\pi}\alpha r}}}{\left(\frac{m}{\alpha a}-1\right)\frac{e^{-\alpha a}}{\sqrt{\frac{2}{\pi}\alpha a}}}\right| = \frac{\alpha\sqrt{ar}}{(\alpha a-m)\,e^{\alpha(r-a)}} = O\left(e^{-\alpha(r-a)}\right),$$

$$\begin{aligned}|P_1(\alpha,z)| &= \alpha(\mathrm{T}\alpha^2-1)\left|\frac{\alpha(1-\mathrm{T}\alpha^2)\cos\alpha z+\omega^2\sin\alpha z}{\alpha^2(1-\mathrm{T}\alpha^2)^2+\omega^4}\right| \\ &\quad\times\left|\int_{-\infty}^{0} f(\zeta)\left[\alpha(1-\mathrm{T}\alpha^2)\cos\alpha\zeta+\omega^2\sin\alpha\zeta\right]\mathrm{d}\zeta\right| \\ &= O\left(\alpha^3\right),\end{aligned}$$

for it follows from Theorem 1 that the integral over ζ is convergent. So we see that when $\alpha > l$,

$$|R_1(\alpha,r)P_1(\alpha,z)| = O\left(\frac{\alpha^3}{e^{\alpha(r-a)}}\right), \quad \text{for} \quad r > a;$$

where $l \cdot a >> m$. Look at the first part of equation (2.15):

$$\left| \int_0^l R_1(\alpha, r) P_1(\alpha, z) \mathrm{d}\alpha \right| \leq \int_0^l \left| R_1(\alpha, r) P_1(\alpha, z) \right| \mathrm{d}\alpha,$$

where $0 \leq \alpha \leq l$. Notice that when α is small,

$$\begin{aligned}
& |R_1(\alpha, r)| \\
= & \left| \sqrt{\frac{\pi}{2\alpha r}} \frac{e^{-\alpha r}}{(m-\frac{1}{2})!} \int_0^\infty e^{-t} t^{m-\frac{1}{2}} \left(1 - \frac{t}{2\alpha r}\right)^{m-\frac{1}{2}} \mathrm{d}t \right| \times \\
& \left| \sqrt{\frac{\pi}{2\alpha a}} e^{-\alpha a} \left[\left(\frac{m}{\alpha a}\right) \frac{1}{(m-\frac{1}{2})!} \int_0^\infty e^{-t} t^{m-\frac{1}{2}} \left(1 - \frac{t}{2\alpha a}\right)^{m-\frac{1}{2}} \mathrm{d}t \right. \right. \\
& \left. \left. - \frac{1}{(m+\frac{1}{2})!} \int_0^\infty e^{-t} t^{m+\frac{1}{2}} \left(1 - \frac{t}{2\alpha a}\right)^{m+\frac{1}{2}} \mathrm{d}t \right] \right|^{-1} \\
= & \left| \frac{\frac{\sqrt{\frac{a}{r}} e^{-\alpha(r-a)}}{(m-\frac{1}{2})!} \int_0^\infty e^{-t} t^{m-\frac{1}{2}} \left(1 - \frac{t}{2\alpha r}\right)^{m-\frac{1}{2}} \mathrm{d}t}{\left(\frac{m}{\alpha a}\right) \frac{1}{(m-\frac{1}{2})!} \int_0^\infty e^{-t} t^{m-\frac{1}{2}} \left(1 - \frac{t}{2\alpha r}\right)^{m-\frac{1}{2}} \mathrm{d}t - \frac{1}{(m+\frac{1}{2})!} \int_0^\infty e^{-t} t^{m+\frac{1}{2}} \left(1 - \frac{t}{2\alpha r}\right)^{m+\frac{1}{2}} \mathrm{d}t} \right| \\
= & \left| \frac{(\alpha a) \sqrt{\frac{a}{r}} e^{-\alpha(r-a)} \int_0^\infty e^{-t} t^{m-\frac{1}{2}} \left(1 - \frac{t}{2\alpha r}\right)^{m-\frac{1}{2}} \mathrm{d}t}{m \int_0^\infty e^{-t} t^{m-\frac{1}{2}} \left(1 - \frac{t}{2\alpha a}\right)^{m-\frac{1}{2}} \mathrm{d}t - (\alpha a) \frac{(m-\frac{1}{2})!}{(m+\frac{1}{2})!} \int_0^\infty e^{-t} t^{m+\frac{1}{2}} \left(1 - \frac{t}{2\alpha a}\right)^{m+\frac{1}{2}} \mathrm{d}t} \right| \\
= & \left| \frac{(\alpha a) \sqrt{\frac{a}{r}} e^{-\alpha(r-a)} \int_0^\infty e^{-t} t^{m-\frac{1}{2}} \left(1 - \frac{t}{2\alpha r}\right)^{m-\frac{1}{2}} \mathrm{d}t}{(\alpha a) \int_0^\infty e^{-t} t^{m} \left(1 - \frac{t}{2\alpha a}\right)^{m+\frac{1}{2}} \left[\frac{m}{\sqrt{t}} \left(\frac{2}{2\alpha a - t}\right) - \frac{(m-\frac{1}{2})!}{(m+\frac{1}{2})!} \sqrt{t} \right] \mathrm{d}t} \right| \\
= & \sqrt{\frac{a}{r}} e^{-\alpha(r-a)} \frac{O\left(\alpha^{\frac{1}{2}-m}\right)}{O\left(\alpha^{-\frac{3}{2}-m}\right)} = O\left(\alpha^2\right),
\end{aligned}$$

for the integrals over t converge with respect to the basic construction of K_m. Also when α is small,

equations are solvable. Method of obtaining solution as well as related issue of the problem will be discussed in another paper.

Theorem 2.2. *The differential operators $\mathcal{L}_1$, $\mathcal{L}_2$, $\frac{\partial}{\partial r}$, $\frac{\partial}{\partial z}$ and $\frac{\partial^2}{\partial z \partial r}$ can be taken into the improper integral over α as shown in the above.*

Proof. First of all, look at the first part of improper integral (2.9):

$$\begin{aligned}
&\int_0^\infty R_1(\alpha, r) P_1(\alpha, z) \mathrm{d}\alpha \\
= \; & -\frac{2}{\pi} \int_0^\infty \frac{K_m(\alpha r)}{\alpha K_m'(\alpha a)} \\
& \times \alpha(1 - \mathrm{T}\alpha^2) \left[\alpha(1 - \mathrm{T}\alpha^2) \cos \alpha z + \omega^2 \sin \alpha z\right] \\
& \times \left\{ \int_{-\infty}^0 f(\zeta) \frac{\alpha(1 - \mathrm{T}\alpha^2) \cos \alpha\zeta + \omega^2 \sin \alpha\zeta}{\alpha^2(1 - \mathrm{T}\alpha^2)^2 + \omega^4} \mathrm{d}\zeta \right\} \mathrm{d}\alpha.
\end{aligned}$$

Again,

$$\begin{aligned}
K_m(r) &= \sqrt{\frac{\pi}{2r}} \frac{e^{-r}}{(m - \frac{1}{2})!} \int_0^\infty e^{-t} t^{m - \frac{1}{2}} \left(1 - \frac{t}{2r}\right)^{m - \frac{1}{2}} \mathrm{d}t, \\
K_m'(r) &= \frac{m}{r} K_m(r) - K_{m+1}(r), \quad r > a,
\end{aligned}$$

and

$$K_m(r) \sim \frac{e^{-r}}{\sqrt{\frac{2}{\pi} r}} \quad \text{when} \quad r >> m.$$

Therefore, the improper integral above can be considered as

$$\int_0^\infty R_1(\alpha, r) P_1(\alpha, z) \mathrm{d}\alpha = \int_0^l R_1(\alpha, r) P_1(\alpha, z) \mathrm{d}\alpha + \int_l^\infty R_1(\alpha, r) P_1(\alpha, z) \mathrm{d}\alpha, \tag{2.15}$$

which constitutes major part of the possible solution of governing equations, and where

$$\begin{aligned} P_1(\alpha, z) &= -\frac{2}{\pi}\int_{-\infty}^{0} f(\zeta)\Big[[\alpha(1-\mathrm{T}\alpha^2)\cos\alpha\zeta + \omega^2\sin\alpha\zeta] \\ &\qquad \times[\alpha(1-\mathrm{T}\alpha^2)\cos\alpha z + \omega^2\sin\alpha z]/[\alpha^2(1-\mathrm{T}\alpha^2)^2+\omega^4]\Big]\mathrm{d}\zeta, \\ Q_1(\alpha, z) &= 2\alpha\cdot\frac{\alpha(1-\mathrm{T}\alpha^2)\cos\alpha z + \omega^2\sin\alpha z}{\alpha^2(1-\mathrm{T}\alpha^2)^2+\omega^4}, \\ R_1(\alpha, r) &= \frac{K_m(\alpha r)}{\alpha K_m'(\alpha a)}. \end{aligned}$$

Note that the modified Bessel function of 2nd kind K_m can be written as

$$\begin{aligned} K_m(r) &= \sqrt{\frac{\pi}{2r}}\frac{e^{-r}}{(m-\frac{1}{2})!}\int_0^{\infty} e^{-t}t^{m-\frac{1}{2}}\left(1-\frac{t}{2r}\right)^{m-\frac{1}{2}}\mathrm{d}t, \\ K_m'(r) &= \frac{m}{r}K_m(r) - K_{m+1}(r), \quad r > a. \end{aligned}$$

When (2.9) is plugged into governing equations, the following integrals

$$\mathcal{L}_1\int_0^{\infty}[P_1(\alpha,z)+\mathrm{T}\mu Q_1(\alpha,z)]R_1(\alpha,r)\mathrm{d}\alpha, \tag{2.10}$$

$$\mathcal{L}_2\int_0^{\infty}[P_1(\alpha,z)+\mathrm{T}\mu Q_1(\alpha,z)]R_1(\alpha,r)\mathrm{d}\alpha, \tag{2.11}$$

$$\frac{\partial}{\partial r}\int_0^{\infty}[P_1(\alpha,z)+\mathrm{T}\mu Q_1(\alpha,z)]R_1(\alpha,r)\mathrm{d}\alpha, \tag{2.12}$$

$$\frac{\partial}{\partial z}\int_0^{\infty}[P_1(\alpha,z)+\mathrm{T}\mu Q_1(\alpha,z)]R_1(\alpha,r)\mathrm{d}\alpha, \text{ and} \tag{2.13}$$

$$\frac{\partial^2}{\partial z\partial r}\int_0^{\infty}[P_1(\alpha,z)+\mathrm{T}\mu Q_1(\alpha,z)]R_1(\alpha,r)\mathrm{d}\alpha \tag{2.14}$$

are encountered. So we have the next Theorem to claim that the differential operators can be taken inside of the improper integral, which suggests that governing

expansion in the following form:

$$\begin{aligned} f(z) &= -\frac{2}{\pi}\int_{-\infty}^{0} f(\zeta)\int_{0}^{\infty}\Big\{[\alpha(1-\mathrm{T}\alpha^2)\cos\alpha z+\omega^2\sin\alpha z] \\ &\quad\times\left[\alpha(1-\mathrm{T}\alpha^2)\cos\alpha\zeta+\omega^2\sin\alpha\zeta\right]/\left[\alpha^2(1-\mathrm{T}\alpha^2)^2+\omega^4\right]\Big\}\mathrm{d}\alpha\mathrm{d}\zeta \\ &\quad -2\omega^2\int_{-\infty}^{0}\frac{e^{k_0(z+\zeta)}}{1+3\mathrm{T}k_0^2}f(\zeta)\mathrm{d}\zeta \\ &\quad +\mathrm{T}\mu\Big\{2\int_{0}^{\infty}\frac{\alpha[\alpha(1-\mathrm{T}\alpha^2)\cos\alpha z+\omega^2\sin\alpha z]}{\alpha^2(1-\mathrm{T}\alpha^2)^2+\omega^4}\mathrm{d}\alpha \\ &\quad +\frac{2\pi k_0}{1+3\mathrm{T}k_0^2}e^{k_0 z}\Big\}, \end{aligned} \tag{2.7}$$

where μ is an arbitrary parameter.

There is a zero term

$$\mathrm{T}\mu\Big\{2\int_{0}^{\infty}\frac{\alpha[\alpha(1-\mathrm{T}\alpha^2)\cos\alpha z+\omega^2\sin\alpha z]}{\alpha^2(1-\mathrm{T}\alpha^2)^2+\omega^4}\mathrm{d}\alpha +\frac{2\pi k_0}{1+3\mathrm{T}k_0^2}e^{k_0 z}\Big\} \tag{2.8}$$

in (2.7). However, the presence of zero term and the independent parameter μ have not been explained. It will become clear after we find the solution. We only note that μ will be determined by the edge condition. This theorem is a powerful utility in solving linearized capillary-gravity waves problem with various linearized edge conditions.

The next theorem is the main result of this paper. By the conjecture of Yeh ([11], p.10-p.11), we obtain the integral

$$\int_{0}^{\infty}[P_1(\alpha,z)+\mathrm{T}\mu Q_1(\alpha,z)]R_1(\alpha,r)\mathrm{d}\alpha, \tag{2.9}$$

2. Complete graphs

The **governing equations** of the problem considered are as follows:

$$\mathcal{L}_2\varphi_\infty(r,z) = \left(\frac{\partial^2}{\partial r^2} + \frac{1}{r}\frac{\partial}{\partial r} - \frac{m^2}{r^2} + \frac{\partial^2}{\partial z^2}\right)\varphi_\infty = 0 \quad \text{in}$$

$$V = (a,\infty)\times(-\infty,0) \text{ for some } a>0; \tag{2.1}$$

$$-\omega^2\varphi_\infty + \varphi_{\infty z} = \mathrm{T}\mathcal{L}_1\varphi_{\infty z} = \mathrm{T}\left(\mathcal{L}_2 - \frac{\partial^2}{\partial z^2}\right)\varphi_{\infty z} \quad \text{on} \quad z=0,\ r>a; \tag{2.2}$$

$$\varphi_{\infty z} \longrightarrow 0 \quad \text{as} \quad z\longrightarrow -\infty, \tag{2.3}$$

$$\varphi_{\infty r} = f(z) \quad \text{on} \quad r=a, \tag{2.4}$$

$$\varphi_\infty \longrightarrow C_0 e^{k_0 z} H_m^{(1)}(k_0 r) \quad \text{as} \quad r\longrightarrow\infty, \tag{2.5}$$

$$\varphi_{\infty rz} = \mathrm{i}\omega\delta\varphi_{\infty z} \quad \text{at} \quad z=0,\ r=a. \tag{2.6}$$

The original process of deriving these equations is shown in **Appendix A,** and the equation (2.6) is **Hocking's Edge Condition.** Notice that φ_∞ is the potential function, T is the surface tension coefficient, ω is the angular frequency, m is the azimuthal number, δ is some real constant, f is an arbitrary smooth function, C_0 is a constant, k_0 is the positive real root of $\alpha(1+T\alpha^2)-\omega^2=0$, and $H_m^{(1)}(\cdot)$ is the Hankel's function of the first kind with order m. The following is an expansion theorem presented by Rhodes-Robinson ([7], p.330) and **proved by Yeh ([11])** when f is an arbitrary smooth function defined on $(-\infty,0)$:

Theorem 2.1. *For an arbitrary smooth function $f(z)$, $z\in(-\infty,0)$, there is an*

1. Introduction

The edge condition has been widely taken as an open question because of its complexity and uncertainty. Edge condition of fluid was first considered in 1968 by Evans ([1], [2],) and Hocking [3] proposed a different model later in 1987. Both models were studied by various papers based on different settings, including Miles ([4], [5]) and Shen *et al* ([8], [9], [10].) Originally Hocking's was considered physically more plausible than Evans's, but Miles ([4], [5]) argued that Hocking's setting was not practical in the case of a heaving cylinder with stick/slip edge condition. The argument was supported by Ting and Perlin [6] through their study on edge condition in 1995, which used modern equipment to record edge condition of various types of fluid and consequently proposed a new edge condition. It has been regarded as the most practical model up to date.

According to the result found by Ting and Perlin, however, one may find that Hocking's edge condition is still valid concerning non-stick/-slip condition. Therefore the problem on non-stick/-slip oscillating wavemaker under Hocking's edge condition needs further study. Constructing the exact solution of this problem in infinite depth case is possible only if convergence of improper integrals related to the problem is thoroughly studied.

Here we focus our attention to the infinite depth problem, present the related operators, and prove the convergence of these improper integrals.

Rigorous Proof: Interchangeability between differential operators and improper integrals involving the problem of Capillary-Gravity Waves in a Special Setting*†

NAI-SHER YEH‡

Department of Mathematics, Fu-Jen Catholic University, Xinchuang District, New Taipei City 24205, Taiwan, R. O. C.

Abstract

The paper aims to prove interchangeability between specific differential operators and improper integrals, which is a fundamental fact constituting solvability of forced capillary-gravity waves problem outside a cylindrical wavemaker of infinite depth under Hocking' s edge condition.

*2010 Mathematics Subject Classi.cation: 76B45, 76D45.
† Key words and phrases: capillary-gravity waves, cylindrical wavemaker, Hocking's edge condition.
‡ mailto: 038300@mail.fju.edu.tw

The Architecture and System maintenance For the Network College of Online Tutoring

Chih-Tien Yang[1], Hong-Yen Lin[2]

[1] *Information Technology Center,*
[2] *Department of Computer Science & Information Engineering,*
Fu Jen Catholic University

Abstract

The education for low develop area always being highly emphasized in civilized society, but the problems of long distance, poor traffic capability and low human resource for faculty always follow the consequence of implement. In this article, we will propose architecture to build a "Network College" which makes the Interaction between District counseling centers and schools can run like the college and divisions in real university. And this system has teaching logging system for teachers to record their systemized tutoring activities to their students in any place, any times, also their teaching materials and process will be recorded. It also will have sub system for Academic affairs, General affairs, Student affairs which can track the learning result of students. This "Network College" should have a highly evaluated and powerful network learning server system which can supply stable network classes for teachers and students to have simultaneously online tutoring. Through the implementation of projects prove that this structure allows teachers and students in every corner of the Internet, through the systematic managed "Network Classroom", can have a systematic teaching process, and establish a large number of records of learning model. What we emphasized here is not only to provide a platform for many online learning discussions, it should offer an environment which run like real college.

Key words: Network college, Online Tutoring, network classroom

6. 林思宇 (2012)。蔣偉寧：數位學習是未來趨勢。取自 http://tw.news.yahoo.com/%E8%94%A3%E5%81%89%E5%AF%A7-%E6%95%B8%E4%BD%8D%E5%AD%B8%E7%BF%92%E6%98%AF%E6%9C%AA%E4%BE%86%E8%B6%A8%E5%8B%A2-112936712.html 。
7. 林宏彥與楊志田 (2012)。網路應用在偏鄉教育 - 遠距課輔無遠弗屆 - 以數位學伴線上課業輔導服務計畫為例。輔仁學誌。第 45 期。第 30-31 頁。
8. 施富川 (2010)。施富川的 e-Learning 布拉格。取自 http://fcshih.blogspot.com/。
9. 馬雨沛 (2009a)。教育差距大 貧富差距就大，Yahoo 奇摩新聞領袖專訪 2009.07– 李家同
10. 馬雨沛 (2009b)。從小就不該讓孩子的功課太差，Yahoo 奇摩新聞領袖專訪 2009.07–李家同
11. 教育部 (2005)。偏鄉數位關懷推動計畫簡介。取自 http://itaiwan.moe.gov.tw/Plan01.aspx。
12. 教育部 (2006)。數位學伴線上課業輔導服務計畫。取自 http://www.dsg.fju.edu.tw。
13. 教育部 (2007)。國民電腦網。取自 https://icare.moe.gov.tw/index.aspx。
14. 教育部 (2010a)。遠距電腦教室建置注意事項。取自 http://www.dsg.fju.edu.tw/dsg/file/l6_4.pdf。
15 教育部 (2010b)。錄影檔案管理、使用辦法。取自 http://www.dsg.fju.edu.tw/dsg/file/l3_7.doc。
16. 教育部 (2011)。網路課輔連線問題處理流程圖。取自 http://www.dsg.fju.edu.tw/dsg/file/l5_2.pdf。
17. 教育部 (2012a)。網路測試檔操作說明。取自 http://www.dsg.fju.edu.tw/dsg/file/l5_3.pdf。
18. 教育部 (2012b)。系統平台故障排除暨提報流程。取自 http://www.dsg.fju.edu.tw/dsg/file/l5_1.doc。
19. 博幼社會福利基金會 (2009)。董事長李家同的遠景目標，取自 http://www.boyo.org.tw/about/about01.htm
20. 楊志田 (2009)。距離不是問題 – 偏鄉中小學網路遠距課業輔導服務 - 以輔仁大學資訊中心教學組的執行經驗探討為例。TANet 2009 台灣網際網路研討會論文集。第 G114-G119 頁。
21. 楊志田、楊嗣婷與林宏彥 (2012)。遠距課輔之系統維運 - 以數位學伴線上課業輔導服務計畫為例。第十六屆全球華人計算機教育應用大會 (GCCCE 2012) 工作坊。
22. 趙涵捷 (2009)。談偏鄉中小學網路課業輔導計畫之緣起與發展。教育部 97-98 偏鄉中小學網路課業輔導服務計畫各分區輔導中心暨夥伴大學團隊九十七學年度第一學期擴大工作會議手冊。第 5 頁。
23. 蔣偉寧 (2012)。教育施政理念與政策。第 136 頁。取自 http://www.edu.tw/pages/list.aspx?Node=392&Type=1&Index=1&WID=6635a4e8-f0de-4957-aa3e-c3b15c6e6ead。
24. 劉佩修 (2009)。孤島校長與他的 26 個孩子。商業週刊第 1110 期，第 84-85 頁。

Recevied Oct 30, 2013
Revised Mar 27, 2014
Accepted Mar 27, 2014

卷可以設計得更細緻，藉以分析探討問題的釐清與資訊的管理。

網路與視訊電腦設備，絕對是網路視訊的基礎。如何提升各校網路的穩定與安全，甚至在有效管控的頻寬政策下，使得有限的網路資源得以發揮最大價值。以及如何管理大量的電腦設備，使能夠穩定正常的運作，這些都是非常重要的。因此建議各參與的學校單位應該要有專業的資訊管理人員投入，而非只是一般老師身兼管理資訊的工作，否則系統維運單位在無法及時處理各單位問題的情況之下，所有的運作都變成虛有，這是非常可惜的。至於各校是否皆有編列此專業人員，建議由教育部規劃督導，列為重要工作。

樂於公益的企業很多，建議教育部應可整合計畫單位的需求以及企業支援的訊息，甚至主動扮演接軌的推手，或是將這些訊息透明於公開平台上，讓各方資源都能歸屬到與實際需求面，造福更多的陪伴學習，孕育培植未來希望的種子。

伍、誌謝

本論文承蒙教育部「數位學伴線上課業輔導服務計畫」的補助，謹致最誠摯的謝意。並向所有參與此計畫的大小朋友們，與輔仁大學呂慈涵老師率領的「輔大偏鄉教育關懷團隊」全心全力投入，致上最高敬意。大家的愛心關懷與努力是人生教育課程中最好的教材，也是激發系統維運更進步的主要動力。

參考文獻

1. 太御科技 (2010)。JoinNet 跟 Co-Life 有何差異。取自 http://blog.joinnet.tw/index.php?op=ViewArticle&articleId=618&blogId=1。
2. 行政院研考會 (2012)。數位機會。取自 http://www.rdec.gov.tw/ct.asp?xItem=4024330&CtNode=12059&mp=100。
3. 行政院經濟建設委員會 (2002)。挑戰 2008：國家發展重點計畫 (2002-2007）。取自 http://www.cepd.gov.tw/m1.aspx?sNo=0001539&ex=3。
4. 呂燕智 (2009)。培養學習熱忱愈早愈好。商業週刊第 1109 期，第 82-84 頁
5. 周原 (2011)。五年視訊陪伴 - 輔大學生帶弱勢兒變狀元。天下雜誌第 473 期， 第 170-171 頁。

生的交流、又一次的陪伴學習，以及認真檢討的過程，內容不限課業，還包含生活與做人處事的道理。在 101-1 學期，全區於 101.09 ～ 102.01，受輔導的學童數有 1,005 位，參與的課輔老師有 1,471 位，所累積的課輔日誌數量為 21,748 篇，上課時數共有 58,339 小時，上傳檔案教材共有 25,728 個。這相當於在這段期間內，至少有 21,748 次的大小學伴透過網路在空中接軌上課，也代表著這麼多次的陪伴學習。這些課輔日誌資料庫將可做為日後檢討追蹤學童學習過程的參考，而這些教材則可作為後輩教學的參考工具。

肆、結論與建議

經營 1,005 位中小學童的線上課輔，結合五個區域輔導中心學校、27 所大學、84 所中小學 /DOC，就架構而言，「區輔導中心 / 中小學」有如「學院 / 學系」，而這樣的學院架構與規模經過計畫的執行，成功順利的完成 21,748 次的陪伴輔導學習，加上問卷結果反應良好，證明了本文提出的網路學院系統維運機制可長期運作成功。這當中包含了幾個要件：有效能的軟體 (教務、學務、總務系統，以及網路課輔平台系統)、不須高規格的硬體 (系統主機、網路課輔平台主機)、經驗累積的維運技術 (包含系統維運單位管控整體課輔平台系統，也包含各學校電腦教室的現場管理單位)、一群服務付出的團隊 (即使軟硬體到位，終究需要人的推動)。

「網路學院」應用在偏鄉教育的模式，已經不是口號而已，而是可以遍地開花的機制，在這機制下，1. 除了小學生可以受到輔助教育與陪伴學習之外，2. 在過程中，可以訓練大學生如何學習「關愛」，並將所學回饋在教育上；3. 對於協助參與的學校，也可以盡一份學校責任，提供師資參與培訓，以及所需硬體設備環境，4. 當中所需要的不足支援，可以尋求企業協助，與企業結合。所以最後不是只有單贏、雙贏，而是多贏，這對整個國家是正面的發展。

經過多年執行遠距網路線上課輔之系統維運經驗，所提機制確實可行，只是每項機制之後仍需要人的執行，而且是一整個團隊許多人的努力才行，否則銜接交付會有空窗，絕對無法順利完成所有需求。雖然不能保證這裡所提的機制是完美的，但是應該可以做為各方參考，共同繼續研發未來更好的機制，甚至推及國際之陪伴學習。希望教育部可以早日將此模式納入大學教育之服務學習系統，建立一套完整的大、中、小學之間的輔助學習架構。

沒有一套工具是完整無缺的，教學課輔平台也是如此，端視我們的需求，並且利用其相關功能研發所需要的程式；計畫推行也必須要多方檢討，期末問

序號	主機編號	網路教室編號	發生時間	斷線對象	斷線原因	網路位置
1	201.1	chinshan01	17:47:20	學生斷線	recv return fails	163.20.33.231
2	201.1	chinshan01	17:52:44	學生斷線	timeout	163.20.33.231
3	201.1	chinshan01	17:56:54	學生斷線	recv return fails	163.20.33.231
4	201.1	chinshan01	19:15:01	學生斷線	timeout	163.20.33.234
5	201.1	chinshan03	17:32:43	老師斷線	too slow	120.125.63.136
6	201.1	chinshan04	19:09:04	老師斷線	recv return fails	120.125.63.136
7	201.1	chinshan06	19:13:30	學生斷線	recv return fails	163.20.33.210
8	201.1	chinshan10	19:16:16	學生斷線	timeout	163.20.33.237
9	201.1	chinshan14	19:32:05	老師斷線	recv return fails	120.125.63.136
10	201.1	chinshan18	18:20:07	老師斷線	recv return fails	120.125.63.136
11	201.1	chinshan19	18:18:06	學生斷線	recv return fails	163.20.242.252
12	201.1	chinshan21	17:45:01	老師斷線	too slow	120.125.63.136
13	201.1	engjianshan03	17:46:52	老師斷線	timeout	140.126.29.12
14	201.1	engjianshan06	17:50:22	老師斷線	recv return fails	140.126.29.12
15	201.1	engjianshan16	17:32:16	老師斷線	too slow	140.126.29.12
16	201.1	engjianshan16	17:39:55	老師斷線	too slow	140.126.29.12
17	201.1	engjianshan19	18:12:33	老師斷線	recv return fails	140.126.29.12
18	201.1	engjianshan19	19:40:36	學生斷線	recv return fails	163.20.242.104
19	201.1	jieshou05	20:01:48	學生斷線	recv return fails	163.30.111.222
20	201.1	jieshou10	19:43:56	學生斷線	timeout	163.30.111.222

表 3 網路教室斷線情況之分散個案分析

主機編號	網路教室編號	發生時間	斷線對象	主機編號	網路教室編號	發生時間	斷線對象
201.2	nemar01	18:42:57	學生斷線	201.2	nemar03	20:21:08	學生斷線
201.2	nemar01	18:53:29	學生斷線	201.2	nemar03	20:21:14	學生斷線
201.2	nemar01	18:54:53	學生斷線	201.2	nemar03	20:29:06	學生斷線
201.2	nemar01	18:56:17	學生斷線	201.2	nemar03	20:36:33	學生斷線
201.2	nemar01	20:21:56	學生斷線	201.2	nemar04	18:42:31	學生斷線
201.2	nemar01	20:29:13	學生斷線	201.2	nemar04	19:44:41	學生斷線
201.2	nemar01	20:37:01	學生斷線	201.2	nemar04	19:47:34	學生斷線
201.2	nemar02	18:40:56	學生斷線	201.2	nemar04	20:20:46	學生斷線
201.2	nemar02	18:53:45	學生斷線	201.2	nemar04	20:37:22	學生斷線
201.2	nemar02	19:27:43	學生斷線	201.2	nemar04	20:43:55	學生斷線
201.2	nemar02	19:47:54	學生斷線	201.2	nemar04	20:46:02	學生斷線
201.2	nemar02	20:22:13	學生斷線	201.2	nemar05	18:53:35	學生斷線
201.2	nemar02	20:29:12	學生斷線	201.2	nemar05	18:54:53	學生斷線
201.2	nemar03	18:42:00	學生斷線	201.2	nemar05	18:56:09	學生斷線
201.2	nemar03	18:42:15	學生斷線	201.2	nemar05	19:26:46	學生斷線
201.2	nemar03	18:53:30	學生斷線	201.2	nemar05	19:30:01	學生斷線
201.2	nemar03	18:55:48	學生斷線	201.2	nemar05	19:30:24	學生斷線
201.2	nemar03	19:26:58	學生斷線	201.2	nemar05	19:47:25	學生斷線
201.2	nemar03	19:43:16	學生斷線	201.2	nemar05	20:21:28	學生斷線
201.2	nemar03	19:47:43	學生斷線	201.2	nemar05	20:55:50	學生斷線

表 4 網路教室斷線情況之群聚現象個案分析

這些分散或是群聚全面斷線的線索可作為後續其他觀察的依據：其中分散式的，表示問題應屬於該電腦教室內部問題，可能是各自電腦發生問題，或是電腦教室的上層網路設備有問題，可以請現場教室管理者做即時檢測確認，甚至這些紀錄可以統計針對發生率高的對象予以更換或重整。如果網路教室斷線是全面性的，則問題可能是該電腦教室的對外網路斷訊，也可能是網路課輔平台主機系統出問題，這時候可盡速聯繫系統維運單位確認；系統維運單位可以很快的交叉比對即知是否主機問題（因為同時在主機上運作連線的還有其他學校，所以可以簡單確認是否為主機全面性的問題），這些紀錄可以統計那些學校對外網路斷訊的次數，或是系統主機服務中斷的情況。

四、陪伴學習數據分析

課輔日誌是除了教學錄影檔案之外，最重要的教與學記錄系統（楊志田、楊嗣婷與林宏彥，2012)[21]。每一篇的課輔日誌，是課輔老師在上完課之後才能填寫的日誌紀錄，每一篇的日誌內容有如前面的文中圖 4 所示，包括：課輔老師端的教學目標、教學進度、教學流程、教學方法、是否準時教課、備課情況、教學檢討、使用教材，以及學童端的是否準時、互動情況、是否專心聽講、學習效果、情緒狀況、吸收狀況等等。並且會由專門輔導老師回復每一篇課輔日誌，以給予指導、安慰、鼓勵。所以每一篇課輔日誌代表的是一對師

雖然鮮少，但是也被列入斷線紀錄當中。3. 基本上，該教學平台系統自動設計針對一分鐘之內的斷線會再行自動回復連線，所以可藉此觀察斷線少於一分鐘的情況 (比例)，這也就是表 2 中的自動回復連線次數與比例。4. 針對較大斷線次數的，可以再觀察表 3、表 4，是否有某學校群聚斷線現象，還是分散的個案，以作為之後處理問題的重要方向。

表 2 網路教室斷線與自動回復連線數據分析

日期	開教室數 (M)	斷線次數 (N)	自動回復連線次數 (K)	自動回復連線比例 (K/N)	平均每一教室當天斷線次數 (N/M)
3	46	8	1	13%	0.17
4	211	91	24	26%	0.43
5	30	12	2	17%	0.40
6	155	40	5	13%	0.26
10	49	69	14	20%	1.41
11	207	62	13	21%	0.30
12	46	13	1	8%	0.28
13	187	132	59	45%	0.71
17	45	19	2	11%	0.42
18	216	74	16	22%	0.34
19	52	9	0	0%	0.17
20	178	64	6	9%	0.36
24	56	15	2	13%	0.27
25	118	31	4	13%	0.26
26	59	50	28	56%	0.85
27	203	252	154	61%	1.24
平均	116.13	58.81	20.69	21.75%	0.49

在表 3 當中，只是節錄斷線記錄當中的一部分，用以介紹觀察方式。可以發現，從序號 1 ～ 12，教室名稱開頭都一樣是「chinshar」，表示是同一個學校，而後面的不同號碼則表示不同教室，但是號碼沒有連續，屬於分散情況，可以看出該校的斷線情況應屬與個案。同樣的，序號 13 ～ 19、19~20 也分別表示其他兩個學校，也都屬於分散的個案情況。在表 4 中，則可看出教室名稱都一樣，且編號是全面連續性，判定當時該校的斷線應該是全面性的。

路課輔平台，在幾年前計畫初始時後也確實沒有這樣效能，應付不到同時 120 人，後經改良才將使用需求降低，甚至使用一般電腦規格就足以應付 400 人同時線上輔導與錄影過程。

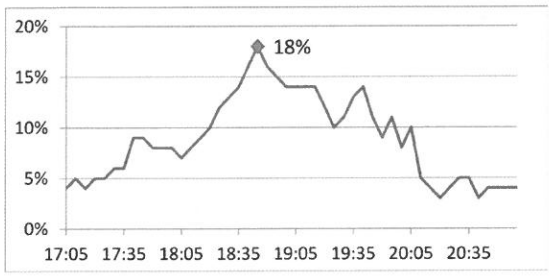

圖 23 課輔平台之 CPU 使用率

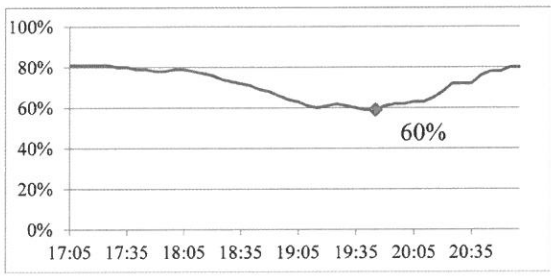

圖 24 課輔平台之記憶體使用剩餘率

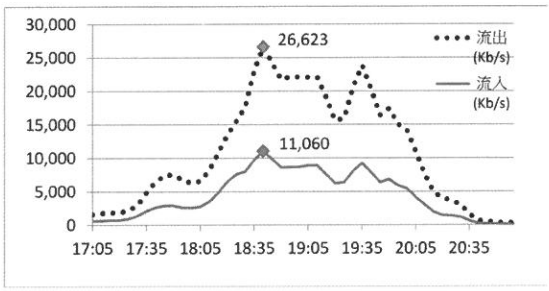

圖 25 課輔平台之網路流量

三、網路教室斷線數據分析

以下表 2 是透過所開發的程式彙整在 2012.12. 某一平台主機的每日斷線情況，其中已經先刪除了沒有紀錄的部分。該表當中有每天的開課教室數量、連線中斷次數、中斷之後有自動回復連線的次數、斷線後有自動回復連線的比例，以及平均每一個網路教室當天中斷連線的次數。

在最後一列，計算出各項的平均值，其中平均每天的斷線總次數為 58.81 次，每間教室的當天斷線次數平均則為 0.49 次，而自動回復連線比例平均為 21.75%。這裡要特別說明一些情況：1. 斷線時間如果不長，使用端是不一定有感覺的，所以不能只靠使用者感覺來計算次數，本系統是利用程式來偵測數據。2. 斷線也可能包含是被老師端踢出教室 (老師端強迫關教室)，這種情況

圖 21 是針對小學伴做的問卷，觀察對於學習成效與學習態度。圖 22 表示全區小學師長對於上課使用的電腦教室與網路環境、教學平台的滿意度結果。發現不滿意 + 非常不滿意的比例都明顯很低，普遍都是滿意以上的情況。

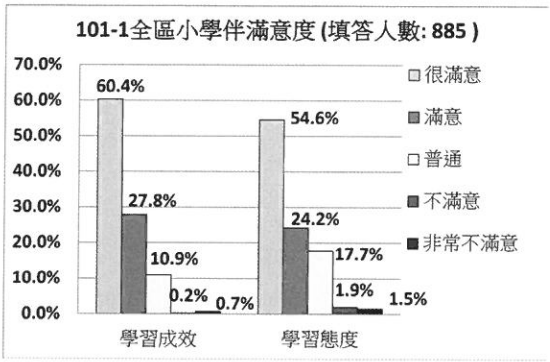

圖 21 全區小學伴滿意度調查

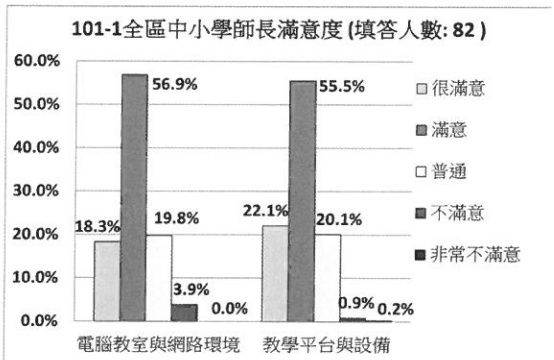

圖 22 全區小學師長滿意度調查

二、主機效能與流量分析

以下是某一課輔平台主機 (規格：Intel 雙核心處理器，時脈頻率 2.4GHz。2G*2 DDR Ⅱ 800MHz 記憶體。這算是普通規格，並非高檔的設備)，針對近 200 對線上課輔時候的 CPU、記憶體、網路流量使用情況。圖 23 顯示，CPU 的最高使用率約為 18%，表示 CPU 資源非常寬鬆。圖 24 顯示，記憶體剩餘情況幾乎都在 60% 以上，所剩資源充分。這兩部份表示主機所需要的資源很低，用一般規格的電腦即可使用本套網路課輔系統應付大量線上課輔需求。

圖 25 則是該平台使用的網路流量情況，發現 200 對 (400 人) 的線上課輔時候，所需的網路頻寬資源，佔用流量最大只有 26,623(Kb/s)，對於本校網路 1G 的頻寬環境來說，算是非常輕微的 (約只佔了本校對外頻寬的 2.66%，若換算為 1000 對，等於 2000 人的線上課輔，所佔用本校對外頻寬則約為 13.3%)。

這些不佔大資源的需求，對於計畫未來可能同時面臨成千上萬人的線上課輔情況而言，是個重要的基礎。因為要應付同時數百上千人的線上課輔，並提供白板書寫、視訊、共同瀏覽網頁等功能，尤其是同時保留所有過程的錄影檔案在主機上面，並非容易的事，對於主機與網路頻寬的要求非常重要 (一般在網路上的視訊工具，是沒有儲存錄影檔案在主機上面的)。而本計畫使用的網

參、數據分析

系統維運最主要的角色在於建立與維繫基礎環境，使整體網路學院的課程得以透過完善規畫管理的網路教室環境進行陪伴學習。以下提列系統維運比較重要的數據分析：101-1 期末滿意度問卷分析、主機效能與流量分析、網路教室斷線數據分析、陪伴學習數據分析。

一、 期末滿意度問卷分析

以下各圖來自於 101-1 學期 (102 年 1 月)，針對參與計畫者所做的問卷調查結果 (題目是教育部之總計畫團隊所擬)。圖 19 表示全區大學伴對於上課使用的電腦教室與網路環境、教學課輔平台的滿意度結果，其中在電腦教室與網路的部分，不滿意 + 非常不滿意的有 18.8%，顯示存在著努力改善的空間，必須和所有參與的大學檢視確認維護的情況，作為下一期開課之前的檢查要項。而對於教學平台的不滿意 + 非常不滿意情況則是較小的 6.8%。圖 20，表示全區大學師長對於上課使用的電腦教室與網路環境、教學平台的滿意度結果，其中在電腦教室與網路的部分，不滿意 + 非常不滿意的有 16.5%，仍然顯示存在著努力改善的空間。而對於教學平台的不滿意 + 非常不滿意情況則是較小的 4.7%。由此二圖，可以發現各區參與的大學，普遍需要再加強所屬電腦教室與網路方面的管理。

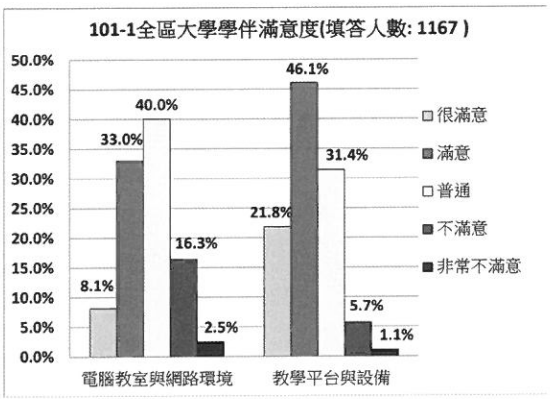

圖 19 全區大學伴滿意度調查

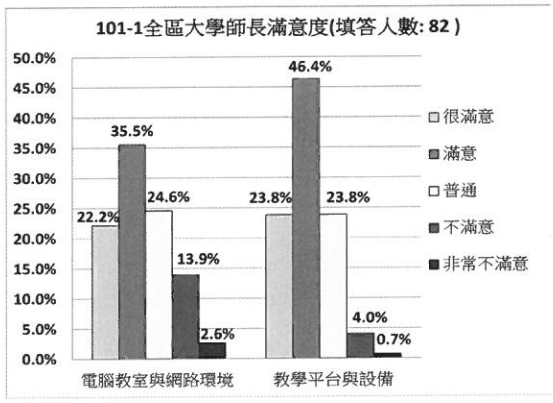

圖 20 全區大學師長滿意度調查

（二）維護網路課輔平台與效能監控

課輔平台是網路學院各教室能執行線上課輔最重要的工具與環境，必須要時時監控以了解系統資源情況與所在網路流量的多寡，並能在所設定的觀測指標到位時候，自動發出警報訊息通知做及時的處理，同時保留監控的紀錄作為之後研究之用。本案我們用 PRTG 軟體設定收集這些需求，可以精確偵測到當時各項硬體情況、服務程式狀態，當設定所發生的情況出現時，由系統自動發警給業務同仁，並能在事後調閱紀錄彙算。在下一單元會說明主機平台的 CPU、記憶體，以及網路流量使用情況。

（三）管理端執行網路連線偵測系統

對於各網路教室的使用情況，建立隨時收集調閱紀錄的機制，以了解在期間內是否有發生網路瞬斷情況以至於在連線上有所延遲甚至停擺現象，收集的數據也可做為日後問題分析之用。目前已經研發程式可以用來收集觀察各網路教室連線的斷線彙整紀錄，可用來判斷問題發生的群聚現象或是單一個案以及發生問題的頻率，做為解決問題的重要依據。在下一部分會說明這些判斷過程。

（四）使用者端執行網路連線檢測系統

當網路視訊發生斷線之時候，需有機制可以盡快確認原因與通報流程，判斷是否為個別機器情況，或是整間教室、學校網路、對外網際網路，甚或是課輔平台的問題。除了從發生問題學校的外面環境做可能的檢測之外，最直接的就是從該學校自己內部做測試並收集直接的線索，這部分可參考系統平台故障排除暨提報流程（教育部，2012b)[18]、網路課輔連線問題處理流程圖（教育部，2011)[16]。如果無法立即解決，則需盡快收集訊息以作為之後判斷的依據，可利用網路測試工具來檢測分析（教育部，2012a)[17]。

（五）規劃各校電腦教室環境設備之開學前置作業

各參與的學校在開課之前，應針對使用的電腦教室環境設定與管理有所準備，以確保各使用環境在軟硬體設定與使用上功能正常，而且方便取用。此部分的機制可以參考「遠距電腦教室建置注意事項」（教育部，2010a)[14]。

（六）建置計畫網站

因為參與者眾，必須提供資料文件往來之平台，以及活動訊息園地，並將所有的管理功能皆放置於網站內：http://www.dsg.fju.edu.tw。

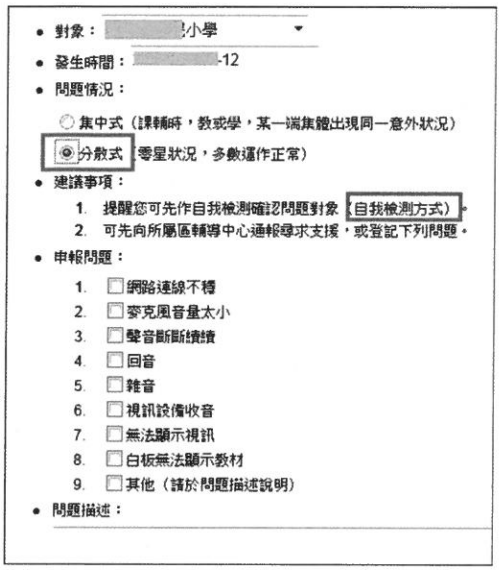

圖 16 障礙提報之分散式問題情況

	問題發生單位	發生時間	提報人	問題情況	問題內容
1.	北區．國立大學	2013-03-11 20:14	國立大學．田	分散式	其他（請於問題描述說明） 帶班老師日誌功能有問題 在寫入日誌時...
2.	北區．國立大學	2012-12-06 16:45	國立大學．楊	集中式	同一區其他學校 "有" 同樣情況 瞬間統一聽不到聲音及視訊停格。...

圖 17 障礙提報問題彙整之截取部分畫面

七、其他系統維運管理

為了維運整個平台運作資源的安全與效能監控，還必須搭配以下系統管理的功能機制。

（一）課輔錄影檔案管理

因為課輔學童非常多，所需要的網路教室也分別開設建立在不同平台主機，每台主機分別產生該主機下的教學錄影檔案。但是檔案太多，且容量需求大，所以不適合長期放置於平台主機內。圖 18 是錄影檔案的備份管理機制：1. 每晚課輔後，自動化流程將各平台主機當中尚未備份過的檔案先行備份到該本機中的暫存工作碟，2. 再將該暫存碟中的檔案備份到集中管理設備 (NAS)，3. 最後再將暫存碟中的檔案搬移至 FTP 主機，提供下載。下載使用必須遵照「教學錄影檔案管理、使用辦法」(教育部，2010b)[15]

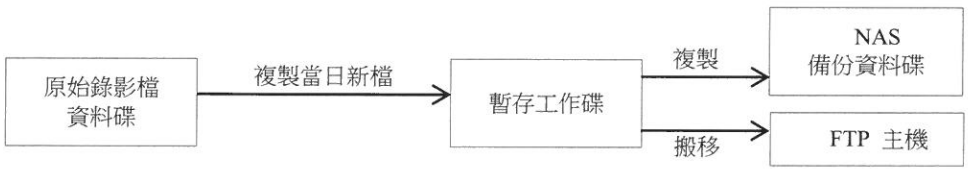

圖 18 錄影檔案自動備份機制

北一區 . 輔仁大學 +

單位	申請數	開設數	密碼	類型	開課日	備註	上課時段
[redacted]國小 -	15	16	[redacted]	一對一	2013-03-12	4/4 清明節 課輔至 6/6	二 1820~1950 四 1820~1950
[redacted]國中 -	18	19	[redacted]	一對多	2013-03-12	4/4 清明節 課輔至 6/6	二 1820~1950 四 1820~1950
[redacted]國中 -	20	21	[redacted]	一對一	2013-03-12	4/4 清明節 課輔至 6/6	二 1820~1950 四 1820~1950

送出　重新載入　區中心確認無誤

●同一單位之多筆申請，密碼也請設定相同，否則系統僅採用最後一組申請的密碼。
●系統維運請輸入開設數以完成核定步驟。

處理進度 ： 待開設
處理紀錄 ： 填寫 .
確認 . 2013-03-12 08:40 . 總計畫 . [redacted]
核定 . 2013-03-12 08:45 . 總計畫 .
開設 .

圖 13 網路教室帳號申請

（二）障礙提報

系統以互動方式引導申報者提供問題的分類，並依據分類主動提供問題研判方向供處理參考。問題的各方處理過程皆有記錄做為日後查詢。圖 14 是障礙提報畫面中針對「集中式」且「同一區有類似情況」下提供的情況分析，提報者可以參考是否所需。圖 15 是針對「集中式」且「同一區沒有類似情況」下提供的情況分析。圖 16 則是針對「分散式」情況所提供的情況分析以及線上自我檢測系統。以上如不能解決問題則填入問題描述當中。圖 17 是障礙問題回報的彙整，可方便事後追蹤問題的處理過程。

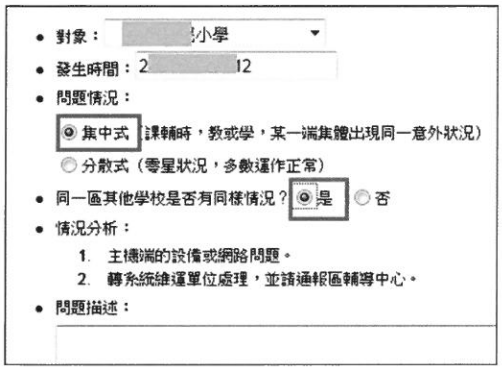

圖 14 障礙提報之集中式問題情況一

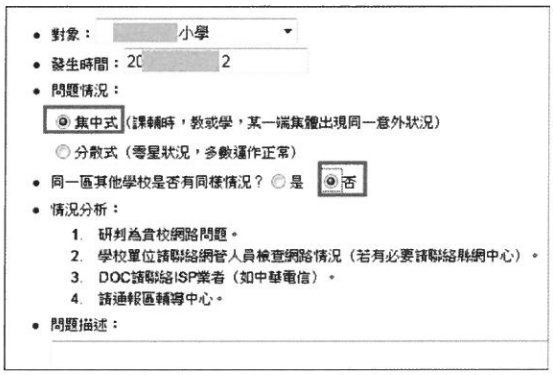

圖 15 障礙提報之集中式問題情況二

是線上問卷系統整理的部分資訊，包含各問卷的標題、開放時間、對象、填答數、執行單位以及報名網址（公布該網址，即可開放問卷）。

	標題	開放時間	類型	問卷網址	填答數	最後更新
3.	101-1 期末滿意度問卷-夥伴中小學師長(北一區)	2012-12-13 15:00 2012-12-29 00:00	計畫人員 限填一次．記名	http://www.dsg.fju.edu.tw/teach2/ques.php?id=NTg2	17	楊嗣婷 2012-12-12 14:24
4.	101-1 期末滿意度問卷-大學學伴(北一區)	2012-12-13 15:00 2012-12-29 00:00	計畫人員 限填一次．記名	http://www.dsg.fju.edu.tw/teach2/ques.php?id=NTg3	336	楊嗣婷 2012-12-12 14:27

圖 11 問卷系統整理資訊之截取部分畫面

（四）交流園地

為了收集參與課輔的所有成員之各方心得與經驗，需要開闢一系統進行關於輔導面、生活面、教學面等各方的感想、回饋與經驗交流。圖 12 紀錄學伴發表不同類別（溫馨小故事、抒發心情、互動故事）的相關分享。

	發表時間	類別	標題	作者	瀏覽	回覆	最後回覆時間
1.	2013-03-08 15:09 五	國語文	嗨!~~~~~~~~~~~~陳[redacted]	蕭[redacted] - 中小學學伴	16	1	2013-03-12 18:14 二
2.	2013-03-06 15:02 三	其他	哈囉!!	羅[redacted] - 中小學學伴	18	3	2013-03-08 15:05 五

圖 12 交流園地整理資訊之截取部分畫面

六、提供總務系統功能

總務系統除了提供薪資管理、設備管理功能之外，還提供關於資源申請、問題提報等系統功能。

（一）網路教室帳號申請與開設系統

因為課輔對象分布各校的數量眾多，必須提供帳號申請系統，並以自動化開設。圖 13 是提供給各區中心，針對所屬輔導學校申請所需教室帳號的畫面，當中包含項目有：使用學校名稱、申請數量、使用密碼、類型（一對一、一對多）、開課日期、上課時段。畫面中並顯示目前處理進度。

曆畫面，左邊的框框表示可依單位查詢，中間的框框表示可依內容類別查詢，右邊的框框則可輸入關鍵字查詢。

（二）活動報名

課輔老師的招募、研習、訓練應避免勞師動眾調查、收集統計資訊，而是需要有系統化的工具進行，圖 10 是報名系統整理的部分資訊，包含各活動名稱、日期、報名人數（包含報名清冊）、執行單位以及報名網址（公布後即可開放報名）。

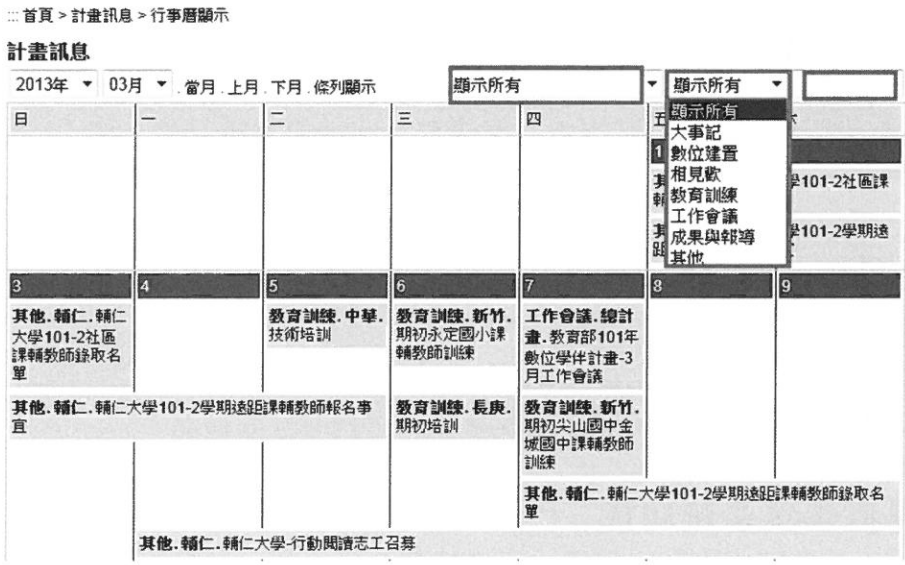

圖 9 對外開放的行事曆查詢

	活動日期+	活動名稱	報名日期	報名網址	報名人數	執行單位
8.	2013-02-26	輔仁大學 101-2 遠距課輔招募說明會報名處	2013-02-06 ~ 2013-02-25	http://www.dsg.fju.edu.tw/teach2/join.php?num=1360127703	117	北一區．輔仁大學
9.	2013-02-20	暨大 101-2 課輔教師招募《新進課輔教師報名處》	2013-01-14 ~ 2013-02-24	http://www.dsg.fju.edu.tw/teach2/join.php?num=1357544251	101	中區．國立暨南國際大學

圖 10 活動報名整理資訊之截取部分畫面

（三）線上問卷

每次舉行活動之前後，對於活動執行情況之意見收集或是課輔期間對於各種情況之調查，都需要有系統化的線上問卷系統才能方便進行與統計。圖 11

目的學習情況，最後給予整體評估，就像是一張學童的學期成績單。

（四）課輔教室目前使用狀況

帶班老師如何知道課輔老師已經上線、學童端是否已經連線上課，須有一系統畫面針對所屬學校呈現當時的上課情況，設計如圖 7，圖中的「學伴已上線」表示課輔老師已經開啟網路教室等待學童上課當中。此項功能也可作為判斷是否發生群體問題的參考之一。

（五）錄影檔案下載

如何完整記錄教學過程，並可作為事後檢討改進用，最直接的想法就是將視訊過程完整錄影下來（這也是平台所需具備的功能）。但是，錄影檔案何其的多，如果每小時產生一堂課的錄影檔，那麼 1,000 位學童在每周會產出 4,000 個錄影檔案。這部分必須在帳號開設時候就要群組規劃，搭配系統自動化的依不同群組儲存備分，之後才可系統化的依所屬學校提供所需時段的錄影檔案。目前提供下載的機制主要有兩種：1.FTP 下載（系統維運開設給各輔導中心下載帳號）、2. 透過瀏覽器由計畫網站透過授權帳號下載，如圖 8。當中左邊的框框，表示「教室名稱 - 年 - 月 - 日 - 幾點 - 幾分」，右邊的框框則表示該次錄影檔案的檔案大小，經由點選左邊項目就可進行下載。

圖 7 課輔教室使用狀況觀察圖

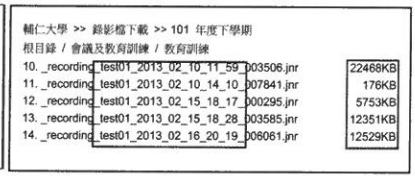

圖 8 錄影檔案下載之截取部分畫面

五、提供學務系統功能

這部分主要提供區輔導中心針對大學伴參加研習、活動等相關功能，例如：學伴通訊錄、研習紀錄彙整統計、配對名單匯出、活動簽到單、保險清單、統一發送給學伴信件、行事曆、線上問卷、交流園地等等。針對部分功能說明如下：

（一）行事曆

提供各課輔單位發布各類訊息於行事曆上，並方便可依單位 / 類別 / 標題關鍵字作線上查詢，確認各單位的活動安排情況。圖 9 為對外開放查詢的行事

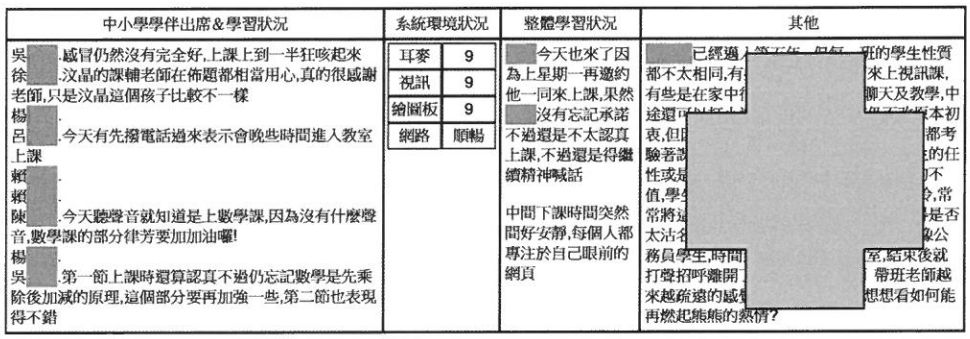

中小學學伴出席&學習狀況	系統環境狀況		整體學習狀況	其他
吳[redacted].感冒仍然沒有完全好,上課上到一半狂咳起來 徐[redacted].汶晶的課輔老師在佈題都相當用心,真的很感謝老師,只是汶晶這個孩子比較不一樣 楊[redacted]. 呂[redacted].今天有先撥電話過來表示會晚些時間進入教室上課 賴[redacted]. 賴[redacted]. 陳[redacted].今天聽聲音就知道是上數學課,因為沒有什麼聲音,數學課的部分律芳要加加油囉! 楊[redacted]. 吳[redacted].第一節上課時還算認真不過仍忘記數學是先乘除後加減的原理,這個部分要再加強一些,第二節也表現得不錯	耳麥	9	[redacted]今天也來了因為上星期一再邀約他一同來上課,果然[redacted]沒有忘記承諾不過還是不太認真上課,不過還是得繼續精神喊話 中間下課時間突然間好安靜,每個人都專注於自己眼前的網頁	[redacted]已經過[redacted]班的學生性質都不太相同,有[redacted]來上視訊課,有些是在家中[redacted]聊天及教學,中途還[redacted]本初衷,但[redacted]都考驗著[redacted]的任性或是[redacted]不值,學[redacted]令,常常將[redacted]是否太沾[redacted]染公務員學生,時間[redacted]室,結束後就打聲招呼離開[redacted]帶班老師越來越疏遠的感[redacted]想想看如何能再燃起熊熊的熱情?
	視訊	9		
	繪圖板	9		
	網路	順暢		

圖 5 帶班老師日誌之截取部分畫面

3. 中小學伴上課記錄

除了課輔老師與帶班老師各司其職記錄上課情況之外，中小學伴也要有所反思回饋，記錄自己上課的情況如圖 6：是否專心聽講、準時、用心回答問題，系統同時會記錄該學童上下課之簽到退時間。

日期	單位	中小學學伴	課程名稱	簽到退	給老師的話（優 5 4 3 2 1 劣）
2012-10-[redacted]-	[redacted]國中	劉[redacted]	週二教室 16．[redacted]英文 徐[redacted]．一對一	18:31 ~ 20:22	準時上課 3　專心聽課 3　用心回答 3　標記 謝謝大姊姊細心的教導，讓我更快的理解英文
2012-10-[redacted]-	[redacted]國中	林[redacted]	週二教室 15．[redacted]數學 莊[redacted]．一對一	18:32 ~ 20:13	準時上課 5　專心聽課 5　用心回答 4　標記 謝謝你 我上課很認真的聽 所以希望我會進步 謝謝你們~~
2012-10-[redacted]-	[redacted]國中	張[redacted]	週二教室 12．[redacted]國文 陳[redacted]．一對一	18:33 ~ 20:12	準時上課 4　專心聽課 5　用心回答 5　標記 哈哈 XD 好久沒一起上課了!!今天看到你很開心唷唷唷:)) 期待下一次的上課:)) Thank you :P

圖 6 中小學伴上課記錄之截取部分畫面

（三）中小學伴學習成效

此部分是以學童為主體，用以觀察該學童該學期以來在各方面的情況。系統整理各位學童的個人資料以及課輔老師對此學童的課輔日誌紀錄、教學目標、程度評估等。其中的程度評估，紀錄該學童的各方面學習態度以及上課科

1. 大學伴課輔日誌

大學伴日誌提供每位課輔老師對其輔導的學童記錄每次上課的情況。例如圖 4 當中包括：課輔老師端的教學目標、教學進度、教學流程、教學方法、是否準時教課、備課情況、教學檢討、使用教材，以及學童端的是否準時、互動情況、是否專心聽講、學習效果、情緒狀況、吸收狀況等等。另外會由專門的輔導老師來回復每一篇日誌，以給予指導、安慰、鼓勵，作為課輔老師檢討的參考，以及日後追蹤觀察學童情況的重要線索。

課程	教學單元進度與教學目標	教學流程及教法（優 5 4 3 2 1 劣）	中小學學伴吸收狀況與教學檢討	教材	老師回覆
[redacted]． **2013-01-[redacted] 二** - 林[redacted]．女 週二教室 11． [redacted]英文 一對一．1.5h． [redacted]3 [redacted]中學 吳[redacted]．男 18:21 ~ 20:10	1.與運動相關的英文 2.與交通工具有關的英文 3.彈奏樂器的英文 4.小王子的文章(簡單板) 5.生活對話練習 6.LOGO 猜謎	1.以圖片介紹 play 運動的用法 2.以圖片介紹 take a 交通工具的用法 3.以圖片介紹 play the 樂器的用法 4.以文章介紹重要且簡單的單字或片語 5.對話:和我一起念一遍 6.由圖案猜 LOGO 的英文 準時 4，互動 4，專心度 3，學習效果 3，心情狀態 4， 準時上課 5，充分備課 4，教學互動 3，師生互動 3，	其實準備很多，想說應該不會上完，但結果上很快，因為問他有沒有哪裡不懂都說沒有，不太會問我問題，我教田徑時，他會說一些田徑的事情，但教田徑的英文他好像就興趣缺缺了，休息回來後感覺變得有點不專心，之前對話都願意和我一起唸這次又不願意了~但至少已經不會有第一二次上課那種完全不想理我的情況了~		[redacted]： 最後一堂課雖然還是不盡完美，但如你所說已有進步，這也是一點小收穫吧！ 寒假到了，好好放鬆一下，把自己充飽電，我們下學期見囉！ 任芝 --- 吳[redacted]老師．帶班日誌內容 吳[redacted]：到課．看過[redacted]的課程我覺得很難,問過[redacted]會嗎? [redacted]說課輔老師會解釋給他聽,還好

圖 4 大學伴課輔日誌之截取部分畫面

2. 帶班老師日誌

因為課輔老師只能透過視訊與所配對的學童一對一交談，所能掌握的也只有該學童的情況。而帶班老師是配置在每間電腦教室，可以整體的觀察電腦設備、網路情況，也可掌握現地的實際出席與學習情況、管理現場秩序，並作為教與學兩端的緊急溝通橋樑。在該次課程結束時將狀況記錄在日誌中，如圖 5 當中紀錄了每位學童的上課情況、設備情況、整體情況描述。

另外，建置「線上教育訓練系統平台」，此平台主要功能有 1. 讓各課輔單位預約網路教室，以進行同時的線上會議與訓練。2. 提供自學功能環境，讓各校皆能放置教材於此平台，學員可在指定的期限內，不受交通與時間的約束，隨時上此平台學習指定的課程。系統設計要求學員寫下心得感想之後才能正常登出系統，這些可作為線上自學記錄的依據。以下圖 3 為線上自學課程系統的登入之後的畫面，當中包含了課程名稱、適用對象、預估時間、課程大綱、完成人數、建立日期、發布單位。

	課程名稱 +	類型 / 建議對象 / 預估時間	狀態	課程大綱	完成	建立日期	最後修訂
3.	數位學伴-偏鄉地區學生的學習特質與困境	基礎課程 所有人員 93m	開放	議題：偏鄉地區學生的學習特質與困境 主講者：唐淑華老師	77	2012-11-01	總計畫 吳佩旻 2012-11-02 17:20 開始學習
4.	數位學伴線上課業輔導服務計畫精神與服務倫理	基礎課程 所有人員 50m	開放	1.了解本計畫之精神與核心概念 2.關於偏鄉的一些反思 3.大學伴的身分與角色	120	2012-10-31	總計畫 吳佩旻 2012-11-02 16:36 開始學習

圖 3 線上自學訓練系統的登入後之截取部分畫面

四、提供教務系統功能

大 / 小學伴在網路學院的角色，分別是課輔老師與學生，關係是藉由課程所串連。在與課程最直接的教務功能中，除了大 / 小學伴學籍資料與設定、大 / 小學伴請假、教材分享系統、線上試卷系統、出席率統計之外，其他說明如下：

（一）課程配對

在學籍資料設定之後，即要開始進行課程配對 (也就相當於是「排課」的工作)。首先設定課程類別，將該中小學所開設的課程名稱、鐘點時數、鐘點費設定於資料庫中，接著再將大 / 小學伴與課程名稱、網路教室編號 (教室編號範圍由系統維運單位事先依帳號申請所建置) 與上課時段進行配對。

（二）日誌系統

日誌對於網路課輔來說是個非常重要的寶典，因為這裡詳實記錄著每一對師生在每一次上課的情況，日誌主要分成：大學伴課輔日誌、帶班日誌、小學伴上課記錄。此處先分別說明日誌的規劃內容，後續再介紹日誌的分析統計數據。

表 1 視訊平台之關鍵差異比較

	J 系統(本案採用)	O 系統
電子白板	● 可接受手繪、文字輸入、文字與圖片剪貼、上傳圖片，與虛擬印表機方式輸入內容。 ● 文字輸入為文字方塊概念，可調整文字方塊大小並有自動換行功能。 ● 手繪線條、上傳文字或圖片均成為繪圖物件，可以選取方式清除特定物件。且清除時不會影響到背景圖片。 ● 透過虛擬印表機功能，各種格式之教材檔亦可選擇列印至 J 系統印表機即完成上傳。	● 可接受手繪、文字輸入、文字與圖片剪貼、上傳圖片等。 ● 文字輸入為文字方塊概念。 ● 手繪線條、上傳文字或圖片均成為繪圖物件，僅能以選取物件方式清除；若以拖曳方式選取物件，只要物件有部分在選取區內便被選取。 ● 物件有層次順序，且透明部分一樣會被選取，舉例寫 1 再畫○成為①，當使用者想點選 1，卻會先點到在其上方的○，除非先寫○再寫 1。
錄影	● 預設為自動啟動錄影功能。 ● 聲音、視訊、對話框、電子白板同時錄製。 ● 專屬錄影格式在播放時，仍可調整各框架大小，例如是否顯示視訊框、捲動電子白板內容或全螢幕播放。 ● 使用者可下載錄影檔，透過 J 系統程式即可播放。管理者亦可統一管理所有錄影檔，例如提供 FTP 下載。	● 使用者須手動啟動錄影功能。 ● 預設錄製格視為 Lync 格式，事實上是把視訊、PPT、電子白板等分別存為 wmv 影片格式或 xml 檔，儲存於使用者端電腦。
動態視訊頻寬	● 可預設控制頻寬需求在 48Kb/s。 ● 音訊使用 10 Kb/s。	● 約需 300Kb/s，畫質佳。 ● 視訊降到 40Kbps 時，嚴重停格，甚至畫面全黑 ● 音訊降至 20K 時，偶有斷音；音訊降至 10Kbps 時，已影響通訊品質。
管理者影響	● 由主機管理者統一開設教室與密碼，課輔老師與學生亦無須學習教室的開設功能。 ● 必要時可隨時調閱任一教室之錄影檔案，也可另行備份存查。	● 帳號必須人工一一建立，且教室代碼為亂數產生。這對管理單位是個嚴重負擔。 ● 必須手動啟動錄影，如此無法保證所有課輔老師都會記得啟動，這會影響錄影檔案的收集完整性。 ● 錄影檔在課輔老師端的電腦內，無法有效與正確的回收管理。

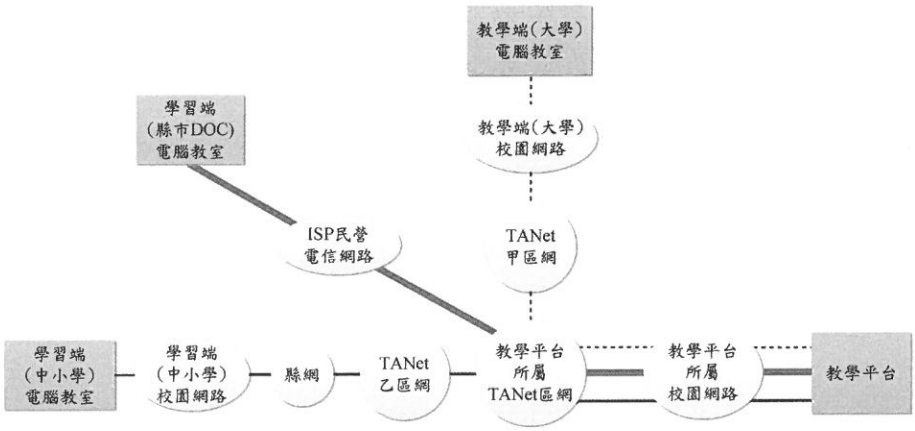

圖 2 視訊連線傳輸執行架構

二、評選網路課輔平台

網路課輔平台不是唯一，各家有其發展的訴求，所需評估的因素很多，本案所採用的是依據團隊過去執行的經驗所作的建議，並非表示此平台在各方面的表現皆是最好。所需的功能主要有：即時語音對傳、視訊影音對傳、共享電子白板、共享網頁、共享圖片、遠端操控、全程錄影、錄影檔案管理。多項功能在各家產品多有提供，表 1 整理 J 系統與 O 系統之間較具有代表性的差異。另外關於 J 系統與 C 系統之間的比較情況可另參考 (楊志田，2009)[20]、(太御科技，2010)[1]、(施富川，2010)[8]，而 J 系統與 A 系統之間的比較情況可參考 (林宏彥與楊志田，2012)[7]。

由表 1 的分析，只有 J 系統可完整達到幾項功能：1. 電子白板可以呈現書寫的筆順過程，而不是直接看到書寫完成的結果。2. 錄影檔案包含聲音、視訊、對話框、電子白板，管理者可以統一管理錄影檔案與正確的選取檔案播放 (因為檔案名稱可以直接識別對應是哪間學童何時上課)。3. 視訊頻寬可以使用最低需求，減少網路負荷。(雖然 O 系統畫面較佳，不過這必須有較佳的網路環境才可行。但是對於多數的偏鄉學校與數位機會中心，不見得有此環境)。4. 具有開設大量帳號的機制，可以應付每次開課需要開設至少 1,000 個網路課輔教室，而且是依照「學院 / 系所」的架構開設帳號。(在實際施行中，帳號是依照「各區輔導中心 / 所屬各中小學」架構開設)。

三、規劃與執行教育訓練機制

因為計畫內的人數眾多，訓練方式與教材部分，除了以文字文件與錄製教學檔案放置於計畫網站之外，若要在有限時間內針對所有各校參與者完成現場教學，需要培養種子教師，以分層負責訓練的方式進行。種子教師的訓練可集中現場進行 (通常搭配期初訓練一同進行)，或是直接透過視訊教學 (事先提供講義讓學員閱讀)，同時可將視訊訓練的過程錄影檔案作為之後複習的教材。必要的訓練課程有：網路課輔平台操作、常見障礙排除、各項系統功能操作。尤其重要的是要讓參與的各學校 / 單位了解整體的視訊連線傳輸執行架構與權責歸屬，以利問題發生時候可以有所邏輯的儘快聯繫分層負責單位解決問題。由圖 2 可以看出：當視訊過程發生問題時，不一定表示教學平台管理單位的網路有問題，且通常與學習端的電腦教室、或是所屬網路有關係，此時可以向所屬管轄單位確認，同時可利用所提供的網路測試工具來檢測分析 (教育部，2012a)[17]。

貳、架構網路學院運作環境之方法

如果只是一位大學生與一位小學生彼此相約以網路視訊進行課業輔導，這位大學生需要先準備幾件事情：先學會使用一套好用的視訊軟體與所需設備（可能需要付費購買），接著與學童預約時間並上線教學。乍看之下，好像沒甚麼問題，可是：如果上課時後發現某一方的電腦突然壞了，是否有備機可用？當時又要如何確認雙方的情況，以避免某一方掛在網路上面空等待？網路頻寬要各自解決付費申請、學童端是否有專心上課聽講，如何得知？初期必須親至學童端教導如何使用、大學生沒有討論交換心得對象、學童沒有共同學習的同學做為激勵…。如果將問題擴及為：一群大學生與一群小學生，雙方各在一電腦教室，各自成對進行網路課輔，則有些事情可以有所改變，例如：教育訓練不用全員各自前往，可以推派代表進行、可以互相分享心得、突然請假時候可以互相替補、設備有問題可以使用教室其他備用機器、學童端的教室如果有巡堂老師，可以督導現場學童是否專心進行。接著，再把範圍擴大為：好幾個學校的大學生，與好幾個學校的小學生，要在各自排好的時段進行配對課輔，那就更需要有所管理機制與整合資源提供，相關方法研究分類如下。

一、組織系統維運管理單位

依據營運需求，規劃營運組織的分工結構，如圖 1。圖中可看出維運管理的主要對象有三：教學平台、設備管理、計畫網站，但是需要行政服務與網路監控的輔助，最終達到能監測教學平台效能、管理教學錄影檔案、提供操作諮詢、維護網站資料、新增網站功能。

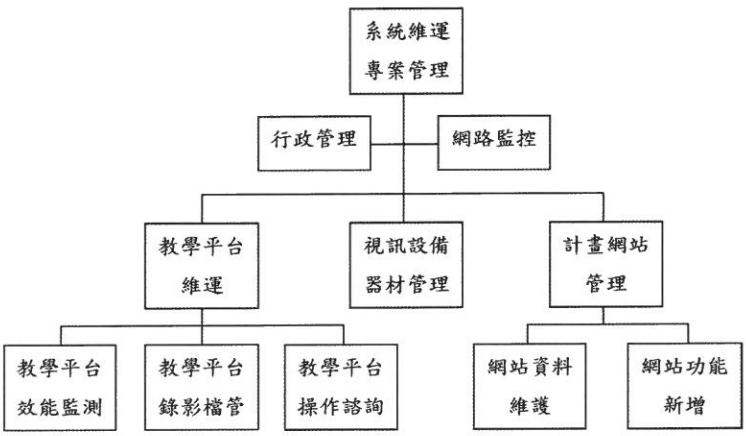

圖 1 系統維運營運機制

果大多數的小學和國中生都達到某一個水準的話，對國家是很重要的一件事情 (馬雨沛，2009a)[9]。因此，他又提到「從小就不該讓孩子的功課太差」(馬雨沛，2009b)[10]。馬祖東莒國小前校長王建華被問到：為什麼要讓孩子這麼忙，對他們這麼嚴格？他回答說：「因為他們真正在東莒的時間只有十二年。十三歲，全部都得離家，沒有人例外」(劉佩修，2009)[11]。並說十三歲離家前要培養的能力，包括「品格、生活自理、讀書的基本能力、耐挫力、勇於表達的能力」。

教育部對於偏鄉教育除了前述期間的建置與推廣，同時推動數位學伴線上課業輔導服務計畫 (教育部，2006)[12]。這計畫主要是從「偏鄉地區中小學網路課業輔導服務計畫」開始，運用網路教學方式，由大學生輔導偏遠地區國民中小學學生，提升偏遠地區學生學習成效，促成學習機會均等。95 年開始的實施範圍為中部偏遠區域，96 年擴展至北部及南部，97-98 年擴大結合東部，並加入國民電腦受贈戶學生及數位機會中心鄰近學生，藉以縮減城鄉學習差距，提升當地教育文化水準。為了擴大服務面向，教育部於 99 年調整計畫名稱為「數位學伴線上課業輔導服務計畫」。目前已進行到 101 年計畫，在 101-1 期參加的學校成員有：27 所大專院校、84 所中小學 /DOC、1,471 位課輔教師、1,005 位課輔學童。

誠如教育部前電算中心主任何榮桂說，「當硬體設備都到位，需要有系統的執行和長時間的關注」(周原，2011)[5]。要經營大規模的網路課輔，需要有具體的運作機制與負責的經營態度。在 (林宏彥與楊志田，2012)[7] 已提出了同時大量遠距課輔之機制，本文進而提出「網路學院」架構之建置研究，希望能完成一套輔助偏鄉遠距教學的網路學院管理系統。規劃將 1,005 位中小學童的線上課輔，結合五個區域輔導中心學校、27 所大學、84 所中小學 / DOC，將「全省各區輔導中心 / 中小學」的架構，建置如「學院 / 學系」的架構，並設計完整追蹤課輔紀錄的日誌系統，包含教務、學務、總務系統功能，以用來日後追蹤課輔的成效。同時評選符合線上課輔功能需求的網路課輔平台，而且需證明主機效能與網路的頻寬足以負荷。本文在第二部分提出架構網路學院運作環境之方法，第三部分提出數據分析，並在最後提出結論與建議。

壹、前言

「數位落差」，是指接近或使用數位產品 (如電腦或是網路) 的機會與能力上的差異。基於縮減數位落差，行政院於「挑戰 2008 國家發展重點計畫」(行政院經濟建設委員會，2002)[3] 研訂「偏遠地區政府服務普及計畫」，自 92 年至 96 年，於偏遠鄉鎮建置上網據點，辦理資訊課程訓練與推廣 (行政院研考會，2012)。並由教育部配合行政院分期執行「偏鄉數位關懷推動計畫」(教育部，2005)[11]：第一期 (94~96 年) 為「縮減數位落差」，整合各部會現有已建構上網據點設備資源，合作共構成為數位機會中心 (Digital Opportunity Center，DOC)。第二期 (97~100 年) 為「創造數位機會」，實施「推動國民電腦應用，照顧弱勢」，其中補助全國 12,701(台) 戶中低、低收入戶家庭 (教育部，2007)[13]。第三期 (101~104 年) 為「深耕數位關懷」，積極協助偏遠地區民眾、弱勢學童資訊應用與數位服務。而對於偏鄉與弱勢對象的教育，國家與社會資源早已著手進行，例如：教育部於 2006 年開始的攜手計畫課後扶助方案 http://asap.moe.gov.tw/、博幼社會福利基金會於 2002 年創立後的課業輔導計畫 http://www.boyo.org.tw/boyo/index.php、永齡教育慈善基金會於 2000 年開始的永齡希望小學課輔計畫 http://www.yonglin.org.tw/ 等等。傳統教學多是以現場面對面直接上課，在執行上會有交通、氣候、距離、時間、人力匯集等諸多問題需要克服，使得成效難以複製大量推廣。如今，電腦與網路科技進步快速，網路視訊教學已被視為是縮減城鄉差距，拓展偏鄉學生學習與溝通的有效方法。教育部長蔣偉寧提到「數位學習是未來的趨勢」(林思宇，2012)[6]，但是網路課輔有其設備環境管理及遠距輔導專業之挑戰，實施品質亦不易掌控 (趙涵捷，2009)[22]。

偏鄉所需要的不是只有硬體設備環境，最終最需要的是教育。OECD(經濟合作暨發展組織) 教育部指標與分析處前總監史萊克：「有些能力可以在 19、20 歲時再培養，但對學習這件事的動機和興趣，及早建立是非常重要的事。」(呂燕智，2009)[4]。博幼基金會董事長李家同認為「窮困孩子的唯一希望來自教育」，並堅持「不能讓窮孩子落入永遠貧困」理念，提出對窮困孩子的願景目標。當中對於學業成就低落，提出的遠景目標是「教育部聘請大學生幫助窮小孩念書」(博幼社會福利基金會，2009)[19]。他同時提出「教育差距大，貧富差距就大」，指出台灣教育目前最重要的問題是要縮小教育上的差距，如

偏鄉教育之網路學院系統維運

楊志田[1] 林宏彥[2]

[1] 輔仁大學資訊中心，[2] 輔仁大學資訊工程系

摘 要

偏鄉教育一直是文明社會所重視的，但是在推行的經驗中卻常常伴隨著距離、交通、人力匯集等問題。本文提出如何建立有如「網路學院」，將「全省各區輔導中心 / 中小學」的架構，建置如「學院 / 學系」的架構，並設計完整追蹤課輔紀錄的日誌系統，包含教務、學務、總務系統功能，以用來日後追蹤課輔的成效。同時評選符合線上課業輔導功能需求的網路課輔平台，而且需證明主機效能與網路的頻寬足以負荷。透過計畫的執行，證明此架構可以讓師、生兩群同時在網路上的各個角落，透過制度化管理的「網路教室」進行有系統的分班教學訓練，並建立學習紀錄與大量管理的模式。這裡強調的是，不只提供一平台可以讓多組師生線上教學討論，且要以管理一個學院的精神、模式，來營運當中的學習環境。

關鍵詞：網路學院、線上課業輔導、網路教室 。

以共沉澱法合成球型化 $LiCoO_2$ 正極材料之電化學特性研究

劉茂煌　黃信達

天主教輔仁大學化學系

摘　要

本研究提出一種具奈米結構的球型化 $LiCoO_2$ 正極材料的合成方式，先以化學共沉澱法製備出球型化的 $CoCO_3$，並進行第一段燒結形成球型化 Co_3O_4 先驅物，再與 LiOH 混和後，進行第二段燒結製備出具奈米結構的球型化 $LiCoO_2$ 正極材料。我們將針對第二段燒結溫度對 $LiCoO_2$ 的結構和電化學性能的影響進行一系列的探討與研究。在室溫的電化學測試結果中，我們可以發現以 800 ºC 所燒結出的 $LiCoO_2$ 具有較佳的電化學特性，在以 0.1C 與 6.0C 放電條件下，放電電容量分別為 146.7 和 125.8 mAh g^{-1}，然而在低溫 (-10 ºC) 的環境下以 0.2 放電，800 ºC 所燒結出的 $LiCoO_2$ 依舊維持著較高的放電電容量 (129.7 mAh g^{-1})，在交流阻抗 (EIS) 測試部分，燒結溫度 800 ºC 以上的材料，由於結構具有較高結晶度，所以電荷傳遞阻抗 (Rct) 明顯小於以 750 ºC 燒結的材料，以定電流間歇滴定法 (PITT) 測試結果可以得知，材料的擴散係數 (D_{app}) 會隨著燒結溫度從 750 ºC 升至 850 ºC 而減少，是因為材料結構中一次粒子的尺寸因燒結溫度的增加而變大，使得材料的結構更為緻密導致擴散係數 (D_{app}) 變小；從本研究的結果可以說明在兼顧電荷傳遞阻抗與鋰離子擴散速率的情況下，以 800 ºC 所燒結出的球型化 $LiCoO_2$ 正極材料，其電化學特性表現是優於以其他溫度所燒結出來 $LiCoO_2$ 正極材料。

關鍵字：鋰電池、正極材料、微結構、共沉澱、球型化。

source on tap density and high rate cycling performance of spherical $Li[Ni_{1/3}Co_{1/3}Mn_{1/3}]O_2$ for advanced lithium-ion batteries, *J Solid State Electrochem* 16 1229–1237 (2012).

21. Fujii Y., Miura H., Suzuki N., Shoji T., Nakayama N., Structural and electrochemical properties of $LiNi_{1/3}Co_{1/3}Mn_{1/3}O_2$: Calcination temperature dependence, *J Power Sources* 171 894–903 (2007).
22. Kawamura T., Makidera M., Okada S., Koga K., Miura N., Yamaki J., Effect of nano-size $LiCoO_2$ cathode powders on Li-ion cells, *J Power Sources* 146 27–32 (2005).
23. Choi S.H., Kim J., Yoon Y.S., Self-discharge analysis of $LiCoO_2$ for lithium batteries, *J Power Sources* 138 283–287 (2004).
24. Zhuang Q.C., Wei T., Du L.L., Cui Y.L., Fang L., Sun S.G., An electrochemical impedance spectroscopic study of the electronic and ionic transport properties of spinel $LiMn_2O_4$, *J Phys Chem C* 114 8614–8621 (2010).
25. Shaju K.M., Subba R.G.V., Chowdari B.V.R., Influence of Li-ion kinetics in the cathodic performance of layered $LiNi_{1/3}Co_{1/3}Mn_{1/3}O_2$, *J Electrochem Soc* 151 A1324–A1332 (2004).
26. Cao F., Prakash J., A comparative electrochemical study of $LiMn_2O_4$ spinel thin-film and porous laminate, *Electrochimica Acta* 47 1607–1613 (2002).
27. Dokko K., Mohamedi M., Fujita Y., Itoh T., Nishizawa M., Umeda M., Uchida I., Kinetic characterization of single particles of $LiCoO_2$ by AC impedance and potential step methods, *J Electrochem Soc* 148 A422–A426 (2001).
28. Levi M.D., Salitra G., Markovsky B., Teller H., Aurbach D., Heider U., Heider L., Solid-state electrochemical kinetics of Li-ion intercalation into $Li_{1-x}CoO_2$: Simultaneous application of electroanalytical techniques SSCV, PITT, and EIS, *J Electrochem Soc* 146 1279–1289 (1999).
29. Tang S.B., Lai M.O., Lu L., Study on Li+-ion diffusion in nano-crystalline $LiMn_2O_4$ thin film cathode grown by pulsed laser deposition using CV, EIS and PITT techniques, *Mater Chem Phys* 111 149–153 (2008).
30. Levi M.D., Aurbach D., Diffusion coefficients of lithium Ions during Intercalation into graphite derived from the simultaneous measurements and modeling of electrochemical impedance and potentiostatic intermittent titration characteristics of thin graphite electrodes, *J Phys Chem B* 10 4641–4647 (1997).

Recevied Oct 29, 2013
Accepted Feb 19, 2014

118–124 (2006).
8. Kumta P.N., Gallet D., Waghrty A., Blomgren G.E., Setter M.P., Synthesis of $LiCoO_2$ powders for lithiun-ion batteries from precursors derived by rotary evaporation, *J Power Sources* 72 91–98 (1998)
9. Valanarasu S., Chandramohan R., Thirumalai J., Vijayan T.A., Improved electrochemical investigation of combustion synthesized Cd-doped $LiCoO_2$ Powders , *J Sci Res* 2 443–452 (2010).
10. Sathiyaraj K., Ganguli B., Bhuvaneswari D., Kalaiselvi N., Effect of reaction temperature on morphology and electrochemical behavior, *Ionics* 17 49–59 (2011).
11. He P., Wang H.R., Qi L., Osaka T., Synthetic optimization of spherical $LiCoO_2$ and precursor via uniform-phase precipitation, *J Power Sources* 158 529–534 (2006).
12. Ying J.R., Wan C.R., Jiang C.Y., Li Y.X., Preparation and characterization of high-density spherical $LiNi_{0.8}Co_{0.2}O_2$ cathode material for lithium secondary batteries, *J Power Sources* 99 78–84 (2001).
13. Park S.H., Shin H.S., Myung S.T., Yoon C.S., Amine K., Sun Y.K., Synthesis of Nanostructured $Li[Ni_{1/3}Co_{1/3}Mn_{1/3}]O_2$ via a Modified Carbonate Process, *Chem Mater* 17 6–8 (2005).
14. Park S.H., Kang S.H., Belharouak I., Sun Y.K., Amine K., Physical and electrochemical properties of spherical $Li_{1+x}(Ni_{1/3}Co_{1/3}Mn_{1/3})_{1-x}O_2$ cathode materials, *J Power Sources* 177 177–183 (2008).
15. Shin H.S., Shin D.W., Sun Y.K., Synthesis and electrochemical properties of $Li[Ni_{0.4}Co_{0.2}Mn_{(0.4-x)})Mg_x]O_{2-y}F_y$ via a carbonate co-precipitation, *Current Applied Physics* 6S1 e12–e16 (2006).
16. Oh S.W., Bang H.J., Myung S.T., Bae Y.C., Lee S.M., Sun Y.K., The effect of morphological properties on the electrochemical behavior of high tap density C–$LiFePO_4$ prepared via coprecipitation, *J Electrochem Soc* 155 A414–A420 (2008).
17. He P., Wang H.R., Qi L., Osaka T., Electrochemical characteristics of layered $LiNi_{1/3}Co_{1/3}Mn_{1/3}O_2$ and with different synthesis conditions, *J Power Sources* 160 627–632 (2006).
18. Yang S.Y., Wang X.Y., Yang X.K., Liu Z.L., Bai Y.S., Wang Y.P., Shu H.B., Influence of preparation method on structure, morphology, and electrochemical performance of spherical $Li[Ni_{0.5}Mn_{0.3}Co_{0.2}]O_2$, *J Solid State Electrochem* 16 2823–2836 (2012).
19. Yang S.Y., Wang X.Y., Chen Q.Q., Yang X.K., Li J.J., Wei Q.L., Effects of complexants on $[Ni_{1/3}Co_{1/3}Mn_{1/3}]CO_3$ morphology and electrochemical performance of $LiNi_{1/3}Co_{1/3}Mn_{1/3}O_2$, *J Solid State Electrochem* 16 481–490 (2012).
20. Yang S.Y., Wang X.Y., Yang X.K., Liu L., Liu Z.L., Bai Y.S., Wang Y.P., Influence of Li

from 750 to 850 ℃ The calcination temperature affects not only the morphology and crystallinity of the prepared powders but also the electrochemical properties. The $LiCoO_2$ prepared at 800 ℃ shows better overall performances as compared to the other spherical $LiCoO_2$ prepared at 750, and 850 ℃ . These superior properties of $LiCoO_2$ (800) are most likely related to an optimized trade-off for both the crystallinity and the appropriate primary-particle size.

5. Acknowledgements

The authors would like to thank the National Science Council of the Taiwan for the financial support of this work under the project number NSC 98-2113-M-030 -005.

Reference

1. Koksbang K., Barker J., Shi H., Sadi M.Y., Cathode materials for lithium rocking chair batteries, *Solid State Ionic* 84 1–21 (1996).
2. Whittingham M.S., Lithium batteries and cathode materials, *Chem Rev* 104 4271 4301 (2004).
3. Ying J.R., Jiang C.Y., Wan C.R., Preparation and characterization of high-density spherical $LiCoO_2$ cathode material for lithium ion batteries, *J Power Sources* 129 264–269 (2004).
4. Sun Y.K., Oh I.H., Hong S.A., Synthesis of ultrafine LiCo02 powders by the sol-gel method, *J Mater Sci* 31 3617–3621(1996).
5. Lakshmanan R., Ganguli B., Bhuvaneswari D., Kalaiselvi N., Temperature dependent surface morphology and lithium diffusion kinetics of $LiCoO_2$ cathode, *Met Mater Int* 18 249–255 (2012)
6. Li Y.X, Wan C.R., Wu Y.P., Jiang C.Y., Zhu Y.J., Synthesis and characterization of ultrafine $LiCoO_2$ powders by a spray-drying method, *J Power Sources* 85 294–298 (2000).
7. Choi K.Y., Kim K.D., Yang J.W., Optimization of the synthesis conditions of $LiCoO_2$ for lithium secondary battery by ultrasonic spray pyrolysis process, *J Mate Proc Technol* 171

boundaries inside the spherical particles of $LiCoO_2$(750) and $LiCoO_2$(800) improve the mass-transfer in charge/discharge process. The property of fast mass-transfer for $LiCoO_2$ could be the key factor of reversible capacity at low temperature.

The poor electrochemical performances of $LiCoO_2$(750) may be attributed to their low crystallinity and electronic conductivity, although the sample particles calcined at lower temperature has a higher Li-ion diffusion coefficient. The abrupt increase in primary particle size of $LiCoO_2$(850) leads to the lower discharge capacity despite its higher crystallinity and electronic conductivity. The present investigation shows that the $LiCoO_2$ calcined at 800 °C is optimized at both electronic conductivity and Li^+ ion diffusion, ensuring the overall electrochemical performances better than other samples.

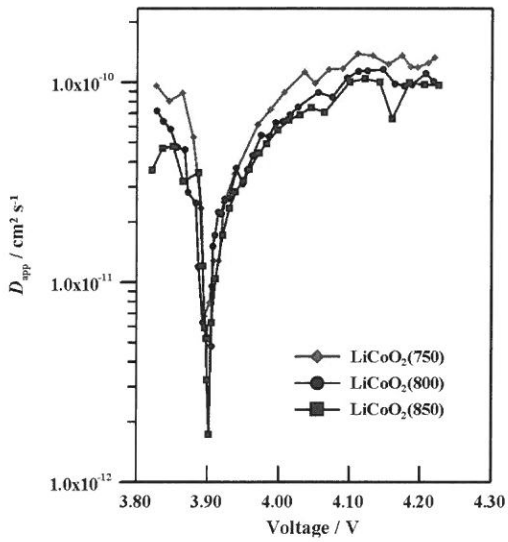

Fig. 8. Apparent Chemical diffusion coefficient (D_{app}) calculated from PITT measurement in Li/$LiCoO_2$(750), Li/$LiCoO_2$(800) and Li/$LiCoO_2$ (850) cells.

4. Conclusions

A spherical $LiCoO_2$ was successfully synthesized using a carbonate co-precipitation followed by solid state reaction method. The $LiCoO_2$ were calcined at different temperatures

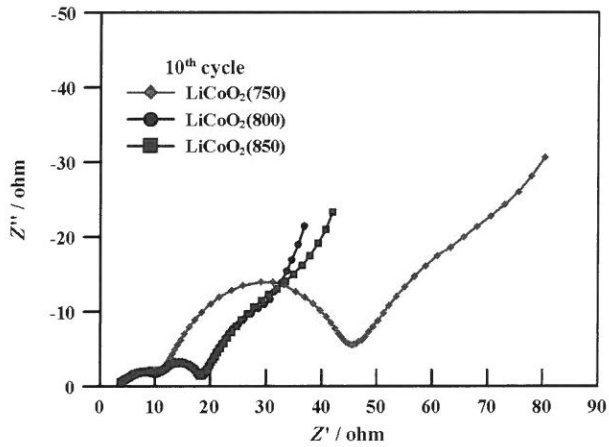

Fig. 7. Nyquist plots for Li/$LiCoO_2$(750), Li/$LiCoO_2$(800) and Li/$LiCoO_2$ (850) cells at the 10th cycles

3.4 Li-ion diffusion coefficient from PITT

Potentiostatic intermittent titration technique (PITT) was also performed for the $LiCoO_2$ cells. I vs. t was measured as a function of potential steps at each increase of 15 mV ranged from 3.820 V to 4.225 V. In order to calculate the apparent chemical diffusion coefficient (D_{app}) from PITT, the following assumptions according to the porous structure of electrode were made: (1) the particle is spherical; and, (2) The average particle radius of 6 μm was used as the characteristic diffusion length for the porous electrode. Therefore, the apparent chemical diffusion coefficient (D_{app}) is preliminary estimated from the slope of the ln I(t) vs. t plot that could be expressed by the following finite-diffusion equation using the long-time definition $t >> l^2 / D_{app}$ [26-30].

$$I = \frac{2nFADC^*}{l^2}\exp\left(\frac{-\pi^2 D}{4l^2}t\right), t >> \frac{l^2}{D_{app}}$$

Fig. 8 shows the variation in the apparent chemical diffusion coefficients (D_{app}) of the Li-ion out the $LiCoO_2$ lattices during the de-intercalation process with the applied potentials. It is found that the D_{app} of $LiCoO_2$ decreases with increasing the calcined temperature from 750 to 850 °C due to the increased primary-particle size. This decrease of D_{app} can be attributed to the longer route required for Li-ion diffusion in primary-particle [22-23]. Therefore, the grain

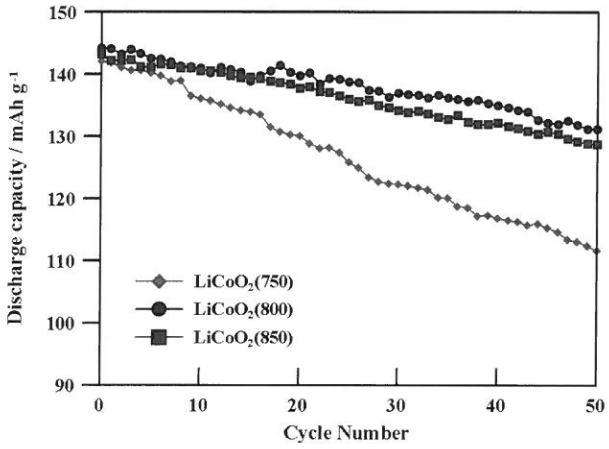

Fig. 6. Cycling performances of Li/$LiCoO_2$(750), Li/$LiCoO_2$(800 and Li/$LiCoO_2$ (850)cells at 0.5C discharge.

3.3 EIS analysis

To further understand the reasons for the differences in electrochemical properties of $LiCoO_2$(750), $LiCoO_2$(800) and $LiCoO_2$(850), EIS was carried out for the $LiCoO_2$ samples in the charged state to 4.2V versus Li/Li^+. Nyquist plots of $LiCoO_2$ cells at the 10^{th} cycle are shown in Fig. 7. The impedance spectrum for the aging cells of $LiCoO_2$ at room temperature shows three overlapped semicircles over the high- to mid-frequency range and an arc line at low frequency. Zhuang [24] and Chowdari [25] reported that (1) a high frequency dispersion because of the presence of a surface layer, (2) a middle to high frequency dispersion related to the electronic properties of the material, (3) a middle frequency semicircle associated with charge transfer, and finally, (4) the very low frequency dispersion attributed to the solid state diffusion. From Nyquist plots, the curves of $LiCoO_2$(800) and $LiCoO_2$(850) are almost overlapped in the high- to mid-frequency range, indicating that electronic resistance of $LiCoO_2$(800) is similar to that of $LiCoO_2$(850). It was observed that the Nyquist plot of $LiCoO_2$(750) has a large arc in mid-frequency range, which is corresponding to the higher charge-transfer resistance of $LiCoO_2$(750). The poor charge-transfer of $LiCoO_2$(750) may be attributed to their lower crystallinity.

Fig. 5 compares the temperature dependence of discharge capacity for $LiCoO_2$(750), $LiCoO_2$(800)and $LiCoO_2$(850) electrodes in half-cells. The Li/$LiCoO_2$(800) cell exhibited lower temperature dependence. For example, the Li/$LiCoO_2$(800) and Li/$LiCoO_2$(750) cells retained 90% of relative capacities at -10 °C, while the Li/$LiCoO_2$(850) cell fell to 74% at -10 °C. The reason for this higher discharge capacities of $LiCoO_2$(800) and $LiCoO_2$(750) could be their smaller primary particle size, which has a shorter lithium-ion diffusion path and therefore increases the Li-ion insertion capabilities [22-23]. However, the iR drop of the $LiCoO_2$(750) is larger, which is a consequence of its higher ohmic resistance. The higher ohmic resistance of $LiCoO_2$(750) may be attributed to that it contained lower crystallinity, a larger amount of primary particle interfaces and poorer conductivity between primary particles. These observations reveal that $LiCoO_2$(800) possess better low temperature performance, which could be attributed to the well crystallinity and better agglomeration of primary particles.

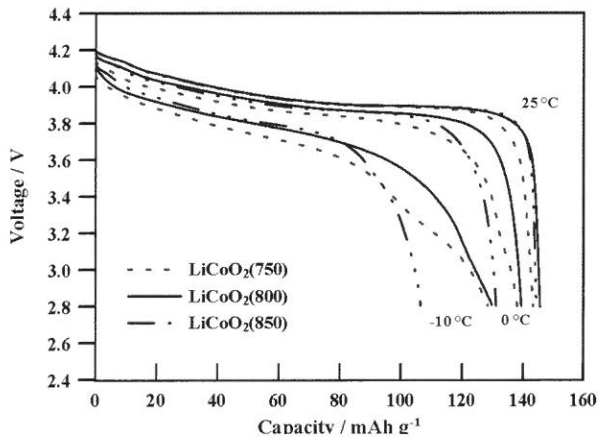

Fig. 5. Capacities of Li/$LiCoO_2$(750), Li/$LiCoO_2$(800) and Li/$LiCoO_2$ (850) cells at various temperatures during 0.2C discharge.

The cycle-life of the $LiCoO_2$ half-cells was also compared, as shown in Fig. 6. The $LiCoO_2$(800) and $LiCoO_2$(850) half-cells lost only ~10% of initial capacities, while the $LiCoO_2$(750) half-cells lost ~21% of capacity after 50 charge/discharge cycles. This result indicates that $LiCoO_2$ calcined above 800 °C has better structural stability.

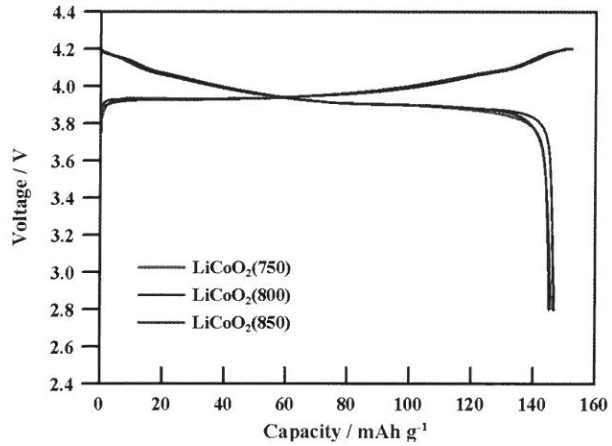

Fig 3. Charge/discharge curves of Li/$LiCoO_2$(750), Li/$LiCoO_2$(800) and Li/$LiCoO_2$ (850) cells during the first cycle.

To further investigate the calcination temperature effects on the electrochemical properties of the spherical $LiCoO_2$ cathode, the C-rate performances at 1C, 2C, 4C and 6C for the $LiCoO_2$ half-cells were measured and compared, as shown in Fig. 4. The rate capabilities of the Li/$LiCoO_2$(800) cells were much better than those of the Li/$LiCoO_2$(750) and Li/$LiCoO_2$(850) cells. At high discharge rates, the electron transfer rate in the particle and the limitations in the kinetics of Li-ion diffusion are the major reasons for the electrode polarization. It is believed that the crystallinity and microstructure of $LiCoO_2$(800) provide a higher electron-transfer rate and a good lithium-transfer pathway.

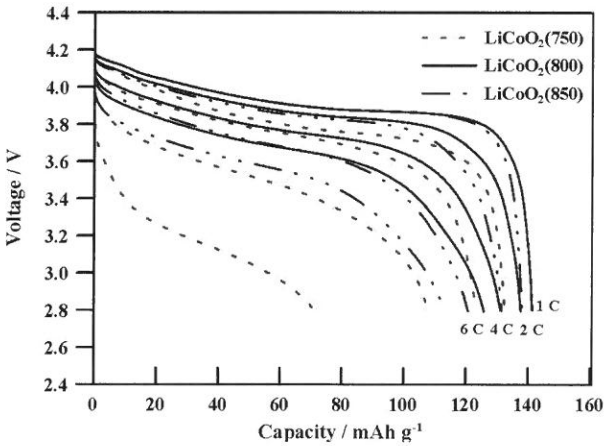

Fig. 4. Rate capacities of Li/$LiCoO_2$(750), Li/$LiCoO_2$(800) and Li/$LiCoO_2$ (850) cells.C-rate = 1, 2, 4, and 6C.

The true densities of $LiCoO_2$(750), $LiCoO_2$(800)and $LiCoO_2$(850) were determined to be 4.93, 4.96 and 5.03 g cm^{-3}, respectively, as measured using a gas pycnometer. The true densities of $LiCoO_2$(750) and $LiCoO_2$(800) were slightly lower than that of $LiCoO_2$(850). The true densities of our spherical $LiCoO_2$ are significant lower than theoretical value (5.06 g cm^{-3}). This discrepancy may be due to the closed-pore volume inside the spherical $LiCoO_2$ that could not be detected by a gas pycnometer. The closed pores within the spherical $LiCoO_2$ particles were formed due to the release of CO_2 gas during de-carbonation. The tap densities of the $LiCoO_2$(750), $LiCoO_2$(800)and $LiCoO_2$(850) reach 2.14, 2.27 and 2.31 g cm^{-3}, respectively, and close to that of commercial $LiCoO_2$. The specific area of $LiCoO_2$(850) powder (0.33 m^2 g^{-1}) was 7-fold lower than that of $LiCoO_2$(750) powder (2.22 m^2 g^{-1}), due to the differences in surface porosity and primary grain size. The physical characteristics of $LiCoO_2$ are summarized in Table 1.

Table 1. Physical characteristics of $LiCoO_2$(750), $LiCoO_2$(800)and $LiCoO_2$ (850) powders

sample	a-axis (Å)	c-axis (Å)	$I_{(003)}$ /$I_{(104)}$	D (nm)	Primary Particle width (μm)	Average Particle size (μm)	True Density (g cm^{-3})	Tap Density (g cm^{-3})	Surface area (m^{-1})
$LiCoO_2$(750)	2.818	14.088	1.206	73.99	0.1~0.2	11~12	4.93	2.14	2.22
$LiCoO_2$(800)	2.816	14.063	1.209	76.10	0.5~0.8	11~12	4.96	2.27	0.74
$LiCoO_2$(850)	2.815	14.051	1.203	85.39	1.0~2.0	11~12	5.03	2.31	0.33

3.2 Electrochemical measurements

The slow charge/discharge (0.1C) capacity behaviors of $LiCoO_2$ samples during the first cycle are shown in Fig. 3. Charge/Discharge capacities of 152.1/145.9, 152.3/146.7 and 152.2/145.2 mAh g^{-1} were obtained for $LiCoO_2$(750), $LiCoO_2$(800)and $LiCoO_2$(850), respectively. The initial specific capacity of $LiCoO_2$(800) is slightly greater than the values obtained for other $LiCoO_2$ of different calcination temperature.

smooth surface compared to the other powders in Fig. 2(e) ~ (h). The primary particle size of all of the powders is estimated to be about 1 ~ 2 μm based on the SEM images. The grain-growth associated with the densification of the $LiCoO_2$ particles may be attributed to the high-temperature calcination.

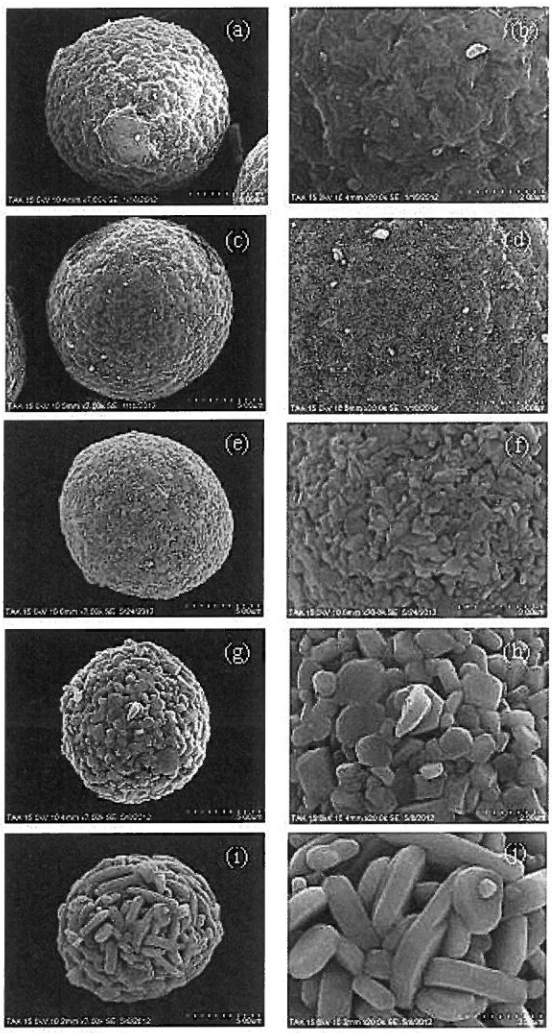

Fig 2. SEM images: (a)(b) $CoCO_3$,(c)(d) Co_3O_4, (e)(f) $LiCoO_2$(750), (g)(h) $LiCoO_2$ (800) and (i)(j) $LiCoO_2$(850)

0.15406 nm and β is the full-width-at-half-maximum (FWHM) of the diffraction peak on a 2θ scale, we can estimate the crystallite size (D) of the $LiCoO_2$ synthesized at different temperatures according to D003 and D104 values, as listed in Table 1. From Table 1 we can see that the D values of $LiCoO_2$ prepared at 750, 800 and 850 °C are 73.99, 76.10 and 85.39 nm, respectively. It is found that the crystallite size increases with increasing the synthesis temperature due to enhanced crystal growth caused by higher reaction temperature.

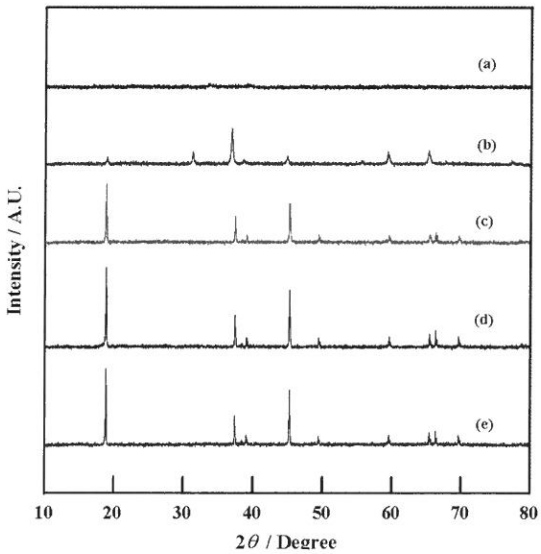

Fig 1. X-ray diffraction patterns of (a) $CoCO_3$, (b) Co_3O_4, (c) $LiCoO_2$(750),(d) $LiCoO_2$(800) and (e) $LiCoO_2$(850) powders.

SEM images of $CoCO_3$, Co_3O_4 and $LiCoO_2$ are shown in Fig. 2. As can be seen in Fig. 2(a) and (b), the prepared $CoCO_3$ particles have spherical shapes with an average diameter of 11~12 μm and no sub-grain on the particle had been observed because the $CoCO_3$ is amorphous. After firing, the amorphous carbonate structure changed to a cubic spinel Co_3O_4 structure. Each of the spherical Co_3O_4 particles is made up of a large number of small grains, as shown in Fig. 2(c) and (d). SEM images of the $LiCoO_2$ powders prepared at different temperatures were used to evaluate the effect of calcination temperature on the morphology of $LiCoO_2$. The images of the powder prepared at 750° C in Fig. 2(e) and (f) show agglomerates consisting of primarily 100~ 200 nm particles. SEM images in Fig. 2(i) and (j) show that the powder prepared at 850° C possesses a larger primary particle size and

a circular disk (12 mm in diameter). The electrode films were preserved in an argon-filled dry box (Unilab, MBrun). In the coin cell, the $LiCoO_2$ electrode disk served as the cathode and the lithium metal foil functioned as the anode. A mixture of ethylene carbonate (EC), diethyl carbonate (DEC), and propylene carbonate (PC) (EC:DEC:PC = 30:50:20 vol. %) solvents containing 1M $LiPF_6$ was used as an electrolyte. The polypropylene membrane was soaked in the electrolyte for 24 hours prior to use. The coin cell was assembled in an argon-filled dry box, in which the moisture and oxygen content were maintained at less than 1 ppm. The coin cell was charged and discharged at various current densities in the range of 2.8-4.2V using a battery testing system (BAT750B, Acutech Systems Co. LTd., Taiwan). EIS and PITT experiments were performed using an electrochemical station (614B, CH Instrument). The impedance spectra were taken in the frequency range of 0.001~100k Hz after cycling between 2.8 and 4.2 V, then charged to 4.2 V. In the PITT measurements, a potential step of 15 mV was applied after the electrode had reached equilibrium as evidenced by the residual current of less than 1 μA.

3. Results and Discussion

3.1 Synthesis and characterization of the sample

Fig. 1 shows the XRD patterns of the $LiCoO_2$ synthesized at different temperatures. Hereafter, the obtained products were labeled as $LiCoO_2$(750), $LiCoO_2$ (800) and $LiCoO_2$(850), respectively. All the peaks are indexed on the basis of the α-$NaFeO_2$ type, space group R-3m . There is no impurity line observed. From Fig. 1, we can also see that the peak intensity of $LiCoO_2$ increased as the calcination temperature increased from 750 to 850 °C. The peak splits of (006)/(102) and (108)/(110) can be clearly observed above 800 °C, indicating that $LiCoO_2$ with good layered structure can be obtained at the higher calcination temperature . The hexagonal lattice parameters, c/a ratio, unit volume and crystallite size are given in Table 1. The lattice parameters of all the samples decrease slightly with the calcination temperature increased from 750 to 850 C, indicating the increase of crystallinity as may result from the growth of primary particle size, ordering of local structure, and release of lattice strain. Based on Scherrer formula $D= k\lambda/\beta\cos\theta$, where k is 0.9, λ is

2. Experimental

2.1 Synthesis

Spherical $LiCoO_2$ was prepared as following steps [13,18]: An aqueous solution of 1.0 M $CoSO_4$ was pumped into a tank reactor (capacity, 5L) with continuous stirring. At the same time, a 1.2 M Na_2CO_3 solution and of a 2.0 M NH_4OH solution, which was used as a chelating agent, were fed separately into the reactor. The pH and temperature were maintained at 7.5 and 60 °C, respectively. After vigorous stirring for 20 hours, the spherical $CoCO_3$ precipitations with particle diameters of approximately 10~15 μm were formed. The carbonate powder was fired at 600 °C for 12 hours to decompose the carbonate into an oxide. The Co content of the resulting oxide was determined to be approximately 71.32 wt% using EDTA titration,. The chemical formula of the oxide compound was determined to be Co_3O_4 by XRD test. The Co_3O_4 precursor was mixed with lithium hydroxide ($LiOH \cdot H_2O$) powder and the mixture were then calcined in a box furnace at 750, 800 or 850 °C in an oxygen atmosphere for 12 hours for the formation of lithium cobalt oxide ($LiCoO_2$) particles.

2.2 Characterization of physical properties

Sintered powder morphology was characterized using a SEM (S3400N, Hitachi). A diffractometer (PANalytical, X' Pert) equipped with Cu/Ka source was used for X-ray diffraction (XRD) studies. True powder densities were measured using a gas pycnometer (AccuPyc 1330, Micromeritics). The specific surface area of these powders was measured in an analyzer (ASAP 2010, Micromeritics) using the Brunauer, Emmett and Teller (BET) method.

2.3 Electrochemical measurements

Electrochemical evaluation of the $LiCoO_2$ sample was carried out using a CR2032 lithium ion coin cell. Cathode films were prepared by mixing active material, KS6 graphite, Super-P carbon black and polyvinylidene fluoride (PVdF), as a binder, in the ratio of 88:4:2:6 (wt. %). *N*-methyl pyrrolidinone (NMP) was used as the solvent. The slurry was obtained after mixing carbon black, active material and PVdF binder with the NMP solvent. The resulting slurry was cast on 20 μm Al foil using a 200 μm doctor blade. The coated Al foil was dried at 120 °C for 2 hours to evaporate the NMP solvent. The coated foil was roll-pressed and punched to form

1. Introduction

Lithiated transition metal oxides, such as $LiCoO_2$, $LiMn_2O_4$, $LiNiCoO_2$ and $LiNiCoMnO_2$have been extensively studied as cathode materials in secondary lithium ion batteries, because the use of these compounds results in high operating voltage, energy density, high specific density and a long cycle life [1, 2]. Despite the high cost of cobalt, $LiCoO_2$ is still the most widely used metal oxide due to its superior thermal and structural stability during battery operation. High energy-density lithium ion batteries need $LiCoO_2$ as cathode materials with both high specific capacity and high packing density. The conventional and commercialized $LiCoO_2$ powders are usually prepared via a solid-state reaction between mechanically mixed lithium and cobalt compounds at 700~1000 °C. These $LiCoO_2$ particles are always in irregular shape, with a broad particle size distribution. Due to significant particle agglomeration and "bridge formation" within the powders composed of irregular particles [3], tight packing of the irregular particles is difficult, preventing the attainment of high tap-density. Furthermore, the low density of $LiCoO_2$ cathode materials limits the final energy density of lithium ion batteries. Therefore, the preparation and use of spherical $LiCoO_2$ particles may effectively increase energy density. In addition, $LiCoO_2$ is normally synthesized via a solid-state reaction at high temperature. The rate-limiting step is the diffusion of atoms or ions through reactants, intermediates and products. Unfortunately, the activation energy of diffusion often becomes an energy barrier for the solid-state reaction, resulting in heterogeneous products. Thus, many researchers have tested advanced processes, such as sol-gels [4-5], spray drying [6], spray pyrolysis [7], freeze-drying rotary evaporation [8], combustion[9], hydrothermal synthesis [10] and co-precipitation [3,11], for the synthesis of high performance materials with high purity and crystallinity. Recently, several researchers [12-21] reported the synthesis of high purity and spherical powders via the co-precipitation routes that could be an effective way to increase the tap-density.

In the present study, spherical $LiCoO_2$ were synthesized using a carbonate co-precipitation method. The influence of calcination temperature on the microstructure and electrochemical properties was systematically investigated. Structural identification, electrochemical impedance spectrometry (EIS) and potentiostatic intermittent titration technique (PITT) for analyzing the mechanisms of different material performances are discussed.

Synthesis and electrochemical characterization of spherical $LiCoO_2$ cathode material via carbonate co-precipitation

Mao-Huang Liu*, Hsin-Ta Huang

Department of Chemistry, Fu Jen Catholic University, New Taipei City, Taiwan 24205

Abstract

We report a novel synthetic approach for creating spherical and multi-grain lithium cobalt oxide ($LiCoO_2$) powders. The synthetic steps include co-precipitations of spherical $CoCO_3$, sintered to spherical Co_3O_4 precursor, then solid-state calcination to $LiCoO_2$. The effects of calcination temperature on the structural and electrochemical properties of the $LiCoO_2$ were systemically studied. Electrochemical testing results at room temperature showed that the best discharge capacities of $LiCoO_2$ calcined at 800 °C are 146.7 and 125.8 mAh g^{-1} at discharging rates of 0.1 and 6C, respectively. Low temperature (-10 °C) discharging results at a rate of 0.2C exhibited that $LiCoO_2$ calcined at 800 °C has a highest capacity (129.7 mAh g^{-1}). Electrochemical impedance spectrometry (EIS) analysis showed that the charge transfer resistance(*Rct*) of $LiCoO_2$ calcined above 800 °C is much lower than that of $LiCoO_2$ calcined at 750 °C due to their higher crystallinity. The results of potentiostatic intermittent titration technique (PITT) showed that the apparent chemical diffusion coefficients (*Dapp*) of $LiCoO_2$ decreases with increasing the calcination temperature from 750 to 850 °C, which is attributed to increase the primary-particle size of $LiCoO_2$. Our results showed that $LiCoO_2$ calcined at 800 °C is optimized trade-off between electronic conductivity and lithium ion diffusion, therefore the electrochemical performances are better than those spherical $LiCoO_2$ calcinized at other temperature.

Key words: Lithium Battery; Cathode material; microstructure; co-precipitation; spherical morphology

*Corresponding author: Tel.: +886 2 29053565; Fax: +886 2 29023209 e-Mail: 061355@mail.fju.edu.tw

BitTorrent K-Hop Rarest First

Chun-Hsien Lu and Nien-An Hsu

Dept. of Computer Science and Information Engineering
Fu Jen Catholic University

Abstract

Traditional client-server architecture has become inadequate in face of today's growing demand of file sharing due to the bandwidth bottleneck and single point failure problems. An effective solution is to use Peer-to-peer (P2P) architecture, among which the BitTorrent (BT) protocol has been most widely used. Because the tracker does not consider the piece distribution and the structure of topology when it sends the peer list to each joining peer, the swarm may not form a topology that facilitates the quick spread of difference pieces. In order to reduce the average file download time, it is important to have good strategies on both the piece selection and request selection. In this paper, we proposed a k-hop rarest first (KHRF) strategy to replace the local rarest first and tit-for-tat strategies in BT. Under this strategy, a peer will choose to first download the piece that is rarest within k hops. When deciding which request to serve, a peer will serve the piece request that has the maximum rareness within k hops. Simulation results show that the KHRF strategy can reduce about 21% of the average download time, and 18% of the total elapsed time. KHRF can improve the availability of BT system.

Key words: BitTorrent, Peer-to-Peer, Piece Selection, Request Selection

12. L. Guo, S. Chen, Z. Xiao, E. Tan, X. Ding, and X. Zhang, "A Performance Study of BitTorrent-like Peer-to-Peer Systems," *in IEEE Journal on Selected Areas in Communications, vol. 25, pp. 155-169*, Jan. 2007.
13. W.-C. Liao, F. Papadopoulos, and K. Psounis, "Performance Analysis of BitTorrent-like Systems with Heterogeneous Users," *in Journal on Performance Evaluation, vol. 64, issue 9-12, pp. 876-891*, 2007.
14. V. Rai, S. Sivasubramanian, S. Bhulai, P. Garbacki, and M. v. Steen, "A Multiphased Approach for Modeling and Analysis of the BitTorrent Protocol," *in Proceedings of the 27th International Conference on Distributed Computing Systems (ICDCS '07)*, June 2007.
15 R. L. Xia and J. K. Muppala, "A Survey of BitTorrent Performance," IEEE Communications Surveys & Tutorials, Second Quarter 2010.
16. W. Chi-Jen, L. Cheng-Ying, and H. Jan-Ming, "Improving the Download Time of BitTorrent-like Systems," *in IEEE International Conference on Communications*, June 2007.
17. P. Sandvik and M. Neovius, "The Distance-Availability Weighted Piece Selection Method for BitTorrent: A BitTorrent Piece Selection Method for On-demand Streaming," *in First International Conference on Advances in P2P Systems*, Oct. 2009.
18. Z. Jianwei, X. Wei, and L. Dongming, "Tracker Algorithm Based on Upload Capacity in BitTorrent Network," *in International Conference on Computer Science and Service System (CSSS)*, June 2011.

Recevied Oct 28, 2013
Accepted Mar 17, 2014

實驗數據顯示，在平均個別下載時間與最後完成時間這兩項指標我們都能夠有顯著地改善。尤其是在特殊拓樸結構中，KHRF 比起原始 BT 在平均個別下載時間此指標有 21% 的改善，在最後完成時間這個指標也有大約 16% 的改善。KHRF 方法所需付出的代價是當 hop 數為 2 以上時會產生大量的訊息，導致一些頻寬的浪費，這將是未來有待改善之處。

參考文獻

1. Felix Oberholzer-Gee and Koleman Strumpf, "The Effect of File Sharing on Record Sales. An Empirical Analysis," *Working Paper, Harvard Business School*, 2004.
2. Napster, http://www.napster.com/
3. eMule, http://www.emule-project.net/home/perl/general.cgi?l=16
4. B. Cohen, "Incentives Build Robustness in BitTorrent," *in Proceedings of first ACM workshop on Economics of Peer-to-Peer System*, Berkeley, CA, USA, June 2003.
5. A. Parker, "The True Picture of Peer-to-Peer File Sharing" , 2004. http://www.cachelogic.com/
6. The Pirate Bay, http://thepiratebay.se/
7. BitComet, http://www.bitcomet.com/
8. J. Pouwelse, P. Garbacki, D. Epema, and H. Sips, "The BitTorrent P2P File-Sharing System: Measurements and Analysis," *in Proceedings of the 4th international conference on Peer-to-Peer Systems*, Berlin, Heidelberg, Nov. 2005.
9. A. R. Bharambe, C. Herley, and V. N. Padmanabhan, "Analyzing and Improving a BitTorrent Networks Performance Mechanisms," *in Proceedings of 25th IEEE International Conference on Computer Communications (INFOCOM'06)*, Apr. 2006.
10. Y. Tian, D. Wu, and K. W. Ng, "Modeling, Analysis and Improvement for BitTorrent-like File Sharing Networks," *in Proceedings of 25th IEEE International Conference on Computer Communications. (INFOCOM '06)*, Apr. 2006.
11. C. Dale and L. Jiangchuan, "A Measurement Study of Piece Population in BitTorrent," *in IEEE Global Telecommunications Conference (GLOBECOM '07)*, Nov. 2007.

圖 7 是固定鄰居總數為 8，變動 hop 數的實驗結果。我們可以發現，訊息量從 hop 數由 1 改成 2 之後出現急遽增長，原因是 KHRF 必須額外傳遞許多訊息給鄰居的鄰居。而 hop 數大於 2 之後的增長較為和緩，原因是我們在程式中設定收到來自同一來源 peer 發出的訊息便不回傳，而在 hop 數大於 2 之後，有些鄰居開始重複，致使訊息數量之增長不致於如此急遽。

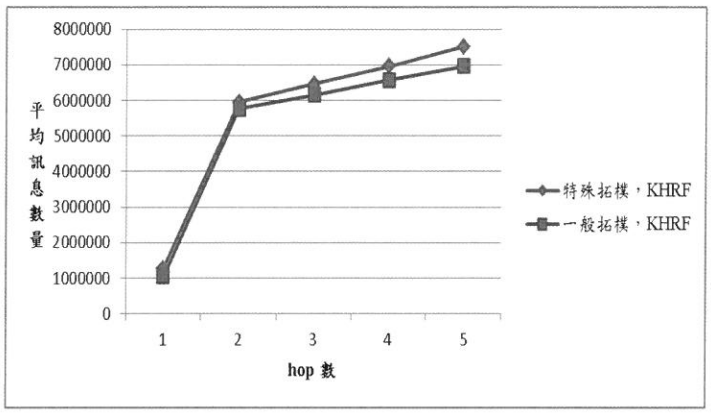

圖 7：平均訊息數量（100 個 peer）

5. 結　論

點對點架構可以有效利用整個群體的頻寬，同時也可避免單一節點失敗的問題。由於 BT 協定內的 tracker 發送清單給新加入的 peer 時，並未考量拓樸的組成結構，因此所建立的拓樸可能對於片段的快速散播不盡理想。在此種情況下，原始 BT 的 LRF 與 TFT 策略無法有效地將群體內較稀有的片段迅速散播出去。我們提出了 KHRF 方法，改變 peer 選擇片段與服務對象的策略。除了將 LRF 的範圍擴大到 K 個 hop 之外，也將局部稀有度設定為發送請求的參數之一，再利用該參數來判斷要優先服務哪個 peer，參數值越大便越優先。

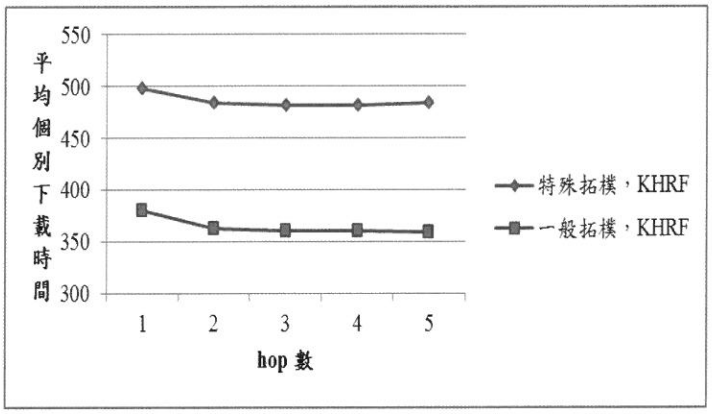

圖 5：平均個別下載時間與 hop 數關係圖（100 個 peer，4 個鄰居）

圖 6 繪出最後完成下載之 peer 所耗時間與鄰居數量之變化，由於平均個別下載時間降低，致使最後完成時間也隨之降低，因此圖 6 的結果與圖 4 類似。在一般拓樸下，KHRF 比起 BT 約改善了 12%。而在特殊拓樸下，KHRF 比起 BT 約改善了 19%。

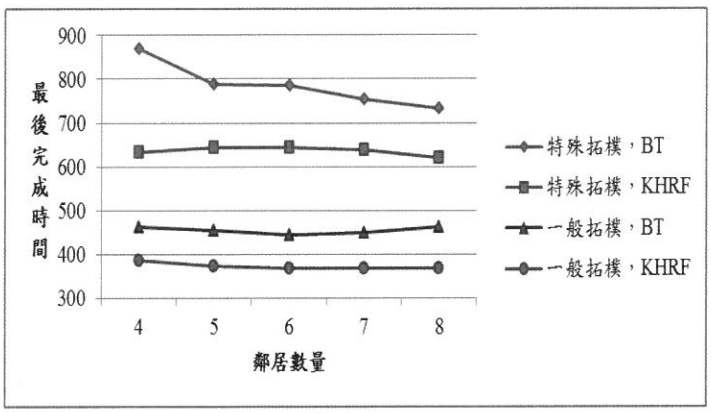

圖 6：最後完成時間比較圖（100 個 peer）

4.2 實驗結果分析

圖 4 顯示鄰居數量與平均下載時間的關係。當鄰居數量增加時，代表可發送請求的對象增加，因此 BT 和 KHRF 的平均個別下載時間皆隨之下降。我們可從圖中觀察到，由於 BT 採用 TFT 策略，其挑選服務對象與頻寬較有關係，因此無法保證善用新增的鄰居。而 KHRF 能夠探索 K 個 hop 以內的 peer，因此在選擇片段與決定服務對象時可以做出較正確的判斷，比起 BT 能夠縮短約 21% 的平均個別下載時間。而在特殊拓樸結構下，KHRF 的平均個別下載時間仍然較短，改善幅度也有 11.6% 至 25.4% 左右。在圖 5 中我們觀察改變 hop 數對下載時間之影響。我們發現，當 hop 數從 1 提升到 2 時有較明顯的改善，當 hop 數超過 2 之後，改善的幅度便趨於平緩。因此將 hop 數設定為 2 似乎是較為理想的做法。

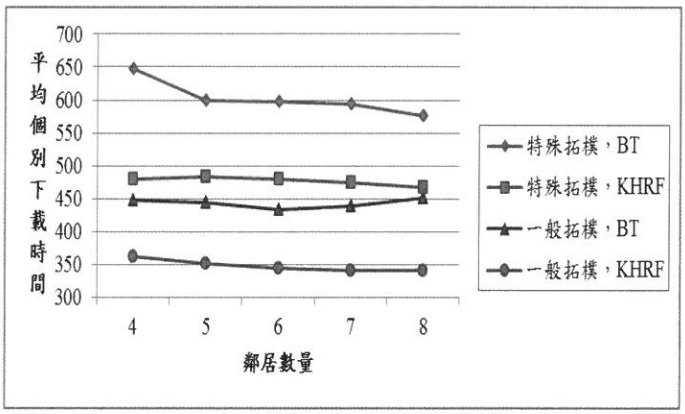

圖 4：平均個別下載時間與鄰居數量關係圖（100 個 peer）

段 1 或片段 3 皆有可能發送請求給 J，同樣會與 A 造成競爭關係。但是 A 的請求的局部稀有度為 8 是三者中最高，因此 J 會選擇 A 做為服務對象，達成我們預期的理想狀態。

4. 效能評估

4.1 模擬環境

我們使用 Python 2.7 撰寫一個模擬程式來評估我們所提出 KHRF 方法之效能，作業系統為 Windows 7，比較對象為標準 BT。本模擬實驗將傳送訊息與請求的時間忽略不計，並且假設 seed 與 peer 之頻寬不會變動。所有 peer 假設於實驗開始即加入，下載完畢之後仍會持續服務其他 peer 不會離開。其餘模擬設定如表 2。

表 2. 模擬實驗設定

Seed 數量	1
Peer 數量	100
Peer 鄰居數量	4 到 8
Seed 最大上傳頻寬	16 Mbps
Peer 最大下載／上傳頻寬	4 Mbps / 2Mbps
檔案大小	64 MB (128 個片段)
片段大小	512 KB
每個 peer 最大可同時服務數量	4 個請求

在本實驗中，我們針對特殊拓樸結構（例如圖 1 之啞鈴式拓樸）和一般拓樸結構（每個 peer 的鄰居節點為隨意挑選）兩種情況下來比較 KHRF 與 BT 之效能。我們比較以下三項數據的平均值：平均個別下載時間、最後完成時間、平均發送訊息數量。

若採用 KHRF 方法，則 peer A 會與 B、C、D、E、F、G、H、I、J、L 交換 BitMap，依照總共 11 個 BitMap 來計算這個局部區域內 peer A 所沒有的片段的局部稀有度，其計算過程如下：

◆片段 4 被 B、F、H、I 持有：局部稀有度為 11 - 4 = 7

◆片段 5 被 I、J、L 持有：局部稀有度為 11 - 3 = 8

由上述結果得知，片段 5 為最稀有的片段，因此 peer A 便會選擇片段 5 來下載，符合我們的目標。

3.2Service Selection

雖然在節 3.1 的範例中 peer A 可以於選擇片段時用 KHRF 方法做出較好的決定，但由於 BT 協定是使用 TFT 策略，無法保證 peer J 會優先服務 peer A 傳來的下載片段 5 的請求。為了確保 peer A 能有較大的機率得到該片段，我們提議每個 peer 於選擇服務對象時改採用 KHRF 方法所計算出來的局部稀有度做為服務依據。每個 peer 發送請求時會附上 KHRF 計算出來的局部稀有度。當 peer 收到多個請求時，會從局部稀有度最大的請求開始服務。以先前的圖三為例，當 peer A 向 peer J 發送請求要求下載片段 5 時，可能會面臨來自 H、I、L 的競爭。表 1 列出 H、I、L 使用 KHRF 選擇片段的結果：

表 1. KHRF 計算結果

Peer	片段	有該片段之 peer	稀有度	決定
H	片段 3	A、J、L、N、S	9-5 = 4	片段 5
	片段 5	I、J、L、S	9-4 = 5	
I	片段 1	A、H、J、S	6-4 = 2	片段 1 或 3
	片段 3	A、J、L、S	6-4 = 2	
L	片段 1	A、H、J、S	9-4 = 5	片段 4
	片段 4	H、I、S	9-3 = 6	

經由以上計算結果可得知，由於 L 選擇片段 4，但 J 沒有片段 4，因此 L 不會直接與 A 競爭。H 雖然會選擇片段 5，有可能會發送請求給 J（另一個可能是發送給 S），造成與 A 皆向同一個 peer 發送請求的競爭關係。而 I 無論選擇片

為了解決上述的片段選擇問題，本論文修改了 LRF 策略，將統計 BitMap 的對象擴大到距離自己 K 個 hop 以內的 peer，稱為 K-Hop Rarest First（簡稱為 KHRF）。以 K = 2 為例，在圖 2 中 peer J 要選擇片段之前原本必須先統計 A、H、I、J、L（共 5 個 peer）的 BitMap，使用 KHRF 方法後則擴大為統計 A、B、C、D、E、H、I、J、K、L、M、N、S（共 13 個 peer）的 BitMap。因此得到新的統計結果如下：

◆片段 4 被 B、H、I、S 持有：局部稀有度為 13 - 4 = 9

◆片段 5 被 I、L、S 持有：局部稀有度為 13 - 3 = 10

由上述結果得知，片段 5 為最稀有的片段（局部稀有度為 10），因此 peer J 便會選擇片段 5 來下載，未來便有機會將片段 5 向右半部的拓樸結構傳遞，進而減少平均個別下載時間，增進用戶的下載體驗。假設 peer J 已經成功下載片段 5，如圖 3，則我們可繼續觀察 peer A 的挑選結果是否會如理想狀態向 peer J 要求下載片段 5。

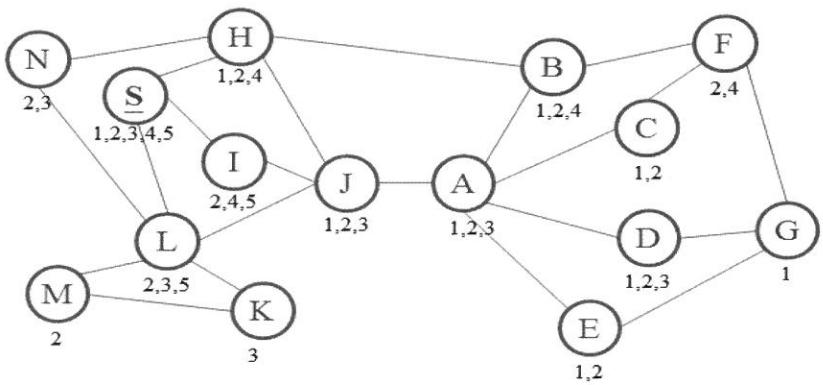

圖 3：Peer J 下載片段 5 之後的情形

在 BT 原始的 LRF 策略中，其計算過程如下：

◆片段 4 被 B 持有：局部稀有度為 6 - 1 = 5

◆片段 5 被 J 持有：局部稀有度為 6 - 1 = 5

由上述結果得知，peer A 便會從片段 4 與片段 5 之中隨機挑選一個來下載（因為局部稀有度皆為 5）。但理想的狀況應該是下載片段 5，因此 LRF 策略可能無法達成我們理想中的結果。

3. 方法設計

3.1Piece Selection – K-Hop Rarest First

圖 2 是一個全體仍在下載中的情境，檔案總共分為 5 個片段。此情境中之拓樸結構較為特殊，整個拓樸可從 peer A 與 peer J 之間劃分為兩個小群組，這兩個小群組之間只有 H ←→ B 與 J ←→ A 這兩條路徑可以溝通，而 Seed（含有底線的 S 節點）存在於左半邊的群組。因此每次 peer H 或 J 要選擇下載檔案片段時，若優先選擇右半群組尚未含有的片段，即可減少右半群組的平均個別下載時間。

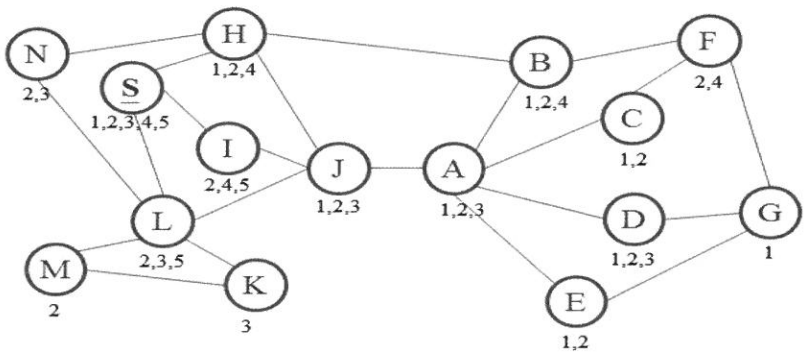

圖 2：特殊拓樸結構

我們以 peer J 為例，當他要選擇片段時，會對於其所缺乏的片段，依照 LRF 策略計算該片段的局部稀有度。其計算結果為：

◆片段 4 被 H、I 持有：局部稀有度為 5 - 2 = 3

◆片段 5 被 I、L 持有：局部稀有度為 5 - 2 = 3

片段 4 與 5 皆為最稀有的片段，因此 peer J 便會從這兩個片段之中隨機挑選一個來下載。但是在圖二的拓樸結構中，右半部的群組只缺乏片段 5 即可讓右半部群組內的所有 peer 自給自足，此時即必須倚賴 peer H 或 J 先得到片段 5，再將片段 5 傳遞給右半部拓樸。然而在 LRF 策略中，peer J 有一半的機率會挑選片段 4，在此種狀況下會導致右半部的群組只能繼續等待 peer H 或 peer J 下載片段 5 再往右傳遞，造成右半部的 peer 平均個別下載時間變長。

peer B 一個固定大小的 block，希望以此達到公平的效果。而 [10] 則是使用一個 α 值來決定要將 peer 上傳速率作為判斷依據時佔有多大的百分比，同時也讓 tracker 紀錄那些不合常理的 peer，在未來發送清單時會將這些隔離，使其無法連線。[14] 的作者指出，為數眾多的使用者在下載最後一個片段時，常常需要很長的時間，因此他們提出了一種名為 Shaking the peer set 的機制。當某個 peer 下載了超過 90% 的片段之後，停止一切下載活動，退出 BT 系統再重新加入，此時 tracker 便會發送一份新的 peer 清單給該 peer，使得該 peer 能與新的鄰居建立連線，有機會得到跟以往不同的片段。經由這種機制，檔案片段在重疊網路中會重新分布，使得每個 peer 完成下載的機率變高。

[16] 的研究目的是將 BT 協定中挑選檔案片段的方式以加上權重的方式改良，目的是期望能減少下載時間。peer 對於某個缺乏的檔案片段 m，如果片段 m 也存在於鄰居 i 的缺乏清單中，則將 F(m) 值加上鄰居 i 目前已下載的片段總數。因此若某個片段同樣只有三個 peer 持有，但是會依據三個人已下載之片段總數的不同而有不同的 F(m) 值，peer 會優先下載 F(m) 值最大的片段。[17] 同樣也是將 BT 挑選 piece 的方式以加上權重的方式改良而成，不同點在於 [17] 的權重與 piece 之間的距離有關。此種方式可使 BT 協定在影音串流的應用下有較好的使用體驗，但是對於一般檔案分享並無太大的益處。[18] 認為 BT 協定中，tracker 傳給 peer 的使用者清單並未善加利用各個 peer 的上傳頻寬資訊，因此他們提出一個基於各個 peer 上傳頻寬的 UC-track 演算法，希望 tracker 能利用這個演算法創造出更好的拓樸環境，以便提高整個 BT 系統的頻寬利用率。

綜觀上述提及之改善方法，目的皆是提高 BT 效能，減少下載時間，但是並沒有任何方法針對網路拓樸出現特殊結構時進行改善。當網路拓樸出現特殊結構時，選擇片段與服務對象的機制變顯得特別重要。因此我們希望能夠透過新的片段與服務對象選擇策略來降低平均個別下載時間與最後完成時間，期望能增進 BT 的效能。

D 的頻寬較大，則 A 可能會持續選擇將檔案片段優先傳給 C 或 D，造成 B 只能等待 optimistic unchoking 的機會來下載檔案，導致最後完成時間與平均個別下載時間皆變長。在本論文中，我們將於發送片段下載請求時都附上一個 k hops 內的局部稀有度參數。而 peer 在決定服務對象時即以此稀有度的大小來決定要優先服務誰，稀有度越大的請求越優先服務。經由上述兩項方法，在挑選欲下載之片段與選擇服務對象時都能做出對整體更有效率的選擇，進而縮短最後完成時間與平均個別下載時間。

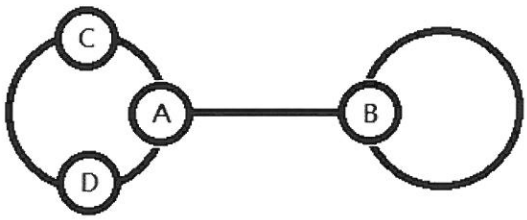

圖 1：啞鈴式拓墣結構

本論文共分為五個部分，接下來將於第二章探討相關研究，第三章提出所設計之方法，第四章為效能評估，第五章則是結論與未來展望。

2. 相關研究

BT 協定從被提出至今已超過十年，在這期間已有許多學者對 BT 提出效能與運作方式上的質疑，並且進行各種研究以便驗證 BT 的優缺點。根據眾多研究結果顯示出 BT 在網路上傳播檔案確實有不錯的效能 [8-15]，但也存在不少議題值得探討與改善。

[9-10] 皆針對 BT 進行測量與分析，其測量結果皆顯示 BT 的 TFT 策略無法有效的公平服務每一個 peer。[9] 提出了一個改良的 block-based TFT 方法，其運作方式是假設有一門檻值Δ，peer A 上傳給 peer B 的量為 Uab，peer A 向 peer B 下載的量為 Dab，則當 Uab ≦ Dab+ Δ 時 peer A 才會允許上傳給

1. 簡　介

近年來，網路頻寬與資訊傳播量皆大幅度地增加，使用者之間互相分享檔案的需求也與日俱增，分享檔案已成為使用者在網路上最常見的活動之一，而且被分享至網路上的檔案仍在急遽增加當中 [1]。為了解決大量檔案分享的需求，點對點（Peer-to-Peer，簡稱 P2P）架構因而被提出。在點對點架構中，每位使用者皆兼具上傳與下載的功能，此種架構比起主從式架構更能有效地利用每一位使用者的頻寬與運算能力，同時也可以避免單一節點失敗的問題。目前已經有許多採用點對點架構的檔案分享服務與軟體陸續被實作出來，例如 Napster [2]、eMule [3]、BitTorrent (BT) [4] 等。其中 BT 是時下最被廣為使用的 P2P 協定。截至 2004 年 6 月為止，BT 協定之流量已在所有點對點架構流量中佔了 53% [5]。

在 BT 協定中，使用者每次要挑選欲下載的片段時會使用 Local Rarest First（LRF）策略，該策略會挑選自己與鄰居中最少數 peer 所擁有的片段。經由此種策略較能確保每個片段的複製份數不會太少，即使遇到檔案供應者或是少數 peer 忽然離開的狀況，剩餘的 peer 仍有較大的機率能將檔案分享完畢。而各個 peer 挑選服務對象時是採用 Tit-for-Tat（TFT）策略。也就是選擇正在上傳片段給自己，同時上傳頻寬最大的前幾位鄰居（BT 預設是 4 位）。此種策略之目的在於鼓勵使用者盡量開放上傳頻寬，讓上傳頻寬較大的使用者能夠得到較高的下載速率，同時未來也能夠利用較大的上傳頻寬將這些檔案片段再次發送給其他尚未下載完畢的 peer。另一方面，此種策略也懲罰只想下載而不想上傳（將上傳頻寬設定為很小的值）的 peer，使其較難得到被服務的機會。

由於 LRF 策略僅能確保每次下載的片段於未來可以服務自己的鄰居，但無法得知該片段是否能夠被鄰居繼續用以服務其他 peer，導致喪失了減少平均個別下載時間的機會。因此本論文對 LRF 策略進行修改，將局部範圍擴展到 k 個 hop 數以內（BT 預設是一個 hop），即在 k 個 hop 數以內被越多 peer 需要越高的片段應越優先被下載，如此一來即提高檔案片段被再度傳播的可能性。至於在服務策略方面，TFT 策略雖然保有公平性，然而在面對某些特殊的拓樸結構時，卻容易因為這樣的機制而使得全體的平均個別下載時間拉長。如圖 1 為啞鈴式的拓樸結構，節點 A、C、D 屬於同一個重疊網路（overlay network）的左側，而 B 屬於重疊網路的右側。在原始的 BT 協定下，若 C 和

在 BitTorrent 中以 K-Hop Rarest First 機制決定檔案片段與服務對象以減少下載時間

呂俊賢　徐念恩

輔仁大學資訊工程系

摘　要

傳統的主從式架構由於頻寬與效能容易成為瓶頸以及單一節點故障等問題，已明顯不敷使用，點對點架構因此應運而生。在各種點對點協定中，又以 BT 協定最被廣為使用。由於 BT 內 tracker 發送清單給新加入的 peer 時並未考量片段分布情形與拓樸的結構，因此可能會建立出對於片段傳播不盡理想的拓樸結構。為了解決此問題，我們提出 K-Hop Rarest First（KHRF）方法，依據 k hops 內的片段稀有度，來決定片段下載順序，以及 peer 對於所收到 request 的服務順序。經由實驗數據證實，我們的方法比起原始 BT 在平均個別下載時間大約有 21% 的改善，在最後完成時間也有 18% 的改善。

關鍵詞：BitTorrent，點對點網路，片段下載，服務順序選擇 。

* Corresponding author, Tel.,+886-2-29052018; fax,+886-2-29021038
E-mail address: lbchang@mail.fju.edu.tw

反相零電流切換雙向轉換器應用於電池等化器之狀態分析與實現

李永勳　鄭明旺*　邱雲源

輔仁大學 電機工程學系
*輔仁大學 應科所

摘　要

本論文中提出非隔離式、雙向功率流控制零電流切換式電容直流對直流轉換器架構。利用狀態空間設計、分析與應用於反向的升壓與降壓型，零電流切換式電容電源轉換器，可以改良在雙向功率流控制時，開關元件的電流應力問題。此轉換器利用四個開關電晶體、一組切換電容和一個小的共振電感，就可以提供 -n 倍和 -1/n 倍的高電壓轉換率。文中提出的零電流切換雙向等化器是一個通用的反向功率流控制方法，它可以用於反向電壓轉換，也可以應用於電池串間不同電壓的電池等化，利用不同電壓轉換率達到加速電池等化。由模擬及實驗結果可證明，反向 2 倍壓對 1/2 倍壓雙向直流對直流轉換器和一倍壓對一倍壓應用於電池等化器的轉換器及等化效能。

關鍵字：零電流切換、切換式電容直流對直流轉換器、
雙向功率流控制、準共振轉換器、電池等化控制。

11. H. S. H. Chung A. Ioinovici, and W. L. Cheung,"Generalized structure of bidirectional switched-capacitor dc/dc converter," *IEEE Trans. on Circuits and Systems-I: Fundamental Theory and Applications*, vol. 50, pp. 743-753, 2003.
12. Y. P. B. Yeung, K. W. E Cheng, D. Sutanto, and S. L. Ho,"Zero-current switching switched-capacitor quasi-resonant step-down converter," *IEE Proceeding, Electric Power Applications*, vol. 149, pp. 111-121, 2002.
13. K. W. E. Cheng,"Dc to dc converter," *U.S. Patent*, 6 853 569 B2, 2005.
14. Y. S. Lee and Y. Y. Chiu,"Zero current switching switched-capacitor bidirectional dc-dc converter," *IEE Proceedings Electric Power Applications*, vol. 152, pp.1525-1530, 2005.
15. M. Shoyama, T. Naka, and T. Ninomiya,"Resonant switched capacitor with high efficiency," *IEEE PESC Conference Record*, vol. 5, pp.3780-3786, 2004.
16. M. Shoyama, F. Deriha, and T. Ninomiya,"Operation analysis and control of resonant boost switched capacitor converter with high efficiency," *IEEE PESC Conference Record*, pp. 1966-1971, 2005.
17. Y. P. Ko, Y. S. Lee, and W. H. Chao,"Analysis, design and implementation of fuzzy logic controlled quasi-resonant zero-current switching switched-capacitor bidirectional converter," *IET Power Electronics*, vol. 6, pp. 683-692, 2011.
18. M. Shoyama and T. Ninomiya,"Output voltage control of resonant boost switched capacitor converter," *IEEE Power Conversion Conference Record*, pp.899-903, 2007.
19. H. Q., J. Zhang, J. S. Lai, and W. Yu,"A High-efficiency grid-tie battery energy storage system," *IEEE Trans. on Power Electronics*, vol. 26, pp. 886-896, 2011.
20. Y. S. Lee, Y. P. Ko, and C. A. Chi,"Multiple output zero-current switching switched-capacitor bidirectional dc-dc converter," *International Journal of Electronics*, vol. 97, pp. 957-971, 2010.

Recevied Oct 25, 2013
Revised Feb 25, 2014
Accepted Feb 25, 2014

high efficiency bidirectional power converter and battery equalization applications under the bidirectional power flow control. When using the proposed QR ZCS EC for the battery strings, each cell can be simultaneously charged / discharged to the end-of-charge voltage with high efficiency.

Reference

1. W. C. Wu and R. M. Bass, "Analysis of charge pumps using charge balance," *IEEE PESC Conference Record*, pp.1491-1496, 2000.
2. Y. P. B. Yeung, K. W. E. Cheng, D. Sutano,"Multiple and fractional voltage conversion ratios for switched-capacitor resonant converters," *IEEE PESC Conference Record*, pp.1289-1294, 2001.
3. Y. C. Lin and D. C. Liaw,"Parametric study of a resonant switched capacitor dc-dc converter," *IEEE TENCON Conference Record*, pp. 710-716, 2001.
4. F. Z. Peng, F. Zhang and Z. Qian,"A magnetic-less dc-dc converter for dual voltage automotive systems," *IEEE Trans. on Industrial Applications*, vol. 39, pp. 511-518, 2003.
5. K. Wang, C. Y. Lin, L. Zhu, D. Qu, F. C. Lee, and J. S. Lai,"Bidirectional dc to dc converters for fuel cell systems, " *Power Electronics in Transportation Conference Record*, pp. 47-51, 1998.
6. Y. P. B. Yeung and K. W. E. Cheng, "Unified analysis of switched-capacitor resonant converters," *IEEE Trans. on Industrial Electronics*, vol. 51, pp. 864-873, 2004.
7. Y. S. Lee and G. T. Cheng,"Quasi-resonant zero current switching bidirectional converter for battery equalization applications," *IEEE Trans. on Power Electronics*, vol. 21, pp. 1213-1224, 2006.
8. Y. S. Lee and M. W. Cheng,"Intelligent control battery equalization for series connected lithium-ion battery strings," *IEEE Trans. on Industrial Electronics*, vol. 52, pp. 1297-1307, 2005.
9. H. S. H. Chung, W. C. Chow, and S. T. S. Lee,"Development of a switched-capacitor dc/dc converter with bidirectional power flow," *IEEE Trans. on Circuits and Systems-I: Fundamental Theory and Applications*, vol. 47, pp. 1383-1389, 2000.
10. A. Ioinovici,"Switched-capacitor power electronics circuits," *IEEE Circuit and System Magazine*, vol. 1, pp. 37-42, 2001.

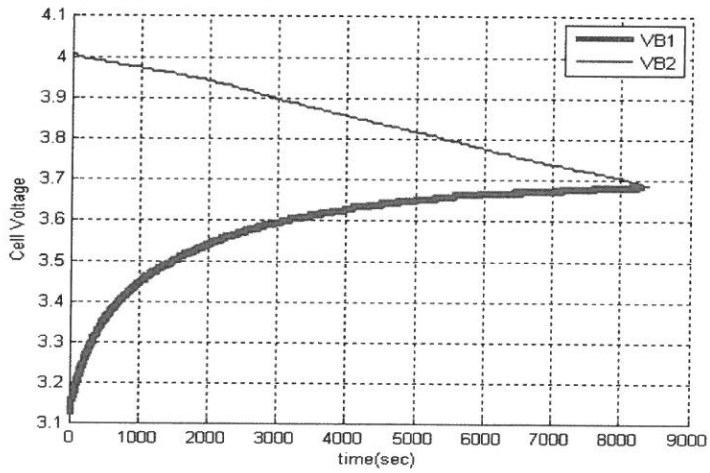

12 (b)

Fig. 12. Experimental results for the battery equalization cell. (a) Inductor current with respect to the driver voltages. (b) Cell voltage trajectories

5. Conclusions

An -n-mode/ -$\frac{1}{n}$ -mode power conversion scheme based on the quasi-resonant zero-current-switching converter theory for a bidirectional converter was investigated using the state space approach. The -2-mode / -$\frac{1}{2}$ -mode and -1-mode / -1-mode power conversion schemes were developed to show the performance of the proposed bidirectional converter and cell balancing control of a series connected battery string, respectively. It was found that the proposed bidirectional converter possesses interesting properties such as reducing the switching loss, increasing the converter efficiency and significantly reducing the MOSFET current stress of the converter. Simulations and experimental results were performed to verify and validate the theoretical analysis of the bidirectional power flow control and cell balancing performance. It was shown that the proposed ZCS SC converter is more suitable for high frequency and

The experimental results for the battery equalization cell that was installed in two-cell lithium-ion battery strings to verify the performance of QR ZCS battery equalizer are shown in Fig. 12. The parameters of the QR ZCS SC battery cell equalizer are L_r = 1μH, C_r = 0.22μF, and f_s = 192.3 kHz. The initial cell voltages are V_{B1} = 4.093(V) and V_{B2} = 3.1(V). Fig. 12 (a) shows the inductor current with respect to the MOSFET gate driver voltages. Figure 12 (b) shows the voltage deviation trajectories between the two cells during the cell equalization processing period. The battery equalizing process will be terminated when each cell simultaneously reaches to the same end-of-charged/discharged voltages.

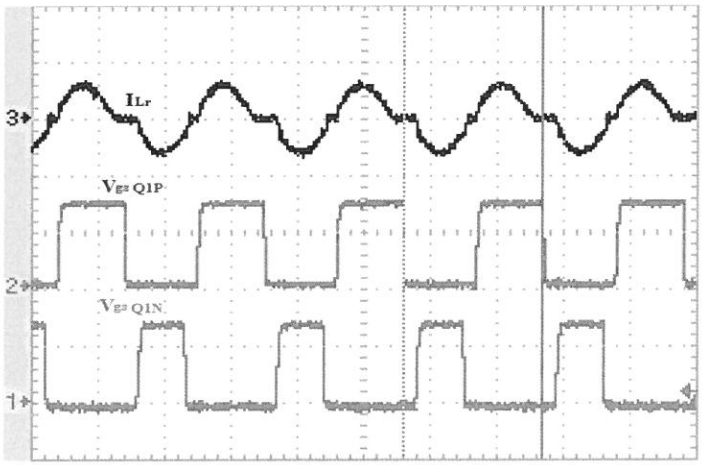

1, 2: 10V/div, 3: 5A/DIV

12 (a)

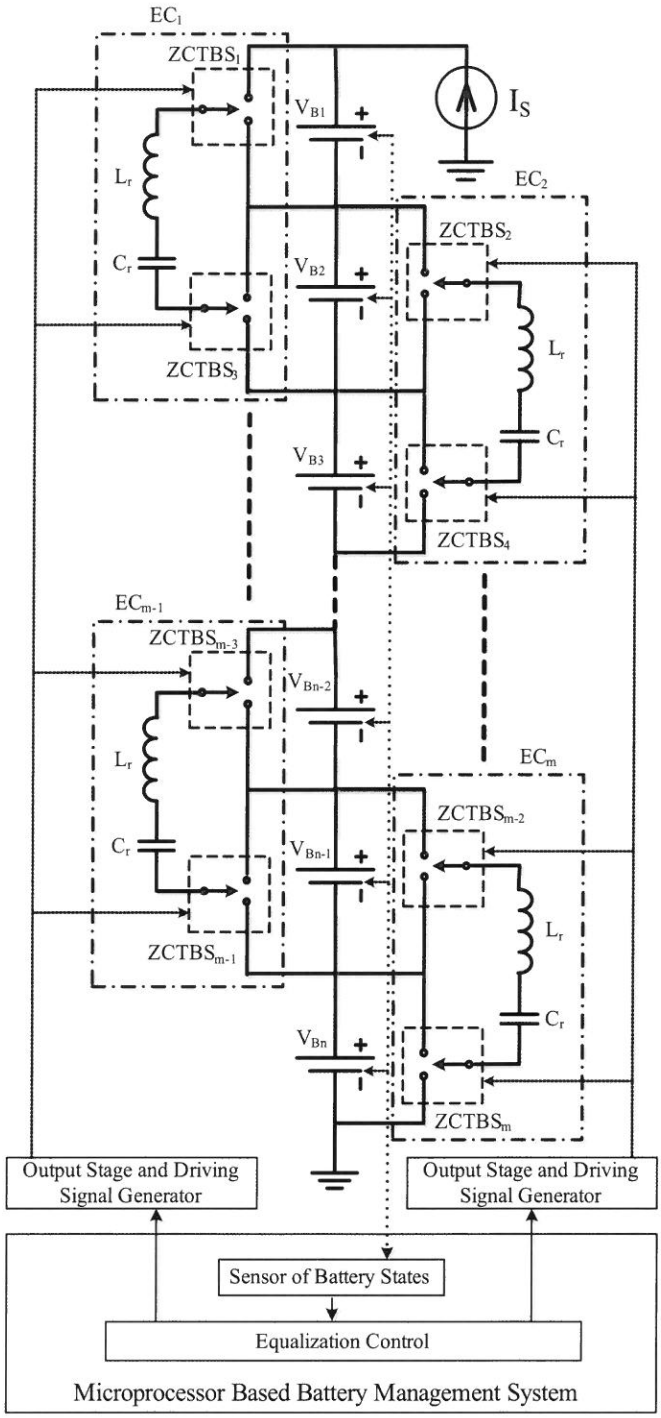

11 (b)

Fig. 11 (a) An inverting type -1-mode/-1-mode ZCS SC QR bidirectional converter, (b) application in battery equalization scheme for BMS

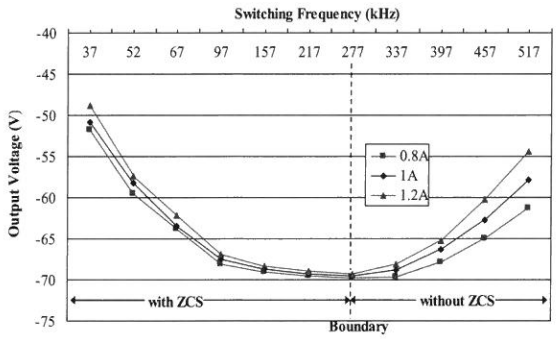

10 (a)

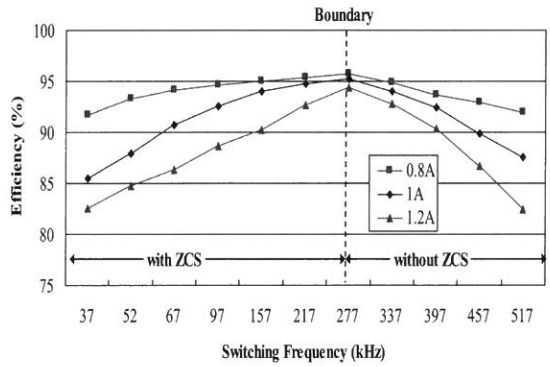

10 (b)

Fig. 10. Characteristics of switching frequency control (a) output voltage versus switching frequency (b) converter efficiency versus switching frequency

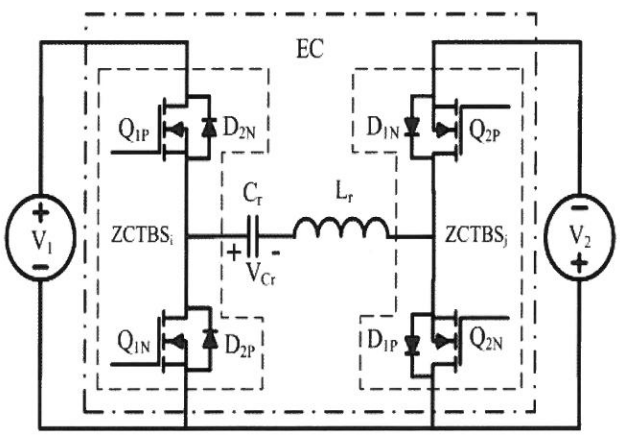

11 (a)

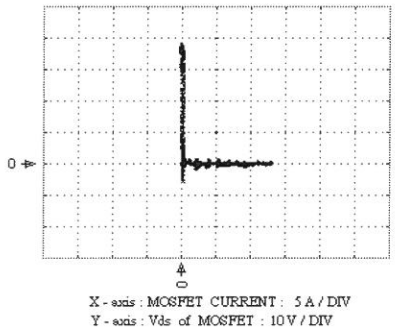

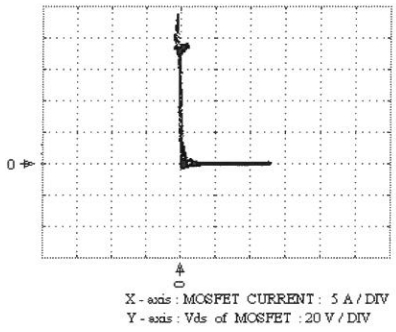

8 (a) 8 (b)

Fig. 8. Experimental switching loci of the main switch in the proposed converter for (a) forward (b) reverse mode

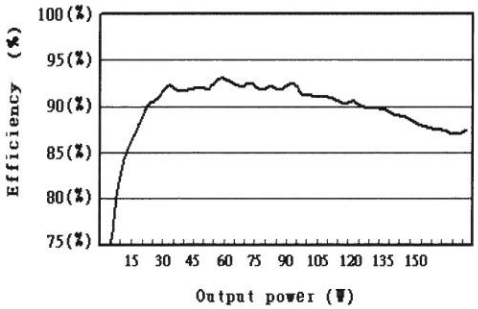

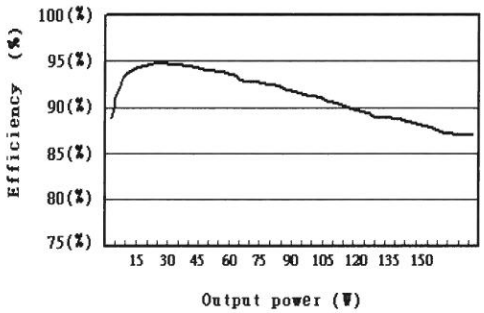

forward power flow reverse power flow

9 (a) 9 (b)

Fig. 9. Experimental efficiency and the corresponding voltage conversion ratio of the -2-mode / $-\frac{1}{2}$ -mode ZCS SC bi-directional converter for (a) forward (b) reverse power flow control

the desired battery equalization applications [7]. Figure 11 (b) shows the proposed converter application in the battery equalization cells (EC) for a series connected battery strings. Where ZCTBSi and ZCTBSj are the single-pole double through bidirectional switches composed of MOSFET switches, (Q_{1P}, D_{2N}, Q_{1N}, D_{2P}) and (Q_{2P}, D_{1N}, Q_{2N}, D_{1P}) in the first set of battery equalizer, EC1, respectively. The cell voltages are controlled by the driving pulse-width modulation (PWM) signals corresponding to the respective cell voltage through the equalization algorithm constructed in the microprocessor based BMS. The proposed battery equalization scheme can reduce the cell voltage deviations and switching losses compared to the conventional equalizing process and maintain safe operations for each cell in the battery strings during the charging/discharging state.

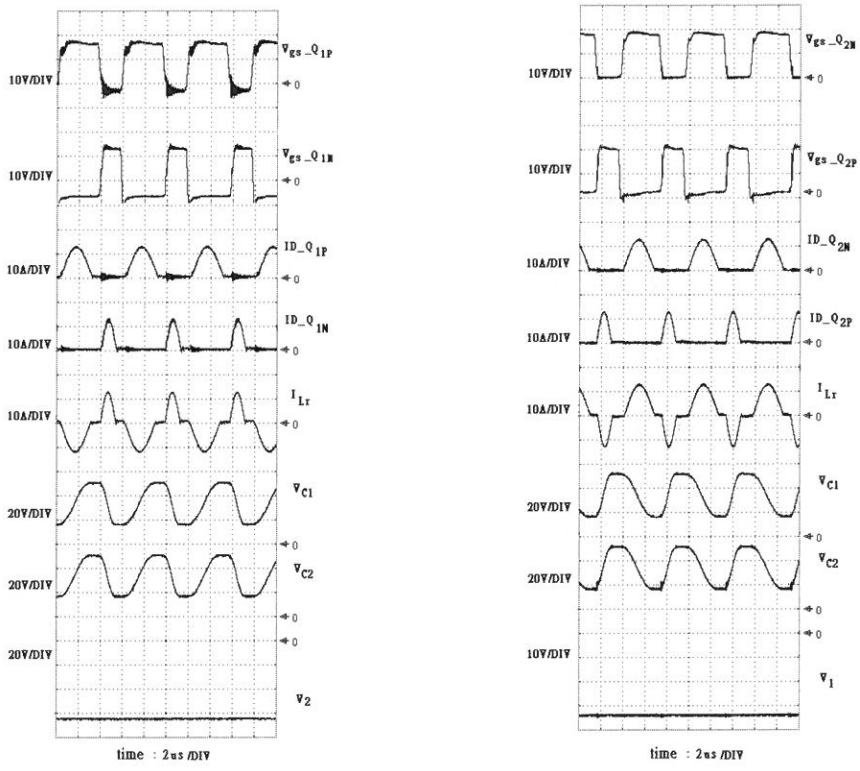

7 (a) 7 (b)

Fig. 7. Experimental results of the double-mode/half-mode ZCS SC dc-dc converter for (a) forward (b) reverse power flow control

Therefore the achieved maximum efficiency in the forward power flow control scheme is lower than that is obtained in the other scheme under the same specified output power.

- The proposed converter scheme is designed to operate as a non-isolation type -n-mode / -$\frac{1}{n}$ -mode bi-directional dc-dc converter for a high voltage conversion ratio power supply applications. The inductor current is operated in a non-symmetrical alternating mode. There is a small dc current component flowing through the inductor that could produce a saturation problem in the choke. It will be considered in selecting high flux magnetic core for the inductor design procedure.
- For high technology power supply applications, only a small magnetic component is required in the bidirectional converter due mainly to the capacitors' stored energy. Therefore, the core size and core losses in the resonant inductor can be reduced.
- The proposed converter only deviates in the low power application due to the switching losses in the parasitic capacitance of the switching devices, which are difficult to accurately estimate.
- The output voltage cannot be regulated by the duty ratio. The designed output voltage is fixed as was the previously mentioned dependent effect. However, the output voltage can be regulated by changing the switching frequency and the closed loop controller can be designed to improve the regulation for meeting the desired specification [15].
- The proposed converter model and the controller design are more difficult to handle than a conventional duty ratio control. The output voltage can be regulated by changing the switching frequency under a wide range of frequency control values [16, 18]. The converter controller design has been addressed in [17].
- The proposed SC ZCS converter is suitable use for fixed gain load system without need to use for accuracy voltage regulation load system. And the related cost to pay for achieving ZCS is only adding one small inductor cost.

The proposed schemes can be applied to many other topologies, such as an inverting type bidirectional converter that can be used in the battery equalization applications for battery management systems [7]. Figure 11 (a) shows the inverting type ZCS switched-capacitor bidirectional converter for designed in -1-mode/-1-mode (n=1). The battery equalization cell (EC) contains the four main switches and a small resonant inductor and capacitor in the converter circuit. The switching sequence (Q_{1P}, Q_{1N} and Q_{2P}, Q_{2P}) in the bidirectional converter are controlled using the gate driving stages of the battery management system (BMS) to meet

using the frequency modulation method, the output voltage is controlled for improving the voltage regulations. The output voltage is regulated by changing the switching frequency under a wide range frequency control [18]. Figure 10 (a) shows the converter output voltages with respect to the switching frequency under various load current for the forward power flow control scheme. The maximum output voltage will occur when the switching frequency f_s is matched with the resonant frequency f_0. These voltages incessantly decrease when $f_s < f_0$ and they are dependent on the output current I_o. The proposed converters are operated at zero-current switching states for the mentioned two situations. Fig. 10(b) shows the corresponding converter efficiency under the mentioned frequency controlled situation. The analysis and design of the closed loop controller remain for further study and will be submitted in the near future. The measured output voltages of the proposed converter under full load condition are -65.3(V) and 33.5(V) in various directional modes, respectively. The output voltage measurements are slightly less than the designed values due to the practical voltage drop caused by the ESRs of the devices in the bidirectional converter. The average efficiency of the forward and reverse power flow control converter under various load conditions is higher than 87%. Some observations of the proposed ZCS SC bidirectional converter can be summarized as follows:

- In the hard-switching designed converters, the switching losses are increased proportional to the converter switching frequency. The proposed converter is designed to operate at zero-current soft switching. The power MOSFETs are turned on and off in the zero-current state to minimize the switching losses. Therefore, the total switching loss and EMI emissions can be significantly reduced. And the switching frequency can be further increased under properly selected the semiconductor switch devices with the fast responding, low parasitic capacitors.
- The current stresses on the MOSFETs are significantly reduced, compared to the conventional switched capacitor converter.
- The maximum efficiency can achieve about 93% and 95% for the forward and reverse power flow control schemes, respectively. The maximum efficiencies are different in the forward and reverse power flow control scheme. Because there are many differences in the actual input/output voltages, enabling semiconductor devices, and the flowing currents in the two power flow control schemes. The enabled MOSFET switches and diodes in this forward control process are greater in number than those are enabled in the reverse control scheme.

resistance (ESR) drop of the active and passive devices in the converter loop.

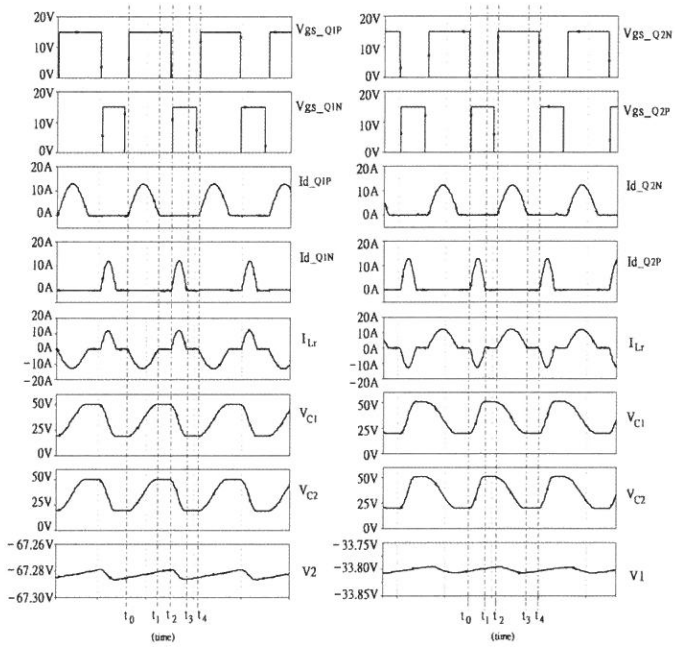

6 (a) 6 (b)

Fig. 6. Simulation waveforms of the double-mode/half-mode ZCS SC dc-dc converter for (a) forward (b) reverse power flow control

Figures 7 (a) and 7 (b) show the experimental results for the corresponding waveforms of the proposed converter under the forward and reverse power flow control mode, respectively. The experimental switching loci of the main switch in the proposed converter for the forward and reverse power flow control schemes are shown in Figs. 8(a) and 8 (b), respectively. It is shown that the proposed ZCS SC bi-directional converter is designed to operate in the zero-current-switching mode to reduce the MOSFET switch power losses. Figures 9 (a) and 9 (b) plot the curves of the converter' s efficiency and the corresponding voltage conversion ratio for the experiments under the forward and reverse modes. There are some reductions in the voltages by around 11.6~12.1% due to the ESR losses and drop in the converter circuit loop. The output voltage is not exactly constant but is slightly dependent on the load. The output voltage characteristics are similar to those of the sinusoidal resonant converters [15,16]. By

4. Simulation and Experimental Results

To verify and validate the performance of the proposed ZCS SC QR bi-directional dc-dc converter, simulations using PSpice software and experiment were carried out for the proposed double-mode/ half-mode (n=2) inverting type ZCS SC dc-dc converter shown in Fig. 5. The power semiconductor devices and the designed parameters are listed as follows: MOSFET switches are IRF3710, Schottky diodes are SBL1060CT (D_{1N} and D_{1P}), and MBR10100CT (D_{2N}, D_{2P}, D_a, D_b, and D_{ab}), $C_1=C_2= 0.33\,\mu F$, f_s = 170 kHz(T_S=5.88μsec), the duty ratios are $Đ_{1P}$ = 0.66(3.88μs) and $Đ_{1N}$ = 0.33(1.94μs), and the duty ratio of the dead time is 0.01(0.059μs) , and the output power is P_o = 120 (W). In one switching period $Đ_{1P}$ turn-off time is 2μs and $Đ_{1N}$ turn-off time is 3.94μs. The dead time select is 1% of switching time, to avoid the short through in switches Q_{1P} and Q_{1N} and to provide maximum MOSFET switching time in one switching period. The input voltages are V_1 = 36 (V) and V_2 = -72 (V) for forward and reverse power flow control, respectively. According to the zero-current switching conditions of the converter, we can derive the design criteria $Đ_{1P}T_S \geqq \pi/\omega_1= \pi\,(L_rC_{S1})^{1/2}$ and $Đ_{1N}T_S \geqq \pi/\omega_3= \pi\,(L_rC_{S3})^{1/2}$.where $C_{s1}=nC_1=2C_1$ and $C_{s3}=C_1/n=C_1/2$. From the given parameters, $T_S=1/f_s=5.88\,\mu$ sec and $C_1=C_2=0.33\,\mu$ F. The resonant inductance should be satisfied $L_r < 2.3\,\mu$ H, we choose the resonant inductance $L_r=1\,\mu$ H to guarantee that the proposed converter is operated at zero-current switching. The proposed converter scheme control method is open loop control system. The effect on the output voltage control for such open-loop control system is that the output voltage regulation cannot accuracy control.

The closed loop control methodology is composed of a compensated controller and a resonant-mode power supply controlled integrated circuit containing a voltage controlled oscillator, a zero-crossing terminated one-shot timer and steering logic and drivers. It will force the output voltage to follow the voltage reference V_{1ref} or V_{2ref} by using the synchronized-switching cross-over-switches. The driving circuit comprises a logic circuit and amplifier to generate the gate trigger signals to drive the switches. Figures 6 (a) and 6 (b) show the simulation results of the proposed double-mode and half-mode ZCS SC converter, respectively. The simulation output voltages of the bidirectional converter in full load condition are -64.48(V) and 32.11(V) under forward and reverse power flow control schemes, respectively. The output voltages of the proposed converters are slightly less than the designed values due to the equivalent series

time, Q_{1N} and $Q_{12},\cdots, Q_{n\text{-}2\ n\text{-}1}$ are turned off at zero current state where $t = t_4$. Let the duty ratio of Q_{1P} and Q_{1N} be denoted by $Đ_{1P}$ and $Đ_{1N}$, respectively. The zero current switching conditions of Q_{1P} and Q_{1N} are then obtained as $Đ_{1P}T_S \geqq \pi/\omega_1$ and $Đ_{1N}T_S \geqq \pi/\omega_3$, where T_S is the switching duty of the proposed bi-directional converter.

Figures 4(a)-4(d) show the alternating equivalent circuits of the proposed -$\frac{1}{n}$-mode bi-directional converter under the reverse power flow control scheme. In stage 1 (Fig. 4(a); $t_0 < t < t_1$): When Q_{2P} is turned on at $t = t_0$, then D_{1N} and $D_{12},\cdots, D_{n\text{-}2\ n\text{-}1}$, are forced to turn on, the sources V_1 and V_2, $C_1,C_2,\cdots$, and C_n are series connected with the switches, Q_{2P} and $D_{12},\cdots$, $D_{n\text{-}2\ n\text{-}1}$, and the resonant inductor L_r. Therefore, the energy is stored to the C_1, $C_2,\cdots$, and C_n through the L_r - C_S resonant tank circuit. The dynamic state equation for stage 1 is the same as (4) with the negative state variables $I_{Lr}(t)$ and $V_C(t)$. In stage 3 (Fig. 4(c); $t_2 < t < t_3$): The main switch Q_{2N} is turned on at $t = t_2$, the diodes D_{2N}, D_1, $D_2,\cdots$, and D_n are then forced to turn on. The stored electric energy in the parallel capacitors $C_p=C_1+C_2+\cdots+C_n = nC$ is discharged into the source V_1 through the switch Q_{2N}, and the diodes D_{2N}, D_1, $D_2,\cdots$, and D_n. The dynamic state equation in this interval is the same as (1) with the negative states. The analytical procedure is similar to that for the bidirectional converter in the forward power flow control and is omitted in this paper.

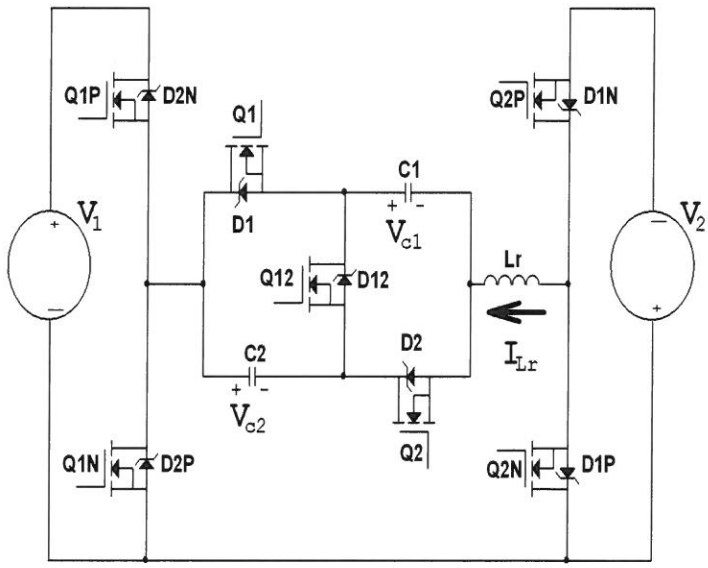

Fig. 5. Circuit realization for the proposed double-mode/half-mode ZCS SC bi-directional converter

Stage 2 (Fig. 3(b); $t_1 < t < t_2$):The main switch Q_{1P} and switched-capacitor switches Q_1, Q_2,$\cdots$, Q_n are still turned on, and the diode D_{1P} cannot reverse into negative current which ceases the current reversing in this interval. The inductor current will still stop at zero state until $t \leqq t_2^-$. The states in this stage are $I_{Lr}(t) = 0$ and $V_{C1}(t) = V_{C2}(t) = \cdot\ \cdot\ \cdot = V_{Cn}(t) = V_C(t) = V_{C02}$.

Stage 3 (Fig. 3(c); $t_2 < t < t_3$): When Q_{1N} and Q_{12}, $\cdots$, $Q_{n\text{-}2\ n\text{-}1}$ are turned on at $t = t_2$, the V_1, C_1, C_2,$\cdots$, and C_n are series connected with the switches, Q_{1N} and Q_1, Q_2,$\cdots$, Q_n, and the resonant inductor L_r. Therefore, the stored energy is transferred into the source V_2 through the L_r - C_{S3} resonant tank circuit. The dynamic state equation in this interval can be expressed by

$$\begin{bmatrix} L_r & 0 \\ 0 & C \end{bmatrix} \begin{bmatrix} \frac{dI_{Lr}(t)}{dt} \\ \frac{dV_c(t)}{dt} \end{bmatrix} = \begin{bmatrix} 0 & -(n-1) \\ -1 & 0 \end{bmatrix} \begin{bmatrix} I_{Lr}(t) \\ V_c(t) \end{bmatrix} + \begin{bmatrix} 0 & -1 \\ 0 & 0 \end{bmatrix} \begin{bmatrix} V_1 \\ V_2 \end{bmatrix} \tag{4}$$

where $C=C_1=C_2 = \cdot\ \cdot\ \cdot = C_n$, the resonant angular frequency in stage 3 is $\omega_3 = 2\pi f_3 = 1/\sqrt{L_r C_{S3}} = 1/\sqrt{L_r C/n}$, $C_{S3} = 1/(\frac{1}{C_1} + \frac{1}{C_2} + \cdots + \frac{1}{C_n}) = \frac{C}{n}$, the normalized impedance is $Z_{r3} = \sqrt{L_r/C_{S3}}$ and I_2 is the output current of the converter. The initial conditions of the differential equations are $I_{Lr}(t_2)=0$, and $V_{C1}(t_2)=V_{C2}(t_2)= \cdot\ \cdot\ \cdot = V_{Cn}(t_2)=V_C(t_2)=V_{C02}$. The solutions of (4) can be obtained as

$$I_{Lr}(t) = \frac{\left(V_{c02} - \frac{V_2}{n}\right)}{Z_{r2}} \sin\omega_2(t-t_2) = \frac{\pi I_2 f_2}{f_S} \sin\omega_2(t-t_2) \tag{5}$$

$$V_c(t) = \frac{V_2}{n} + \left(V_{c02} - \frac{V_2}{n}\right) \cos\omega_2(t-t_2) \tag{6}$$

The inductor current will decrease along the sinusoidal function to the negative peak value and continuously fall to zero at $t = t_3$. After I_{Lr} resonates back to zero, diodes D_{1N} and D_{1P} are biased in reverse and this operation stage is terminated.

Stage 4 (Fig. 3(d); $t_3 < t < t_4$): In this interval, the inductor current will stay in zero current state, the states are $I_{Lr}(t)=0$ and $V_{C1}(t) = V_{C2}(t) = \cdots = V_{Cn}(t) = V_C(t) = V_{C03}$. After a specified

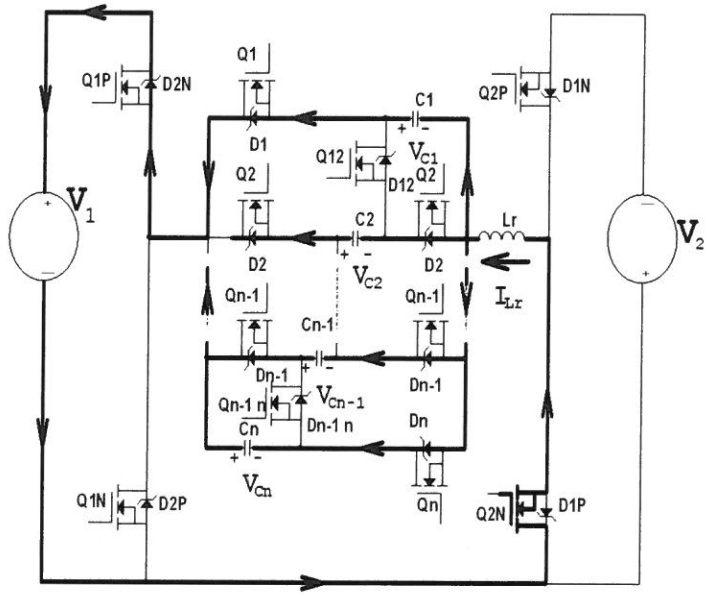

4 (c)

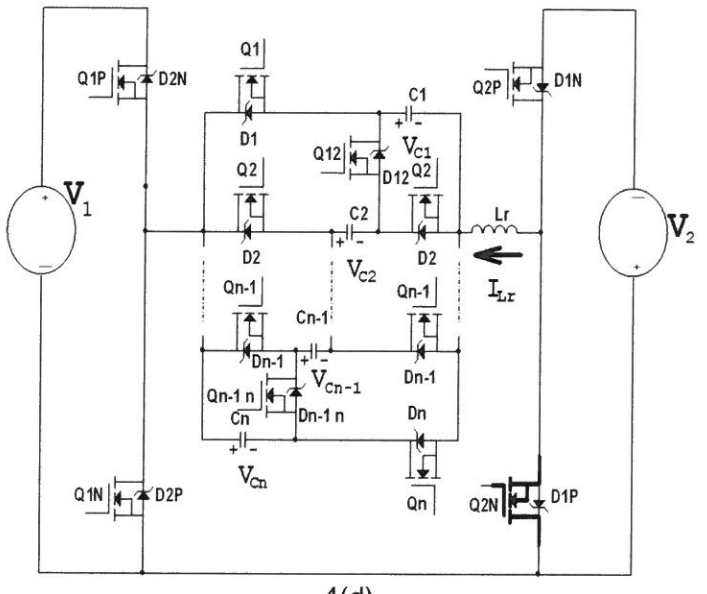

4(d)

Fig. 4. Equivalent circuit of various operation stages for $-\frac{1}{n}$ -mode ZCS SC bi-directional dc-dc converter with reverse power flow for, (a) $t_0<t<t_1$ (b) $t_1<t<t_2$ (c) $t_2<t<t_3$ (d) $t_3<t<t_4$

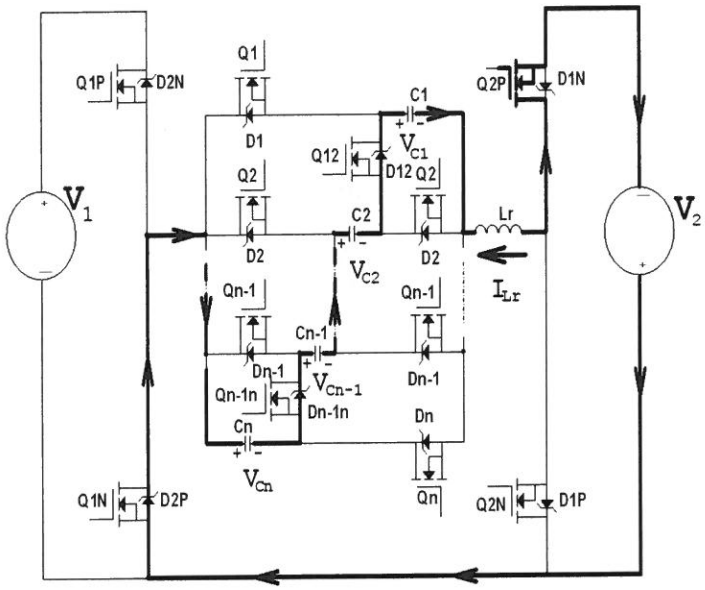
Q1P
D2N
Q1
D1
Q12
C1
V_{C1}
D12
Q2P
D1N
Q2
Q2
C2
Lr
V_1
V_2
D2
D2
V_{C2}
I_{Lr}
Qn-1
Qn-1
Cn-1
Dn-1
V_{Cn-1}
Dn-1
Qn-1n
Dn-1n
Dn
Cn
V_{Cn}
Qn
Q1N
D2P
Q2N
D1P

4 (a)

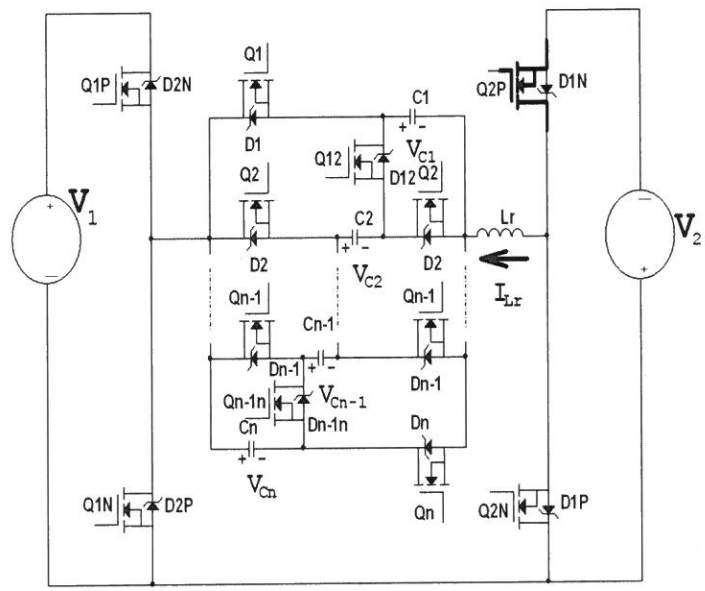
Q1P
D2N
Q1
D1
Q12
C1
V_{C1}
D12
Q2P
D1N
Q2
Q2
C2
Lr
V_1
V_2
D2
D2
V_{C2}
I_{Lr}
Qn-1
Qn-1
Cn-1
Dn-1
V_{Cn-1}
Dn-1
Qn-1n
Dn-1n
Dn
Cn
V_{Cn}
Qn
Q1N
D2P
Q2N
D1P

4(b)

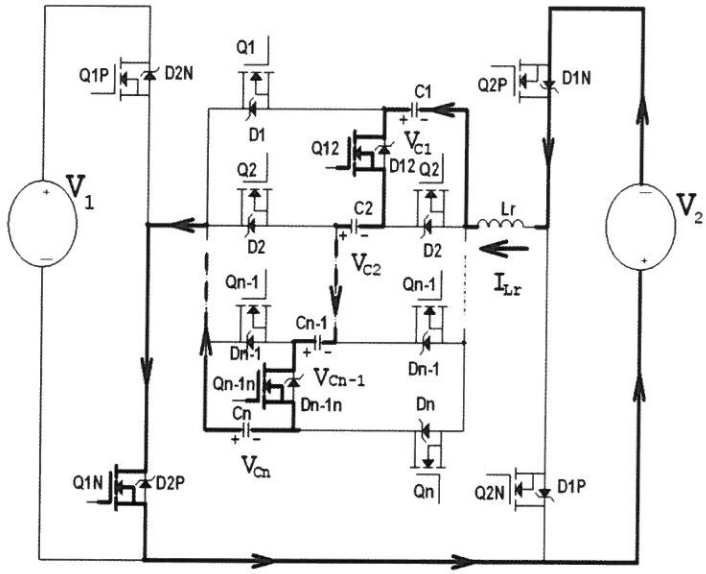

3 (c)

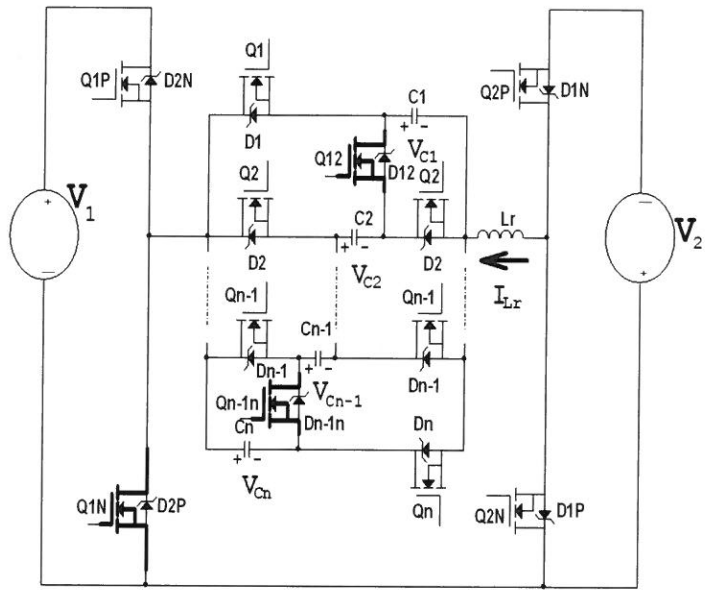

3 (d)

Fig. 3. Equivalent circuit of various operation stages for -n-mode ZCS SC bi-directional dc-dc converter with forward power flow for, (a) $t_0<t<t_1$ (b) $t_1<t<t_2$ (c) $t_2<t<t_3$ (d) $t_3<t<t_4$

, where CS1 = C1+C2+···+Cn = nC, f_s is the switching frequency of the converter, the normalized impedance is $Z_{r1} = \sqrt{L_r/C_{S1}}$, and I_2 is the output current of the converter. The inductor current $I_{Lr}(t)$ will increase to reach the peak value and substantially decrease to zero at $t = t_1$.

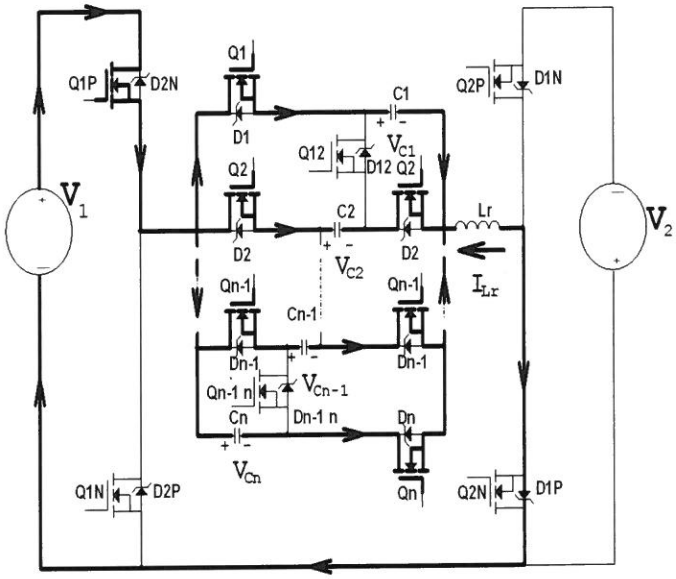

3 (a)

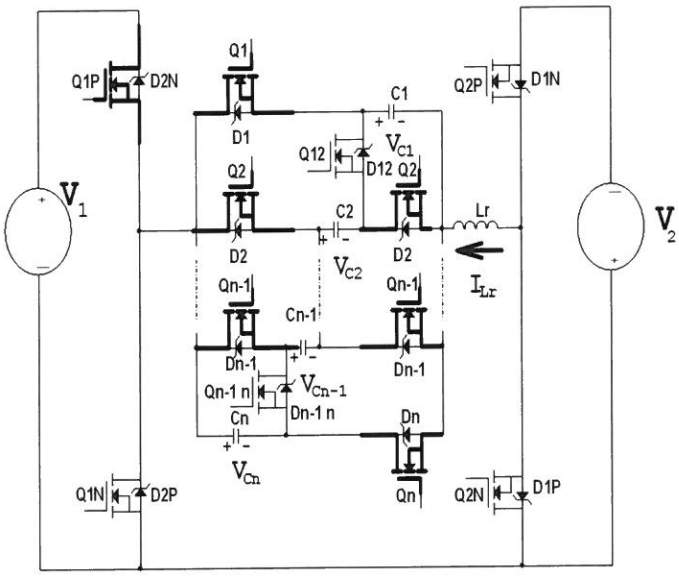

3 (b)

3. State Space Analysis

The equivalent circuit, shown in Fig. 2(b), for the proposed non-inverting type -n-mode/ $-\frac{1}{n}$ -mode ZCS SC bidirectional converter is depicted in Figs. 3(a)-3(d) and Figs. 4(a)-4(d) under the forward and reverse power flow control scheme, respectively. Some assumptions are necessary to analyze the dynamic circuit operation: (i). the resonant inductor Lr is a small inductance with negligible equivalent series resistance (ESR), (ii). the semiconductor switches and diodes are ideal, (iii). the capacitors in the switched-capacitor bank are ideal.

The resonant current ILr is controlled by the MOSFET switches Q1S and Q2S for the forward and reverse power flow control modes, respectively. The direction of the controlled current is determined according to the switched-capacitor charging/discharging situation and/or the desired power flow control orientation for the converter system. The detailed equivalent circuits for the proposed converter scheme are shown in Figs. 3(a)-3(d) at different time intervals under forward power flow control mode. The state space dynamics of all operation modes are easily analyzed in the following stages:

Stage 1 (Fig. 3(a); $t_0 < t < t_1$): The main switch Q_{1P} and switched-capacitor switches Q_1, Q_2,$\cdots$, Q_n are turned on at $t = t_0$, the source V_1 provides current through MOSFET switch Q_{1P}, D_{1P}, the paralleled C_1,$\cdots$, C_2, and C_n, and the resonant reactance L_r stores the electric energy in the capacitors $C_1 = C_2 = \cdots = C_n = C$. The dynamic state equation in this interval is given by

$$\begin{bmatrix} L_r & 0 \\ 0 & nC \end{bmatrix} \begin{bmatrix} \frac{dI_{Lr}(t)}{dt} \\ \frac{dV_C(t)}{dt} \end{bmatrix} = \begin{bmatrix} 1 & 0 \\ 0 & 0 \end{bmatrix} \begin{bmatrix} I_{Lr}(t) \\ V_C(t) \end{bmatrix} + \begin{bmatrix} 1 & 0 \\ 0 & 0 \end{bmatrix} \begin{bmatrix} V_1 \\ V_2 \end{bmatrix} \tag{1}$$

with the initial conditions $I_{Lr}(t_0)=0$ and $V_{C1}(t_0)=V_{C2}(t_0)=\cdots=V_{Cn-1}(t_0)=V_c(t_0)=V_{C01}$. The solutions of (1) can be obtained as

$$I_{Lr}(t) = \frac{V_1 - V_{c01}}{Z_{r1}} \sin \omega_1 (t - t_0) = \frac{-\pi I_2 f_1}{f_S} \sin \omega_1 (t - t_0) \tag{2}$$

$$V_c(t) = V_1 + (V_{c01} - V_1) \cos \omega_1 (t - t_0) \tag{3}$$

where the resonant angular frequency in stage 1 is $\omega_1 = 2\pi f_1 = 1/\sqrt{L_r C_{S1}} = 1/\sqrt{L_r nC}$

The following sections of this paper will analyze the proposed non-inverting type -n-mode/ $-\frac{1}{n}$ -mode ZCS SC bidirectional dc-dc converter.

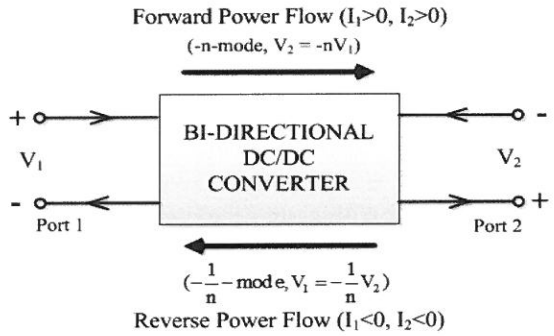

2 (a)

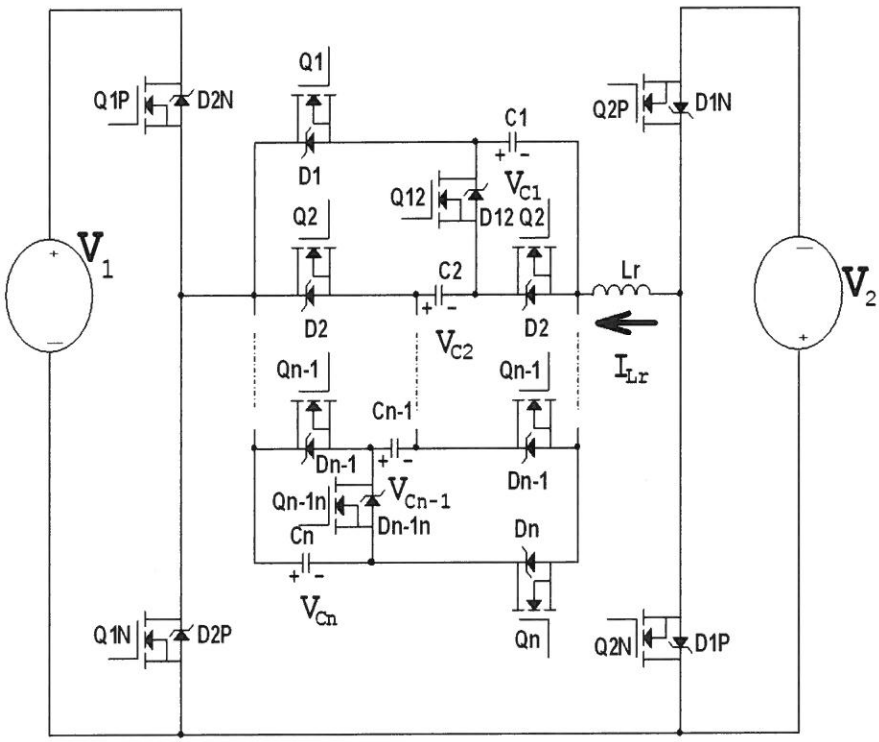

2 (b)

Fig. 2. -n-mode/ $-\frac{1}{n}$ -mode ZCS SC bi-directional dc-dc converter (a) block diagram, (b) realized circuit configuration

developed based on the ZCS SC QR converter theory. The proposed switching topologies and the switched-capacitor bank ensure bidirectionality in the current flow while maintaining the negative polarity of the dc voltage at either end unchanged. The energy is transferred from port 1 to port 2, called forward power flow control, the output voltage V_2 equals $-nV_1$ which is called -n-mode dc-dc converter. If the energy is transferred from port 2 to port 1, it is called reverse power flow control, the output voltage V_1 equals $-\frac{1}{n}V_2$ which is called $-\frac{1}{n}$-mode dc-dc converter. The circuit is composed of four MOSFET main switches paralleled with Schottky diodes. Only a very small inductor series connected with a set of switched-capacitors is needed to construct the resonant tanks in the converter. The resonant inductor L_r is connected in series with a set of switching capacitors comprised of C_1, C_2,$\cdots$, and C_{n-1} to achieve resonant characteristics by controlling the switches during the operating interval. The forward power flow control can be achieved by switching on one of the switches (Q_{1P} and Q_{1N}) according to the proposed switching sequence in the specified interval, as shown in Fig. 3. Switching on one of the switches (Q_{2P} and Q_{2N}) can achieve reverse power flow control in the same interval according to the proposed switching sequence shown in Fig. 4. The switches can be designed to switch on and -off at the zero-current state while the L_r-C resonant current is rising and falling to zero to achieve zero current switching for reducing the MOSFET switch power losses. The switches Q_1, Q_2,$\cdots$, Q_n and Q_{12},$\cdots$, $Q_{n-2\ n-1}$ are used to control the switched-capacitors, connecting them either in parallel or series, during the charging or discharging state, respectively. Figure 3 shows a non-inverting type step-up ZCS SC dc-dc converter under various operation stages. Turned on/off switches Q_{1P} or Q_{1N} and the switched-capacitor switches Q_1, Q_2,$\cdots$, Q_{n-1} or Q_{12},$\cdots$, $Q_{n-2\ n-1}$ can control the forward power flow from the source V_1 to the other source V_2 as a -n-mode converter (i.e. $V_2 = -nV_1$) shown as Figs. 3(a)-3(d). The turned on/off switches Q_{2P} or Q_{2N} and the switched-capacitor switching diodes D_1, D_2,$\cdots$, D_n or D_{12},$\cdots$, $D_{n-2\ n-1}$ can also control the reverse power flow from V_2 to V_1 as a trisection mode converter (i.e. $V_1 = -V_2/n$) shown in Figs. 4(a)-4(d). When the resonant current I_{Lr} increases to a peak value and decreases to zero current, it cannot reverse into negative current because there is a diode in the resonant circuit loop of the converter that ceases current reversal and maintains the current at zero until the next switching time. It also enables the MOSFET switch to switch on at zero current to reduce the switching losses. Figures 3(a)-3(d) and Figs. 4(a)-4(d) show the equivalent circuit of the proposed non-inverting type ZCS SC bidirectional dc-dc converter with forward and reverse power flow control scheme under the various operating time intervals, respectively.

capacitor -n-mode /- $\frac{1}{n}$ -mode bidirectional dc-dc converter are elucidated in sections 2 and 3, respectively. Section 4 demonstrates the simulations corresponding to the research experiments for the proposed converter under n = 2 and the application in the cell equalization for the series connected battery strings. The switching loss and efficiency are proposed in graphic form as well. In addition, the output voltage control using the frequency modulation method is addressed in this section. The conclusion is described in section 5.

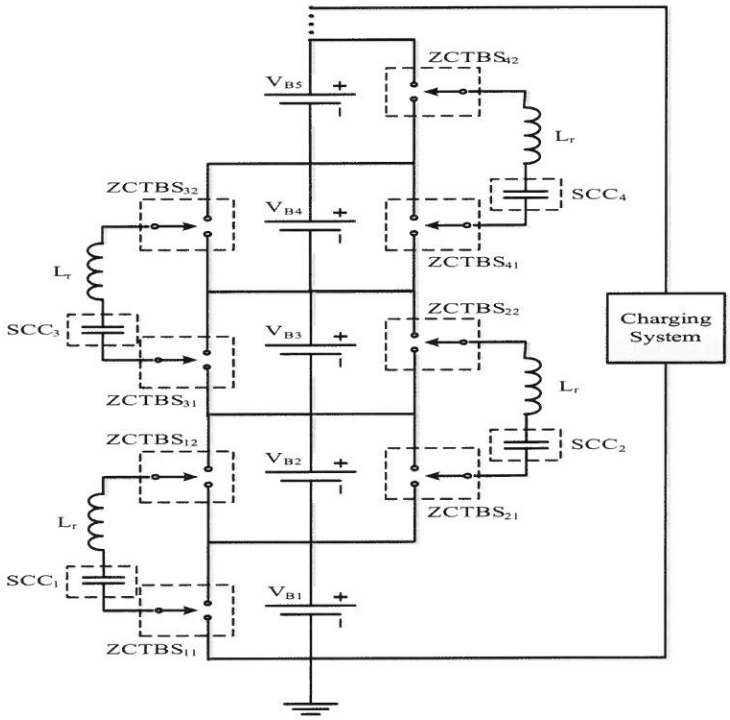

Fig. 1. Quasi-resonant zero current transient bidirectional switches for cell balancing control of a abttery string

2. Topologies Description

Figures 2 (a) and 2 (b) show the block diagram and realized circuit configuration of the proposed inverting type -n-mode/- $\frac{1}{n}$ -mode ZCS SC bi-directional converter, respectively. It was

proposed in [13]. The non-inverting-type zero-current switching switched-capacitor bidirectional converter is proposed in reference [14]. It cannot be used in the cell balancing control schemes for a series connected battery string. The proposed zero-current switching bidirectional converter is a generalized structure with the inverting power flow control scheme that can be applied to the battery balancing control applications for a series connected battery string. The converter scheme can achieve zero current soft switching and reduce the MOSFET switches power losses to increase the converter efficiency. The high switching current stresses can also be reduced under the bi-directional power flow control schemes. The proposed non-isolation bidirectional converter is designed for a voltage conversion ratio -n / $-\frac{1}{n}$ under various control strategies of the switched-capacitor networks. The inverting type converters are designed with fixed gain from -n to -1/n. They are suitable for fixed gain and low noise inverting type power supply applications. Because the proposed converters can be designed to operate at zero-current soft switching under quasi resonant condition, the switching losses and EMI noise are suppressed. The converter efficiency is improved in comparison with the conventional switched-capacitor converter. The output voltage can be regulated using the frequency modulation under a specified load variation when the switching frequency (f_s) is selected less than the resonant frequency (f_r). Two designed experiments for the inverting ZCS SC converters were conducted to verify and validate the predicted performance of the bidirectional power flow control and application in cell balancing control of a series connected battery string.

Figure 1 shows a battery charging system configuration for a series connected battery stack with the quasi-resonant zero current switching bidirectional converter for cell balancing control. Much literature has discussed battery string equalization [7-8]. An integrated infrastructure for these cell voltage balancing schemes is particularly necessary in modern battery management systems [19, 20]. The nondissipative current diverter cell balancing control scheme is a bidirectional converter with a switched capacitor cell bank (SCC) and a small series connected inductor (L_r) to obtain the soft switching in the zero-current transient bidirectional switches (ZCTBS). The bidirectional cell balancing control scheme has many advantages such as higher equalization efficiency for zero current switching, bidirectional energy transformation capability and a modular design approach [7]. The cell voltage balancing speed and efficiency of the proposed converter are therefore higher than using the conventional flying capacitor cell balancing control scheme for battery equalization applications.

Theoretical analysis and the operating principle for the inverting quasi-resonant switched-

1. Introduction

The switched-capacitor dc-dc converter is a non-magnetic converter that requires only a capacitor bank and MOSFET switches in the power stage. This converter has the following features: light weight, smaller size and fabrication on a semiconductor integrated circuit chip. However, the larger switching loss and current stress are the essential drawbacks in the conventional high frequency switching dc-dc converter [1-3]. Quasi-resonant converters that are able to operate at constant switching frequency with zero-current or zero-voltage switching (ZCS or ZVS) have been used to reduce the switching loss in the converter to overcome the aforementioned problems. This work presents a new zero-current switching switched-capacitor quasi-resonant (ZCS SC QR) converter that can operate at high switching frequency with less switching loss for increased converter efficiency with fewer switches [2, 3]. Although the ZCS SC QR converter has numerous advantages, its power flow control is only unidirectional.

Bidirectional dc-dc power conversion is of great interest in systems fed by dc power including electric vehicles hybrid energy systems, fuel-cell systems, aerospace systems, and telecom systems [4-6]. The bidirectionality in these applications involves current flow while the polarity of the dc voltage at either end remains unchanged.

This device is applied in battery equalization schemes where the stronger energy of this system is transferred into a weaker energy subsystem using the bidirectional power flow control scheme [7,8]. A class of soft switching bi-directional dc-dc converters is the expected candidate for applications such as uninterruptible power supply (UPS), battery charging and discharging control in telecom power systems, HEV auxiliary power supply, and dual voltage automotive systems [6, 8]. A switched capacitor based bi-directional dc-dc converter providing the step-down/step-up voltage capability is proposed in [9-10]. The input/output current pulsating peaks of the bidirectional SC converter are mitigated but the switching losses and the overall converter efficiency are not significantly improved [11-17]. A double-mode boost type resonant switched-capacitor converter with synchronous rectifiers and the output voltage control method are proposed and addressed in [18].

This paper presents a non-isolation switched-capacitor quasi-resonant bidirectional dc-dc converter designed to operate at -n-mode/ -mode and constant frequency. A study of the fundamental scheme for the inverting type ZCS switched-capacitor bidirectional converter is

State Space Analysis and Implementation of Inverting ZCS Bidirectional Converter for Battery Equalization Application

*Yuang-Shung Lee[12a)], Ming-Wang Cheng[1b)] and Yin-Yuan Chiu[2a)]

[1] *Graduate Institute of Applied Science and Engineering, Fu-Jen Catholic University*
[2] *Department of Electrical Engineering Fu-Jen Catholic University*
510 Chung-Cheng Rd., Hsin-Chuang Dist., New Taipei City 24205, Taiwan
Tel: +886-2-29031111-3791 Fax: +886-2-29042638
[a)] *002877@mail.fju.edu.tw* [b)] *m.w.cheng@hotmail.com*

Abstract

The proposed non-isolation zero-current switching switched-capacitor (ZCS SC) dc-dc converters are with an inverting bidirectional power flow control conversion scheme. The state space approach to the design, analysis and applications of the inverting ZCS SC step-up/step-down bidirectional converters are presented that can improve the current stress problem during bidirectional power flow control processing. It can provide a high voltage conversion ratio of -n /- $\frac{1}{n}$ (-n-mode/- $\frac{1}{n}$ -mode) using four power MOSFET main switches, a set of switched-capacitors and a small resonant inductor. The proposed zero-current switching bidirectional converter is a generalized structure with an inverting power follow controlled scheme. It can be used in the inverting type power supply applications, and also be applied to the cell balancing control applications for a series connected battery string under different voltage conversion selections for properly speeding-up the balancing process. Simulation and experimental results are carried out to verify the performance of the proposed inverting type double-mode/half-mode bidirectional dc-dc converter, and the one-mode/one-mode converter applied in battery cell balancing control.

Key words: Zero current switching, switched-capacitor dc-dc converter, bidirectional power flow control, quasi-resonant converter, battery cell balancing control

* To whom all correspondence should be addressed.

使用差動差分電流傳輸器和電流隨耦器合成電流式二階泛用濾波器

鄞永昌　劉鴻裕

輔仁大學電機工程學系

摘　要

本文提出一個新型電流式泛用二階濾波器。這個電路使用了四個差動差分電流傳輸器和二個電流隨耦器當主動元件配合一些接地電容與接地電阻當被動元件。此濾波器結構可合成低通，高通，帶通，帶拒和全通濾波器五種濾波器。而且此濾波器具有許多優良特性，如：低的被動靈敏度，品質因素與中心頻率為正交且透過接地電阻亦為可調，較少的電壓軌跡誤差等等之優良特性。另外由於所有的被動元件都接地，所以本新結構二階電流式濾波器適合合成積體電路。最後本文以三個實驗驗證本文之理論預測。

關鍵字：差動差分電流傳輸器，電流隨耦器，靈敏度，主動濾波器，類比電路設計，連續時間濾波器。

23. H.O.Elwan and A.M.Soliman, "Novel CMOS differential voltage current conveyor and its applications" , IEE Proceding-Circuits Devices System, No.144, 1997, pp.195-200
24. M. BIALOKOW, , and NEWCOMB, R. W.: 'Generation of all finite linear circuits using the integrated DVCCS' , IEEE Trans., CT-18, pp.733-736, 1971.
25. M. BIALOKOW, W.SIENKO and R. W. NEWCOMB: 'Active synthesis using the DVCCS/DVCVS' , Int. J. Circuit Theory & Appl., 2, pp.23-38, 1974.
26. R. NANDI.: ' New Ideal Active Inductance and Frequency-Dependent Negative Resistance using D.V.C.C.S./D.V.C.V.S.: Applications in Sinusoidal-Oscillator Realization' , Electron. Lett.,14, pp. 551-553,1978.
27. A. Muhammed Ibrahim, Shahram Minaei and Hakan Kuntman, "A 22.5 MHz current-mode KHN-biquad differential voltage current conveyor and grounded passive elements" , International Journal of Electronics and Communications, pp.311-318, 2004.
28. Y.C.Yin, "Realization of Current-Mode Filters Using Two Differential Voltage Current Conveyors" , 2010 Intelligent Living Technology Conference, pp.103-107, 2010
29. Y.C.Yin "Current-Mode Multifunction Filters using Single Differential Voltage Current Conveyor" , 2010 Workshop on Consumer Electronics, pp.275-278, 2010
30. S.I.Liu, J.J. Chen and J.H.Tsay," New insensitive notch and all-pass filters with current follower" , Electron. Lett, vol. 27, pp. 1712-1713, 1991
31. S.I.Liu, J.J. Chen, H.W.Taso and J.H.Tsay," Design of biquad filters with a single current follower" , IEEE Proceeding-G, vol. 14, pp. 165-170, 1993.
32. S.I.Liu, J.J. Chen, andY.S.Hwang," New current mode biquad filters using current followers" , IEEE Transactions on Circuits and Systems-I: Fundamental Theory and Applications, vol. 42, pp. 380-383, 1995.
33. A. Muhammed Ibrahim, Hakan Kuntman and Oguzhan Cicekoglu," First-Order All-Pass Filter Canonical in the Number of Resistors and Capacitors Employing a Single DDCC" , Circuits, Systems and Signal Processing Volume 22, Issue 5 , pp 525-536, 2003.
34. A. Muhammed Ibrahim, Hakan Kuntman and Oguzhan Cicekoglu," Single DDCC Biquads with High Input Impedance and Minimum Number of Passive Elements" , Circuits, Systems and Signal Processing Volume 43, Issue 1 , pp 71-79, 2005
35. Wen-Ta Lee and Yi-Zhen Liao "New voltage-mode high-pass, band-pass and low-pass filter using DDCC and OTAs" , International Journal of Electronics and Communications Volume 62, Issue 9, Pages 701–704, 2008.
36. B. Metin, O. Istanbul Cicekoglu, and K. Pal, "DDCC based all-pass filters using minimum number of passive elements" , Circuits and Systems, MWSCAS 2007. 50th Midwest Symposium on, 2007.
37. Varun Aggarwal," Novel Canonic Current Mode DDCC Based SRCO Synthesized Using a Genetic Algorithm" , Analog Integrated Circuits and Signal Processing, Volume 40, Issue 1, pp 83-85, 2004.
38. Surapong Siripongdee and Witthaya Mekhum," A Design of Electronically Tynable Voltage-mode Universal Filter with High Input Impedance" , International Journal of Electronics and Electrical Engineering, Volume 6, Pages 44–47, 2012.

Recevied Oct 1, 2013
Revised Feb 24, 2014
Accepted Feb 24, 2014

REFERENCES

1. A.S.Sedra, and K.C.Smith, "Microelectronic circuit" , sixth edition, Florida: Holt, Rinehart and Winston, 2011.
2. M. A. Ibrahim, S. Minaei, and H. A. Kuntman, "A 22.5MHz current-mode KHN-biquac using differential voltage current conveyor and grounded passive elements" , International Journal of electronics and Communications(AEU), vol.59, pp.311-318, 2005.
3. B. Wilson, "Recent Developments in Current Conveyors and Current-Mode Circuits" , IEE Proc-G, vol. 137, no. 2, pp.63-77, 1990.
4. G. W. Rober and A. S. Sedra, "All Current-Mode Frequency Selective Circuits" , Electron. Lett., Vol.25, pp.759-761, 1989.
5. C.Toumazou and E.J.Lidgey, "Universal active filter using current conveyous" , Electron. Lett.,vol. 22, pp.662-664, 1986.
6. Y.Sun and J.K.Fidler, "Versatile active biquad based on second-generation current conveyors" , Int. J Electron., vol. 76, pp91-98, 1994.
7. V.K.Singh and R.Senani, "New multifunction active configuration employing current conveyors" , Electron. Lett., vol. 26, pp.1814-1816, 1990.
8. G.W.Robert and A.S.Sedra, "A general class of current amplifier-based biquadratic filter circuits" , IEEE Transactions on Circuits and Systems, vol. 39, pp.257-263, 1992.
9. C.M.Chang, "Universal active current filters using single second-generation current conveyors" , Electron. Lett., vol. 27, no.18, pp.1614-1617 , 1991
10. C.M.Chang and P.C.Chen, "Universal active current filter with three inputs and one output using current conveyors" , Int. J Electron., vol. 71, no.5, pp.817-819, 1991.
11. C.Toumazou and E.J.Lidgey, "Universal active filter using current conveyous" , Electron. Lett.,vol. 22, pp.662-664, 1986.
12. Y.Sun and J.K.Fidler, "Versatile active biquad based on second-generation current conveyors" , Int. J Electron., vol. 76, pp91-98, 1994.
13. E.O.Gues and F. Anday, "Realization of current-mode universal filter using CFCCIIps " , Electron. Lett., vol. 32, pp.1081-1082 , 1996.
14. C.M. Chang and S.H. Tu, "Universal current-mode filters employing CFCCIIps" , Int. J Electron., vol. 85, no.6, pp.749-754, 1998.
15. Y.C.Yin, "Current-Mode Biquad Using Two CFCCIIps" , Fu Jen Studies: Science and Engineering, No.37, pp.64-74, 2003.
16. Y.C.Yin, Y.C. Liou "Realization of Current-Mode Highpass Lowpass and Bandpass Biquad Filters using Single CFCCIIp" , Fu Jen Studies: Science and Engineering, No.38, pp.89-99, 2004.
17. Y.C.Yin, "Realization of Current-Mode Notch and Allpass Filters using Single CFCCII" , Fu Jen Studies: Science and Engineering, No.39, pp.11-22, 2005.
18. Y.C.Yin, "Active simulation of grounded inductor using CFCCIIs" , Fu Jen Studies: Science and Engineering, No.40, pp.71-79, 2006.
19. Y.C.Yin, "Floating Inductance using Four-terminal Active Current Conveyors" , Fu Jen Studies: Science and Engineering, No.41, pp.47-56, 2007.
20. Y.C.Yin, "Floating Inductance using CFCCIIs and Earthed Passive Elements" , 2008 Workshop on Consumer Electronics, pp.755-758, 2008
21. Y.C.Yin, "Realization of current-mode universal filter using Four-terminal Active Current Conveyors" , 2009 Workshop on Consumer Electronics, pp.275-278, 2009
22. K. PAL,: 'Modified current conveyors and their applications' , Microelectronics Journal, 20, vol.4, pp.37-40, 1989.

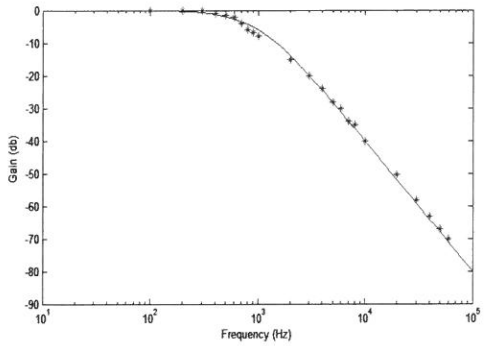

(e) Lowpass filter gain response

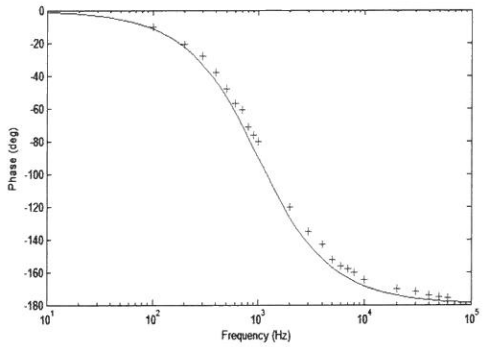

(f) Lowpass filter phase response

Fig-6. (a): Bandpass filter gain response
(b): Bandpass filter phase response
(c): Highpass filter gain response
(d): Highpass filter phase response
(e): Lowpass filter gain response
(f): Lowpass filter phase response
*: experimental result for gain
+: experimental result for phase
–: ideal curve

IV. CONCLUSION

A new current-mode universal biquadratic filter circuit based on DDCCs, CFs and grounded passive elements has been presented. It can perform lowpass, highpass, bandpass, notch and allpass functions from the same circuit configuration without component matching conditions. The proposed filter also offers several advantages, such as low sensitivities to passive components, orthogonal control of both ω_o and Q through grounded resistors, and the use of grounded passive elements which is an IC implementation ideal. Finally, three experimental results confirmed the theoretical analysis presented herein. The results will be useful in analogue signal processing applications.

Hewlett Packard network/spectrum analyzer 4195A. The experimental results of Fig. 4 are shown in Fig.6. The bandpass result is shown in Fig. 6 (a) and (b), where $G_1 = 0$, $C_5 = 0$, $G_3 = G_4 = G_5 = G_6 = 10^{-3}\ (\Omega)^{-1}$ and $C_2 = C_6 = 1\ \mu$F. The highpass result is shown in Fig. 6 (c) and (d) where $G_1 = G_5 = 0$, $G_3 = G_4 = G_6 = 10^{-3}\ (\Omega)^{-1}$ and $C_2 = C_5 = C_6 = 1\ \mu$F. The lowpass result is shown in Fig. 6 (e) and (f), where $G_5 = C_5 = 0$, $G_3 = G_4 = G_1 = G_6 = 10^{-3}\ (\Omega)^{-1}$ and $C_2 = C_6 = 1\ \mu$F. Fig. 6 shows the experimental results of the bandpass, highpass and lowpass filters. Experimental results confirm the results of the theoretical analysis.

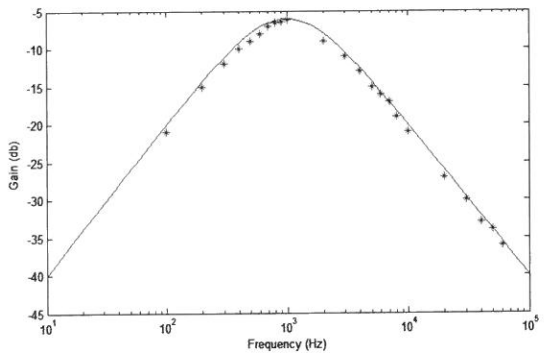

(a) Bandpass filter gain response

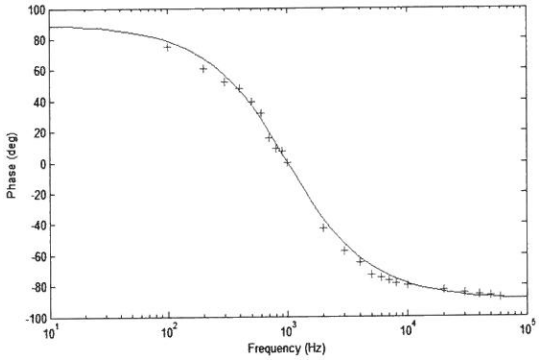

(b) Bandpass filter phase response

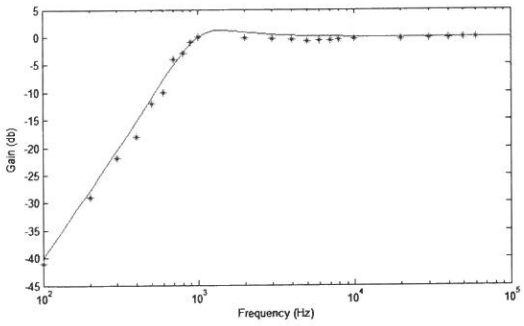

(c) Highpass filter gain response

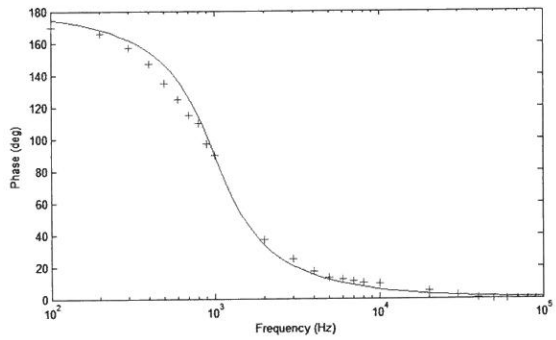

(d) Highpass filter phase response

Five filters are constructed from the proposed circuit, shown in Fig.4. From equation (2), the resonance angular frequency ω_o and the quality factor Q of the universal current mode filter can be expressed as

the resonance angular frequency $\omega_o = \sqrt{\frac{G_3 G_4}{C_2 C_6}}$

the quality factor $Q = \frac{1}{G_6}\sqrt{\frac{G_3 G_4 C_6}{C_2}}$

It is clear that ω_o and Q are orthogonally tunable.

By relating a sensitivity parameter F to the element of variation X_i,

$$S_{X_i}^{F} = \frac{X_i}{F}\frac{dF}{dX_i}$$

The passive sensitivities for the circuit of Fig.2 are given by

$S_{G_3}^{\omega_o} = S_{G_4}^{\omega_o} = -S_{C_2}^{\omega_o} = -S_{C_6}^{\omega_o} = 1/2$

$S_{G_3}^{\vartheta} = S_{G_4}^{\vartheta} = S_{C_6}^{\vartheta} = -S_{C_2}^{\vartheta} = 1/2$

$S_{G_6}^{\vartheta} = -1$

All the passive sensitivities are quite small.

III. EXPERIMENTAL RESULTS

Finally, to verify the theoretical prediction of the proposed circuit, a bandpass, a highpass and a lowpass filter prototypes have been constructed with discrete components. The DDCCs and CFs are constructed by employing AD844 IC. The Matlab has carried out simulating the ideal curves of the proposed filters. The experimental results above are measured using the

$$\frac{I_o}{I_{in}} = \frac{sC_2G_5}{s^2C_2C_6 + sC_2G_6 + G_3G_4} \quad \text{.....(5)}$$

(4).Notch:

Similarly, for equation (2), if $G_5 = 0$, then the transfer function has a biquadratic notch characteristic with

$$\frac{I_o}{I_{in}} = \frac{s^2C_2C_5 + G_1G_4}{s^2C_2C_6 + sC_2G_6 + G_3G_4} \quad \text{.....(6)}$$

(5).Allpass:

Fig.5 shows the circuit for the realization of negative impedance using one DDCC. From circuit inspection, it is apparent that the input impedance can be expressed as:

$Z_{eq} = -G$ .....(7)

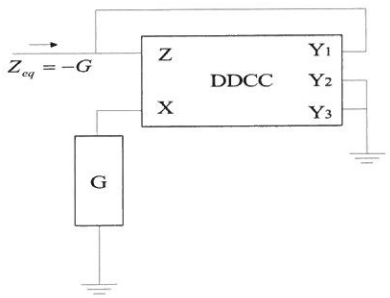

Fig-5 The realization of negative impedance with Z_{eq} = -G

Let $G_5 = -G_5$, where "$-G_5$" can be obtained by the circuit shown in Fig. 4. Equation (2) can be expressed as

$$\frac{I_o}{I_{in}} = \frac{s^2C_2C_5 - sC_2G_5 + G_1G_4}{s^2C_2C_6 + sC_2G_6 + G_3G_4} \quad \text{.....(8)}$$

Thus, a second-order allpass filter can be achieved.

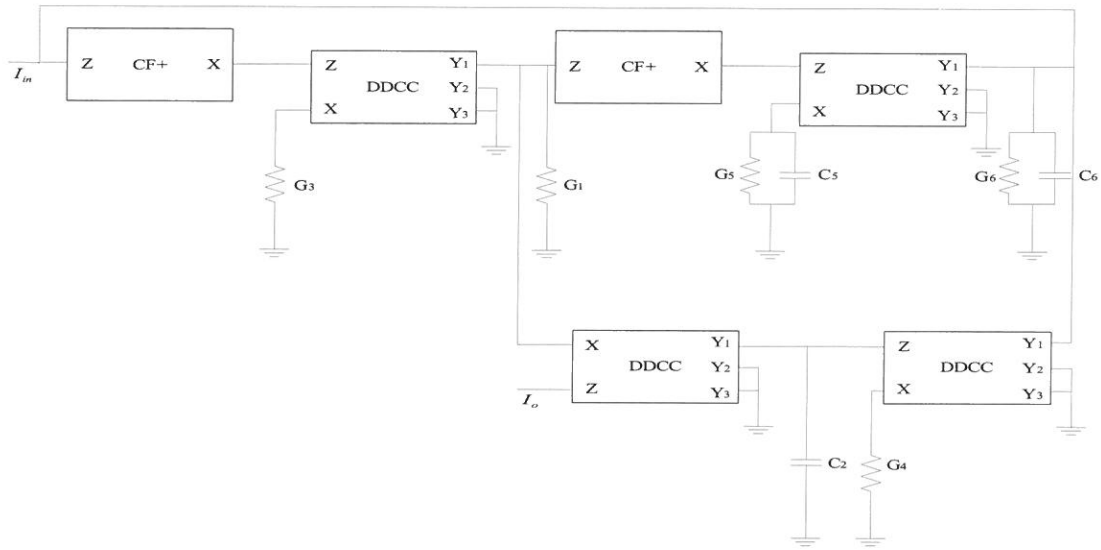

Fig-4 Proposed current - mode universal biquad filter for equation (2)

Thus, five second order filter circuits can be realized from equation (2)

(1).Lowpass:

For equation (2), if $G_1 = C_5 = 0$, then the transfer function has a biquadratic lowpass characteristic with

$$\frac{I_o}{I_{in}} = \frac{G_1 G_4}{s^2 C_2 C_6 + s C_2 G_6 + G_3 G_4} \quad \text{.....(3)}$$

(2).Highpass:

For equation (2), if $G_1 = G_5 = 0$, this circuit is a biquadratic highpass filter, with

$$\frac{I_o}{I_{in}} = \frac{s^2 C_2 C_5}{s^2 C_2 C_6 + s C_2 G_6 + G_3 G_4} \quad \text{.....(4)}$$

(3).Bandpass:

For equation (2), if $G_1 = C_5 = 0$, this circuit performs a second order bandpass function, with

The proposed filter circuit employing four DDCCs, two CF+s and some grounded passive elements is shown in figure 3. From a routine analysis of the current-mode configuration, the transfer function of the Fig.3 can be represented by the following equation:

$$\frac{I_o}{I_{in}} = \frac{Y_2Y_5 + Y_1Y_4}{Y_3Y_4 + Y_2Y_6} \quad \text{.....(1)}$$

where $Y_1 - Y_6$ are admittances.

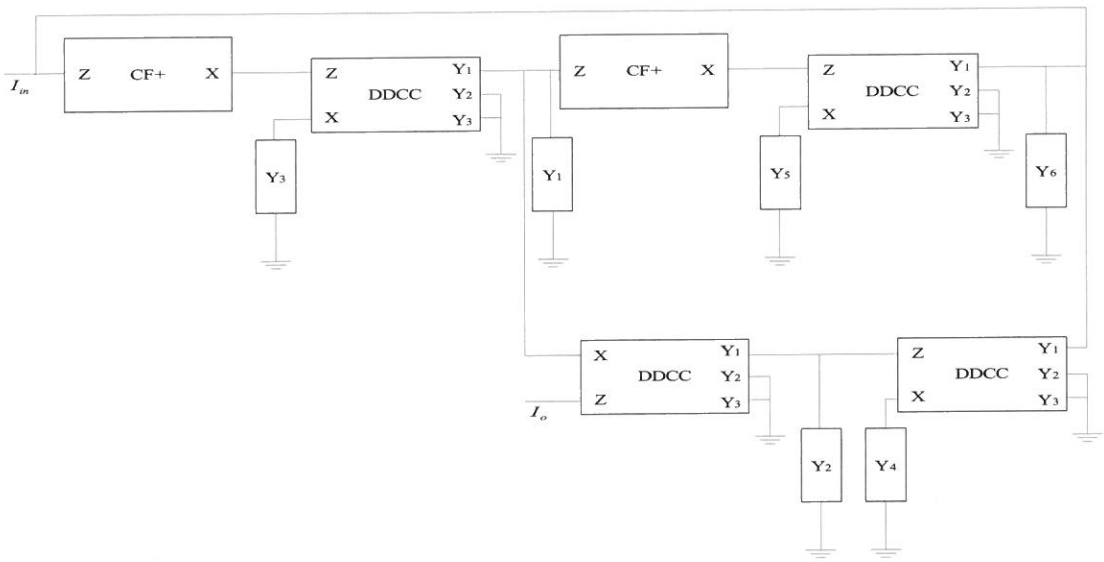

Fig-3 Configuration for realizing current mode universal biquad filter

If the admittances are chosen as $Y_1 = G_1$, $Y_2 = sC_2$, $Y_3 = G_3$, $Y_4 = G_4$, $Y_5 = sC_5 + G_5$ and $Y_6 = sC_6 + G_6$, the equation (1) can be expressed as

$$\frac{I_o}{I_{in}} = \frac{s^2C_2C_5 + sC_2G_5 + G_1G_4}{s^2C_2C_6 + sC_2G_6 + G_3G_4} \quad \text{.....(2)}$$

The proposed circuit is shown in Fig. 4.

elements is proposed. The new configuration of current-mode filter circuit can realize either notch or all-pass or lowpass or highpass or bandpass filter. The output current signals of the proposed circuits are taken out through Z of a DDCC. Because of high output impedance, it may be used in cascade without any additional matching circuit. The passive sensitivities of the proposed circuit are also derived, and they are small. Therefore, this newly designed universal current-mode filter is better than any of the previously designed universal current-mode filters. The comparison between this paper and the recent one [38] is shown in the table 1.

Paper / Filter	Low-pass	High-pass	Band-pass	Notch	All-pass
Surapong Siripongdee and Witthaya Mekhum (2012)	V	V	V	X	X
Yin and Liu (present)	V	V	V	V	V

Table1. Comparison of the filter function

Finally, three experimental results are given to confirm the mentioned afore theoretical analysis.

II. CIRCUIT DESCRIPTION

The port relations of a DDCC, shown in Fig.1, can be characterized as $I_z = I_x$, $V_x = V_{y1} - V_{y2}$, and $I_{y1} = I_{y2} = I_{y3} = 0$. A CF+, shown in Fig.2, is a two-port network whose terminal characteristics can be described as $V_x = 0$ and $I_z = I_x$.

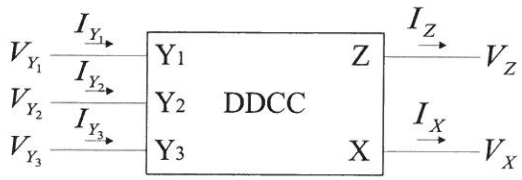

Fig.1. A DDCC symbol

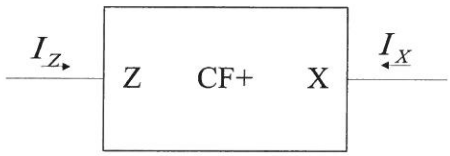

Fig.2. A plus-type CF symbol

I. INTRODUCTION

An analog filter is an important building block, because it can be widely used for continuous-time signal processing applications [1]~[2]. The analog filters have been found in the communication, measurement, instrumentation and control system fields. For example, current conveyors, four-terminal active current conveyors and differential voltage current conveys have been widely used in the various circuit applications of analogue circuits [3]~[29]. Current followers (CFs) and Differential Difference Current Conveyors (DDCCs) are also versatile current mode building blocks. CF can avoid any voltage tracking error because of the virtual earth at the input terminals [30]~[32]. DDCC can circumvent the finite gain-bandwidth limitation of the conventional operational amplifier and have many advantages such as large signal bandwidth, great linearity, wide dynamic range, high input impedance and arithmetic operation capability. Therefore, The realizations and applications of universal biquad using DDCCs have received considerable attention [33]~[38]. First, Muhammed A. Ibrahim, Hakan Kuntman and Oguzhan Cicekoglu used some DDCCs to present a voltage-mode canonical first-order all-pass filter [33]. Secondly, Muhammed A. Ibrahim, Hakan Kuntman and Oguzhan Cicekoglu then synthesized bandpass, low-pass and high-pass filter functions employing one DDCC as active elements [34]. Third, Wen-Ta Lee and Yi-Zhen Liao constructed a voltage-mode biquad filter using one DDCC, two single-ended operational transconductance amplifiers and two grounded capacitors. The proposed circuit can realize low-pass, high-pass and band-pass filters from the same configuration [36]. Fourth, Istanbul Cicekoglu and Pal realized the all-pass filters using some DDCCs and the minimum number of passive elements [33]. Fifth, Varun Aggarwal proposed a novel DDCC based canonic current mode Single-Resistor Controlled Oscillator, which uses a voltage controlled voltage source and a single current terminal to take out the output [36]. Sixth, Siripongdee and Mekhum constructed the voltage-mode low-pass, high-pass and band-pass filters employing some DDCCs and current controlled current conveyors as active elements [37]. However, all of the proposed circuits have some disadvantages, such as: (1) high sensitivity, (2) without any orthogonal control of the resonance angular frequency and the quality factor, and (3) without low-pass, high-pass, notch, allpass and band-pass filters from the same configuration. In this paper, a new universal current-mode filter using four DDCCs and two CF+s as active elements together with some grounded passive

Current-mode Universal Biquad using Differential Difference Current Conveyors and Current Followers

Yung-Chang Yin and Hong-Yu Liu

Department of Electrical Engineering

Abstract

In this paper, a current-mode universal biquad is presented. This proposed circuit employs four Differential Difference Current Conveyors (DDCCs), two plus-type Current Followers (CF+s) as active elements together with some grounded capacitors and grounded resistors as passive elements. The proposed circuit can realize lowpass, highpass, bandpass, notch and allpass five filter functions and enjoy many advantages which include low sensitivity to passive components, fewer voltage tracking errors and orthogonal tuning of the parameters Q and ω_0 through grounded resistors. Because all of the passive elements are grounded, the fabrication of the proposed circuit is easy in IC implementation processes. Finally, three experimental results are included to certify the theoretical prediction.

Key words: Differential Difference Current Conveyor, Current Follower, sensitivity, active filter, analogy circuit design, continuous-time filter

一個心電訊號放大及濾波電路

黃奕豪　林妙珊　沈鼎嵐

輔仁大學電機工程學系

摘　要

本文發展了一個適用於心電訊號截取的放大濾波積體電路。前端的放大電路採用三個兩級架構運算放大器構成的儀表放大器。放大電路後串接了一個四階的巴特沃斯低通濾波器以抑制高頻干擾。為了免除積體電路上外接的元件，在低通濾波器中所需要的高電阻值電阻採用將 MOS 電晶體偏壓在次臨界區域的方式來實現。整體電路採用 0.35μm CMOS 製程技術設計，其晶片主動面積為 0.085mm^2。放大電路最大放大增益為 60dB，所設計的低通濾波器頻寬為 200Hz。

關鍵字：心電圖，儀表放大器，巴特沃斯低通濾波器，次臨界區域。

Reference

1. W. Wattanapanitch, M. Fee, and R. Sarpeshkar, "An energy-efficient micropower neural recording amplifier," IEEE Trans. Biomed. Circuits Syst., vol. 1, no. 2, pp. 136–147, Jun. 2007.
2. T.-H. Tsai, J.-H. Hong, L.-H. Wang, and S.-Y. Lee, "Low-power analog integrated circuits for wireless ECG acquisition systems," IEEE Trans. Inf. Technol. Biomed., vol. 16, no. 5, pp. 907–917, Sep. 2012.
3. Y. Tseng, Y. Ho, S. Kao, and C. Su, "A 0.09 μ W low power frontend biopotential amplifier for biosignal recording," IEEE Trans. Biomed. Circuits Syst., vol. 6, no. 5, pp. 508–516, Oct. 2012.
4. R. F. Yazicioglu, C. V. Hoof, and R. Puers, Eds., Biopotential Readout Circuits for Portable Acquisition Systems. Springer, 2008.
5. M. Mollazadeh, K. Murari, G. Cauwenberghs, and N. Thakor, "Wireless micropower instrumentation for multimodal acquisition of electrical and chemical neural activity," IEEE Trans. Biomed. Circuits Syst., vol. 1, no. 3, pp. 388–397, Dec. 2009.
6. E. Greenwald, M. Mollazadeh, C. Hu, W. Tang, E. Culurciello, and N. V. Thakor, "A VLSI neural monitoring system with ultra-wideband telemetry for awake behaving subjects," IEEE Trans. Biomed. Circuits Syst. vol.5, no.2, pp.112-119, Apr. 2011.
7. J. G. Webster, Ed., Medical Instrumentation Application and Design, 4th ed. John Wiley & sons, 2010.
8. S. Franco, Design with Operational Amplifiers and Analog Integrated Circuits, 3rd ed. McGraw-Hill, 2002.
9. R. Schaumann and M. E. V. Valkenburg, Design of Analog Filters. Oxford, 2001.
10. M.-T. Shiue, K.-W. Tao, and C.-S. A. Gong, "Tunable high resistance voltage-controlled pseudo-resisotr with wide input voltage swing capability," IEL Electronics Letters, vol. 47, no. 6, pp. 377–378, Mar. 2011.

Recevied Aug 29, 2013
Accepted Jan 24, 2014

Table 1. Performance Specification

Technology	CMOS 0.35 μm
Supply Voltage	3.3 V
Gain	60 dB
Bandwidth	0.1~200 Hz
CMRR	57.2 dB
Power Dissipation	11.19 mW
Active Area	0.085 mm^2

4. Conclusion

This paper presents an integrated ECG amplification and filtering circuit with a 0.35μm CMOS technology at a single supply voltage of 3.3V. The applied ac coupling input prevents the demand at the conventional right-leg driven electrode. The utilized on-chip pseudo-resistors with high resistance replacing the off-chip components in the filter effectively save the area requirement of IO pads. This front-end circuit profits the integrated development of the ECG acquisition system.

Acknowledgment

The authors thank the support of Ministry Science and Technology under the grant NSC 101-2221-E-030-024- and the simulation assistance of National Chip Implementation Center (CIC).

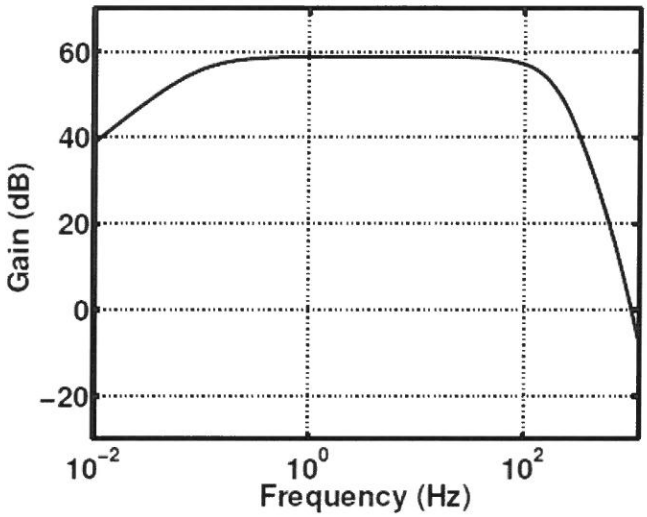

Figure 11. Overall frequency response.

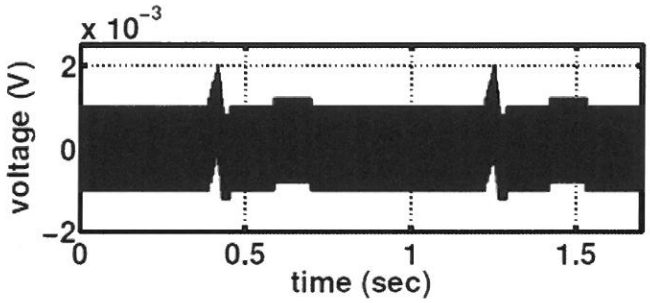

(a)

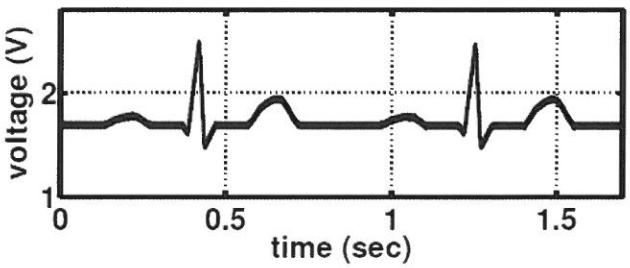

(b)

Figure 12. ECG simulation results of (a) input coupled with the 500 Hz sine wave and (b) output.

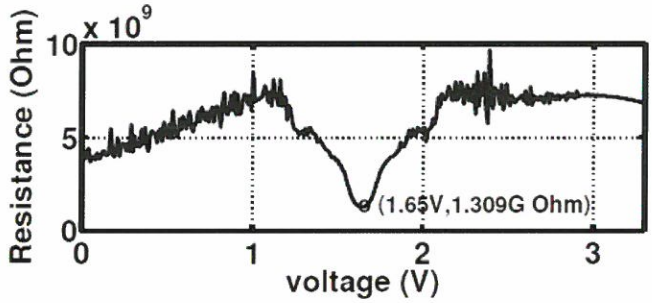

(a)

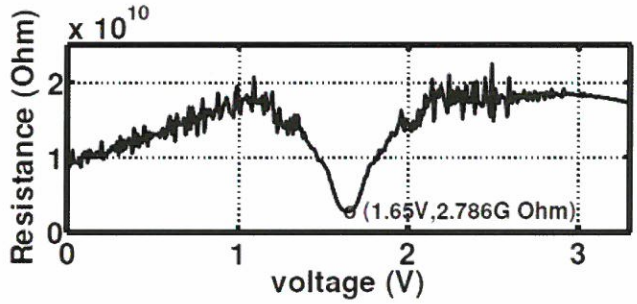

(b)

Figure 9. Simulation results of (a) pseudo resistor 1 and (b) pseudo resistor 2.

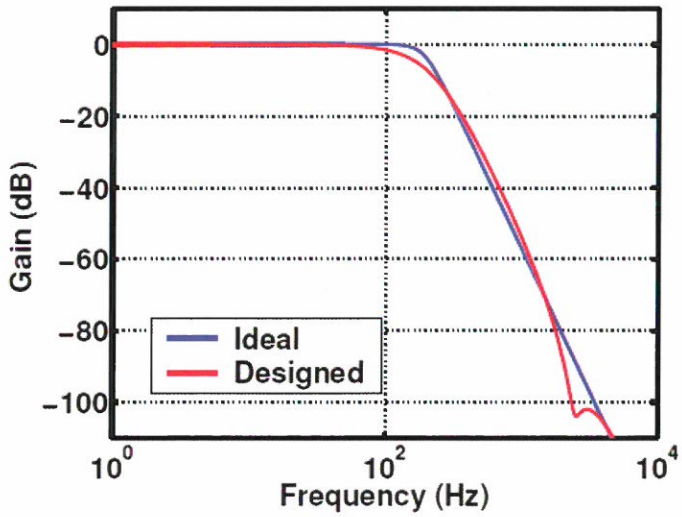

Figure 10. Low-pass filter frequency response.

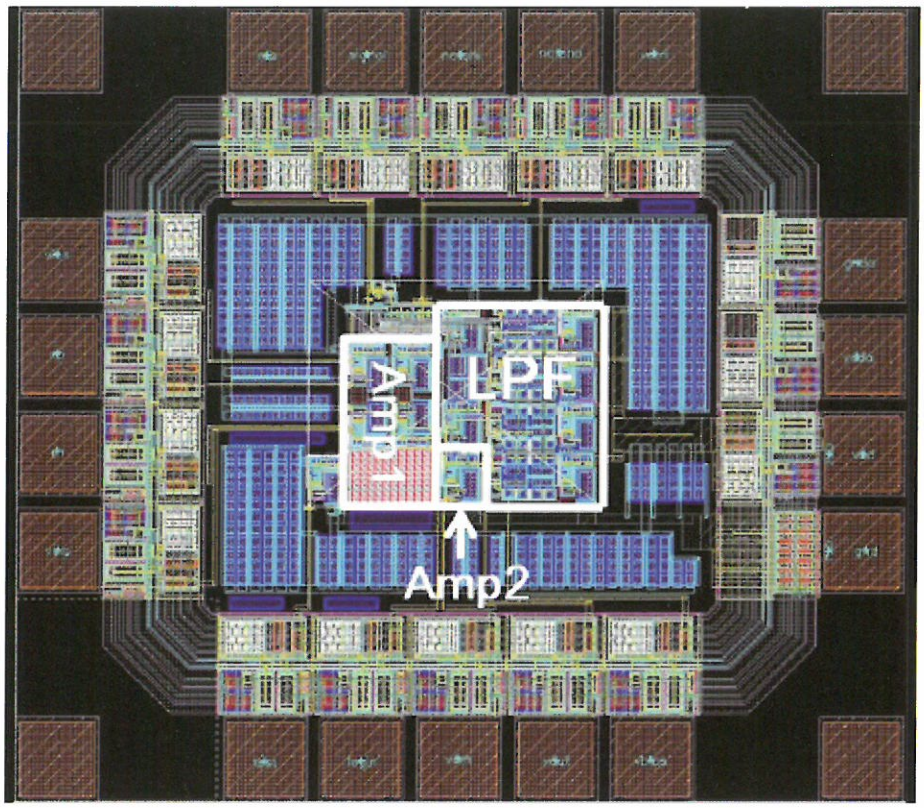

Figure 8. Chip layout

gain of 31 dB. Consequently, this ECG amplification and filtering circuit presents the amplification of 60 dB with bandwidth of 200 Hz.

3. Simulation Results

This work is designed with a 0.35-μm CMOS technology. The chip layout is depicted in Fig. 8. The area occupation is 1.017×0.906 mm^2 including pads and the active area is 0.085 mm^2. The simulations of pseudo resistors are depicted in Fig. 9. The x-axis stands for the dc sweep of V_a at a fixed voltage V_b of 1.65 V in Fig. 6. The results indicate that as V_a and V_b near the V_{cm} at 1.65 V, the resistance value of pseudo resistor1 and resistor2 are 1.309 GΩ and 2.786 GΩ, respectively. The frequency response of this designed LPF and the ideal LPF are shown in Fig. 10. Although the passband response at the designed LPF is not as flat as ideal one within 200 Hz, the roll-off response of the designed LPF almost matches the ideal one. The overall frequency response is shown in Fig. 11. The lower 3-dB frequency is 0.1 Hz and the upper 3-dB frequency is 200 Hz. The midband gain is near 60 dB. The ECG signal coupled with the sine wave at the frequency of 500 Hz and amplitude of 1 mV as shown in Fig. 12 is input to this front end circuit for simulation. The output waveform reveals that this circuit amplifies the magnitude from 1 mV to 1 V and effectively suppresses the high frequency interference. The simulated CMRR in the pass band is obtained as 57.2 dB. The CMRR can be further improved with the fully differential operation. The power dissipation is about 11.19 mW. The performance specification of this amplification and filtering circuit is summarized in Table 1.

as depicted in Fig. 6 [10] is utilized to act as the demanded resistor in the Sallen-Key circuit. The main principle of the active pseudo resistor principle of this active pseudo resistor is to operate the PMOS transistors in subtreshold condition to achieve high-equivalent resistance. The V_{ctrl} determines the voltage difference between V_f and V_g to obtain the demanded resistance. When $V_a > V_b$, $V_a \simeq V_f$ and $R_{ab} = R_{M1} + R_{M2}$. By symmetry, when $V_a < V_b$, $V_b \simeq V_f$ and $R_{ab} = R_{M3} + R_{M4}$. Consequently, by designing $M_1 = M_4$ and $M_2 = M_3$, the R_{ab} are near constant with different polarities of V_a and V_b.

2.6.On-chip Circuits

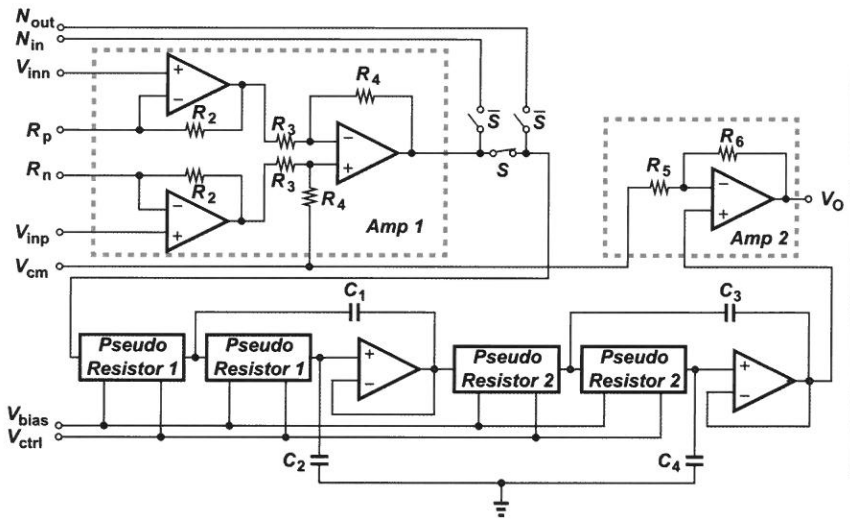

R_2	10 kΩ
R_3	4 kΩ
R_4	20 kΩ
R_5	1 kΩ
R_6	39 kΩ
C_1	700 fF
C_2	94 fF
C_3	661.5 fF
C_4	368 fF
Pseudo Resistor 1	2.786 GΩ
Pseudo Resistor 2	1.309 GΩ

Figure 7. The on-chip circuit diagram and the corresponding design parameters.

The on-chip circuits and the design parameters are shown in Fig. 7. The IA acts as the first stage, *Amp1*, with the gain of 29 dB. The switches, S and $\overline{S}$ s, provide the individual test path of the IA and the following circuits. Moreover, if the interference of 60 Hz electricity is too serious, the off-chip notch filter can be joined through these switches. A 4th order Butterworth LPF of 200 Hz bandwidth with pseudo resistors are cascaded after the switches. Because the amplitude of original ECG signal is about few millivolt, the magnifying scale of *Amp1* is not adequate for applications. Therefore, an additional stage, *Amp2*, provides the supplementary

When $R_1 = R_2 = R$, $C_1 = C$, $C_2 = C/m$,

$$T(s) = \frac{\frac{m}{R^2C^2}}{s^2 + s\frac{2}{RC} + \frac{m}{R^2C^2}}. \tag{4}$$

By comparing (4) with the first second-order equation of (2), the RC = 2.08×10^{-3}s when the pass bandwidth is about 200 Hz ($\omega_0 = 400\pi$) and m = 6.83. Similarly, the second second-order equation is obtained as $RC = 8.61 \times 10^{-4}$s and m = 1.17.

2.5.Pseudo Resistor

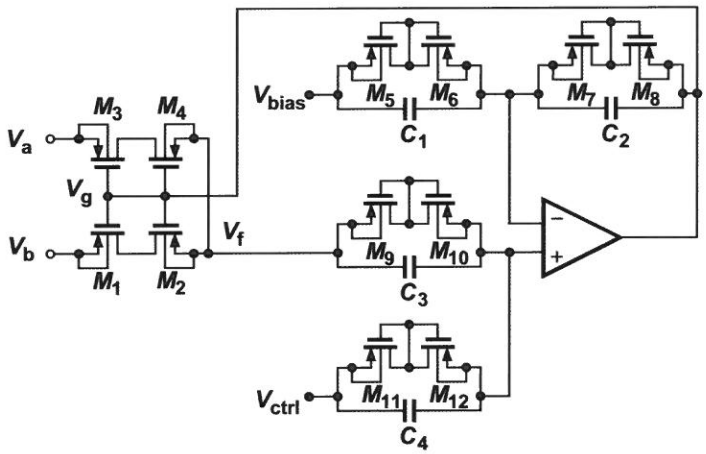

Figure 6. The active pseudo resistor.

To design a proper capacitance value that the capacitor is realizable on the chip. The value of the capacitance is selected as the order of pico faraday. Therefore, the demanded value of the resistance will be the order of giga ohm. Such highvalue resistance is difficult to be realized in modern technology with passive liner resistor. To avoid the pad area requirements of external resistors' connections, the active pseudo resistor with high resistance

The nature modes of a 4th-order Butterworth filter can be determined from the s-plane shown in Fig.4. The poles' location are given by

$$p_1 = \omega_0\left(-\cos 67.5^\circ + j\sin 67.5^\circ\right),$$
$$p_2 = \omega_0\left(-\cos 22.5^\circ + j\sin 22.5^\circ\right),$$
$$p_3 = \omega_0\left(-\cos 22.5^\circ - j\sin 22.5^\circ\right),$$
$$p_4 = \omega_0\left(-\cos 67.5^\circ - j\sin 67.5^\circ\right).$$

Combining p_1 with its complex conjugate p_4 and p_2 with its complex conjugate p_3 yields the 4th-order complete transfer function as

$$T(s) = \frac{\omega_0^4}{\left(s^2 + s0.7654\omega_0 + \omega_0^2\right)\left(s^2 + s1.8478\omega_0 + \omega_0^2\right)}. \tag{2}$$

2.4.Sallen-Key Biquad

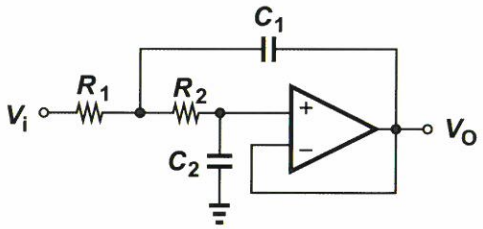

Figure 5. The Sallen-Key biquad circuit.

For the single-amplifier-biquad (SAB) of Sallen-Key circuit in Fig. 5, its transfer function is obtained as

$$T(s) = \frac{\dfrac{1}{R_1R_2C_1C_2}}{s^2 + s\left(\dfrac{1}{R_1} + \dfrac{1}{R2_2}\right)\dfrac{1}{C_1} + \dfrac{1}{R_1R_2C_1C_2}}. \tag{3}$$

in Fig. 3. Modern circuits are required to operate from a single supply voltage. To provide a proper input reference, voltage V_{cm} acts as common-mode voltage. Capacitors C_h and R_h resistors Rh perform the ac coupling high-pass filter (HPF) with corner frequency of 0.1 Hz. With this coupling circuit, the dc offset voltage is blocked and only the difference signal of ECG is fed into the IA. Consequently, the conventional right-leg driven electrode can be eliminated with this approach. The voltage gain of the IA is known as

$$A_v = \frac{R_4}{R_3}\left(1+\frac{2R_2}{R_1}\right), \tag{1}$$

The external resistor, R_1, furnish the gain adjustment for various candidates. The maximum available gain of this IA is 29 dB.

2.3.Butterworth Filter

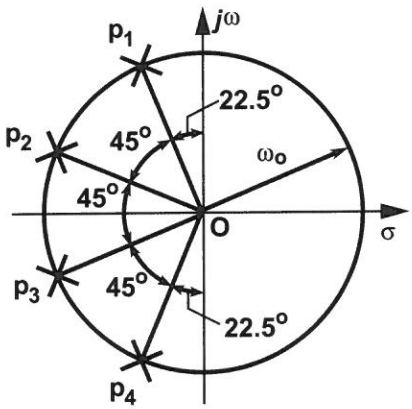

Figure 4. Poles location of a 4th order Butterworth filiter in the s-plane.

2. Circuit Description

2.1.Operational Amplifier

To obtain the lower noise, wider output swing, and larger driving capability, the two stage topology with PMOS inputs in Fig. 2 is adopted as the opamp in this work. This opamp is design as the dc gain of 66.8 dB, the unity-gain frequency of 679.6 MHz, and the phase margin of 68.5 degree.

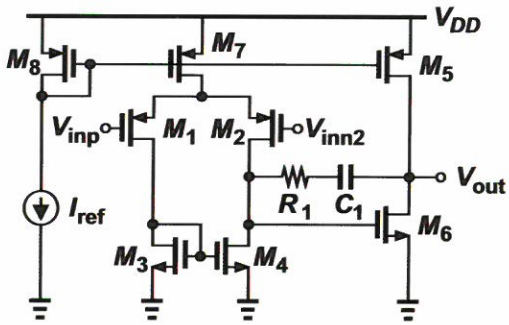

Figure 2. The applied two-stage amplifier.

2.2.Instrumentation Amplifier

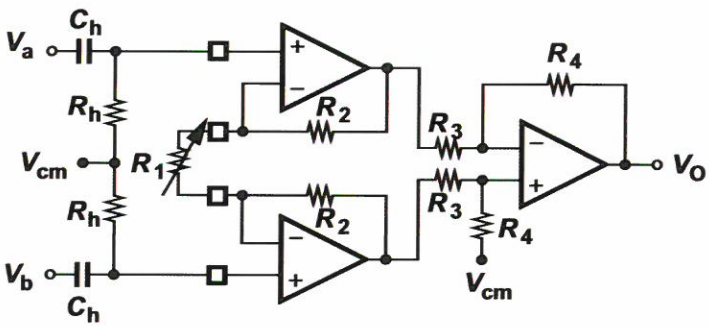

Figure 3. Three-opamp instrumentation amplifier with ac coupling networks.

The front end amplification stage applies the three-opamp instrumentation amplifier (IA)

1. Introduction

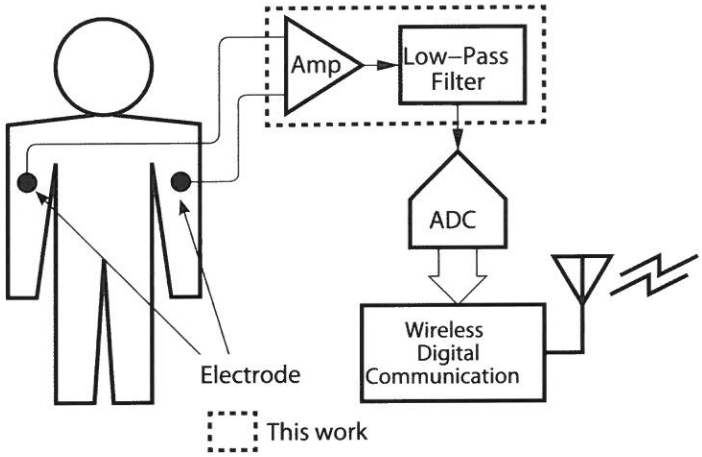

Figure 1. Modern approach of ECG acquisition.

The ECG is one of the most important electrophysiological signals from the human body. Many syndromes of the cardiopathy and life signs can be obtained from the ECG. The demanding of long-term ECG monitoring has driven the development of the front-end amplification circuits toward small volume and low power dissipation [1], [2], [3]. Since the body-surface potential difference induced by the cardiac activity is about few millivolt or less and the frequency range of the cardiac signals are low, the acquisition system usually consist of the electrodes, an amplifiers, and a LPF. With the progress of portable intelligence devices, the acquired signals are converted through the analog-to-digital converter (ADC) for the wireless digital communication as shown in Fig. 1 [4], [5], [6]. Because the amplitude of the primary ECG signal is about few millivolt, the amplifier needs to equip with high common-mode rejection ratio (CMRR) to suppress the common-mode interference.

In this work, the three-opamp instrumentation amplifier (IA) [7], [8] with high CMRR is utilized as the amplification stage at the front end. The external off-chip resistor provides the gain adjustment. The 4th order Butterworth LPF [9] with maximum flat response in the pass band is designed at the cutoff frequency of 200 Hz and cascaded behind the IA.

An ECG Amplification and Filtering Circuit

Yi-Hau Huang, Miao-Shan Lin and Ding-Lan Shen*

Departement of Electrical Engineering
Fu Jen Catholic University, New Taipei City, Taiwan

Abstract

This paper develops an integrated amplification and filtering circuit for the acquisition of the electrocardiogram (ECG) signals. The three-opamp instrumentation amplifier with two-stage topology is applied in the front end of amplification. A fourth order Butterworth low-pass filter (LPF) is cascaded to suppress the high-frequency interference. To avoid the external components in the integrated circuit, the resistors with high resistance value in the LPF are fulfilled with MOS transistors in subthreshold region. The corresponding circuit is designed with a 0.35-μm CMOS technology and its active chip area is 0.085 mm^2. The maximum gain for amplification is 60 dB and the bandwidth of the designed LPF is 200 Hz.

Key words: electrocardiogram, instrumentation amplifier, Butterworth low-pass filter, subthreshold region.

*Corresponding author: Tel: (02)2905-3739 E-mail address: dlshen@ee.fju.edu.tw

A study on multi-modal music graph [3]

Student : Chiu-Yuan Ho Advisor : Jia-Lien Hsu [4]

Department of Computer Science and Information Engineering
Fu Jen Catholic University

Abstract

In this paper, we propose a graph-based framework dedicated for music information retrieval; and the problem of features semantic gap. The semantic gap between cross-modal music features such as MIDI and emotion tag, play an important role on performance of the application in the music. In this paper, we use a graph to organize music features (i.e., multi-modal music graph), In order to reduce the complexity of graph, we introduce the graph projection operator to refactor the structure of the graph. Graph projected reduce the complexity of graph and compress the graph accordingly from feature domain. In this graph-based framework, we carry out music clustering and auto tagging application. Also, we perform experiments to show performance of our approach. According to our experiment study, the performance of projected graph is better than that of unprojected graph in the two applications.

Key words: Graph projection, Cross-modal, Graph

[3] This research was supported by the National Science Council under Contract No. NSC-101-2221-E-030-008 and No. NSC-102-2218-E-030-002.

[4] All correspondence should be sent to: The Department of Computer Science and Information Engineering. Fu Jen Catholic University, Taiwan (R.O.C.), E-mail: alien@csie.fju.edu.tw

International Conference on Advances in Social Networks Analysis and Mining (ASONAM), pp. 326–330, 2010.
12. P. Hoff, A. Raftery, and M. Handcock, "Latent space approaches to social network analysis," Journal of the American Statistical Association (ASA), vol. 97, no. 460, pp. 1090–1098, 2002.
13. T. Li, M. Ogihara, W. Peng, B. Shao, and S. Zhu, "Music clustering with features from different information sources," IEEE Transactions on Multimedia, vol. 11, no. 3, pp. 477–485, 2009.
14. R. Cilibrasi, P. Vitanyi, and R. De Wolf, "Algorithmic clustering of music," in Proceedings of the Fourth International Conference on Web Delivering of Music (WEDELMUSIC), pp. 110–117, IEEE, 2004.
15. D.-M. Kim, K.-S. Kim, K.-H. Park, J.-H. Lee, and K.-M. Lee, "A music recommendation system with a dynamic k-means clustering algorithm," in Proceedings of the International Conference on Machine Learning and Applications, pp. 399–403, IEEE, 2007.
16. Y. Panagakis and C. Kotropoulos, "Automatic music tagging by low-rank representation," in Proceedings of the IEEE International Conference on Acoustics, Speech and Signal Processing (ICASSP), pp. 497–500, 2012.
17. R. Miotto and G. Lanckriet, "A generative context model for semantic music annotation and retrieval," IEEE Transactions on Audio, Speech, and Language Processing, vol. 20, no. 4, pp. 1096–1108, 2012.
18. L. Chen, P. Wright, and W. Nejdl, "Improving music genre classification using collaborative tagging data," in Proceedings of the Second ACM International Conference on Web Search and Data Mining, pp. 84–93, 2009.
19. Y. Linde, A. Buzo, and R. Gray, "An algorithm for vector quantizer design," IEEE Transactions on Communications, vol. 28, no. 1, pp. 84–95, 1980.
20. L. Ertoz, M. Steinbach, and V. Kumar, "A new shared nearest neighbor clustering algorithm and its applications,in Proceedings of Workshop on Clustering High Dimensional Data and its Applications at 2nd SIAM International Conference on Data Mining, pp. 105–115, 2002.
21. D. J. Cook and L. B. Holder, Mining graph data. 1st ed. John Wiley & Sons, 2006.
22. L. Page, S. Brin, R. Motwani, and T. Winograd, "The pagerank citation ranking: Bringing order to the web.," Technical Report 1999, Stanford Digital Library, 1999.
23. D. Ellis, "Classifying music audio with timbral and chroma features," in Proceedings of the International Conference on Music Information Retrieval (ISMIR), pp. 339–340, 2007.
24. T. Sergios and K. Konstantinos, Pattern recognition. 3rd ed. Academic press, 2006.

Recevied Oct 30, 2013
Revised Mar 19, 2014
Accepted Mar 19, 2014

果並不突出，但我們的方法是一個通用的框架。可以適用於不同的應用，這是我們的貢獻之一。

在未來的研究，將針對投影的方法改良。SNN 只是計算相似度的方法之一。我們可以提供多種相似度計算方法，針對不同的需求選擇。圖形投影為運算元的一種，我們可以加入各種不同的運算元豐富框架的功能性。

參考文獻

1. Z.-Y. Fu, G.-J. Lu, K.-M. Ting, and D.-S. Zhang, "A survey of audio-based music classification and annotation," IEEE Transactions on Multimedia, vol. 13, no. 2, pp. 303–319, 2011.
2. 蔡振家 , 音樂認知心理學 . 1st ed. 國立台灣大學出版中心 , 2013.
3. J.-L. Hsu and Y.-F. Li, "A cross-modal method of labeling music tags," Multimedia Tools and Applications, vol. 58, no. 3, pp. 521–541, 2012.
4. 黃建彰、徐嘉連 , "音樂物件之社群標籤 ," 輔仁學誌第 45 期 , 輔仁大學 , 2012.
5. A. Bae, D. Park, S. Lee, and J. Park, "Social network analysis of classical music and possible uses in ubiquitous vr," in Proceedings of the International Symposium on Ubiquitous Virtual Reality (ISUVR), pp. 34–38, 2013.
6. M. Zsuzsanna and C. Sacarea, "Using conceptual graphs to represent modern music," in Proceedings of the IEEE International Conference on Intelligent Computer Communication and Processing (ICCP), pp. 137–140, 2011.
7. J.-Y. Pan, H.-J. Yang, C. Faloutsos, and P. Duygulu, "Automatic multimedia cross-modal correlation discovery," in Proceedings of the ACM SIGKDD International Conference on Knowledge Discovery and Data Mining, pp. 653–658, 2004.
8. P. Cremonesi, A. Tripodi, and R. Turrin, "Cross-domain recommender systems," in Proceedings of the IEEE 11th International Conference on Data Mining Workshops (ICDMW), pp. 496–503, 2011.
9. P. Dunker, C. Dittmar, A. Begau, S. Nowak, and M. Gruhne, "Semantic high-level features for automated cross-modal slideshow generation," in Proceedings of the International Workshop on Content-Based Multimedia Indexing (CBMI), pp. 144–149, IEEE, 2009.
10. F.-F. Kuo, M.-F. Chiang, M.-K. Shan, and S.-Y. Lee, "Emotion-based music recommendation by association discovery from film music," in Proceedings of the 13th Annual ACM International Conference on Multimedia, pp. 507–510, 2005.
11. N. Benchettara, R. Kanawati, and C. Rouveirol, "Supervised machine learning applied to link prediction in bipartite social networks," in Proceedings of the

表 12: 音樂分群結果 (以音樂物件為投影的 domain)

	Graph	Parameters	Rand-index	th_{SNN}
Artist20 dataset	Unprojected	Q=15,r=1,α=0.1	0.06	N/A
	Projected	Q=15,r=1,$level_x$=2,$level_y$=1	0.18	14
ISMIS dataset	Unprojected	Q=15,r=1,α=0.1	0.13	N/A
	Projected	Q=15,r=1,$level_x$=2,$level_y$=1	0.30	21

表 13: 音樂自動標籤結果 (以音樂物件和 Target 為 pFD 投影的 domain)

	Graph	Parameters	Accuracy	th_{SNN}
Artist20 dataset	Unprojected	Q=15,r=1,α=0.1	42%	N/A
	Projected	Q=15,r=1,$level_x$=2,$level_y$=1,α=0.1	53%	11
ISMIS dataset	Unprojected	Q=15,r=1,α=0.1	53%	N/A
	Projected	Q=15,r=1,$level_x$=2,$level_y$=1,α=0.1	63%	15

5.Conclusion

在本研究中，我們完成了對音樂分析的多模態圖形框架。我們實作出一個系統與使用者介面，並提供了多種運算元供我們對圖形分析。利用分析的結果可對音樂進行音樂分群、音樂自動標籤、計算音樂相似度等應用。在這系統中可以完成一系列特徵擷取、建立圖形、運算元分析與結果輸出的功能。在系統中提供圖形視覺化，可以配合分析的顯示對應的視覺化結果。集合多種功能成為一個豐富的音樂圖形分析框架。

我們定義了多模態音樂圖形，並使用圖形投影解決語意落差的問題。將音樂與特徵視為圖形上的節點。以此建立圖形結構，並在一致的架構下完成自動標籤及音樂分群的應用。我們使用圖形投影方法對圖形重構。實驗結果顯示，投影後的實驗結果比原始圖形還要好。

在自動標籤的應用中，對 Artist20 做歌手辨識與 ISMIS 資料集的風格辨識實驗中，分別可以達到 53% 與 63% 的準確率。在音樂分群中，對投影後的圖形做分群可以得到更好的 *Rand-index*。在 Artist20 與 ISMIS 資料集的音樂分群中。分別有 0.18 與 0.30 的 *Rand-index*。雖然與其他方法相比，實驗的結

- 投影特徵域的選擇 *ad*
  投影的目的是為了降低特徵 token 的 dominate 效果，可以降低辨識力較弱且有 dominate 的特徵 token 影響力。但同樣的會降低辨識力較高且有 dominate 的特徵 token 的影響力。ad 為投影的特徵域，我們保留辨識力較高的特徵域。
- 計算 SNN 時的參數設置 $level_x$ 與 $level_y$
  在進行投影時，$level_x$ 和 $level_y$ 與 r 以及 th_{SNN} 會影響投影後的圖形。
- 建構投影圖結構的參數 th_{SNN}
  我們先找出讓所有節點都至少有一個邊的 th_{SNN}。再將 th_{SNN} 調高，最後找出表現最好的 th_{SNN}。
- 計算 Pagerank 時的阻尼系數 α
  當我們計算 Pagerank 時，α 在 0.1 的時候會得到較好的效果。隨著 α 值上升，得到的準確率會跟著下降。

4.4. 實驗結果

在 Artist20 資料集中，我們使用全部的 1413 首歌曲。將歌手當作 Target，總共有 20 個 Target。對歌手做音樂分群與音樂自動標籤。ISMIS 資料集包含 12495 筆資料。因為 Matlab 的記憶體限制，計算全部的歌曲會使程式超過記憶體範圍。因此我們從資料集隨機挑選 1200 首歌做實驗，將風格當作 Target，總共有 6 個 Target。我們對風格做分群與音樂自動標籤。

在音樂分群的實驗中，我們對分群的結果計算 *Rand-index* 來評估分群的好壞。參考表 12 的分群實驗結果，我們將圖形投影成只有音樂物件的 domain 再對音樂分群。從結果可以發現，投影過後的圖形在分群的表現比較好，分別提升了 12% 和 17% 的 *Rand-index*。

在音樂自動標籤的實驗中，我們計算自動標籤的 *Accuracy*。參考表 13 的實驗結果，我們將圖形投影成音樂物件與 Target 的 domain，並對 Target 自動標籤。實驗結果顯示，投影圖的實驗結果較好，分別提升了 11% 與 10%。

我們定義 a=|SS|, b=|SD|, c=|DS| 和 d=|DD|，參考表 9 我們可以得知 a=4, b=0, c=2, d=9，則可以計算 *Rand-index* R：

$$R = \frac{(a+d)}{(a+b+c+d)} \tag{21}$$

代入後可以得到 R=0.86，R 界於 0 到 1 之間，越高的 R 值代表分群的效果越好。

(b)Evaluation measures of classification

在自動標籤中，我們計算 *Accuracy* 當作預測品質的標準。在表 10 表示分別有 3 種不同的 class，共 23 筆測試資料。*Accuracy* 為預測正確的筆數除以測試資料總數。以表 10 為例，*Accuracy* 為 0.69。*Accuracy* 的數值越高代表預測的效果越好。

4.3. 因數

表 11: 因數列表

Symbol	Meaning
q	特徵量化的 Token 數
r	量化特徵 Token 的相似 Token 連接數
ad	被投影的特徵 Domain
$level_x$	計算 SNN 相似度時，節點 x 的鄰接節點距離
$level_y$	計算 SNN 相似度時，節點 y 的鄰接節點距離
th_{SNN}	SNN 相似度的門檻值
α	Pagerank 的 damping factor

表 12 列出會影響實驗結果的因數，我們從圖形結構到音樂應用的參數依序說明。以下分成五個部份討論：

- 建構特徵域時的參數 q 與 r

  參考表 12 因數列表。q 代表量化的數目。為了配合實驗，我們統一將每種特徵各別量化為 q 個 token。r 表示特徵域的 token 與最相似的 r 個 token 連接，不同的 r 會產生不一樣的特徵域結構。

為基礎的各式特徵，其中包含 20 維的 MFCCs 特徵，每一維以單一高斯分布表示。我們將每一維高斯分布量化為數個 Token，以量化的 Token 代表各維度的 MFCCs。資料集的 Target 為風格。

4.2. 測量

在驗證的部份，我們對分群使用 *Rand-index* [24] 驗證分群效果。對自動標籤實驗時用 *10-fold cross-validation* 進行實驗，並計算 *Accuracy*。

(a)Clustering validity

在分群驗證的部份，我們使用 *Rand-index* 作為驗證分群效果的方法，給定資料的 Ground truth 為 C_{act}，預測分群的結果 C_{pre}，我們可以透過 *Rand-index* 計算分群效果得到一個界於 0 與 1 之間的 *R* 值。舉例說明，假設有 6 個音樂物件 $X=\{x1, x2, ..., x6\}$，原始的分群為 $C_{act}=\{\{x1, x2, x3\},\{x4, x5\}, \{x6\}\}$，預測的分群為 $C_{pre}=\{\{x1, x2, x3\}, \{x4, x5, x6\}\}$，對於每個預測的分群 *X*，有以下四種情況：

- *SS*：同一類的音樂被分到同一群
- *SD*：同一類的音樂被分到不同群
- *DS*：不同類的音樂被分到同一群
- *DD*：不同類的音樂被分到不同群

表 9:Rand-index 配對矩陣

	x_1	x_2	x_3	x_4	x_5	x_6
x_1		SS	SS	DD	DD	DD
x_2			SS	DD	DD	DD
x_3				DD	DD	DD
x_4					SS	DS
x_5						DS
x_6						

表 10: 標籤預測範例

	C_1	C_2	C_3
C_1	5	2	0
C_2	2	6	2
C_3	0	1	5

4.Experiment

在本研究中，我們對圖形投影成指定域的結構並降低結構複雜度，提升圖形的辨識力，在圖形中能更清楚表示各節點之間的關係。因此我們比對音樂應用在投影圖形與未投影圖形之間的結果。實驗顯示在投影過後的應用結果，可以比未投影的圖形還要好。

我們也利用框架的優點，提供多種不同的音樂應用，例如：音樂分群與音樂自動標籤。我們比較在兩種應用中，投影圖形的表現，並以實驗的數據進行討論。在實驗的部份我們先介紹使用的資料集：ISMIS[5] 資料集與 Artist20 [23] 資料集。接著討論驗證的方法以及實驗的因數，接著列出分群與自動標籤的實驗結果，最後列出我們實作的系統。

4.1. 設置

在在實驗中，我們使用兩種實驗資料集：ISMIS 2011 Contest: Music Information Retrieval 的 Music genre 資料集與 USPOP2002 子資料集 Artist20。兩個資料集包含不同的特徵，我們利用資料集的特徵建立多模態音樂圖形，並完成實驗。實驗的程式使用 MatlabR2010b 撰寫，電腦配備為 Intel i7，4GB Ram，並在 Windows 7 作業系統下執行。我們利用 Voicebox toolbox[6] 以及 Audio content analysis toolbox[7] 擷取特徵與訓練聲學模型。

(a)USPOP2002 subset Artist20

在 USPOP2002 子資料集 Artist20 中包含 1413 首歌曲，20 位歌手，格式為 32kbps 的單聲道 MP3 檔案，每首歌曲有 30 秒的長度。在建立圖形時，我們擷取 13 維的 MFCCs 特徵，將 MFCCs 對應歌手建立高斯混合模型。最後訓練出 20 個不同的高斯混合模型，並將每個模型視為 MFCCs 的 Token。此資料集的 Target 為歌手。

(b)ISMIS 2011 Contest: Music Information Retrieval Music Genre dataset

在 ISMIS 資料集中，有 12495 筆資料，6 種風格。此資料集提供以 MPEG-7

[5] ISMIS dataset : http://tunedit.org/challenge/music-retrieval?m=summary
[6] Voicebox toolbox : http://www.ee.ic.ac.uk/hp/staff/dmb/voicebox/voicebox.html
[7] Audio content analysis toolbox : http://www.audiocontentanalysis.org/code/

在對測試音樂自動標籤時，將測試音樂物件 Test 加入圖形。以圖 9 為例：$Test_{Tempo}=\{96\}$、$Test_{Average\ spectral\ centroid}=\{3.1\}$。在圖形中 Test 物件沒有與 Tag 的 Token 連接。表 8 為節點的 Pagerank 值。對於音樂自動標籤，我們觀察在 Tag domain 的 Pagerank 數值。選擇最高 Pagerank 數值的 Token 代表測試資料的預測 Tag。由 9 可知，在 Tag domain 最高的數值為 Rock 的 0.02。所以我們選擇 Rock 為預測的 Tag。

表 8: 各節點的 Pagerank 數值

Token	$\overrightarrow{PR}$
O_1	0
O_2	0.01
O_3	0.01
O_4	0.05
O_5	0.01
O_6	0.06
$Token_{Tempo}55$	0.01
$Token_{Tempo}73$	0.04
$Token_{Tempo}96$	0.29
$Token_{Tempo}109$	0.05
$Token_{Average\ spectral\ centroid}1.1$	0
$Token_{Average\ spectral\ centroid}1.4$	0.01
$Token_{Average\ spectral\ centroid}2.8$	0.06
$Token_{Average\ spectral\ centroid}3.1$	0.29
$Token_{Tag}Jazz$	0.01
$Token_{Tag}Rock$	0.02
Test	0.08

與馬可夫矩陣類似，當 i 增加到一定程度後，給定一個門檻 δ 使 $\| \overrightarrow{PR_i} - \overrightarrow{PR_i} \text{-}1 \| < \delta$ 後。我們得到一個遞迴式 (18)

$$\overrightarrow{PR} = M\overrightarrow{PR} \tag{18}$$

在 Pagerank 的計算過程中，若 M 不是機率轉移矩陣，當圖形中的節點沒有連出的邊或是連至 sink 節點時，則所有節點的 Pagerank 值 (i.e., $\{ \overrightarrow{PR_i}(i) | \ i = 1, 2, \ldots, n\}$) 不會穩定，使數值無法收斂。只有當矩陣為 Strong connected 時才會使 Pagerank 值迭代至收斂。為此加入阻尼係數 $(1-\alpha)$ 使矩陣符合 Strong connected。我們給定矩陣的節點為 α /n，我們修改 (18) 得到 (19) 的公式

$$\overrightarrow{PR_{i+1}} = (1-\alpha)M\overrightarrow{PR_i} + \alpha\vec{p}, \ where \ \vec{p} = [1/n]_{n\times 1} \tag{19}$$

也可以將 (19) 表示為 (20) 的形式

$$\overrightarrow{PR_{i+1}} = \begin{bmatrix} PR_{i+1}(1) \\ PR_{i+1}(2) \\ \vdots \\ PR_{i+1}(n) \end{bmatrix} = (1-\alpha)\begin{bmatrix} M_{1,1} & \cdots & M_{1,n} \\ M_{2,1} & \cdots & M_{1,n} \\ \vdots & \ddots & \vdots \\ M_{n,1} & \cdots & M_{n,n} \end{bmatrix} \times \begin{bmatrix} PR_i(1) \\ PR_i(2) \\ \vdots \\ PR_i(n) \end{bmatrix} + \alpha \begin{bmatrix} 1/n \\ 1/n \\ \vdots \\ 1/n \end{bmatrix} \tag{20}$$

利用 Pagerank 演算法做查詢時，我們以 $\vec{P}$ 作為查詢的 V_{query}。V_{query} 為 n-by-1 的向量。用 V_{query} 來代表查詢的節點。將向量中第 r 個元素的值設為 1，其他為 0。在音樂自動標籤的應用中，$\overrightarrow{PR}$ 為計算出來的結果，PR_1 到 PR_n 為測試資料對應圖形節點的 Pagerank 數值。此數值代表節點與查詢向量 V_{query} 的關聯度。

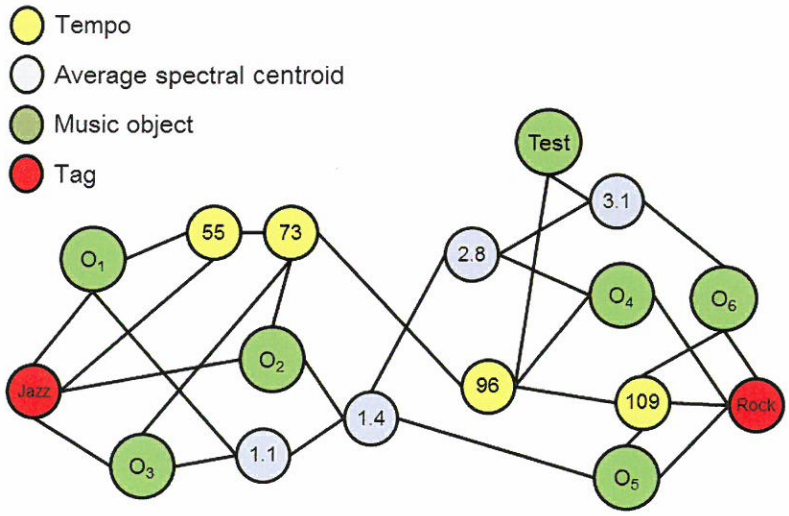

圖 9: 將測試資料加入圖形

表 7: 分群結果

Cluster	O_1	O_2	O_3	O_4	O_5	O_6
1	1	1	1	1	1	1
2	1	1	1	2	2	2
3	2	1	2	3	3	3
4	4	3	4	1	2	2
5	1	5	2	3	4	4
6	1	2	3	4	5	6

3.4.2. 音樂自動標籤

給定一個音樂資料集，我們根據資料集建立多模態音樂圖形 G。對每首音樂擷取不同的音樂特徵 FD，多模態音樂圖形包含各種不同的節點 $FD_{k,i}$，每個節點代表音樂的不同資訊。在自動標籤應用中，以建立好的多模態音樂圖形做為訓練資料集，對測試的音樂資料做自動標籤。

給定測試音樂物件 t，對 t 擷取音樂特徵。在自動標籤應用中，根據擷取出的 t 特徵，將音樂物件 t 與多模態音樂圖形中的特徵 Token 連接，將音樂物件 t 加入多模態音樂圖形 G。我們可以利用運算元對圖形做進一步的應用，例如：圖形投影。使應用的結果產生不一樣的效果。

最後我們利用 Pagerank [22] 演算法計算圖形 G 裡節點的 Pagerank 數值 PR。在音樂風格自動標籤的應用中，計算多模態音樂圖形各節點的 PR 值，在代表風格節點的 domain 中，以 PR 值最高的節點作為測試資料的風格標籤。

參考公式 (16)，給定一個節點 q，節點個數 n，$PR(q)$ 是由 In-link 節點 p 的 $PR(p)$ 根據 $Degree(p)$ 分散給每一個 Out-link 節點的數值，在最後加總的結果。

$$PR(q) = \sum \frac{PR(p)}{Degree(p)} \tag{16}$$

在圖形 $G = (V,E)$ 不包含 Isolated 節點時，若 $link\ (p,q) \in E$，則矩陣表示為 $M_{p,q} = 1/Degree(p)$。若否，則矩陣 $M_{p,q}$ 表示為 0。所有節點的 Pagerank 值可以表示為

$$\overrightarrow{PR_{i+1}} = \begin{bmatrix} PR_{i+1}(1) \\ PR_{i+1}(2) \\ \vdots \\ PR_{i+1}(n) \end{bmatrix} = M \times \begin{bmatrix} PR_i(1) \\ PR_i(2) \\ \vdots \\ PR_i(n) \end{bmatrix} = M \times \overrightarrow{PR_i} \tag{17}$$

接著合併所有群集之中最相近的兩個群集，產生一個新的群集。反覆合併群集的步驟直到只剩一個群集，就完成所有的分群。我們列出常見的距離定義：

- 單一連結聚合演算法 (Single-linkage agglomerative algorithm) 兩個群集之間的距離定義為兩群集之間，所有節點的兩兩距離之最小值
- 完整連結聚合演算法 (Complete-linkage agglomerative algorithm) 兩個群集之間的距離定義為兩群集之間，所有節點的兩兩距離之最大值
- 平均連結聚合演算法 (average-linkage agglomerative algorithm) 兩個群集之間的距離定義為兩群集之間，所有節點的兩兩距離之平均值

表 6: 最短距離矩陣

	O_1	O_2	O_3	O_4	O_5	O_6
O_1	0	1	1	2	3	3
O_2	1	0	1	1	2	2
O_3	1	1	0	2	3	3
O_4	2	1	2	0	1	1
O_5	3	2	3	1	0	1
O_6	3	2	3	1	1	0

以圖 6 為例子，我們以投影圖示範音樂分群。令 $level_x = 2$、$level_y = 1$、pFD 為 O、$th_{SNN}= 2$ 對 G 投影得到 PG。表 6 為圖形 PG 的最短距離矩陣 M。我們使用單一連接聚合演算法，對矩陣 M 做階層式分群。圖 8 是分群的 Dendrogram，表 7 為分群的結果

圖 8: 分群樹狀圖

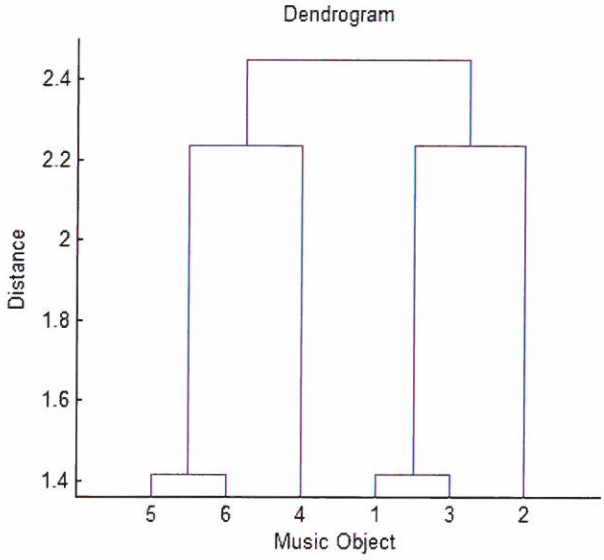

3.4. 圖形運算元

在我們提出的框架中包含許多的圖形運算元 [21]，利用運算元對圖形計算的結果完成音樂應用，詳細的運算元參考表 5 所示。

表 5: 圖形運算元列表 [21]

Operator	Function
Betweenness centrality	Graph metrics of path
Closeness centrality	Finding center
Average path length	Path length
Average cycle length	Cycle length
Shared nearest neighbors	Node metrics
Graph projection	Graph structure
Clustering coefficient	Graph metrics
Shortest paths	Link analysis
Homogeneity	Finding sub-graph
E-to-I ratio	Edge metrics
Graph degree	Edge metrics
Density	Graph metrics
Girth	Finding cycle
Diameter	Graph metrics
Radius	Graph metrics
Pagerank	Link analysis
HITS algorithm	Link analysis
Maximum clique	Finding sub-graph

應用

經過特徵擷取與建立圖形後，我們利用此架構進行一系列的音樂應用。利用框架提供的運算元，我們以音樂分群 與音樂自助標籤 的應用作為說明。

3.4.1. 音樂分群

我們利用階層式分群 (Hierarchical clustering) 對音樂分群。

Definition 6. 給定一個圖形 G，計算圖形各節點之間距離，得到距離矩陣 M。將每一個節點視為一個群集 (Cluster)。假設有 n 個節點，初始就有 n 個群集。

和他們各自的 Token。給定 $level_x = 2$、$level_y = 1$，pFD 為 O 和 FD_3。首先對 G 計算 SNN-based similarity，表 4 為音樂物件的相似度矩陣。

表 4: 音樂相似度矩陣

	O_1	O_2	O_3	O_4	O_5	O_6	Jazz	Rock
O_1	0	3	3	0	1	0	2	0
O_2	3	0	3	2	1	0	2	1
O_3	3	3	0	1	1	0	2	0
O_4	0	2	1	0	3	3	0	2
O_5	1	1	1	3	0	2	1	2
O_6	0	0	0	3	2	0	0	2
Jazz	2	2	2	0	1	0	0	1
Rock	0	1	0	2	2	2	1	0

參考表 4 我們得到 Token 之間的相似度。我們給定一個 Threshold th_{SNN}，對 pFD 的邊重構：將節點之間低於 th_{SNN} 的相似度視為沒有連線，在 pFD 中，初始就有音樂物件與 Tag 的邊，在投影後依舊保留著。參考圖 7，我們列出不同 th_{SNN} 的投影圖。

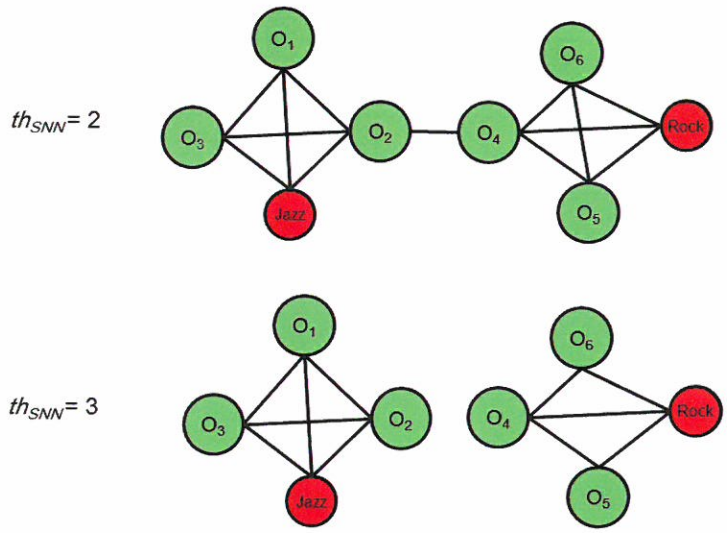

圖 7: 不同 th_{SNN} 下的投影圖

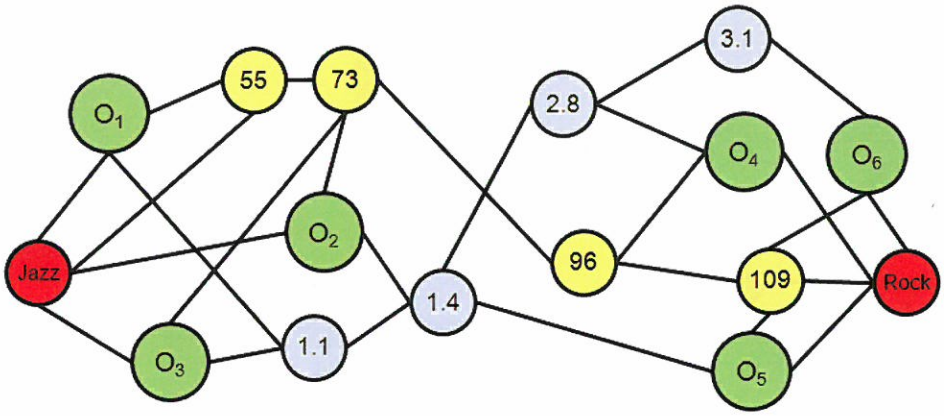

圖 6: 多模態音樂圖形

Definition 5 (SNN-based similarity). 對任意兩個節點 x 和 y 且 $x,y \in V$ 在 $level$ 內的 SNN-based similarity：

$$Sim_{SNN}(x,y,level_x,level_y) = |NN(x,level_x) \cap NN(y,level_y)| \quad (14)$$

$$NN(i,level_i) = \{node \mid node \in V, Shortest\text{-}path\text{-}length(node,i) \le level_i\} \quad (15)$$

參考表 3 我們對圖 6 用不同的 $level_x$ 與 $level_y$ 計算 $Sim_{SNN}(O_1,O_5, level_x, level_y)$。

表 3: 不同 levelx 下的 SNN 相似度

$level_x$	$level_y$	Sim_{SNN}
1	1	0
2	1	1
3	1	2
4	1	4
$level_x$	$level_y$	Sim_{SNN}
1	1	0
1	2	1
1	3	2
1	4	4

Example 6. 以圖 6 為例，給定多模態音樂圖形 $G = (V,E)$，G 包含不同的特徵域

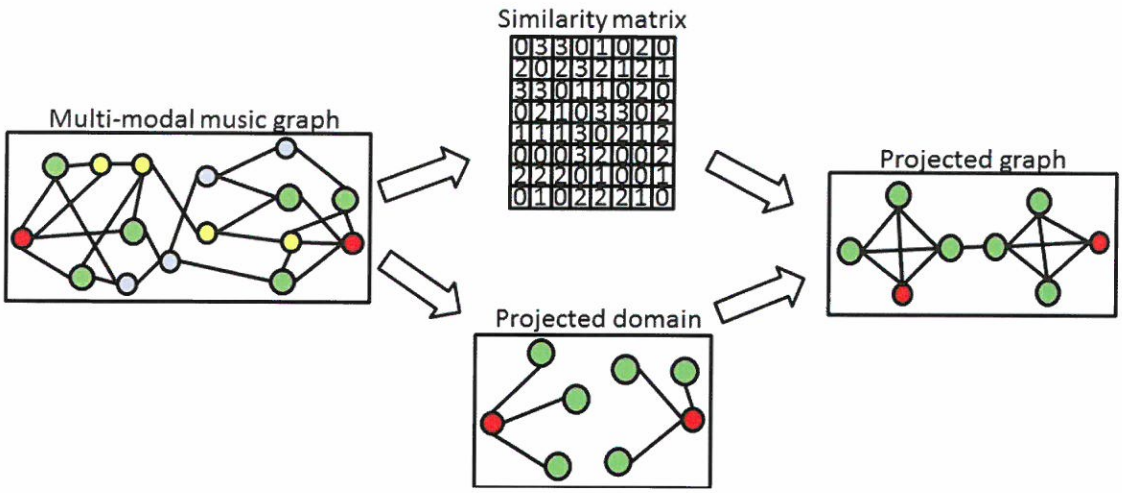

圖 5: 圖形投影示意圖

Definition 4 (Graph projection). 令給定一個多模態關聯圖 G = (V,E)

$$PG = Project_{SNN}(G, pFD, level_x, level_y, th_{SNN}) \tag{9}$$

pFD 為投影的 domain，$level_x$ 與 $level_y$ 是比較 SNN 相似度的鄰近節點範圍，th_{SNN} 為重構的門檻值。我們以 pFD 為基礎，以 SNN 相似度重構 pFD 的邊

$$pFD \subseteq V \tag{10}$$

$$V_{PG} = V_{pFD} \tag{11}$$

$$E_{PG} \subseteq V_{PG} \times V_{PG} \tag{12}$$

$$E_{PG} = \{(x,y) \mid x \in V_{PG}, y \in V_{PG}, Sim_{SNN}(x,y,level_x,level_y) > th_{SNN}\} \tag{13}$$

在多模態音樂圖形中，我們根據各種定義將節點連接。例如：將音樂擷取出的特徵連接至所屬的音樂物件。我們計算 pFD 中，兩節點之間的相似度：計算 x 在 $level_x$ 範圍內與 y 的 $level_y$ 範圍內共同節點的個數。我們以共同節點的數量作為 x 與 y 的相似度。

- E_{FF} 是連接 FD_k 的 Token，根據 Token 與同 FD_k 的其他 Token 之相似度。選擇最相似的 1 個 Token 連接。

我們說明圖形中另外兩種類型的邊：E_{OO} 與跨 FD 的 E_{FF}。

Example 5. E_{OO} 為音樂物件之間的邊。E_{FF} 為不同 FD 之間的 Token 連線。在建立多模態音樂圖形時，沒有定義 E_{OO} 與不同 FD 的 E_{FF} 邊，E_{OO} 與不同 FD 之間的 E_{FF} 可以經由 Operator 或使用者定義而產生。

圖 4 為表 2 的多模態音樂圖形 G。

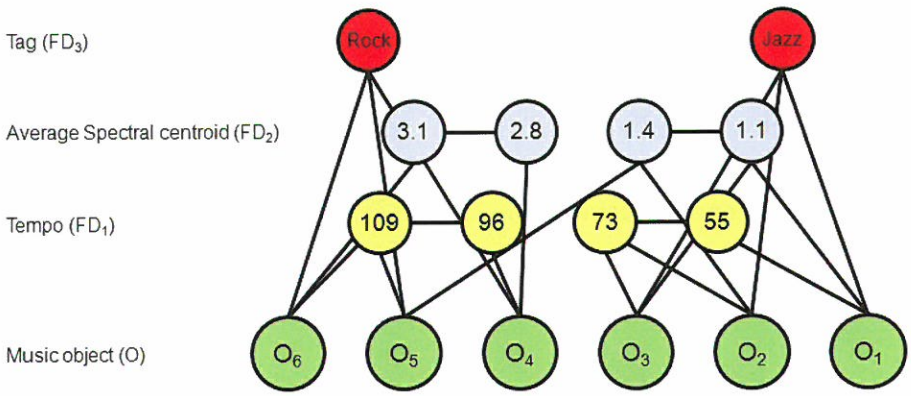

圖 4: 多模態音樂圖形與特徵域

3.3. 圖形投影

參考圖 5 的示意圖，對於多模態音樂圖形 G，圖形投影將圖形結構轉換為指定特徵域的對應關係。我們利用 *Shared nearest neighbors* [20] 計算節點之間的相似度，並以相似度重構圖形的邊。

Example 2. 參考表 2 的資料，我們說明量化的 Token。特徵有 Tempo，Average Spectral centroid 和 Tag，共三種特徵域。我們給定 FD_1 為 Tempo、FD_2 為 Average spectral centroid、FD_3 為 Tag。其中連續類型的特徵有兩種 FD_1= { '55' , '73' , '96' , '109' }、FD_2= { '1' , '1.4' , '2.8' , '3.1' }。而離散類型的特徵為 FD_3= { *'Jazz'* , *'Rock'* }。

Definition 2 (Graph). 給定音樂物件 O = { 'O_1' , 'O_2' ,… }，特徵域 FD，我們建立一個多模態音樂圖形 G

$$G = (V, E) \tag{3}$$

$$V = O \cup FD \tag{4}$$

$$E \subseteq V \times V \tag{5}$$

在初始的圖形中，我們定義音樂物件與特徵的連接關係。我們將音樂物件與所屬的特徵 Token 以邊連接。

Definition 3 (Edge construction). E_{OF} 為特徵節點與音樂物件之間的邊。E_{FF} 為特徵 Token 與特徵 Token 之間的邊。v_a 是音樂物件，v_b 是從音樂物件 v_a 擷取的特徵 token。

$$E = E_{OF} \cup E_{FF} \tag{6}$$

$$E_{OF} = \{(v_a, v_b) \mid v_a \in O, v_b \in FD\} \tag{7}$$

$$E_{FF} = \{(v_c, v_d) \mid v_c, v_d \in FD_i, \textit{the token } v_c \textit{ is 'similar' to the token } v_d\} \tag{8}$$

Example 3. 參考表 2 的資料。對任意 FD 裡的 Token $FD_{k,i}$，計算相同 FD_k 裡的所有 Token 之相似度。將相似度與 $FD_{k,i}$ 較高的 r 個 Token 連接在一起。

Example 4. 參考表 2 的資料集，我們建立多模態音樂圖形。在這個圖形中，有 6 個音樂物件 O = { *'O1'* , *'O2'* , *'O3'* , *'O4'* , *'O5'* , *'O6'* }，3 個特徵域。FD_1 為 Tempo 特徵、FD_2 為 Average spectral centroid 特徵、FD_3 為 Genre tag 特徵。在 FD_k 中包含各自的 Token。其中音樂物件 O_1 與 *'55'* 、*'1.1'* 、*'Jazz'* 的 Token 相連。O_2 與 *'73'* 、*'1.3'* 、*'Jazz'* 的 Token 相連，以此類推。

● 我們建立 E_{OF} 將音樂物件與 FD 連接，各自連接到所屬的特徵 Token 上。

的方法。對於離散的特徵，例如：風格標籤、情緒標籤的標籤類特徵。我們將每一個標籤視為一個 Token，或是基於 *Ontology-based* 相似度將多個標籤視為一個 Token。

表 2: 原始資料與量化後的資料

Source data				Quantized data			
Music	Tempo	Average spectral centroid	Tag	Music	Tempo	Average spectral centroid	Tag
O_1	55	1	Jazz	O_1	55	1.1	Jazz
O_2	75	1.3	Jazz	O_2	73	1.4	Jazz
O_3	71	1.2	Jazz	O_3	73	1.1	Jazz
O_4	96	2.8	Rock	O_4	96	2.8	Rock
O_5	113	1.5	Rock	O_5	109	1.4	Rock
O_6	105	3.1	Rock	O_6	109	3.1	Rock

Example 1. 以表 2 的表格為範例，我們有 6 首歌曲，3 種特徵域 (Feature domain)。對連續類型的特徵 Tempo 與 Average spectral centroid 特徵各量化為 4 個 Token，離散類型的 Tag 特徵則是每個 Tag 各視為一個 Token。

3.2. 建立圖形

在得到音樂的特徵以及各種特徵之間的關係後，我們定義特徵域 FD 和多模態音樂圖形 G：

Definition 1 (Feature domain). 給定音樂物件的特徵域為

$$FD = FD_1 \cup FD_2 \cup ... \cup FD_k \tag{1}$$

其中每個特徵域裡的 Token 為

$$FD_k = \{FD_{k,1}, FD_{k,2}, ...\} \tag{2}$$

特徵域的類型有連續與離散的特徵。

- 我們量化連續類型的特徵，將量化後的特徵視為不同的 Token。
- 對於離散類型的特徵，例如：標籤。將不同的標籤皆視為不同的 Token。
- 各種類型的特徵皆可以依照使用者的定義，將不同的 Token 合併為一個 Token。

3.1. 特徵

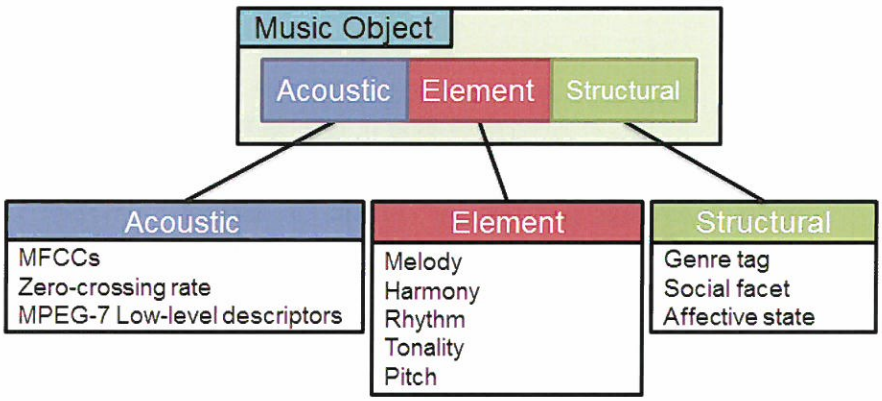

圖 3: 音樂特徵分類 [4]

參考圖 3 的特徵類型 [4]，我們歸納音樂物件的特徵，並將特徵分成三類：聲學特徵 (Acoustic feature)、元素特徵 (Element feature)、結構特徵 (Structural feature) 三種分類，以這三種類形的特徵描述音樂。

- 聲學特徵

  聲學特徵是針對聲音訊號的物理量之描述。聲學特徵擷取是一個聲音訊號壓縮的過程，使用數值描述聲音的各種狀態。例如：過零率 (Zero-crossing rate)、頻率 (Frequency) 和梅爾倒頻譜係數 (Mel-frequency cepstral coefficients, MFCCs)。

- 元素特徵

  元素特徵是針對音樂形式的基本元素之描述。元素特徵有連續 (Successive) 的特性，用以描述一個音樂片段，表示音樂在一段時間內的變化。例如和聲 (Harmony)、旋律 (Rhythm)、音調 (Tonality) 和節奏。

- 結構特徵

  結構特徵是表示人們對音樂意義的描述，包含對音樂的理解及抽象的詮釋。例如風格標籤 (Genre tag)、情緒 (Emotion)。

特徵的內容分為連續與離散的類型。對於連續的數值類特徵，例如：過零率、MFCCs，我們將連續類型的特徵利用量化分成數個 Token，用這些 Token 代表被量化的特徵。例如使用 *Linde-Buzo-Gray Algorithm (LBG)* [19] 演算法作為量化

參考圖 2 的系統架構圖，在本研究中提出一套整合型的音樂分析框架。將音樂資料建立圖形結構，建構特徵之間的關係。我們利用多模態音樂圖形解決特徵的語意落差問題，將不同模態的音樂特徵組織成音樂圖形，建立模態之間的關聯性。為了降低圖形的複雜度，並降低語意落差的影響，我們加入圖形投影運算元，重構節點之間的邊，將圖形轉換為指定域的對應關係。最後利用此框架完成多種音樂應用：音樂分群、音樂自動標籤、音樂相似度計算。以下分成五個功能區塊並且依各小節分別說明。

- 特徵
  對音樂擷取各類型的音樂特徵，說明音樂特徵的性質。依照資料類型，我們的特徵有連續與離散的類型。連續特徵是在一定的區間內，可以任意取值的連續數值，我們可將連續的數值量化為數個 Token；離散特徵則否，例如：標籤。我們將每類標籤單獨視為 Token，或是基於 Ontology-based 相似度將數個標籤視為一個 Token，並以這兩類特徵的 Token 當作圖形中的特徵節點。
- 建立圖形
  利用特徵 Token 建立圖形，並建構多模態音樂圖形的結構。我們經過特徵擷取之後得到許多特徵 Token，連接特徵 Token 與音樂物件，並定義各類型 Token 之間的關係。
- 圖形投影
  我們介紹運算元之一的圖形投影。在多模態音樂圖形中，當音樂數量增加時會衍生出相關的圖形結構問題，使圖形的鑑別力下降。我們設計圖形投影方法去解決這個問題，以提升特徵的鑑別力。
- 圖形運算元
  我們在這一節列出框架中的 Operators 與類型。
- 應用
  這一節描述如何利用 Operators 對圖形完成音樂應用，並說明音樂分群與自動標籤的應用的方法。

測模型，並且依照模型的預測結果，對音樂自動標籤。在 Yannis Panagakis 和 Constantine Kotropoulos [16] 的研究中，利用 Low-rank representation 對多標籤 (Multi-label) 的音樂進行自動標籤並且有 50% 的 Precision 和 23% 的 Recall。在 Riccardo Miotto 和 Gert Lanckriet [17] 的研究中以標籤之間的關係建立模型，對每個標籤與音樂建立語意多項式來代表每個標籤對音樂的機率；以 Dirichlet 混合模型評估標籤的語意。將音樂標籤映射在 Dirichlet 混合模型中，並根據在空間裡的分布完成自動標籤應用。以 CAL500dataset 實驗，利用 SVM 與標籤預測可以得到 0.475 的 Precision 與 0.235 的 Recall。在 Ling Chen、Phillip Wright 和 Wolfgang Nejdl [18] 的研究中利用標籤特徵做分析，並藉由 Collaborative tagging data 增加音樂風格的辨識率。使用從社群網路上得到的資料：如 Last.fm 網站得到的標籤作為特徵，實驗的結果有 87.23% 的準確率。

3.Approach

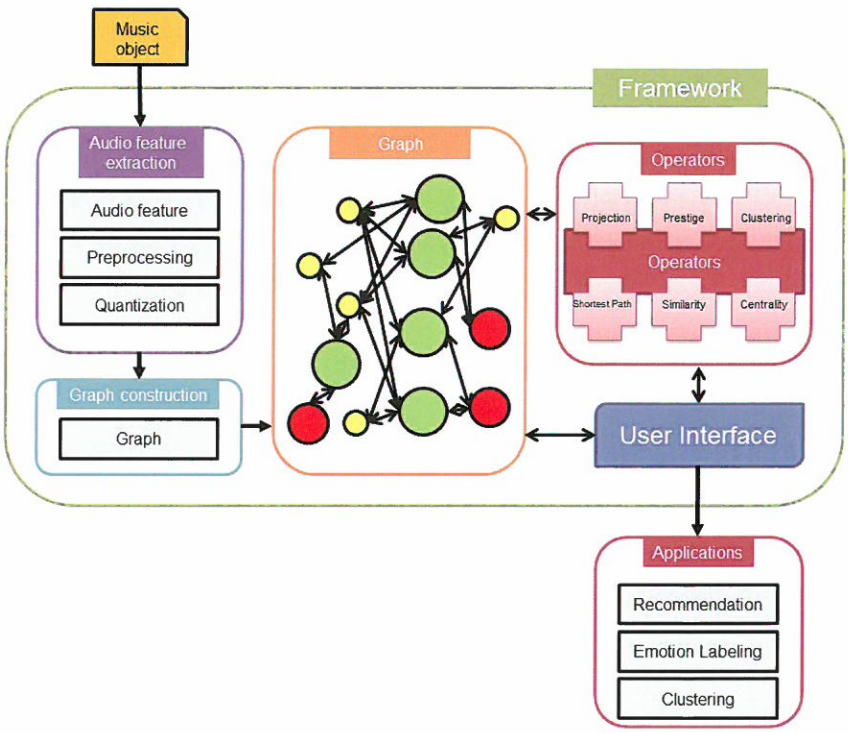

圖 2: 系統架構圖

feature 和 Low-level feature 之間有語意落差。若在圖形上表示跨模態，可以通過特徵節點之間的連接定義其關係。在 Peter Dunker、Christian Dittmar、Andre Begau、Stefanie Nowak 和 Matthias Gruhn [9] 的研究中，針對音樂的高階特徵如情緒和風格特徵進行應用。針對語意做分類，設計一個應用程式播放音樂和圖片。讓使用者定義兩者的關係，將音樂與圖片作跨模態的應用。在 Fang-Fei Kuo、Meng-Fen Chiang、Man-Kwan Shan 和 Suh-Yin Lee [10] 的研究中利用情緒做音樂推薦，提出一個新的模型用來表示情緒。並利用 MMG 建立圖形，對電影音樂建立模型。將情緒與音樂特徵做連接，有 85% 的準確率。

2.4. 圖形投影

在社群網路分析的網路定義中，其中一種是將社群網路分為 One-mode network 和 Two-mode network [11]。One-mode network 指的是只有一種角色 (Actor set) 的關係網路，最常見的人與人之間構成的網路即是此類，單純是物件與物件之間的關係。而 Two-mode network 為內部有兩種不同種類的節點。在社群網路分析中投影是將 Two-mode network 轉換成 One-mode network，以針對單一角色的網路作分析。在 Peter Hoff、Adrian Raftery 和 Mark Handcock [12] 的研究中提出一個人際關係模型，認為影響人與人之間關係的因素，存在於在無法觀測到的空間。透過投影方法將無法觀測到的網路空間，呈現在可觀察的空間裡。並藉此探討網路中的關係。

2.5. 音樂分群應用

從音樂集合中找出相似的音樂分群。在 Tao Li、Mitsunori Ogihara、Wei Peng、Bo Shao 和 Shenghuo Zhu [13] 的研究中，利用 Bimodal learning 根據不同特徵分群，並且提出一個分群的框架，有 47% 的準確率。在 Rudi Cilibrasi、Paul Vitanyi 和 Ronald De Wolf [14] 的研究中，針對音樂 MIDI 文件做分群。利用壓縮的觀念以 Kolmogorov complexity 方法對 MIDI 編碼。得到 0.86 的 Normalized tree benefit score。 在 Dong-Moon Kim、Kun-Su Kim、Kyo-Hyun Park 和 Jee-Hyong Lee 和 Keon-Myung Lee [15] 的研究中，從使用者的音樂播放清單分析使用者的喜好。並提出 Dynamic k-means clustering algorithm 對使用者音樂播放清單中的音樂分群，並利用分群的結果去推薦使用者可能喜歡的音樂。

2.6. 音樂自動標籤應用

以人力標記大量音樂的標籤是耗時費力的。為了增加效率，研究者建立預

樂物件資訊之間的關係。在 Arram Bae、Doheum Park、Sehee Lee 和 Juyong Park [5] 的研究中以社群網路分析的方法，對大型數據的古典音樂做資料探勘。將音樂的各種資訊以圖形連接，並且使用各種網路分析的參數：Eigenvector centrality、Betweenness centrality 以證明音樂的圖形結構是有效的，其音樂圖形的結構和特性與一般的網路結構類似，可以進行各種應用。在 Marian Zsuzsanna 和 Christian Sacarea[6] 的研究中，嘗試定義音樂物件的組成，認為音樂存在音樂基因 (Music genes)。音樂基因由許多特徵組成，將音樂基因連接在一起可以形成一首音樂，進一步提出組成音樂的邏輯；利用概念圖 (Conceptual graphs) 來描述音樂，並以人類邏輯定義音樂。將音樂特徵分為不同的層次，連接不同特徵與音樂物件，並使音樂有圖形的基礎。

2.2. 跨模態方法

在本研究中，模態是不同類型的特徵或屬性，例如：文字與聲音。以文字為例，許多文字可以組成一篇文章，我們可以在一篇文章中搜尋文字；對於聲音，我們可以聽出同一種聲音。以上為單一模態的辨識應用，而跨模態則是利用單一模態去應用各種不同模態的方法。例如文字與聲音屬於不同的模態，利用文字去搜尋聲音就是一種跨模態的應用。在文字與聲音之間存在語意落差問題，結合不同模態應用是跨模態應用的難處。在 Jia-Yu Pan、Hyung-Jeong Yang、Christos Faloutsos 和 Pinar Duygulu [7] 提出的 Mixed media graph (MMG) 架構中，將多媒體的各種多模態特徵連接在一個圖形結構中；利用 Random Walk With Restart (RWR) 計算節點之間的相似性，並應用於跨模態分析。在 Paolo Cremonesi、Antonio Tripodi 和 Roberto Turrin [8] 的研究提到，過去的推薦系統主要是針對單域的方法，例如論文的引用情形；而 Cross-modal 則是針對多域的應用，例如推薦看電視的行為時，使用者可以看電影、聽音樂、找朋友、可以推薦的項目涉及到多種領域。基於此種關係提出一個共同的框架，利用使用者的協同過濾 (Collaborative filtering) 提出一個圖形的結構，並連接使用者與各種領域的屬性，在圖形上找出與使用者類似的結構，藉此找到跨模態關係，並利用此關係建立推薦系統。

2.3. 跨模態的音樂資訊檢索

跨模態的音樂檢索，利用跨模態的性質，從已知的音樂特徵去發掘不同領域的特徵。例如在音樂特徵的分類上，Zhou-Yu Fu et al. [1] 的研究中將其分為 Top-level、Mid-level、Low-level；並在其中認為 Top-labels feature 與 Mid-level

標籤預測的應用中，針對 Pagerank 的計算方法提出 Algebraic solution 與 Iterative method。兩種方法預測標籤的準確率均有 75%，而 Algebraic solution 只需要 Iterative method 的 20% 的計算時間。

在本研究中，我們針對語意落差提出解決的方法，利用圖形組織音樂與特徵，建構各種音樂特徵與音樂物件的關係，建立多模態音樂圖形。另外，我們也觀察到，在多模態音樂圖形中，特徵的數量固定，當音樂物件的數量遠大於音樂特徵時，少數的特徵會被大量的音樂連接，造成特徵的 Degree 大幅上升，使圖形複雜化。例如：路徑分析，因為可替代路徑增多，我們難以利用路徑判斷節點之間的關係。

為了解決圖形結構的問題，我們利用圖形投影 (Graph projection) 重構圖形。將圖形結構從音樂物件對特徵節點的結構，投影成我們指定的結構。例如：在「音樂物件、音量、風格」的圖形中，以音量為基礎，將圖形投影成「音樂物件、風格」的結構。將特徵節點重構成指定域 (Domain) 之間的邊，以期能更清楚表達物件之間的關係。

最後我們提出一個音樂分析框架，整合多模態音樂圖形與圖形運算元完成多項音樂應用：音樂分群、音樂自動標籤、音樂相似度計算。我們在音樂應用中使用圖形投影調整圖形結構，提升音樂應用的效果，例如：音樂自動標籤的 Accuracy 與音樂分群的 Rand-index。

2.Related work

在這一章我們列出多模態音樂圖形的相關研究。首先是圖形架構與跨模態方法，在基於圖形的音樂資訊檢索方法與跨模態方法中，我們討論如何利用圖形組織音樂，與跨模態應用的方向。在跨模態的音樂資訊檢索中，我們介紹各種音樂上的跨模態應用，接著是圖形投影應用的範圍，最後是音樂分群應用與音樂自動標籤應用的相關研究。

2.1. 基於圖形的音樂資訊檢索方法

基於圖形的音樂資訊檢索，其特色是以圖形的形式完成各項應用。圖形以節點和邊組成，將音樂物件與特徵定義為節點並以邊相連。將多首音樂物件組成的圖形連接形成一個音樂資訊集合，以規劃好的特徵節點作為連接的路徑，用以表示音

態特徵解決音樂應用問題便是一項挑戰。

在音樂檢索的領域中，研究多模態音樂應用是重要的任務。在 The International Society for Music Information Retrieval (ISMIR) 研討會中有許多音樂相關應用，例如：音樂情緒辨識、音樂自動標籤、音樂分群等，這些多是針對特定應用所設計的方法。我們在本研究中提出一個音樂應用框架，此框架利用圖形整合不同模態的特徵，利用此框架可以完成不同的音樂應用。

在音樂特徵之間有著語意落差的問題。參考圖 1 在 Zhou-Yu Fu、Guo-Jun Lu、Kai-Ming Ting 和 Deng-Sheng Zhang [1] 的研究中將聲音特徵分為三類：低階特徵 (Low-level feature)、中階特徵 (Mid-level feature)、高階標籤 (Top-level labels)；並認為高階標籤與中低階特徵之間存在著語意落差的問題，難以利用中低階特徵去描述高階標籤。例如：風格是「Rock」的音樂中，其低階聲音特徵「過零率」與「梅爾倒頻譜係數」的數值就各不相同，難以找到合適的低階特徵去定義高階標籤。在 [1] 說明，要解決語意落差問題時，需要將 Mid-level 與 Low-level features 對應 Top-level labels 建立模型；使得聲音訊號可以映射 (Mapping) 至 Top-level 的各項特徵，讓各種應用可以透過機率模型來實現。參考表 1 以 CAL500 數據集針對音樂標記 (Music annotation) 的應用為例，展示了利用 MFCCs 特徵和各種分類器的效果。

此外，我們也考慮音樂內容之間的關聯性。在音樂認知心理學中，蔡振家 [2] 認為音樂包含四種層次：聲學層次 (Acoustic level)、語彙層次 (Lexical level)、句法層次 (Sentence Level)、言談層次 (Discourse level)。聲學層是對聲音的辨識，語彙層是對音樂歌詞意義的認知，句法層是辨識句子組成片段結構後的意義，言談層是句子之間的前後文關係，例如：主歌與副歌的關聯。由此可知在音樂的組成中，每個層次皆有一定的關聯，我們可以利用音樂的關聯性解決特徵之間的語意落差問題，將不同模態的屬性建立相互關係。

在我們過去的研究中，Jia-Lien Hsu 和 Yen-Fu Li [3] 提出了利用圖形描述音樂物件與特徵之間的關係，完成以圖形為基礎的標籤預測。將音樂物件與特徵定義為圖形上的節點，在圖形上分為音樂物件層與各種特徵層，並且定義特徵與特徵之間的邊為 FF link (Feature-Feature link)，音樂物件與特徵之間的邊為 OF link (Object-Feature link)。在標籤預測的應用中，將訓練資料建立圖形結構，再將測試資料加入圖形中，並計算每個節點的 Pagerank 數值；根據各節點的數值進行標籤預測，有 75% 的準確率。在 Chien-Chang Huang 和 Jia-Lien Hsu [4] 的研究中以圖形為基礎，提出一個音樂應用框架，用一致性的方法完成多個 MIR 應用。在

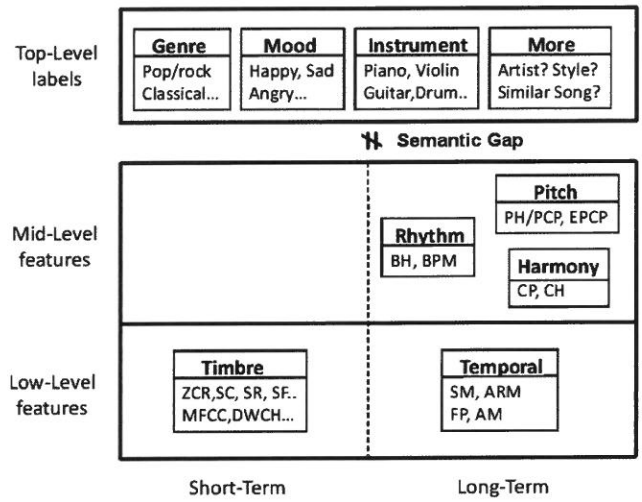

圖 1: 聲音特徵與語意落差 [1]

表 1: CAL500 數據集在音樂標記演算法的表現 [1]

Method	Features	Classifier	Precision-At-10	AUC
MixHier	dMFCCs	GMM	0.265±0.007	0.71±0.004
Autotag	dMFCCs	Adaboost	0.281	0.678
CBA	dMFCCs	CBA	0.286	0.765
AudioSVM	dMFCCs*MuVar^2	SVM	N/A	0.78
AffinitySVM	dMFCCs*MuVar^2	SVM+SG	N/A	0.85

These methods are cited from [1]

1.Introduction

音樂有多種模態，這些不同模態的之間不一定有相關性，我們稱為語意落差。在分析音樂時，不同模態的特徵對應用的鑑別力各不相同，例如：專輯與每分鐘節拍數 (BPM)。以查詢歌手的應用為例：使用專輯去搜尋會比搜尋 BPM 來得有效率。但在搜尋歌曲的節奏時，BPM 又比專輯更有鑑別力。所以，如何運用不同模

多模態音樂圖形之研究[1]

學生：何邱元　指導教授：徐嘉連[2]
輔仁大學 資訊工程學系

摘　要

在本研究中我們提出一個基於圖形的音樂檢索框架，用以解決音樂特徵的語意落差與完成音樂的多模態應用。不同模態的音樂特徵之間有語意落差的問題，例如 MIDI 和情緒標籤的語意落差，會影響音樂應用的效果。在本研究中，我們利用圖形組織音樂特徵，例如：多模態音樂圖形。為了降低圖形的複雜度，我們提出圖形投影 (graph projection) 運算元。以節點之間的相似度為基礎，從特徵 domain 重構圖形的結構，降低圖形的複雜度。我們利用此圖形框架實現音樂分群與音樂自動標籤的應用，並實驗圖形投影對這些應用的效果。根據實驗的結果，在這兩種應用中，投影過的圖形得到的實驗結果比未投影的圖形好。

關鍵詞：圖形投影、多模態、圖形 。

[1] 本論文為國科會 (國科會計劃編號 NSC-101-2221-E-030-008 和 NSC-102-2218-E-030-002) 之補助研究
[2] 論文通訊作者：新北市新莊區中正路 510 號，輔仁大學資訊工程學系 E-mail: alien@csie.fju.edu.tw

The study and implementation of Nd-doped cw all-solid-state red lasers at 671 nm

Lien-Bee Chang[1] and Yu-Yun Chen

Department of Physics, Fu Jen Catholic University, Taipei 242, Taiwan, ROC

Abstract

Diode-pumped Nd-doped continuous-wave lasers with different doping concentration operating at 1342 nm and red lasers at 671 nm generated by intra-cavity frequency doubling using a type-I critical phase-matched nonlinear optical crystal LiB_3O_5 (LBO) were investigated.

At the incident pump power of 12 W, over 1.8 W of 1342 nm radiation was obtained when a 6-mm-thick, 0.5-at.% Nd:YVO_4 laser crystal was used and the corresponding optical conversion efficiency reached 15%. In addition, about 130 mW at 671 nm was generated by a combination of a 10-mm long LBO nonlinear crystal and either a Nd:$GdVO_4$ or a Nd:YVO_4 crystal with Nd-doping concentration of 0.3 at.% and a dimension of 3x3 mm^2 in cross-section and 8 mm in length as the pump power increased to 20 W.

Key words: Nd:YVO_4、Nd:$GdVO_4$、LBO、1342 nm、671 nm、Nonlinear optics

[1] Corresponding author. Tel., +886-2-29052018; fax, +886-2-29021038
E-mail address: lbchang@mail.fju.edu.tw

12. C. Du, S. Ruan, Y. Yu, and F. Zeng, "6-W diode-end-pumped Nd:$GdVO_4$/ LBO quasi-continuous-wave red laser at 671 nm," Opt. Express, vol. 13, p.2013, 2005.
13. T. Jensen, V.G. Ostroumov, J.P. Meyn, *et al.*, "Spectroscopic characterization and laser performance of diode-laser pumped Nd:$GdVO_4$," Appl. Phys. B, vol. 58, p. 373, 1994.
14. J. Saikawa, Y. Sato, T.Taira , O. Nakamura and Y. Furukawa, "Efficient 1.3- m laser oscillation and heat generation characteristics in $NdGdVO_4$ laser under direct pumping into $^4F_{3/2}$ emitting level" , Conference on Lasers & Electro-Optics (CLEO), P.334, 2005.
15. CASTECH, NLO crystal "Lithium triborate (LiB_3O_5, LBO)," product catalog (Fuzhou, Fujian, China).
16. J. A. Armstrong, N. Bloembergen, J. Ducuing, and P. S. Pershan, "Interactions between Light Waves in a Nonlinear Dielectric," Phys. Rev., vol. 127, pp. 1918-1939, 1962.

Recevied Oct 30, 2013
Revised Mar 31, 2014
Accepted May 7, 2014

遠。這是因為無論是在晶體本身的純度上或者是雷射鏡片的鍍製上，仍然具有極大的改善空間。

References

P. Zeller and P. Peuser, "Efficient, multi-watt, continuous-wave laser operation on the $^4F_{3/2}$- $^4I_{9/2}$ transition of Nd:YVO_4 and Nd:YAG," Opt. Lett., vol. 25, pp. 34-36, 2000.

V.A. Sychugov, V.A. Mikhailo, V.A. Kondratyuk, *et al.*, "Short-wavelength (λ=914 nm) microlaser operating on an Nd:YVO4 crystal," Quantum Electron., vol.30, p. 13, 2000.

H. Zhang, J. Liu, J. Wang, *et al.*, "Characterization of the laser crystal Nd:$GdVO_4$," J. Opt. Soc. Am. B, vol. 19, p. 18, 2002.

Y.D. Zavartsev, A.I. Zagumennyi, F. Zerrouk, *et al.*, "Diode-pumped quasi-three-level 456-nm Nd:$GdVO_4$ laser," Quantum Electron., vol. 33. pp. 651-652, 2003.

C. Czeranowsky, M. Schmidt, E. Heumann, *et al.*, "Continuous wave diode pumped intracavity doubled Nd:GdVO4 laser with 840 mW output power at 456 nm," Opt. Commun., vol. 205, pp. 361-363, 2002.

A. Agnesi, G.C. Reali, and P.G. Gobbi, "430-mW single-transverse-mode diode-pumped Nd:YVO_4 laser at 671 nm," IEEE J. Quantum Electron., vol. 34, p. 1297, 1998.

J.L. He, G.Z. Luo, H.T. Wang, *et al.*, "Generation of 840 mW of red light by frequency doubling a diode-pumped 1342 nm Nd:YVO_4 laser with periodically-poled $LiTaO_3$," Appl. Phys. B, vol. 74, p. 537, 2002.

A.Y. Yao, W. Hou, X.C. Lin, *et al.*, "High power red laser at 671 nm by intracavity-doubled Nd:YVO_4 laser using LiB_3O_5," Opt. Commun. vol. 231. p. 413, 2004.

A. Agnesi, A. Guandalini, and Giancarlo Reali, "Efficient 671-nm pump source by intracavity doubling of a diode-pumped Nd:YVO_4 laser," J. Opt. Soc. Am. B, vol. 19, p. 1078, 2002.

A. Agnesi, A. Guandalini, G. Reali, *et al.*, "High-brightness 2.4-W continuous-wave Nd:$GdVO_4$ laser at 670 nm," Opt. Lett., vol. 29, pp. 56-57, 2004.

H. Zhang, C. Du, J. Wang, *et al.*, "Laser performance of Nd:$GdVO_4$ crystal at 1.34 m and intracavity double red laser," J. Crystal Growth, vol. 249, pp. 492-493, 2003.

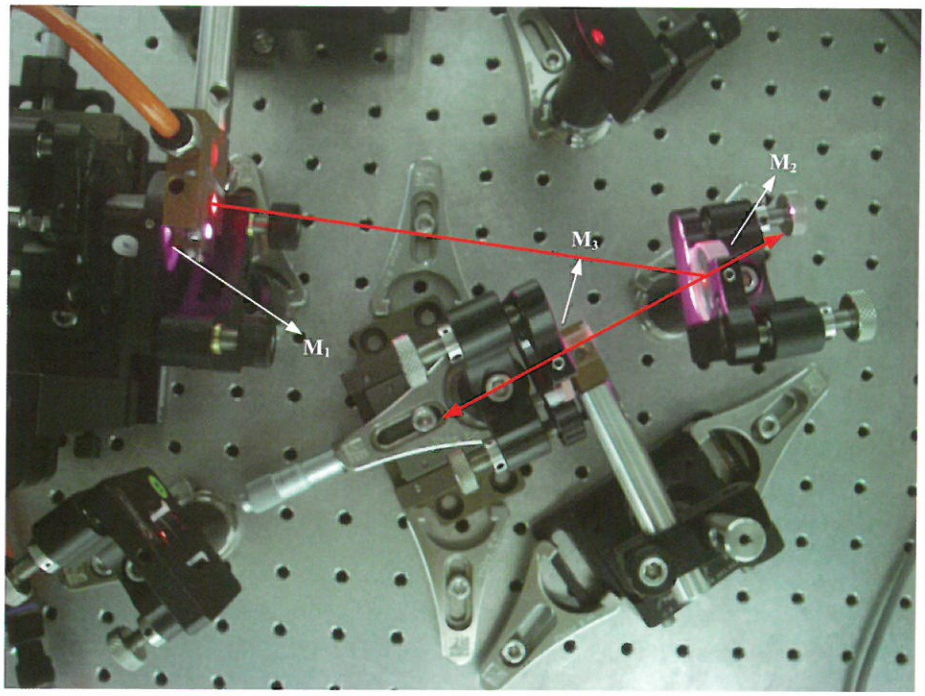

圖八紅光雷射實際光路圖

結　論

以自製雷射鏡，架設紅外光及紅光雷射系統。以不同 Nd 原子摻雜濃度的 $Nd:YVO_4$ 及 $Nd:GdVO_4$ 作為增益介質，測量其輸出功率的大小。

在 1342 nm 雷射輸出功率方面，當 Pump Power 為 12W 下，0.5 % $Nd:YVO_4$ 具有最大輸出功率約為 1.8 W，其斜率為 21 %。其他三種增益介質的轉換斜率分別為：0.3 % $Nd:YVO_4$ 時，斜率為 20 %， 而 $Nd:GdVO_4$ 時，斜率為 19.4 %，0.5 % $Nd:GdVO_4$ 時，斜率為 20.3 %。

在 671 nm 紅光雷射部分，其輸出功率分別為：0.3 % $Nd:YVO_4$ 輸出功率為 131 mW，而 0.3 % $Nd:GdVO_4$ 輸出功率為 125 mW，這與文獻十 Agnesi 等人以 10 W 的 808 nm 半導體雷射光激發，產生 2.4 W 的 671 nm 的紅光轉換效率相去甚

最後針對所有增益介質的輸出功率做比較，如圖七所示。由圖中可明顯看出，當增益介質摻雜濃度較高時，其 1342 nm 雷射光輸出功率皆高於摻雜濃度較低的增益介質。增益介質的長度相較於摻雜濃度來說，並未對輸出功率產生太大的影響，這可能是激發光源的有效被吸收長度遠短於增益介質實際長度的緣故。

Nd原子摻雜濃度為0.5 % 的Nd:YVO_4增益介質在具有最大輸出功率約為1.8 W。

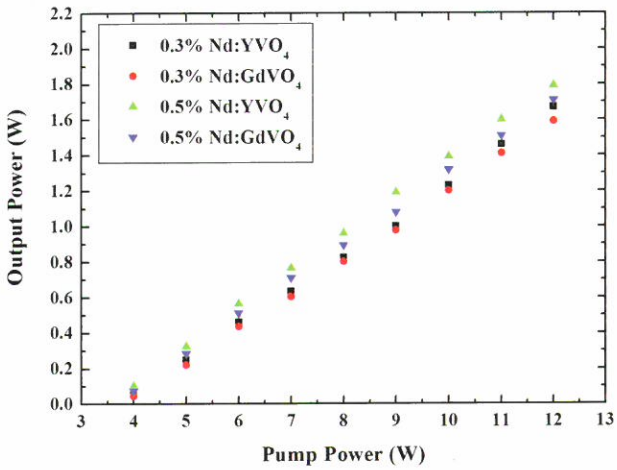

圖七 所有增益介質的輸出功率比較

二、671 nm 紅光雷射

圖八為紅光雷射實際光路圖。分別以 0.3 % Nd:YVO_4 及 0.3 % Nd:$GdVO_4$ 作為增益介質，並且理論計算出適當的斑點尺寸 (spot size) 進而決定穩定共振腔的長度。當波長為 1342 nm 的紅外雷射光輸出穩定後，於共振腔中加入倍頻晶體 LBO，並調整晶體角度以符合其相位匹配角。當紅光出現後，再進行微調使其功率達到最大。實驗使用的 pump power 為 20 W。

增益介質為 0.3 % Nd:YVO_4 時，連續式紅光輸出功率為 131 mW。當增益介質換成 0.3 % Nd:$GdVO_4$ 時，連續式紅光輸出功率 125 mW。

Power 皆為 4 W。由關係圖可以發現當增益介質為 $Nd:YVO_4$ 時的輸出功率皆大於增益介質為 $Nd:GdVO_4$ 時的功率。原因可能與 $Nd:YVO_4$ 對於波長為 1342 nm 的增益較大有關，故相對於 $Nd:GdVO_4$ 而言，$Nd:YVO_4$ 具有較大輸出功率。圖六中當摻雜濃度為 0.5 % $Nd:YVO_4$ 時，其斜率為 21 %，摻雜濃度為 0.5 %$Nd:GdVO_4$ 時，斜率為 20.3 %，而兩晶體開始有受激輻射輸出時的 Pump Power 同樣為 4 W。在圖中仍然可看出與圖五相同的現象。$Nd:YVO_4$ 相對於 $Nd:GdVO_4$ 而言，1342 nm 雷射光的輸出功率仍然較大。

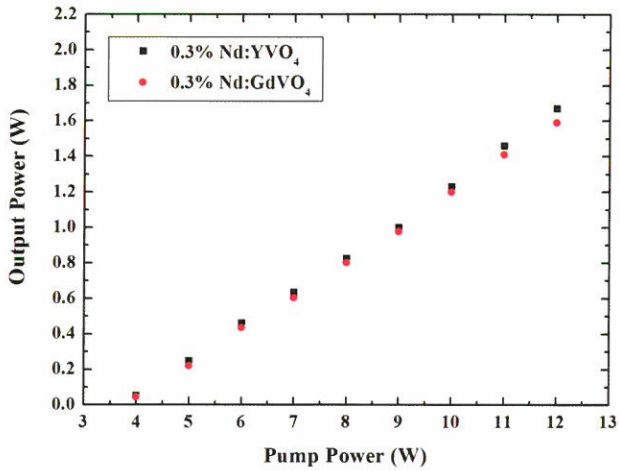

圖五 Nd 原子摻雜濃度為 0.3 % 輸出功率的比較

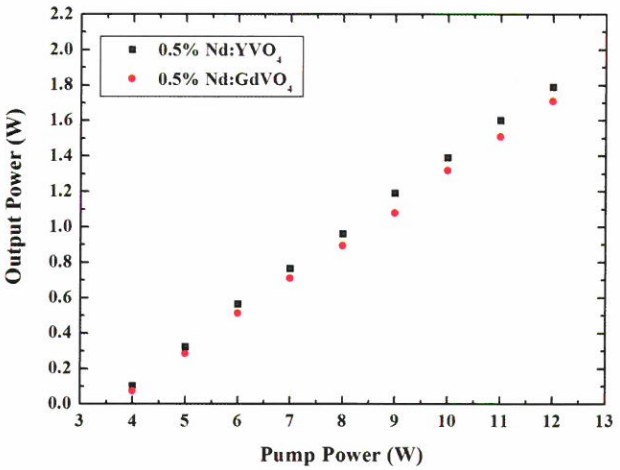

圖六 Nd 原子摻雜濃度為 0.5 % 輸出功率的比較

二、 671 nm 雷射架構

671 nm 雷射實驗架構如圖四所示。在此實驗中加入了一曲率為 100 mm 的凹透鏡 M_2，並且在其兩鏡面分別鍍製了 1342 nm 波長的高反射膜及 671 nm 抗反射膜。M_1 使用的是與 1342 nm 雷射相同的 Input Coupler。M_3 為在 1342 nm 波長具有高反射率的雷射鏡片，此外，利用晶體長度為 10 mm LBO 倍頻晶體將波長為 1342 nm 的紅外雷射光倍頻成波長為 671 nm 的紅色雷射光。增益介質使用方面分別為 0.3 % $Nd:YVO_4$ 及 0.3 % $Nd:GdVO_4$，且在其晶體座上通以冷卻水，避免增益介質過熱。共振腔長分別為 M_1 與 M_2 之間的距離為 17 cm，M_2 與 M_3 之間的距離為 5 cm。

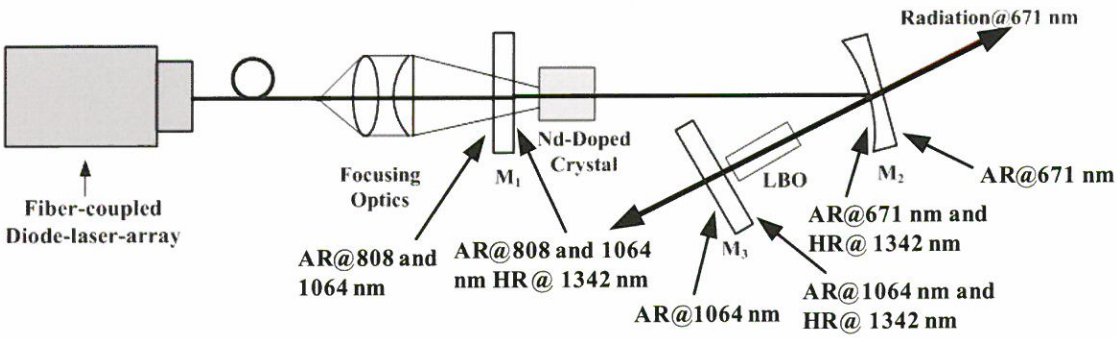

圖四 671 nm 雷射實驗架構

實驗結果與討論

一、1342 nm 紅外光雷射輸出功率的比較：

自行鍍製的 output coupler 其穿透率為 5%。為了研究不同摻雜濃度的增益介質對於輸出功率與轉換效率的影響，實驗利用 0.3 %、0.5 % $Nd:YVO_4$ 及 0.3 %、0.5 % $Nd:GdVO_4$ 在不同的 Pump Power 下測量其輸出功率的變化情形。 圖五與圖六分別為不同摻雜濃度的 $Nd:YVO_4$ 及 $Nd:GdVO_4$ 隨著 Pump Power 的變化所得到的輸出功率。圖五中當摻雜濃度為 0.3 % $Nd:YVO_4$ 時，其斜率為 20 %，摻雜濃度為 0.3 % $Nd:GdVO_4$ 時，斜率為 19.4 %，而兩增益介質開始有受激輻射出時的 Pump

由於半導體雷射在不同的 LD 溫度下所對應的中心波長將有所偏差，故會調整雷射二極體的溫度，使激發的中心波長為 808 nm。首先激發光源會經過一透鏡組合，光束將因此而被聚焦在增益介質中 (進入增益介質的光點大小約 300 μm)，增益介質因受激發而產生居量反轉。此時配合共振腔兩平面鏡上的鍍膜，使得共振後所產生的雷射光其波長為 1342 nm。再對每一個光學元件及增益介質作微調，調整到輸出功率最大為止。雷射光的功率可以利用雷射功率計 (Coherent, 3 Σ sigma, Laser Power Energy Meter) 量測得到。

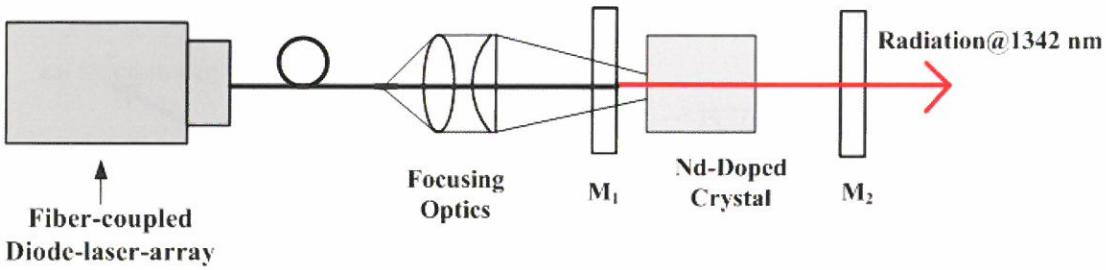

圖三 1342 nm 雷射實驗架構

表四 雷射鏡片規格

Input Coupler	R1=∞, R2=∞	S1:AR coating @808and 1064 nm and HR coating @1342 nm S2:AR coating @808 and 1064 nm
Output Coupler	R1=∞, R2=∞	S1:AR coating @1064 nm and PR coating (R=95%)@1342 nm S2:AR coating @1064 and 1342 nm

表五 增益介質

0.3% Nd:YVO_4	3×3×8 mm^3	S1:AR coating @808and 1342 nm S2:AR coating @1342 nm
0.3% Nd:$GdVO_4$	3×3×8 mm^3	S1:AR coating @808and 1342 nm S2:AR coating @1342 nm
0.5% Nd:YVO_4	3×3×6 mm^3	S1:AR coating @808and 1342 nm S2:AR coating @1342 nm
0.5% Nd:$GdVO_4$	3×3×6 mm^3	S1:AR coating @808and 1342 nm S2:AR coating @1342 nm

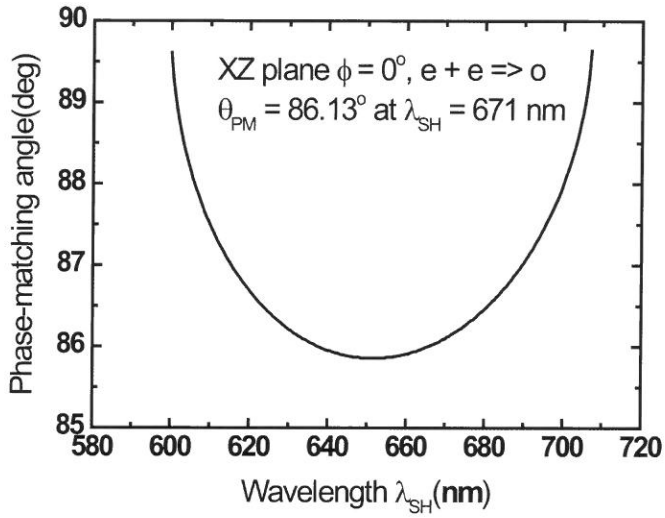

圖二 type I 在 XZ 平面的相位匹配角對二倍頻波長的關係

實驗儀器裝置

一、 1342 nm 雷射架構

1342 nm 固態雷射的實驗架構如圖三所示，實驗中使用的激發光源為 Coherent, FAP-81-12.0C-800-B 的半導體雷射，其激發波長為 808 nm，共振腔為兩平面鏡所組成，共振腔長度為 10 cm，平面鏡依實驗所需而有不同規格的鍍膜條件 (表四)。

在增益介質方面，使用的是 $Nd:YVO_4$ 及 $Nd:GdVO_4$，兩種增益介質皆有不同摻雜濃度與長度，而增益介質表面皆有不同規格的鍍膜條件 (表五)。此外；增益介質固定在一銅製晶體架上並且接上冰水機通以冷卻水，藉此避免增益介質因過熱而裂掉，使得雷射光束的品質及功率受到嚴重影響。

在進行固態雷射系統架設前，首先利用一台低功率的市售綠光雷射、兩反射鏡及兩個可調式光圈 (Iris) 來進行光的準直。經由此一過程，在光學桌上建立一準直的光束。當架設雷射系統時，系統中的每一個光學元件及增益介質皆利用這道光束來進行準直。

非線性光學轉換

利用非線性光學晶體將 1.3 μm 的紅外雷射光倍頻至 0.67 μm 的紅色雷射光，即 $\omega_f+\omega_f \rightarrow \omega_{SH} = 2\omega_f$，其轉換的方式如耦合方程式 (1) 及 (2) 所描述的。

$$\frac{dE_f}{dz} = -j\left(\frac{d_{eff}}{c}\right)\left(\frac{\omega_f}{n_f}\right)E_{SH}E_f^* \tag{1}$$

$$\frac{dE_{SH}}{dz} = -j\left(\frac{d_{eff}}{2c}\right)\left(\frac{\omega_{SH}}{n_{SH}}\right)E_f^2 \tag{2}$$

其中 ω_f 及 ω_{SH} 代表參與非線性轉換之基頻光和倍頻光的頻率而 E_f 及 E_{SH} 分別代表基頻光和倍頻光的電場強度，d_{eff} 為非線性晶體的等效非線性係數。在滿足相位匹配條件及小信號條件近似下 (轉換效率小於 10%)，轉換效率 $\eta \equiv \frac{P_{2\omega}}{P} \propto I_\omega d_{eff}^2 l^2$ ，其中 是基頻雷射光的強度， 是非線性晶體的長度。

我們在 LBO 晶體的主軸座標 XZ 平面上利用 type I $e(\omega)+e(\omega) \rightarrow o(2\omega)$ 的方式進行非線性轉換，其相位匹配角為 $\phi = 0°$，$\theta = 86.1°$。在此相位匹配下，所對應的等效非線性係數 $d_{eff} \sim 0.98$ pm/V。由於非線性晶體 LBO 具有極高損傷閥值 (damage threshold)，在 1.3 ns 脈寬的 1053 nm 雷射光照射下，其損傷閥值可高達 10 GW/cm^2。

因此為了提高轉換效率，可將基頻光的斑點尺寸 (spot size) 縮小至 100 μm 以下，以增加其強度。詳細的 type I $e(\omega)+e(\omega) \rightarrow o(2\omega)$ 在 XZ 平面上的相位匹配角對二倍頻波長的關係請見圖二。

非線性光學晶體

LBO crystal (Lithium Triborate, LiB_3O_5)

LBO 似乎是目前將 1.34 μm 的紅外雷射光倍頻至 0.67 μm 的紅色雷射光最佳的非線性光學晶體 [10, 12]。它是負的雙軸晶體，晶體分類為點群 mm2，其詳細的光學及非線性光學特性請參考表三。

表三 LBO 光學及非線性光學特性 [15]

Transparency Range	160-2600 nm
SHG Phase Matchable Range	551 ~ 2600 nm (Type I) 790-2150 nm (Type II)
Therm-optic Coefficient (°C, λ in μm)	$dn_x/dT=-9.3\times10^{-6}$ $dn_y/dT=-13.6\times10^{-6}$ $dn_z/dT=(-6.3-2.1\lambda)\times10^{-6}$
Absorption Coefficient	<0.1%/cm at 1064 nm <0.3%/cm at 532 nm
Angle Acceptance	6.54 mrad-cm (ϕ, Type I, 1064 nm SHG) 15.27 mrad-cm (θ, Type II,1064 nm SHG)
Temperature Acceptance	4.7°C-cm (Type I, 1064 nm SHG) 7.5°C-cm (Type II,1064 nm SHG)
Spectral Acceptance	1.0nm-cm (Type I, 1064 nm SHG) 1.3nm-cm (Type II,1064 nm SHG)
Walk-off Angle	0.60° (Type I, 1064 nm SHG) 0.12° (Type II, 1064 nm SHG)
NLO Coefficients	$d_{eff}(I) = d_{32}\cos\Phi$ (Type I in XY plane) **$d_{eff}(I) = d_{31}\cos^2\theta + d_{32}\sin^2\theta$ (Type I in XZ plane)** $d_{eff}(II) = d_{31}\cos\theta$ (Type II in YZ plane) $d_{eff}(II) = d_{31}\cos^2\theta + d_{32}\sin^2\theta$ (Type II in XZ plane)
Non-vanished NLO	$d_{31} = 1.05 \pm 0.09$ pm/V $d_{32} = -0.98 \pm 0.09$ pm/V $d_{33} = 0.05 \pm 0.006$ pm/V
Sellmeier Equations (λ in μm)	$n_x^2 = 2.454140 + 0.011249/(\lambda^2-0.011350) - 0.014591\lambda^2 - 6.60\times10^{-5}\lambda^4$ $n_y^2 = 2.539070 + 0.012711/(\lambda^2-0.012523) - 0.018540\lambda^2 + 2.0\times10^{-4}\lambda^4$ $n_z^2 = 2.586179 + 0.013099/(\lambda^2-0.011893) - 0.017968\lambda^2 - 2.26\times10^{-4}\lambda^4$

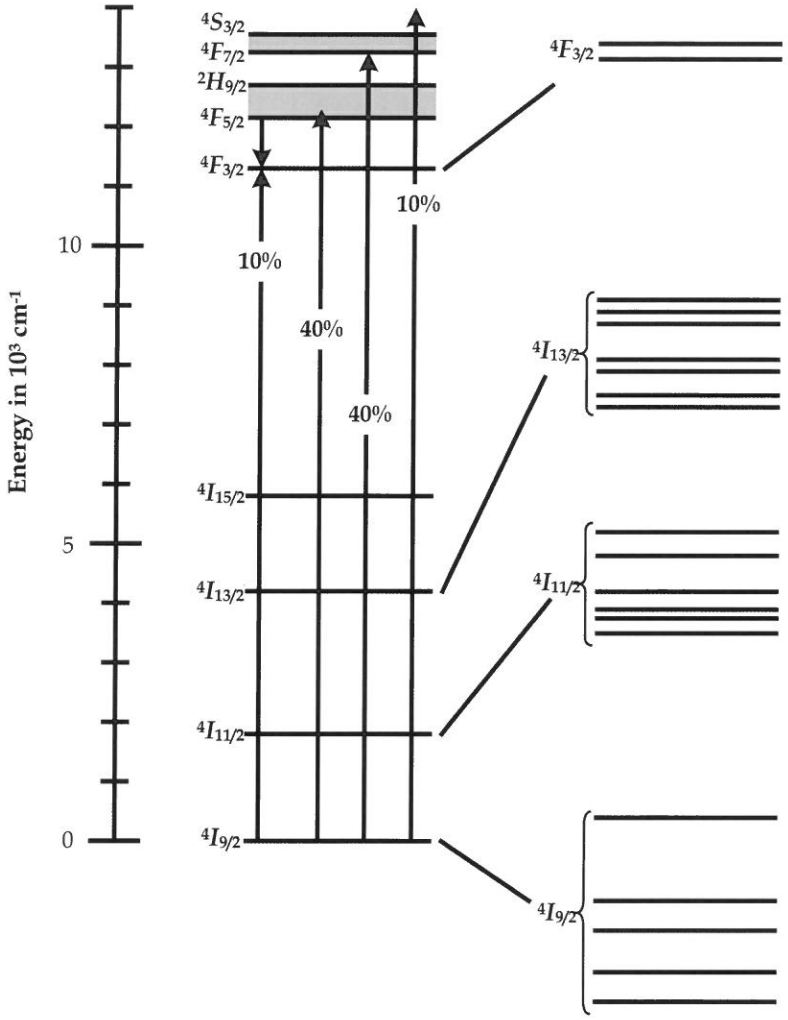

圖— Nd^{+3} 雷射釹離子能階圖

增益介質

一、Nd:YVO_4

Nd:YVO_4 在激發波長為 808 nm 時，其吸收係數約為 Nd:YAG 的 5 倍。Nd:YVO_4 在波長為 1064 nm 的受激輻射截面約為 Nd:YAG 的 5.6 倍。此外；在波長為 1.3 μm 的受激輻射截面約為 Nd:YAG 的 4 倍。其寬吸收帶、高雷射損傷閥值 (damage threshold)，高硬度，化學惰性，折射率溫度係數小，沒有材料內部應力，且易於製造等特性，皆使其成為固態雷射中雷射晶體的最佳選擇。此外；產生的雷射光具有線偏振的特性，有利於作非線性光學轉換。

但是相對 Nd:YAG，Nd:YVO_4 偏低的熱傳導能力不利於大功率的操作且較短的螢光生命期 (fluorescent lifetime) 不利於居量反轉 (population inversion) 的累積，因此在共振腔 Q 值切換 (Q-switching) 模式操作下所產生脈衝無法具有較大的能量。

二、Nd:$GdVO_4$

除了 Nd:YAG 及 Nd:YVO_4 這兩種增益介質外，另一種發展較晚的 Nd:$GdVO_4$ 也逐漸被使用作為固態雷射的增益介質。Nd:$GdVO_4$ 在激發波長為 808 nm 時其吸收係數約為 Nd:YAG 的 7 倍。在波長為 1064 nm 的受激輻射截面約為 Nd:YAG 的 2.7 倍。晶體特性與 Nd:YVO_4 相似。

此外；在室溫下 (300 K)，Nd:$GdVO_4$ 的熱傳導係數 (11.7 W m^{-1} K^{-1}) 較 Nd:YVO_4(5.1 W m^{-1} K^{-1}) 還要大，但卻與 Nd:YAG 的熱傳導係數 (14 W m^{-1} K^{-1}) 相近，利於大功率的操作。Nd:$GdVO_4$ 可以說是同時具備了 Nd:YAG 及 Nd:YVO_4 的優良特性。在低摻釹原子濃度時，其在激發波長為 808 nm 時吸收帶寬 (1.6 nm) 較 Nd:YVO_4(1.3 nm) 及 Nd:YAG($<$ 1nm) 來得大 [4]。Nd:$GdVO_4$ 螢光生命期 (fluorescent lifetime) 與 Nd:YVO_4 相近，因此在共振腔 Q 值切換 (Q-switching) 模式操作下所產生脈衝亦無法具有較大的能量。釹離子 Nd^{+3} 詳細的能階圖如圖一所示。

表 1.2 釹原子增益介質相關的光學及物理的特性 [4, 6, 13]

Crystal	**Nd:YVO_4**	**Nd:$GdVO_4$**	**Nd:YAG**
Laser wavelengths	1064.3 nm, 1342.0 nm	1063.1 nm, 1340 nm	1064.1 nm, 1319.2 nm
Emission bandwith (linewidth at 1.06 μm)	0.8 nm	Not available	0.45 nm
Stimulated emission cross section at 1.06 μm at 1.3 μm	$15.6\times10^{-19}cm^2$, $2.8\times10^{-19}cm^2$	$7.6\times10^{-19}cm^2$, $1.8\times10^{-19}cm^2$	$2.8\times10^{-19}cm^2$, $0.7\times10^{-19}cm^2$
Polarization	Parallel to c-axis	Parallel to c-axis	Unpolarized
Fluorescent lifetime at. 1% Nd doping	100 μs	95 μs	230 μs
Pump wavelength	808.5 nm	808.4 nm	807.5 nm
Peak pump absorption at. 1% doping	$41cm^{-1}$	$57\ cm^{-1}$	$8\ cm^{-1}$
Thermal conductivity 300 K (W/mK)	5.1	11.7	14
Doping concentration range	0.1-3.0%	0.1-3.0%	0.1-2.0%
Radiation wavelength at the $^4I_{13/2} \rightarrow I_{9/2}$	914 nm	912 nm	946 nm
The uppermost Stark level $^4I_{9/2}$ (cm^{-1})	439	409	857
Stimulated emission cross section	$0.5\times10^{-19}cm^2$	$0.7\times10^{-19}cm^2$	$0.64\times10^{-19}cm^2$

緒 論

在晶體內摻雜稀土元素所形成的雷射增益介質 (gain medium)，並結合非線性光學轉換技術，使得全固態雷射獲得突飛猛進的發展。近三十年來，不僅在雷射科學研究上獲得極大的成果，而且已廣泛地應用在醫學、軍事與工業上。

尤其是釹原子 (Nd) 常被摻入晶體中，作為雷射增益介質 (以下簡稱增益介質) 如 Nd:YAG、Nd:YVO_4、Nd:$GdVO_4$ 等。許多研究中常以 Nd:YVO_4 作為增益介質使用。相對於其它的增益介質而言，其在波長 808 nm 的激發光具有較大的吸收截面，故常用它來產生 0.9 μm、1 μm 及 1.3 μm 紅外雷射光。近來由於 Nd:$GdVO_4$ 其晶體的基本特性與 Nd:YVO_4 相近，且具有較高的熱傳導係數，故成為增益介質的另一選擇。利用非線性光學晶體及內腔式架構將近紅外雷射光轉換成紅、綠、藍可見雷射光。有關增益介質詳細的資料見表 1.1 及表 1.2。

本文的研究主題為紅光雷射的研製。首先利用自行鍍製之鏡片，並且搭配不同 Nd^{3+} 濃度 Nd:$GdVO_4$ 與 Nd:YVO_4 雷射晶體，再利用 808 nm 的半導體雷射作為激發光源，通過增益介質後產生 1342 nm 近紅外雷射光，並藉由非線性光學晶體 LBO 產生波長為 671 nm 的連續式 (continuous-wave) 紅色雷射光。

表 1.1 釹原子增益介質主要的輻射頻譜 [1-12]

電子躍遷能階	輻射譜線 Nd：YAG	倍頻波長	輻射譜線 Nd：YVO_4	倍頻波長	輻射譜線 Nd：$GdVO_4$	倍頻波長
$^4F_{3/2} \rightarrow I_{9/2}$	946 nm	473 nm	914 nm	457 nm	912 nm	456 nm
$^4F_{3/2} \rightarrow {}^4I_{11/2}$	1064 nm	532 nm	1064 nm	532 nm	1063 nm	532 nm
$^4F_{3/2} \rightarrow {}^4I_{13/2}$	1319 nm	660 nm	1342 nm	671 nm	1341 nm	670 nm

摻釹原子全固態連續式紅光雷射之研製

張連璧* 陳譽云
輔仁大學 物理系

摘 要

利用簡單的線性共振腔，研究不同種類及不同濃度的摻釹原子增益介質所產生波長為 1342 nm 之紅外雷射光其輸出功率及轉換效率，並利用 L 型的共振腔及非線性光學晶體 LBO 成功地將 1342 nm 之基頻紅外雷射光倍頻為 671 nm 紅色雷射光。研製紅外光與紅光雷射共振腔所需要的鏡片是自行鍍製的。當泵浦功率為 12 瓦時，釹原子濃度 0.5 at.% 之 $Nd:YVO_4$ 其基頻紅外雷射光之最大輸出功率為 1.8 瓦而轉換效率約為 15 %。同時將泵浦功率進一步提升至 20 瓦，並利用一顆 4x4x10 mm^3 的 LBO 晶體及釹原子濃度皆為 0.3 at.% 的 $Nd:YVO_4$ 和 $Nd:GdVO_4$ 的增益介質可以產生 130 毫瓦之紅色雷射光。

關鍵詞：$Nd:YVO_4$、$Nd:GdVO_4$、LBO、1342 nm、671 nm、非線性光學。

* Corresponding author, Tel.,+886-2-29052018; fax,+886-2-29021038
E-mail address: lbchang@mail.fju.edu.tw

製程能力指標 $C''_{pp}(a,b)$ 的廣義樞紐量之研究

陳思勉　呂婉綺

輔仁大學 數學系

摘　要

本文首先運用廣義樞紐量的概念，提出一個製程能力指標 $C''_{pp}(a,b)$ 的估計式，進而定義兩種找出 $C''_{pp}(a,b)$ 之信賴下界的方法，並計算此二方法之涵蓋率及平均區間長度。

關鍵字：廣義樞紐量，廣義新賴區間。

Reference

1. Chan, L. K. Cheng, S. W. and Spiring, F. a., (1988). A new measure of process capability index: C_{pm}. *Journal of Quality Technology*. 20: 162-175.
2. Chang, Y. P. (2001). Generalized condence intervals for process capability indices. *Journal of the Chinese Institute of Industrial Engineers*. 18(2):11-20.
3. Chen, K.S. (1998). Incapability Index with Asymmetric Tolerances. *Statistica Sinica* 8: 253-262.
4. Greenwich, M. and Jahr-Scharath, B.L. (1995). A process incapability index. *Inernational Journal of Quality Reliability Management*. 12: 58-71.
5. Hsu, B. M., Wu, C. W. and Shu, M. H. (2008). Generalized condence intervals for process capability Index C_{pm}. *Metrika* 68: 65-82.
6. Jose, K.K. and Luke, J. A. (2011). Condence intervals for process capability indices for the unbalanced one-way random eect ANOVA model. *Quality and Reliability Engineering International*. (DOI:10.1002/qre.1247).
7. Jose, K.K. and Luke, J. A. (2012). Comparing two process capability indices under balanced one-way random eect model. *Quality and Reliability Engineering International*. (DOI:10.1002/qre.1297).
8. Kotz, S., Lovelace, C. R. (1998). *Process Capability Indices in Theory and Practice*. London: Oxford University Press Inc.
9. Kurian, K.M., Mathew, T. and Sebastian, G. (2008). Generalized condence intervals for process capability Indices in the one-way random model. *Metrika* 67: 83-92.
10. Lehmann, E. L. (1983). Theory of point estimation John Wiley & Sons.
11. Mathew, T, Sebastian, G. and Kurian, K.M. (2007). Generalized condence intervals for process capability indices. *Quality and Reliability Engineering International*. 23:471-481 (DOI:10.1002/qre.828).
12. Myers, R. H. and Montgomeray, D.C. (1995). Response Surface Methodology. New York: John Wiley.
13. Pan, J.N. and Lee C. Y. (2009). Development of a new process incapability index with an application to the evaluation of manufacturing risk. *Communications in Statistics: Theory & Methods 38*(12):1133-1153.
14. Weerahandi, S. (1993). Generalized condence intervals. *Journal of the American Statitical Association*. 88:899-905.
15. Ye, R. and Ma T., Wang, S. (2011). Generalized condence intervals for the process capability indices in general random eect model with balanced data. *Stat Papers*. 52:153-169.

Recevied Aug 14, 2013
Revised Apr 14, 2014
Accepted Apr 14, 2014

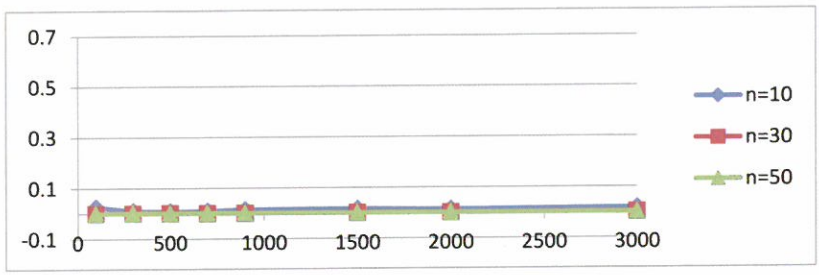

(a) For process with $C''_{pp}(a,b)=0.091068$

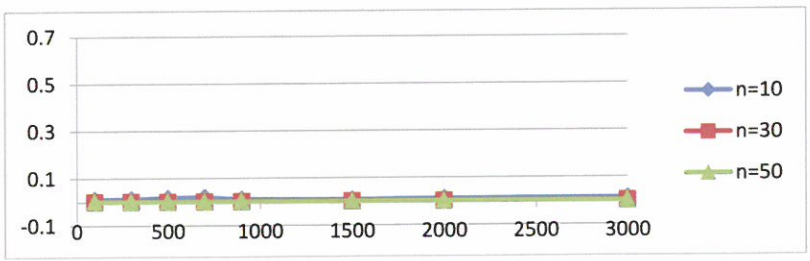

(b) For process with $C''_{pp}(a,b)=0.129551$

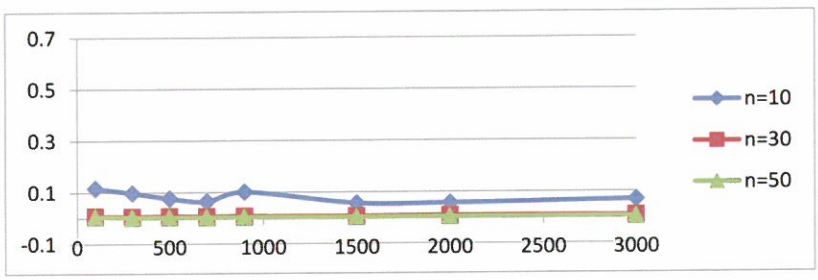

© for process with $C''_{pp}(a,b)=0.311027$

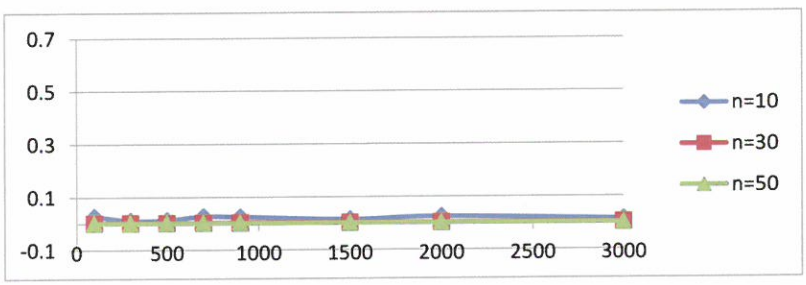

(d) for process with $C''_{pp}(a,b)=0.406406$

Figure 2: Differences between the MSE of PLE and GPE

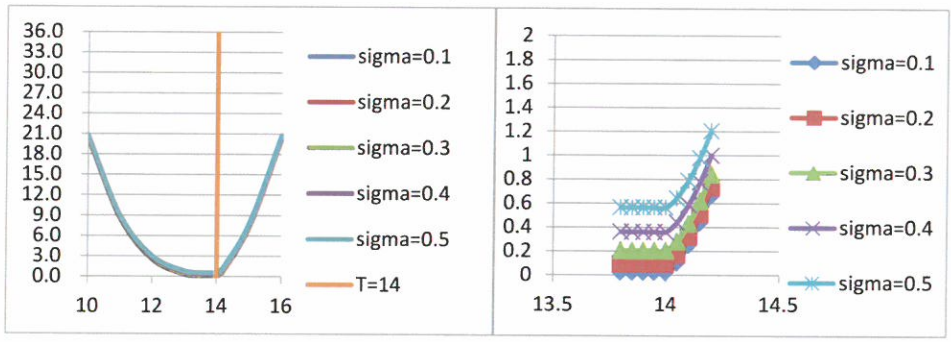

(a) $C''_{pp}(a,b)$ vs μ

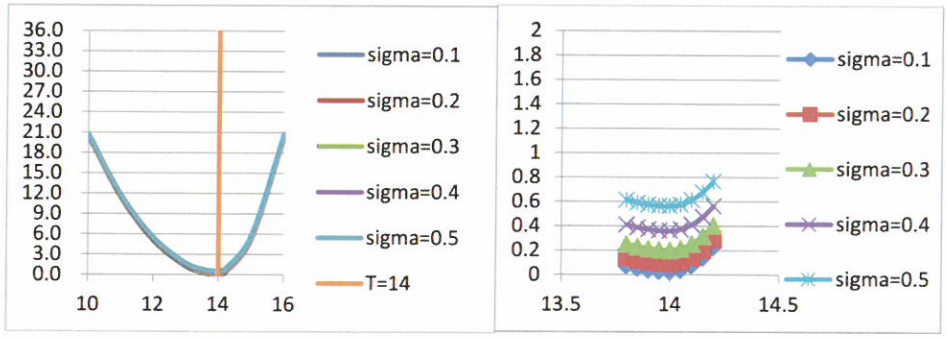

(b) C''_{pp} vs μ

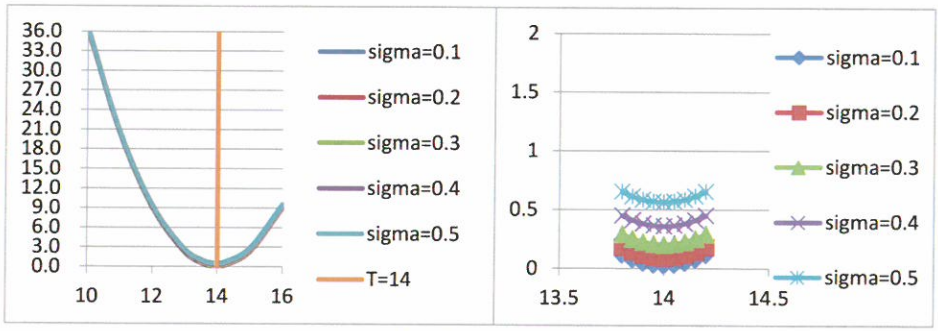

© C_{pp} vs μ

Fig 1: Values of indices for processes with $\mu \in (10,16)$ and $\sigma \in \{0.1, 0.2, 0.3, 0.4\}$.

Table 3(a): Level of quality based on the rule of C''_{pp} when μ is fixed.

quality	(μ, σ)	C''_{pp}	$C''_{pp}(a,b)$	C_{pp}	C^*_{pm}
super	(13.80, 0.11)	0.077850	0.029756	0.117225	2.920722
excellent	(13.80, 0.30)	0.253125	0.205031	0.292500	1.849001
good	(13.80, 0.38)	0.375525	0.327431	0.414900	1.552488
capable	(13.80, 0.42)	0.447525	0.399431	0.486900	1.433112
marg. capable	(13.80, 0.48)	0.569025	0.520931	0.608400	1.282051
inadequate	(13.80, 0.65)	1.001250	0.953156	1.040625	0.980286
super	(13.90, 0.11)	0.039881	0.027541	0.049725	4.484478
excellent	(13.90, 0.33)	0.257681	0.245341	0.267525	1.933382
good	(13.90, 0.40)	0.372656	0.360316	0.382500	1.616904
capable	(13.90, 0.44)	0.448256	0.435916	0.458100	1.477474
marg. capable	(13.90, 0.50)	0.575156	0.562816	0.585000	1.307441
inadequate	(13.90, 0.67)	1.022681	1.010341	1.032525	0.984124
super	(14.10, 0.11)	0.077850	0.253628	0.049725	4.484478
excellent	(14.10, 0.30)	0.253125	0.428903	0.225000	2.108184
good	(14.10, 0.38)	0.375525	0.551303	0.347400	1.696622
capable	(14.10, 0.42)	0.447525	0.623303	0.419400	1.544137
marg. capable	(14.10, 0.48)	0.569025	0.744803	0.540900	1.359695
inadequate	(14.10, 0.66)	1.030725	1.206503	1.002600	0.998703
super	(14.20, 0.11)	0.229725	0.667585	0.117225	2.920722
excellent	(14.20, 0.16)	0.260100	0.697960	0.147600	2.602898
good	(14.20, 0.27)	0.366525	0.804385	0.254025	1.984093
capable	(14.20, 0.33)	0.447525	0.885385	0.335025	1.727673
marg. capable	(14.20, 0.40)	0.562500	1.000360	0.450000	1.490712
inadequate	(14.20, 0.60)	1.012499	1.450360	0.900000	1.054093

Table 3(b): Level of quality based on the rule of C''_{pp} when σ is fixed.

quality	(μ, σ)	C''_{pp}	$C''_{pp}(a,b)$	C_{pp}	C^*_{pm}
super	(13.90 , 0.30)	0.215156	0.202816	0.225000	2.108184
excellent	(13.65 , 0.30)	0.357539	0.216066	0.478126	1.446202
good	(13.60 , 0.30)	0.405000	0.222750	0.562499	1.333334
capable	(13.50 , 0.30)	0.518906	0.242051	0.765000	1.143324
marg. capable	(13.30 , 0.30)	0.822656	0.311027	1.304999	0.875376
inadequate	(13.05 , 0.30)	1.344726	0.473779	2.233124	0.669181
super	(14.05 , 0.30)	0.215156	0.282546	0.208125	2.191986
excellent	(14.10 , 0.30)	0.253125	0.428903	0.225000	2.108184
good	(14.20 , 0.30)	0.405000	0.842860	0.292500	1.849001
capable	(14.25 , 0.30)	0.518906	1.097432	0.343125	1.707158
marg. capable	(14.30 , 0.30)	0.658126	1.378920	0.405000	1.571348
inadequate	(14.40 , 0.30)	1.012498	2.013712	0.562499	1.333334

Table 2: Coverage rate and expected length of GCI and EMP.

			GCI		EMP	
$C''_{pp}(a,b)$	m	n	C.R.	E.L.	C.R.	E.L.
0.129550	300	10	0.9600	0.372545	0.9600	0.323164
	400		0.9675	0.336872	0.9675	0.312949
	300	30	0.9500	0.197714	0.9500	0.195792
	400		0.9750	0.199294	0.9750	0.195948
	300	50	0.9600	0.172630	0.9600	0.171939
	400		0.9675	0.175226	0.9675	0.174768
	300	70	0.9533	0.165911	0.9566	0.164915
	400		0.9575	0.166846	0.9575	0.166461
	300	90	0.9466	0.160748	0.9466	0.160442
	400		0.9575	0.159239	0.9550	0.158934
0.311027	300	10	0.9466	0.804080	0.9466	0.734324
	400		0.9550	0.838429	0.9550	0.751157
	300	30	0.9733	0.460773	0.9700	0.455749
	400		0.9675	0.461094	0.9650	0.460149
	300	50	0.9466	0.414853	0.9466	0.412728
	400		0.9650	0.420999	0.9600	0.420217
	300	70	0.9666	0.399090	0.9666	0.397340
	400		0.9675	0.404117	0.9675	0.398484
	300	90	0.9500	0.383505	0.9500	0.382453
	400		0.9675	0.381648	0.9675	0.381023
0.503714	300	10	0.9600	0.613362	0.9600	0.604596
	400		0.9500	0.613119	0.9500	0.606632
	300	30	0.9600	0.548331	0.9600	0.547276
	400		0.9475	0.550039	0.9425	0.549047
	300	50	0.9500	0.537127	0.9500	0.536522
	400		0.9550	0.538185	0.9550	0.537797
	300	70	0.9766	0.534315	0.9766	0.533866
	400		0.9500	0.532290	0.9475	0.531973
	300	90	0.9633	0.529990	0.9633	0.529645
	400		0.9525	0.527684	0.9525	0.527406

Table 1: Comparison between PLE and GPE of a process with $C''_{pp}(a,b)$.

		PLE				GPE			
$C''_{pp}(a,b)$	n	estimate	bias	s.e.	MSE	estimate	bias	s.e.	MSE
0.091068	10	0.090149	-0.000918	0.044559	0.001986	0.134675	0.043607	0.129521	0.018677
	30	0.091491	0.000423	0.022616	0.000512	0.101811	0.010743	0.038834	0.001623
	50	0.090798	-0.000270	0.017747	0.000315	0.096649	0.005581	0.027906	0.000810
0.129551	10	0.129835	0.000284	0.046868	0.002197	0.169094	0.039543	0.113152	0.014367
	30	0.130054	0.000503	0.020813	0.000433	0.140796	0.011246	0.038422	0.001603
	50	0.129358	-0.000192	0.016282	0.000265	0.135439	0.005888	0.027590	0.000796
0.311027	10	0.308631	-0.002396	0.082062	0.006740	0.400538	0.089511	0.233188	0.062389
	30	0.309997	-0.001031	0.053969	0.002914	0.334422	0.023395	0.092918	0.009181
	50	0.310360	-0.000667	0.042166	0.001778	0.324767	0.013740	0.068032	0.004817
0.406406	10	0.408680	0.002274	0.088868	0.007903	0.457395	0.050988	0.173324	0.032641
	30	0.408034	0.001628	0.040318	0.001628	0.419778	0.013371	0.063288	0.004184
	50	0.407919	0.001513	0.032767	0.001076	0.414381	0.007975	0.048583	0.002424

for indices C_{pp} and C^*_{pm}, the values are the same when the process means are symmetric to the target. See Table 3. Over all speaking, the value of $C''_{pp}(a,b)$ is highly asymmetric compare with the other two incapability indices.

When parameters are unknown, the PLE performs well even for small sample. However, it is hard to derived a pivot quantity based on PLE because the lack of information about the distribution. In addition, for a given sample, PLE is just a single value, and it is impossible to create a confidence interval from it. On the other hand, for a given sample, the generalized pivot estimator $T_{C''_{pp}(a,b)}$ is a function of a standard normal variate and a chi-square variate, and is therefore random. Therefore, a confidence interval of $C''_{pp}(a,b)$ can be achieved via the sampling distribution of $T_{C''_{pp}(a,b)}$. In the current study, both GCI method and EMP method are based on the generalized pivot quantity $T_{C''_{pp}(a,b)}$. And the simulation result shows that the generalized confidence bound provides the inteneded coverage even though the true coverage rate may not be exactly the nominal value $1-\alpha$. In practice, use the information derived from both PLE and GPE, one should get a good idea about the information of $C''_{pp}(a,b)$ and therefore the quality of a process. Furthermore, the graphs show that the standard deviation does not affect the value of the indices too much.

It was mentioned in literature that a process is categorized as inadequate if $C''_{pp} > 1$, as marginally capable if $0.56 < C''_{pp} \leq 1$, as capable if $0.44 < C''_{pp} \leq 0.56$, as good if $0.36 < C''_{pp} \leq 0.44$, as excellent if $0.25 < C''_{pp} \leq 0.36$, as super if $C''_{pp} \leq 0.25$. In order to set up a similar standard about the boundaries of the quality of a process based on $C''_{pp}(a,b)$, we may use the above standard to find a proper range of process mean and then transform back to $C''_{pp}(a,b)$. However, from Table 3(a) and 3(b), problems have occured. For instance, with different μ and σ, the quality of a process with $C''_{pp}(a,b) = 0.520931$ is classified as marginal capable if $\mu < 14$. Nevertheless, for a process with $\mu > 14$, with the same incapability index value, the process will be classified to have quality between excellent and good based on the rule set up for the incapability index C''_{pp}. So, how to set up a reasonable boundry for $C''_{pp}(a,b)$ will be a research problem for further study.

Step 4. Compute $T_{\mu} = \bar{x} - \frac{Z}{\sqrt{W}} \cdot s$, and $T_{\sigma^2} = \frac{n}{W} \cdot s$, and the GPE $T_{C''_{pp}(a,b)}$ based on formula (1);

Step 5. Repeat Step 3 and Step 4 $l = 10^5$ times to get $T_{C''_{pp1}(a,b)}, T_{C''_{pp2}(a,b)}, \cdots, T_{C''_{ppl}(a,b)}$ and also compute their average;

Step 6. Find the $100(1-\alpha)^{th}$ percentile $T^{1-\alpha}_{C''_{pp}(a,b)}$ of $T_{C''_{pp1}(a,b)}, T_{C''_{pp2}(a,b)}, \cdots, T_{C''_{ppl}(a,b)}$.

Step 7. Define $k_1 = 1$ if $C''_{pp}(a,b) \leq T^{1-\alpha}_{C''_{pp}(a,b)}$;

Step 8. Solve equation (2) via Newton method for the value of the upper confidence bound c. The approximation stops when the difference between two consecutive solutions is less than 10^{-5}. The initial value of c is set at PLE.

Step 9. Define $k_2 = 1$ if $C''_{pp}(a,b) \leq c$;

Step 10. Repeat Step 1 to Step 9 m times to get $k_{11}, \cdots, k_{1m}$ and $k_{21}, \cdots, k_{2m}$, $T^{1-\alpha}_{C''_{pp}(a,b),1}, \cdots, T^{1-\alpha}_{C''_{pp}(a,b),m}$ and $c_1, \cdots, c_m$;

Step 11. The coverage rate of the EMP-method is $\sum_{i=1}^{m} k_{1i}/m$.

Step 12. The coverage rate of the GCI-method is $\sum_{i=1}^{m} k_{2i}/m$.

Step 13. The expected length of the confidence interval of $C''_{pp}(a,b)$ based on EMP-method is $\sum_{i=1}^{m} T^{1-\alpha}_{C''_{pp}(a,b),i}/m$;

Step 14. The expected length of the confidence interval of $C''_{pp}(a,b)$ based on GCI-method is $\sum_{i=1}^{m} c_i/m$;

From Table 2, the simulation result indicates that the confidence bound based on either methods do provide coverage probability close to the nominal confidence level. Surprisingly, the coverage rates of both methods are quite similar. But the expected length from EMP-method is shorter than the expected length from GCI-Method, Since the EMP-method is much easier and faster to compute, the EMP-method is highly recommended than GCI-method.

4 Concluding Remarks

From the left panel in Figure 1, when the mean shifts away from the targe value T towards LSL, $C''_{pp}(a,b)$ is more conservative than C''_{pp} and C_{pp} regardless the value of the process variance. However, the situation is reversed if the process mean shifts away from T towards the USL. In either cases, $C''_{pp}(a,b)$ can detect the shift faster than the other two incapability indices. Same behavior occurs for the case when the target is 12. In conclusion, based on $C''_{pp}(a,b)$, it is easier to detect the shifts when the mean locates at the side while the specification limit is closer to the target. From the right panel of Figure 1, for $\mu \in (13.8, 14.2)$, the zoom in figure shows that for processes with the same process standard deviation, $C''_{pp}(a,b)$ always has smaller value when the mean μ is on the left side of the target value than when $\mu > T$. The minimum is reached when the mean is exactly at the target value. The level of the difference between these two situations becomes smaller when the standard deviation increases. Same thing happens to C''_{pp}. However,

$$
\begin{aligned}
1-\alpha &= P(T_{C''_{pp}(a,b)} \le c) \\
&= P(\frac{1}{D^2}\{d^2[\frac{T+Z\frac{s}{\sqrt{W}}-\bar{x}}{D_l}]^a+\frac{ns^2}{W}\} \le c \text{ and } -\infty < \bar{x}-Z\frac{s}{\sqrt{W}} \le T) \\
&+ P(\frac{1}{D^2}\{d^2(\frac{\bar{x}-Z\frac{s}{\sqrt{W}}-T}{D_u})^b+\frac{ns^2}{W}\} \le c \text{ and } T < \bar{x}-Z\frac{s}{\sqrt{W}} < \infty) \\
&= P(0 \le T+Z\frac{s}{\sqrt{W}}-\bar{x} \le D_l(\frac{cD^2-\frac{ns^2}{W}}{d^2})^{\frac{1}{a}},\ W > \frac{ns^2}{cD^2}) \\
&+ P(0 \le \bar{x}-Z\frac{s}{\sqrt{W}}-T \le D_u(\frac{cD^2-\frac{ns^2}{W}}{d^2})^{\frac{1}{b}},\ W > \frac{ns^2}{cD^2}) \\
&= \int_{\frac{ns^2}{cD^2}}^{\infty} \Phi[(D_l(\frac{cD^2-\frac{ns^2}{w}}{d^2})^{\frac{1}{a}}+\bar{x}-T)\frac{\sqrt{w}}{s}]f_W(w)dw \\
&- \int_{\frac{ns^2}{cD^2}}^{\infty} \Phi[-(D_u(\frac{cD^2-\frac{ns^2}{w}}{d^2})^{\frac{1}{b}}-\bar{x}+T)\frac{\sqrt{w}}{s}]f_W(w)dw
\end{aligned}
$$

where $W \sim \chi^2_{n-1}$.

3 Simulation Study

In this section, the comparison between EMP-method and GCI-method is made via a simulation study. Consider the case when the lower specification limit $LSL = 10$, the upper specification limit $USL = 16$ and the target $T = 14$. The sample size n considered are 10, 30, 50. Larger sample sizes were also studied, however, the results did not vary too much, so here we only list the results from small samples. The confidence level is $1-\alpha = 0.95$. For each combination of (μ, σ, n), an upper confidence bound of $C''_{pp}(a,b)$ based on the EMP-method is achieved by using 100000 replications. And then the whole process is repeated m times, where $m = 100(100)400$ (To save the space, here we only list the results for 300 and 400). The coverage rates of both methods are the proportion of times that the true index value $C''_{pp}(a,b)$ lies below the empirical $(1-\alpha)^{th}$ quantile $T^{1-\alpha}_{C''_{pp}(a,b)}$ or below the $100(1-\alpha)\%$ generalized upper confidence bound c which can be derived from equation (2). In addition, the estimated expected lengths for GCI-method and EMP-method are the average of the m $T^{1-\alpha}_{C''_{pp}(a,b)}$ and the average of the m c, respectively.

The algorithm of the simulation study is given below:

Step 1. Generate $x_1, \cdots, x_n$ from $N(\mu, \sigma^2)$ and compute the incapability index $C''_{pp}(a,b)$;

Step 2. Compute $\bar{x} = \sum_{i=1}^n x_i/n$, $s^2 = S_n^2 = \frac{\sum_{i=1}^n (X_i-\bar{X})^2}{n}$ and the PLE $\hat{C}''_{pp}(a,b)$;

Step 3. Generate Z from $N(0,1)$ and W from χ^2_{n-1};

By comparing the bias, standard error and the mean square error of the PLE and GPE, it can be seen that in general PLE performs better than GPE. However, when the sample size increases, the performance of both estimators are about the same, see Table 1. Figure 2 is the differences between the MSE of PLE and the MSE of GPE for process with different quality. As we can see, the difference between the MSE of PLE and MSE of GPE are quite small.

Even though the point estimator PLE may perform better than the GPE for small to moderate samples, a confidence region can provide more information about the unknown parameters. However, the explicite form of the true distribution of PLE is almost impossible to get. And for a given sample the PLE is only a single number without randomness. On the other hand, based on the design of the GPE $T_{C''_{pp}(a,b)}$, with the same sample, $T_{C''_{pp}(a,b)}$ is a random variable. A confidence bound of $C''_{pp}(a,b)$ can therefore be found by the sampling distribution of $T_{C''_{pp}(a,b)}$ even for small samples. In what follows, all the disucssion will base on GPE.

Let $T^{1-\alpha}_{C''_{pp}(a,b)}$ be the $100(1-\alpha)^{th}$ percentile of the sampling distribution of $T_{C''_{pp}(a,b)}$. Then, $T^{1-\alpha}_{C''_{pp}(a,b)}$ can be treated as a $100(1-\alpha)\%$ generalized upper confidence limit for $C''_{pp}(a,b)$. We shall call this approach EMP-method in the latter discussion.

On the other hand, from a theoretical point of view, let c be the value which satisfies the equality $P(T_{C''_{pp}(a,b)} \leq c) = 1-\alpha$, then c can be considered as the minimum performance of a process, and is therefore a $100(1-\alpha)\%$ generalized upper confidence bound (GUCB) c for $C''_{pp}(a,b)$. We shall call this approach GCI-method.

Theorem 1 Let $X_1, \cdots, X_n$ be a random sample from $N(\mu, \sigma^2)$. Then the GUCB c of $C''_{pp}(a,b)$ is the solution of the following equation:

$$1-\alpha = \int_{\frac{ns^2}{cD^2}}^{\infty} \{\Phi[\frac{\sqrt{w}}{s}(D_l(\frac{cD^2 - \frac{ns^2}{w}}{d^2})^{\frac{1}{a}} + \bar{x} - T)] - \Phi[\frac{\sqrt{w}}{s}(-D_u(\frac{cD^2 - \frac{ns^2}{w}}{d^2})^{\frac{1}{b}} + \bar{x} - T)]\} f_W(w)dw \quad (2)$$

where $f_W(\cdot)$ is the pdf of a chi-square distribution with degrees of freedom $n-1$.

proof:

Since c is a $100(1-\alpha)\%$ confidence limit of $C''_{pp}(a,b)$, implies that

which is a function of the unbiased estimators $\bar{X} = \sum_{i=1}^{n} X_i/n$ of μ and the uniformly minimum variance unbiased estimator (UMVUE) $S_{n-1}^2 = \sum_{i=1}^{n}(X_i - \bar{X})^2/(n-1)$ of σ^2 (Lehmann (1983)). However, the explicit form of the distribution of $\hat{C}_{pp}''(a,b)$ is not available hence a pivot quantity based on $\hat{C}_{pp}''(a,b)$ is hard to reach either.

In order to concure such drawback of regular pivot quantity, Weerahandi (1993) extended the definition of a pivotal quantity and proposed a generalized pivotal quantity as the following:

Def 1 : Let $T(\mathbf{X}; \mathbf{x}, \tilde{\theta})$ be a function of $\mathbf{X}$, $\mathbf{x}$, and $\tilde{\theta}$, then T is called a generalized pivotal quantity if (i) T has a probability distribution free of unknown parameters and (ii) the observed pivotal, defined as t_{obs}=$T(\mathbf{x}; \mathbf{x}, \tilde{\theta})$ does not depend on the nuisance parameter $\tilde{\theta}_2$.

In addition, for a given generalized pivotal quantity $T(\mathbf{X}; \mathbf{x}, \tilde{\theta})$, a subset $C_{1-\alpha}$ of the sample space of T is a confidence region of $\tilde{\theta}$ with confidence level $1-\alpha$ if $Pr(T \in C_{1-\alpha}) = 1-\alpha$.

Now, let $X_1, \cdots, X_n$ be a random sample from $N(\mu, \sigma^2)$ where μ and σ^2 are both unknown. To construct a generalized confidence interval for the incapability index $C_{pp}''(a,b)$, two quantities T_μ and T_σ will be used:

$$T_\mu(\mathbf{X}; \mathbf{x}, \mu, \sigma) \stackrel{\triangle}{=} T_\mu = \bar{x} - \frac{Z}{\sqrt{W}} \cdot s$$

$$T_{\sigma^2}(\mathbf{X}; \mathbf{x}, \mu, \sigma) \stackrel{\triangle}{=} T_{\sigma^2} = \frac{n}{W} \cdot s^2,$$

where $\bar{x}$ and s^2 are observed value of the sample mean X and the maximum likelihood estimator $S_n^2 = \frac{\sum_{i=1}^{n}(X_i - \bar{X})^2}{n}$, respectively. $Z = \sqrt{n}(\bar{X} - \mu)/\sigma$ is a random variable from $N(0,1)$ and $W = (n-1)S_{n-1}^2/\sigma^2$ is from χ_{n-1}^2. It is obvious that T_μ and T_{σ^2} satisfy conditions (i) and (ii) in Def 1 given above and are therefore the generalized pivotal quantities for μ and σ^2 respectively.

Define

$$T_{C_{pp}''(a,b)} = \begin{cases} \frac{1}{D^2}\{d^2[\frac{T-T_\mu}{D_l}]^a + T_{\sigma^2}\} & \text{if } -\infty < \bar{x} - \frac{Z}{\sqrt{W}} \cdot s \leq T \\ \\ \frac{1}{D^2}\{d^2[\frac{T_\mu - T}{D_u}]^b + T_{\sigma^2}\} & \text{if } T < \bar{x} - \frac{Z}{\sqrt{W}} \cdot s < \infty \end{cases} \tag{1}$$

where T is the target value. Notice that if $\bar{X} = \bar{x}$ and $S = s$, then the observed value of $T_{C_{pp}''(a,b)}$ is exactly the incapability index $C_{pp}''(a,b)$, which is independent of any nuisance parameters. Furthermore, the distribution of $T_{C_{pp}''(a,b)}$ only depends on a standard normal and a chi-square distribution, and is free of any unknown parameters. According to Def 1 given above, $T_{C_{pp}''(a,b)}$ is a generalized pivotal quantity of the incapability index $C_{pp}''(a,b)$, for convenience, let's denote it as GPE.

$$C''_{pp}(a,b) = C''_{pp}(3,3/2) = \begin{cases} \frac{9}{4}\{9 \cdot (\frac{14-\mu}{4})^3 + \sigma^2\} & \text{if } \mu < 14, \\ \\ \frac{9}{4}\{9 \cdot (\sqrt{\frac{\mu-14}{2}})^3 + \sigma^2\} & \text{if } \mu > 14. \end{cases}$$

On the other hand, when the target locates at the left hand side of the mid point of the specification interval, assume $T = 12$, then $D = 2/3, d = 3, D_u = 4, D_l = 2, a = 3/2, b = 3$, and

$$C''_{pp}(a,b) = C''_{pp}(3/2,3) = \begin{cases} \frac{9}{4}\{9 \cdot (\sqrt{\frac{12-\mu}{2}})^3 + \sigma^2\} & \text{if } \mu < 12, \\ \\ \frac{9}{4}\{9 \cdot (\frac{\mu-12}{4})^3 + \sigma^2\} & \text{if } \mu > 12. \end{cases}$$

Values of indices $C''_{pp}(a,b)$, C''_{pp} and C_{pp} when the target $T = 14$ are computed under different combinations of process mean μ and process standard deviation σ. From the right panel of Figure 1, the value of incapability indices increases as the process mean shifts away from the target, which is not surprising. But the amount of increaments on both sides are quite different. The increament on both sides are not symmetric and increases much faster when the process mean locates at the right hand side of the target especially the indices $C''_{pp}(a,b)$ and C''_{pp}. And, compare to the curves of C''_{pp} and C_{pp}, the curve of index $C''_{pp}(a,b)$ shows smoother pattern when the process shifts away from the target value toward the lower specification limit. But the situation changed when the mean is on the right hand side of the target. $C''_{pp}(a,b)$ increases more rapidely than C''_{pp} does on either sides, which means that $C''_{pp}(a,b)$ can detect the shift of the mean faster than C''_{pp} can do. To see the effect of σ, those processes with mean close to the target values are zoomed in as shown in the left panel of Figure 1. As one can expect, the larger the standard deviation, the larger the value of the incapability indices.

As was emphasized in Kotz and Lovelace (1998), results of calculations of process capability indices should always be qualified via confidence regions with a discussion of the impact of the sample size and sampling scheme on the index estimation. On the other hand, as in Hsu et al. (2008), since the minimun performance of a process is required for quality assurance, a lower confidence bound (LCB) of a capability index can therefore be used to provide critcal information regarding process performance. Therefore, an upper confidence bound of the incapability index $C''_{pp}(a,b)$ is worth to study.

Let $\mathbf{X}$ be an observable random vector with the cdf $F(\mathbf{x}|\tilde{\theta})$, where $\tilde{\theta} = (\tilde{\theta}_1, \tilde{\theta}_2)$ is a vector of unknown parameters, $\tilde{\theta}_1$ is the parameter vector of interest, and $\tilde{\theta}_2$ is a vector of nuisance parameters. A conventional approach to construct confidence intervals of θ is based on a certain kind of pivotal quantity. However, statistical inferences of such kind of pivote quantity may not be easy to handle. For instance, in the current case, Pan and Lee proposed the natural estimator of $C''_{pp}(a,b)$ as the following (for convenience, let's denote it as PLE):

$$\hat{C}''_{pp}(a,b) = \begin{cases} \frac{1}{D^2}\{d^2[\frac{T-\bar{X}}{D_l}]^a + S^2_{n-1}\} & \text{if } \bar{X} < T \\ \\ \frac{1}{D^2}\{d^2[\frac{\bar{X}-T}{D_u}]^b + S^2_{n-1}\} & \text{if } \bar{X} > T, \end{cases}$$

$$C''_{pp}(a,b) = \frac{md(a,b)}{D^2} + (\frac{\sigma}{D})^2,$$

where the modified desirability function $md(a,b)$ is defined as :

$$md(a,b) = \begin{cases} \frac{d^2}{D_l^a}(T-\mu)^a & \text{if } \mu < T \\ \\ \frac{d^2}{D_u^b}(\mu - T)^b & \text{if } \mu > T. \end{cases}$$

It was further suggested that the two parameters $a = \frac{USL-LSL}{D_u}$ and $b = \frac{USL-LSL}{D_l}$. Notice that $a > b$ if $D_l > D_u$ and $a < b$ if $D_l < D_u$. In addition, $C''_{pp}(2,2) = C''_{pp}$, and $C''_{pp}(2,2) = C_{pp}$ when the target T is at the midpoint of the specification limits. Furthermore, when $\mu = T$, $C''_{pp}(a,b)$=C''_{pp}= C_{pp}=$(\frac{\sigma}{D})^2$. Even though the moments of the natural estimator $\hat{C}''_{pp}(a,b)$ of $C''_{pp}(a,b)$ were derived in Pan and Lee (2009), the distribution of the estimator is hard to get and is not easy to find the confidence bound of $C''_{pp}(a,b)$ either. Another approach for finding the confidence bound of the index is via generalized pivot quantity which was porposed by Weerahandi (1993).

There have been many researches apply the idea of generalized pivot quantity to discuss confidence limits on several process capability indices. Among them are Chang (2001), Mathew *et al.* (2007), Kurian *et al.* (2008), Hsu *et al.* (2008), Jose and Luke (2011, 2012) and Ye *et al.*(2011). In this article, we would like to discuss the confidence bound of the incapability index $C''_{pp}(a,b)$ based on a generalized pivot quantity. Throughout this article, all discussions are made assuming that a process is in a state of statistical control and the characteristic under investigation arises from a normal distribution with mean μ and standard deviation σ.

The rest of this paper is organized as the following: In section 2, based on the generalized pivot quantity, a point estimator and two methods for confidence bound of $C''_{pp}(a,b)$ are introduced. In section 3, a simulation study is conducted for the comparison between the natural estimator and the generalized pivot estimator, also the comparison between the two types of confidence bounds. In section 4, concluding remarks are given.

2 Generalized Condence bound of $C''_{pp}(a,b)$

As an example, consider the case when $LSL = 10, USL = 16$ and assume $T = 14$ which locates at the right hand side of the mid point of the specification interval. Then the parameters $D = 2/3, d = 3, D_u = 2, D_l = 4, a = 3, b = 3/2$. This implies that

1. Introduction

Let X be the process quality characteristic of interest with mean μ and standard deviation σ. Chan et al. (1988) proposed a general form C^*_{pm} of the process capability index C_{pm} to handle the problem of asymmetric tolerance where $C^*_{pm} = \frac{D}{\sqrt{\sigma^2+(\mu-T)^2}}$, $D = min\{D_l/3, D_u/3\}$, $D_l = T - LSL$, $D_u = USL - T$, LSL and USL are the lower and upper specification limits, respectively. T is the target (nominal) value such that $LSL < T < USL$. Greenwich and Jahr-Schaffrath (1995) modified the index further and introduced the incapability index C_{pp} by taking a reciprocal squared transformation of C^*_{pm} and is defined as $C_{pp} = ((\mu - T)/D)^2 + (\sigma/D)^2$. Notice that the transformation is bijective, therefore the C_{pp} index contains the same information as that of C^*_{pm}. In addition, C_{pp} provides an uncontaminated separation between information concerning the process precision and process accuracy. The advantage of this separation is the indication of the degree the process inaccuracy contribute to the process being incapable of meeting the specifications.

Even though the separated information of C_{pp} can be used to recongnize the processes which have different levels of proportion of conforming output, unfortunately, the advantage of handling asymmetric tolerance is disappeared. Chen (1998) pointed out that for processes with asymmetric tolerances, it might happen that processes with the same C_{pp} can have very different expected proportions non-conforming. For example, by assuming that the target $T = \{3 \cdot USL + LSL\}/4$ and $\sigma = d/3$, where $d = (USL - LSL)/2$ is the half length of the specification interval. Consider two processes with mean $\mu_1 = T - d/2$=(LSL+USL)/2 (the midpoint of the specification interval), and $\mu_2 = T + d/2 = USL$, respectively. It is obvious that the quality of these two processes are different and the exp cted propo tions non-conforming are approximately 0.27% and 50%. But it turns out that $C_{pp1} = C_{pp2} = 13$. Apparently, the index C_{pp} inconsistently measures process capability and process potential and can not properly reflect the true manufacturing risk for asymmetric tolerances.

To overcome such problem, by taking into account the asymmetry of the tolerances and the asymmetry of the corresponding loss function, Chen (1998) proposed a new incapability index C''_{pp} as $C''_{pp} = (A/D)^2 + (\sigma/D)^2$, where $A = max\{(\mu - T)d/D_u, (T - \mu)d/D_l\}$. Under the same parameter setting as the previous example, $C''_{pp1} = 8$, $C''_{pp2} = 40$, which leads to the same conclusion as the expected proportions non-conforming that the first process performs better than the second one.

By shifting the means of both processes given in Chen (1998) by one unit to the left, Pan and Lee (2009) pointed out that $C''_{pp1} = C''_{pp2} = 13$, but leads to very different nonconforming rates, namely 1.23% and 22.66% respectively. It means that the index C''_{pp} can't properly reflect the true manufacturing risk for asymmetric tolerances either. Therefore, Pan and Lee (2009) further proposed a modified incapability index $C''_{pp}(a,b)$ based on the idea of desirability function (Myers and Montgomery (1995)) as the following:

Inference on the process incapability index $C''_{pp}(a,b)$ based on Generalized Pivot Quantity

Sy-Mien Chen and Wen-Chi Lu

Department of Mathematics
Fu-Jen Catholic University, Taiwan, R.O.C.
smchen@math.fju.edu.tw

Abstract

Instead of process capability index, Greenwich and Jahr-Scharath (1995) provided an incapability index C_{pp} which can tell the process accuracy and precision separately. However, it only works for process with symmetric tolerance. Chen (1998) proposed a modified incapability index C''_{pp} which works fine for process with asymmetric tolerance. Pan and Lee (2009) modified C''_{pp} further to get a new incapability index $C''_{pp}(a, b)$, which not only preserve the advantages that C_{pp} and C''_{pp} have, but also perform well for extreme cases. In this article, we proposed a generalized pivot estimator based on the idea of generalized pivot quantity proposed by Weerahandi (1993). Two methods of finding confidence bound are derived based on the generalized pivot estimator. The coverage rate and the average length of these confidence intervals are also computed.

Key words: Process incapability index; Generalized pivot quantity; Generalized condence interval

2010 Mathematics Subject Classication : 62.

*Corresponding author: Tel: (02)2905-2451 E-mail address: smchen@math.fju.edu.tw

FU JEN STUDIES

SCIENCE AND ENGINEERING

No.47, May 2014

CONTENTS

輔仁學誌—理工類

中華民國103年5月　　第四十七期

目　錄

頁次